OFFSHORE WIND FARM CFD MODELLING: UNCERTAINTY QUANTIFICATION AND POLYNOMIAL CHAOS

A thesis submitted to the University of Manchester for the degree
of Doctor of Philosophy in the Faculty of Science and Engineering

2021

Diego M. Araya A.

Department of Mechanical, Aerospace and Civil Engineering

BLANK PAGE

Contents

List of Tables **9**

List of Figures **11**

List of Symbols **17**

List of Abbreviations **21**

Abstract **23**

Declaration **24**

Copyright Statement **25**

Acknowledgement **26**

Dedication **27**

Chapter 1: Introduction, Motivation and Aims **29**

1.1 Climate Change 29

1.2 Wind Energy 30

1.2.1 Offshore wind 31

1.2.2 Upscaling 32

1.2.3 Floating offshore wind 33

1.3 Challenges and Opportunities 33

1.4 Summary, aims and objectives of this work 35
1.4.1 Main objective 36
1.4.2 Specific objectives 36
1.5 Thesis structure 37
Chapter 2: Literature Review and Background Theory 39
2.1 Introduction 39
2.2 Wind energy physical system 40
2.2.1 Atmospheric boundary layer 40
2.2.2 Atmospheric stability 41
2.2.3 Wind shear profiles 44
2.2.4 Offshore wind climate 47
2.2.5 Wake effects 51
2.2.6 Time and length scales 54
2.3 Computational models 55
2.4 1D Momentum theory 56
2.5 Blade Element Momentum method 60
2.5.1 Reynolds Averaged Navier Stokes (RANS) Equations 65
2.5.2 Turbulence Modelling for Wind Farms 67
2.5.3 Wind turbine CFD models 69
2.6 Wind farm optimization 73
2.6.1 Micrositing 73
2.6.2 Active wake control 74
2.7 Uncertainty quantification in wind energy 78

2.7.1 Uncertainty quantification in wind energy 79

2.7.2 Polynomial Chaos 81

2.8 Summary and Conclusions 83

Chapter 3: Uncertainty Quantification **87**

3.1 Introduction 87

3.2 Uncertainty quantification 88

3.2.1 Uncertainty characterisation 89

3.2.2 Uncertainty propagation 90

3.2.3 Monte Carlo propagation 91

3.2.4 Spectral methods for uncertainty propagation 92

3.3 Generalised Polynomial Chaos 93

3.3.1 Non-Intrusive Spectral Projection (NISP) 97

3.3.2 Expected Value and Variance 98

3.3.3 Convergence of L^2Norm 99

3.3.4 Sobol's indices 100

3.4 Implementation and examples 100

3.4.1 Polynomial chaos library - gpcPy 100

3.4.2 Examples 101

3.5 Advantages and limitations of gPC 104

3.6 Summary and conclusions 108

Chapter 4: Wind turbine rotor modelling **109**

4.1 Introduction 109

4.2 ADM Implementation in OpenFOAM 109
4.2.1 Overview 109
4.2.2 Model description 111
4.2.3 Tip and root corrections 116
4.2.4 Force distribution 119
4.2.5 Nacelle and Hub Modelling 121
4.3 ADM Validation 122
4.3.1 Wind tunnel experiments 122
4.3.2 Benchmark Models 126
4.3.3 Cases of Interest for Validation 127
4.3.4 Simulations Setup 128
4.3.5 Results and Discussion 130
4.4 Summary and Conclusions 145

Chapter 5: Atmospheric Boundary Layer Model 147

5.1 Introduction 147
5.2 Modelling neutral ABL 148
5.3 OpenFOAM boundary conditions 151
5.3.1 Wall function for momentum equation 152
5.3.2 Wall functions for turbulent quantities 155
5.4 Neutral HHABL test cases 156
5.4.1 Domain and grids 156
5.4.2 Standard $k-\varepsilon$ base case 160
5.4.3 $k-\omega-SST$ base case 169

5.4.4 Summary of new BCs implemented 171
5.5 Mesh sensitivity analysis 174
5.5.1 Near wall refinement 174
5.5.2 Horizontal Resolution 174
5.6 Reference velocity and aerodynamic roughness 177
5.6.1 Changing the inflow reference velocity 177
5.6.2 Changing the aerodynamic roughness 177
5.7 Testing SnappyHexMesh grid 180
5.8 Summary and conclusions 185
Chapter 6: UQ Framework - gpcADM **187**
6.1 Introduction 187
6.2 UQ Framework - gpcADM 187
6.2.1 Pre-processing 188
6.2.2 Running 191
6.2.3 Post-processing 191
6.3 Test Cases Description 191
6.3.1 Turbine arrays tested 192
6.3.2 Computational meshes 193
6.3.3 Random Variables and Operating Conditions 195
6.3.4 gPC Settings 196
6.3.5 Test Cases Nomenclature 197
6.4 Results and discussion 198
6.4.1 Test 1: gPC-A1-L-U0WD 198

6.4.2 Test 2: gPC-A1-L-z0WD 203

6.4.3 Test 3: gPC-A3-L-U0WD 207

6.4.4 Test 4: gPC-A3-L-z0WD 215

6.5 Summary and conclusions 217

Chapter 7: Conclusions and future work **219**

Bibliography **225**

Appendix A: Orthogonal Polynomials **241**

A.1 Orthogonal Polynomials 241

A.2 Legendre Polynomials 242

A.3 Hermite Polynomials 243

Appendix B: Experimental test cases **245**

B.1 NREL UAE Phase VI (NREL-VI) 245

B.2 MEXICO Experiments 246

Appendix C: Benchmark models **253**

Appendix D: ADM Sensitivity to cell size and smearing parameter ϵ **257**

D.1 Mesh Resolution Sensitivity 257

D.2 Smearing parameter ϵ 262

Word count: 39,073

List of Tables

3.1 Single- and multi-indexing correspondence in 2 dimensions 96

4.1 Benchmark models used for validation of ADM 127

4.2 NREL-VI cases used for validation of ADM 128

4.3 New-MEXICO cases used for validation of ADM 128

5.1 Mesh details for testing ABL model and BCs 158

5.2 Base case for testing boundary conditions for ABL model 161

5.3 New boundary conditions implemented 171

6.1 List of random variables used in gPC cases 196

6.2 gPC settings. 197

6.3 Summary of statistical parameters for gpc case series gPC-A1-L-U0WD. 202

6.4 Summary of statistical parameters for gpc case series gPC-A1-L-z0WD. 206

6.5 Summary of statistical parameters for gpc case series gPC-A3-L-U0WD. 213

B.1 NREL UAE Phase VI blade geometry. 246

B.2 S809 lift coefficient C_l as function of AOA and Re_c 247

B.3 S809 drag coefficient C_d as function of AOA and Re_c 248

B.4 MEXICO rotor blade geometry 249

B.5 MEXICO rotor blade geometry with interpolated values 249

B.6 2D Airfoil data for DU91-W2-250 airfoil (2D rough $Re_c = 0.5 \times 10^6$) . 250

B.7 2D Airfoil data for RISO-A1-21 airfoil (2D rough $Re_c = 1.6 \times 10^6$) . . 250

B.8 2D Airfoil data for NACA-64-418 airfoil (2D clean $Re_c = 0.7 \times 10^6$) . 251

B.9 2D Airfoil data for NACA-64-418 airfoil (2D rough $Re_c = 0.7 \times 10^6$) . 251

List of Figures

2.1 Variability of stability at Rødsand mast in the baltic sea 48

2.2 Turbulence intensity from Rødsand mast in the Baltic Sea 50

2.3 Turbulence intensity against wind speed from FINO1 in the North Sea 50

2.4 Schematic representation of a turbine wake 52

2.5 Control volume for momentum balance in the axial direction 57

2.6 Maximum C_P as a function of the TSR with wake rotation 59

2.7 Control volume for BEM 61

2.8 Lift and drag decomposition into thrust and torque. 61

2.9 Velocity triangle at airfoil section. 62

3.1 Schematic representation of Monte Carlo propagation 91

3.2 Schematic representation of spectral methods for UQ. 92

3.3 Example 1 exact surface and contour plots 102

3.4 Example 2 exact surface and contour plots 103

3.5 Example 3 exact surface and contour plots 104

3.6 Example 1 gPC response surfaces and relative error 105

3.7 Example 2 gPC response surfaces and relative error 106

3.8 Example 3 gPC response surfaces and relative error 107

4.1 Flow diagram showing how `turbineDisk` works. 111

4.2 Actuator disk schematic representation 112

4.3 Difference between standard ADM models and `turbineDisk` ADM . 114

4.4 Smearing factor η_ϵ as a function of ϵ 120

4.5 NREL-VI experiment at NASA Ames Research Centre 123

4.6 MEXICO experiment at DNW Large Scale Low-Speed Facility (LLF) 125

4.7 Torque and thrust comparisons NREL-VI 131

4.8 Reynolds number Re_c along the blades NREL-VI. 132

4.9 NREL-VI comparison of normal and tangential forces along the blades 134

4.10 NREL-VI comparison of AOA and induced velocities along the blades 135

4.11 New-MEXICO Power an Thrust coefficients as a function of TSR . . 137

4.12 New-MEXICO Normal and tangential forces along the blades 140

4.13 New-MEXICO AOA and induced velocities along the blades 141

4.14 New-MEXICO Axial traverses of axial, radial and tangential velocities 142

4.15 New-MEXICO upstream radial traverses of axial, radial and tangential velocities 143

4.16 New-MEXICO downstream radial traverses of axial, radial and tangential velocities 144

5.1 Schematic representation of the domain for structured grids. 157

5.2 Mesh sections showing the horizontal and near wall refinement 159

5.3 Vertical profiles of U_x, k and ε along the domain 162

5.4 Influence of top boundary condition for momentum equation 164

5.5 Effect of prescribing fixed values k and ε at the top boundary 166

5.6 Effect of U based friction velocity to calculate the corrected eddy viscosity $\nu_{t,c}$ 168

5.7 Test cases of ABL model using the $k - \omega - SST$ turbulence closure . 170

5.8 HHABL obtained with new boundary conditions for both the $k - \varepsilon$ and the $k - \omega - SST$ models 173

5.9 Effect of the near wall refinement in streamwise gradients 175

5.10 Effect of the horizontal resolution in streamwise gradients 176

5.11 Influence of the inflow reference velocity U_{ref} 178

5.12 Influence of the aerodynamic roughness z_0 179

5.13 Example of *SnappyMesh* generated with `blockMesh`, `snappyHexMesh` and `extrudeMesh`. 180

5.14 Unstructured grid - SnappyMesh 182

5.15 Comparisons of HHABL profiles between structured and unstructured grids 183

5.16 Comparisons of HHABL error profiles between structured and unstructured grids 184

6.1 Flow diagram showing how `gpcADM` works. 189

6.2 Layout of tubine array $A1$ 192

6.3 Layout of tubine array $A3$ 193

6.4 Mesh details around the rotor and close to the ground 194

6.5 Section of computational grid of array $A1$ showing mesh refinement . 194

6.6 Section of computational grid of array $A3$ showing mesh refinement . 195

6.7 Response surfaces of **Power** at each turbine of array $A1$ gPC-A1-L-U0WD 199

6.8 Response surfaces of **Thrust** at each turbine of array $A1$ gPC-A1-L-U0WD 200

6.9 Probability density functions for **Power** and **Thrust** gPC-A1-L-U0WD 201

6.10 Convergence of L^2Norm for **Power** and **Thrust** at each turbine in gPC-A1-L-U0WD 202

6.11 Response surface of **Power** at each turbine gPC-A1-L-z0WD 203

6.12 Probability density functions for **Power** and **Thrust** at each turbine gPC-A1-L-z0WD 205

6.13 Convergence of L^2Norm for **Power** and **Thrust** at each turbine in gPC-A1-L-z0WD 205

6.14 Contour plots of velocity magnitude $|\vec{U}|$ at hub height 208

6.15 Contour plots of vertical velocity component U_z at hub height 209

6.16 Response surface of **Power** at turbines $T1$, $T2$, $T3$ and $T4$ with the highest order $p = 11$ gPC-A3-L-U0WD 210

6.17 Response surface of **Power** at turbine $T4$ increasing order $p = 1, 3, 5, 7, 9, 11$ gPC-A3-L-U0WD 211

6.18 Response surface of the **Total Power** of the array increasing order $p = 1, 3, 5, 7, 9, 11$ gPC-A3-L-U0WD 212

6.19 Convergence of L^2Norm for **Power** and **Thrust** at each turbine gPC-A3-L-U0WD 213

6.20 Probability density functions for **Power** (left) and **Thrust** (right) at each turbine gPC-A3-L-U0WD 214

6.21 Response surface of **Power** at turbine $T4$ increasing order $p = 5, 7, 9, 11$ gPC-A3-L-z0WD 215

6.22 Convergence of L^2Norm for **Power** and **Thrust** at $T4$ gPC-A3-L-z0WD 216

6.23 Probability density functions for **Power** (left) and **Thrust** (right) at each turbine gPC-A3-L-z0WD 216

A.1 The first six Legendre polynomials up to order $p = 5$. 242

A.2 The first six Hermite polynomials up to order $p = 5$. 243

D.1 Loadings along the blades of New-MEXICO experiment varying the grid resolution 258

D.2 Axial traverses for U_x, U_r and U_t velocity components varying grid resolution 259

D.3 Radial traverses for axial U_x, U_r and U_t velocity components varying grid resolution 260

D.4 Sensitivity of power and thrust coefficients (C_P, C_T) to the grid resolution 261

D.5 Loadings along the blades of New-MEXICO experiment varying the smearing parameter ϵ 263

D.6 Axial traverses for U_x, U_r and U_t velocity components varying smearing parameter ϵ 264

D.7 Radial traverses for U_x, U_r and U_t velocity components varying ϵ . . . 265

D.8 Sensitivity of power and thrust coefficients to the smearing parameter ϵ 266

BLANK PAGE

List of Symbols

Symbol	Description	Units
a	Axial induction factor	–
a'	Rotational induction factor	–
A	Wind turbine rotor area	m^2
B	Number of blades	units
c	Airfoil chord length	m
C_P	Power coefficient	–
C_T	Thrust coefficient	–
C_l	Lift coefficient	–
C_d	Drag coefficient	–
c_p	Specific heat	$\mathrm{kJ\ kg^{-1}\ K^{-1}}$
C_μ	Ratio between turbulent shear stress and turbulent kinetic energy	–
D	Wind turbine rotor diameter	m
F	End effects correction factor in ADM (tip and root corrections)	–
F_T	Thrust force	N
F_θ	Tangential force (producing torque)	N
F_M	Torque	Nm
F_t	Tangential force (chordwise component)	N
F_n	Normal force (normal to chord length)	N
F_L	Lift force	N
F_D	Drag force	N
g	Acceleration of gravity	$\mathrm{m\ s^{-2}}$

List of Symbols (continued)

Symbol	Description	Units
G	Geostrophic wind velocity	m s^{-1}
TI	Turbulence intensity	%
k	Turbulent kinetic energy	m^2s^{-2}
L	Monin-Obukhov length	m
N	Number of random variables	units
n_{q_i}	Number of quadrature points for random variable i	units
P_k	Production of turbulent kinetic energy	m^2s^{-3}
P	Power	W
p	Order of polynomial expansion	−
p	Pressure	Pa
p_0	Surface pressure	Pa
R	Gas constant	kJ kg^{-1} K^{-1}
s	A mathematical model	−
s_k	Polynomial expansion coefficients of model s	−
S_i	Sobol index for random variable ξ_i	−
T	Temperature	K (° C)
$\vec{U}$	Velocity vector field	m s^{-1}
U	Velocity magnitude	m s^{-1}
U_{ref}	Velocity magnitude at reference height z_{ref}	m s^{-1}
U_0	Free stream velocity magnitude	m s^{-1}
U_R	Mean axial velocity at rotor area	m s^{-1}
U_W	Mean axial velocity in far wake region	m s^{-1}
$U_{\theta,R}$	Tangential velocity at the rotor plane	m s^{-1}
$U_{\theta,R,rel}$	Tangential velocity at the rotor plane relative to airfoil section	m s^{-1}
U_{ai}	Axial induced velocity	m s^{-1}
U_{ti}	Tangential induced velocity	m s^{-1}
U_x	Axial velocity component	m s^{-1}

List of Symbols (continued)

Symbol	Description	Units
U_t	Tangential velocity component	m s^{-1}
U_r	Radial velocity component	m s^{-1}
u_*	Friction velocity based on turbulent kinetic energy k	m s^{-1}
u_τ	Friction velocity based on wall shear stress τ_w	m s^{-1}
V_{rel}	Relative velocity at airfoil section	m s^{-1}
z	Height (within ABL)	m
z_{ref}	Reference height	m
z_{bl}	Atmospheric boundary layer height	m
z_0	Aerodynamic roughness	m
α	Angle of attack (AOA)	deg (°)
α_P	Power law exponent also known as wind shear coefficient	−
α_{Ch}	Charnock parameter	−
β	Blade pitch angle	deg (°)
γ	Blade local twist angle	deg (°)
γ_l	Atmospheric lapse rate	K m^{-1}
Γ_p	Polynomial terms of order p in chaos expansion	−
ϵ	Smearing parameter in ADM	−
ε	Turbulent dissipation rate	m^2 s^{-3}
ζ	Stability parameter defined as z/L	m
η	Efficiency	−
η_ϵ	Smearing factor in ADM	−
θ	Potential temperature	K (° C)
θ_v	Virtual potential temperature	K (° C)
κ	von Karman constant	−
λ	Tip speed ratio (TSR)	−

List of Symbols (continued)

Symbol	Description	Units
μ	Dynamic viscosity	kg m^{-1} s^{-1}
ν	Kinematic viscosity	m^{2}s^{-1}
ν_t	Turbulent kinematic viscosity	m^{2}s^{-1}
$\boldsymbol{xi}$	Multivariate random variable	$-$
ρ	Air density	kg m^{-3}
σ	Standard deviation	$-$
σ_s	Solidity	$-$
τ	shear stress	Pa
τ_w	Wall shear stress	Pa
ϕ	Angle of incidence of relative velocity vector	°
$\mathbf{\Psi}$	Orthogonal basis in polynomial chaos expansion	$-$
ψ	Family of orthogonal polynomials	$-$
Ω	Stability correction function for shear profiles	$-$
ω	Rotational speed of wind turbine rotor	rad s^{-1}(rpm)
Re	Reynolds Number	$-$
Re_c	Reynolds Number based on chord length	$-$
Ri	Richardson Number	$-$
Ri_b	Bulk Richardson Number	$-$
Ri_{cr}	Critical Richardson Number	$-$

List of Abbreviations

Abbreviation	Meaning
ABL	Atmospheric boundary layer
ADM	Actuator disk model
AEP	Annual energy production
ALM	Actuator line model
BEM	Blade element momentum theory
CFD	Computational fluid dynamics
DNS	Direct numerical simulation
EAWE	European Academy of Wind Energy
EVM	Eddy viscosity model
FRS	Full rotor simulation (blade resolved simulation)
GHG	Greenhouse gas
GPC	Generalised polynomial chaos
HAWT	Horizontal axis wind turbine
HHABL	Horizontally homogeneous boundary layer
IPCC	Intergovernmental Panel on Climate Change
IRENA	International Renewable Energy Agency
LCOE	Levelised cost of energy
LES	Large eddy simulation
MEXICO	Model Experiments in Controlled Conditions
MOST	Monin-Obukhov similarity theory
NDC	Nationally determined contribution
NISP	Non-intrusive spectral projection
NLEVM	Non-linear eddy viscosity model

List of Abbreviations (continued)

Abbreviation	Meaning
NREL	The U.S. National Renewable Energy Laboratory
NREL-VI	NREL Unsteady Aerodynamics Experiment Phase VI
NREL-5MW	5 MW reference turbine from NREL
RANS	Reynolds averaged Navier-Stokes
SCADA	Supervisory control and data acquisition system
SOWFA	Simulator fOr Wind Farm Applications from NREL
TSR	Tip speed ratio
UNFCCC	United Nations Framework Convention on Climate Change
UQ	Uncertainty quantification
WFABL	Wind farm atmospheric boundary layer

Abstract

Wind energy will play an essential role in the fight against climate change. By 2050 it is expected to be about a quarter to one third of the total electricity generation. One of the main disadvantages of wind energy is its high variability and low predictability, influenced by physical phenomena at a wide range of time and length scales. The chaotic nature of wind limits the ability of engineering models to predict the performance of wind farms. Furthermore, as wind turbines and wind farms continuously increase in size, thereby increasing their contribution to the power generation industry, the need to better understand the aerodynamic interaction between wind turbines and the atmospheric boundary layer has also increased. Computational fluid dynamics has become an essential tool to enhance our understanding of wind turbine aerodynamics, however, uncertainties are usually overlooked, due to the high computational cost and the lack of characterisation of the different sources of uncertainties.

This thesis presents the development of a new computational framework for uncertainty quantification in offshore wind farms. Uncertainty quantification has been identified as one of the key research challenges in the wind energy industry and this work aims to provide a tool that facilitates the propagation of uncertainties in CFD models of wind farms. It is expected that this tool can help to increase our understanding of the wind energy physical system by increasing the amount of information obtained from CFD models providing greater insights and improving the accuracy and confidence on their predictions.

The framework implemented integrates the generalized polynomial chaos method (gPC) with OpenFOAM, where a non-axisymmetric actuator disk model (ADM) has been implemented. The ADM was validated against MEXICO and NASA Ames NREL-Phase-VI experiments, and other state-of-the-art numerical models. The framework has been named `gpcADM` and it has been tested with relatively simple wind turbine arrays considering inflow parameters as random variables. `gpcADM` captures the response of the system and provides probability density functions for any quantity of interest with a reduced number of deterministic evaluations compared to other traditional sampling strategies.

Declaration

No portion of the work referred to in the thesis has been submitted in support of an application for another degree or qualification of this or any other university or other institute of learning.

Copyright Statement

i The author of this thesis (including any appendices and/or schedules to this thesis) owns certain copyright or related rights in it (the Copyright) and s/he has given The University of Manchester certain rights to use such Copyright, including for administrative purposes.

ii Copies of this thesis, either in full or in extracts and whether in hard or electronic copy, may be made only in accordance with the Copyright, Designs and Patents Act 1988 (as amended) and regulations issued under it or, where appropriate, in accordance with licensing agreements which the University has from time to time. This page must form part of any such copies made.

iii The ownership of certain Copyright, patents, designs, trademarks and other intellectual property (the Intellectual Property) and any reproductions of copyright works in the thesis, for example graphs and tables (Reproductions), which may be described in this thesis, may not be owned by the author and may be owned by third parties. Such Intellectual Property and Reproductions cannot and must not be made available for use without the prior written permission of the owner(s) of the relevant Intellectual Property and/or Reproductions.

iv Further information on the conditions under which disclosure, publication and commercialisation of this thesis, the Copyright and any Intellectual Property and/or Reproductions described in it may take place is available in the University IP Policy (see http://documents.manchester.ac.uk/DocuInfo.aspx?DocID=24420), in any relevant Thesis restriction declarations deposited in the University Library, The University Librarys regulations (see http://www.library.manchester.ac.uk/about/regulations/) and in The Universitys policy on Presentation of Theses.

Acknowledgement

I would like to thank my supervisors, Dr Imran Afgan and Prof Timothy Stallard, for their guidance and support throughout this study.

I would also like to thank my examiners, Prof Kürsad Melih Güleren and Dr David Apsley, for their valuable feedback that significantly contributed to improve the quality of this work.

I also want to thank the IT Services team that manages the Computational Shared Facility (CSF) for High-Performance Computing at the University of Manchester.

This work was funded by the National Agency for Research and Development (ANID), from the Chilean Ministry of Science, Technology, Knowledge and Innovation. Scholarship Program: *Becas para doctorado en el extranjero – convocatoria 2016*. Therefore, I am grateful to all taxpayers in Chile, since everyone of them has made a tiny contribution that made this work possible.

Finally, I would like to express my gratitude to my colleagues for all the very good times we shared and the MACE PGR Society that promotes a positive working environment.

Dedication

This work is dedicated:

To my parents, for their unconditional love and support in this unprecedented journey, for all the sacrifices you have done that made this possible.

&

To my wife, for being the perfect partner in this endeavour.

&

To my sister and brothers, for encouraging me to pursue my dream and for caring for our parents in my absence in these difficult times.

To all of you, I will be for always grateful.

BLANK PAGE

Chapter 1

Introduction, Motivation and Aims

1.1 Climate Change

One of the biggest challenges that humanity is currently facing is climate change. Anthropogenic greenhouse gas emissions are causing long-term changes in the climate system, increasing the global mean temperature and sea levels, causing extreme weather events, affecting the ecosystem and the services they provide to human activities. Biodiversity loss and changes in precipitation patterns threaten our food security, water supply and economic growth. Global warming has already altered many ecosystems and the services they provide and it is likely the impacts caused will be irreversible, particularly if the temperature increase is above 1.5°C (IPCC, 2018).

By the end of 2015, the Paris Agreement was established by the United Nations Framework Convention on Climate Change (UNFCCC), which main objective is to limit the increase of global average temperature below 2°C above pre-industrial levels and make all efforts to limit the increase even further to 1.5°C above pre-industrial levels (United Nations, 2015). The IPCC (2018) report stated that a possible pathway to limit temperature increase to 1.5°C would require a decline in

CO_2 emissions by 45% of 2010 levels by 2030 and reaching net zero by 2050. However, recently the Emission Gap Report (United Nations Environment Programme, 2020) revealed that GHG emissions have increased at an average rate of 1.3% per year since 2010, and that even with full implementation of unconditional nationally determined contributions (NDCs) under the Paris Agreement it is estimated that global averaged temperature will be 3.2°C higher by the end of the century. Fortunately, an increasing number of countries have set net-zero emission targets by 2050, including the UK, which was the first major economy to pass a net-zero emission law through parliament in 2019 (UK Government, 2019).

The energy sector (electricity, heat and transport) accounted for 73.2% of the total Greenhouse Gas Emissions worldwide by 2016 (Ritchie and Roser, 2020). Therefore, considering a continuously increasing energy demand as global population rises, decarbonising the energy sector is essential if net-zero emissions are to be achieved. In this context, renewable energy sources such as solar and wind, have quickly become competitive alternatives to fossil fuels for electric power generation, and with the growing interest in Power-to-X technologies, such as green hydrogen, it is likely that these renewable sources will contribute decarbonising the heat and transport sectors as well.

1.2 Wind Energy

Wind energy is rapidly increasing its participation worldwide. In 2019, the new installed capacity of wind energy globally was 60.4 GW reaching a total of 651 GW (Lee and Zhao, 2020). In Europe, since 2016 wind energy is the second largest installed capacity of power generation (Wind Europe, 2018) and in 2019, when 15.4 GW were added to the grid, wind supplied 15% of the electricity consumed that year (Wind Europe, 2020). As more countries have set ambitious targets, as part of plans for the economic recovery after the COVID-19 pandemic, the Global Wind Energy Council estimates that 71 GW of wind will be installed each year until 2024 adding 355 GW (Lee and Zhao, 2020). That would be more than a 50% increase in just five years. Overall, it is expected that wind will be a primary source of power generation accounting for up to one-quarter to one-third of the total electricity demand by 2050 (Veers et al., 2019). In 2019, the International Renewable Energy Agency (IRENA) estimated that the global cumulative installed capacity of onshore and offshore wind by 2050 would be about 5000 GW and 1000 GW respectively (IRENA, 2019).

1.2.1 Offshore wind

From a global perspective, it could be argued that offshore wind is just starting. In 2017 offshore wind represented 3.5% of the total global wind capacity with 18.8 GW, but in 2019 new installation reached a record high with 6.1 GW increasing the total offshore capacity to 29 GW representing a 4.5% of the total installed wind capacity (Lee and Zhao, 2020). However, a significant increase in offshore wind is expected in the coming years. For instance, the UK alone plans to install 40 GW of offshore wind by 2030 (UK Government, 2020). This is about half the total installed capacity of major UK power stations in 2020 ($\sim$ 80.4 GW).

The offshore climate is considerably different to onshore. Changes in thermo-physical properties, as well as the topography, between the ground and sea surfaces produce distinctive wind characteristics (e.g. wind shear, atmospheric stability, and turbulence intensity). Offshore wind offers some important advantages compared to onshore wind. First of all, stronger winds at lower altitudes increase the load factors. In Europe, offshore load factors are around 33% to 43% (Wind Europe, 2017). Secondly, offshore wind is in general more consistent with lower turbulence due to the smooth sea surface, increasing the lifespan of the turbines. Thirdly, there are fewer transportation constraints. And finally, there is very high wind energy potential with plenty of available space, currently limited mainly by the distance to shore and water depth for fixed bottom turbines (i.e. up to 50-60 m), but this will be extended up to 1 km for floating wind turbines being developed.

1.2.2 Upscaling

Up-scaling of wind turbines and wind farms have changed the scenario in recent years, reducing the costs and making it more competitive with conventional power sources (Global Wind Energy Council, 2018). One approach to reduce the costs consists in up-scaling the size of wind turbines and wind farms. The power output of wind turbines is proportional to the square of the rotor diameter ($P \propto D^2$), besides the wind speed increases with altitude and the power is proportional to the cube of wind speed ($P \propto U^3$). Therefore it is clear that up-scaling is the natural evolution of wind turbines to increase the power output. However, the weight and the loads scale up proportional to the cube of the diameter (D^3), and as a result, structural design, materials and building methods have to be improved. Up-scaling has also a positive effect in reducing wake losses. Since the power output increases with the square of the rotor diameter and the wake losses decrease linearly with turbine spacing, for a given area and power rating for a wind farm, large wind turbines will increase the turbine spacing reducing wake losses (Barthelmie et al., 2011).

According to Wind Europe (2017), the average offshore turbine size (rated capacity) installed in 2016 was 4.8 MW. In the same year, the first 8 MW turbines were installed in the Irish Sea as part of the Burbo Bank Extension project, with 32 turbines of 164 m rotor diameter and 105 m hub height. In 2018, General electric announced a 12 MW wind turbine named Heliade-X, and in 2020 launched an uprated version, the Heliade-X 13 MW wind turbine, with a 220 m rotor diameter, and it will supply 190 units for the UK's Dogger Bank Wind Farm (General Electric, 2020). Similarly, Siemens Gamesa launched in 2020 a 14 MW offshore wind turbine with a 222 m rotor diameter with serial production planned for 2024 (Siemens Gamesa Renewable Energy, 2020).

Furthermore, not only the size of individual wind turbines is increasing, but also the size of the wind farms. In 2016 the averaged size of offshore wind farms connected to the grid was about 380 MW (Wind Europe, 2017). In 2018, the Walney Extension and London Array were the first and second largest offshore wind farms in the world, with 659 MW and 630 MW respectively (both in the UK). Currently, the Hornsea 1 is the largest wind farm with 1.2 GW and the project Hornsea 2 is expected to add 1.4 GW by 2022 (Ørsted, 2018). Furthermore, two additional Hornsea projects are being developed, the Hornsea 3 and the Hornsea 4.

1.2.3 Floating offshore wind

Floating wind brings new challenges and opportunities. It extends the offshore wind potential to waters deeper than 60 m where is estimated that about 80% of the global offshore wind resource is located. Further out to the sea, due to stronger and more consistent winds, less affected by coastal effects, higher capacity factors are expected. Besides, floating systems are anticipated to be easier to install having the potential to be fully assembled at construction ports reducing more risky labour at the sea. By 2018 seven utility scale floating turbines had been installed worldwide testing their feasibility and currently there are about 229 MW of floating wind plants being developed (Barter et al., 2020). Nevertheless, as a new technology there are plenty of new challenges and open questions, from the design of the wind turbines, the floating substructures and mooring lines, to the dynamic reponse of the system with additional degrees of freedom. Without any doubt, an exciting new field of research has been opened.

1.3 Challenges and Opportunities

Although wind energy has been developed to a competitive level, there are still many challenges that need to be faced for wind energy to take a role as a primary source of power generation. One of the main drawbacks of wind energy is its high variability and low predictability. Accurate predictions of power output are critical for its integration into the grid as wind energy becomes a significant part of the total power generation. The cost of wind energy is influenced by the environment. Consequently, the accuracy in its prediction is limited by our capacity to characterise, understand and model the physics of all the relevant phenomena at all the appropriate time and length scales. To a great extent, this understanding is constrained to our measuring and computing capabilities.

So far, the design of wind turbines and wind farms has relied on simplified engineering tools. Typically, the inflow wind is characterised by simple wind shear models. Turbulence characteristics and stability conditions are obtained from mast measurements. Note that all these characteristics are governed by the properties of the environment upstream such as the aerodynamic roughness or land use, temperature gradients, moisture, clouds, etc. Similarly, simplified engineering wake models have been used to optimize wind farm layouts reducing wake effects and maximising the estimations of the Annual Energy Production (AEP). All these engineering tools have contributed significantly to the development of wind energy, but as wind turbines and wind farms become larger, the underlying assumptions in such models are no longer valid. For instance, large wind turbines are very likely to operate outside the surface layer at certain times, particularly under stable atmospheric conditions, where the logarithmic wind shear profile is not suitable and where the characteristics of the wind are not yet completely understood. Another example comes from Bleeg et al. (2018), who showed that wind farm blockage effects cannot be analysed with traditional wake superposition methods.

On the other hand, computational fluid dynamics (CFD) has proven to be an effective way of improving our understanding of wind turbine aerodynamics providing insights that sometimes cannot be easily measured in an experiment (Sanderse et al., 2011; Schepers et al., 2012, 2014, 2018). However, because CFD models are still relatively expensive, the uncertainty in input parameters (e.g. boundary conditions and model coefficients) is usually overlooked. Fortunately, as computers have become more and more powerful over the years, new opportunities arise to improve existing and create new computational tools. Some studies have incorporated wind direction uncertainty in modelling wind turbines and wind farms by running an ensemble of simulations at different directions and computing weighted averaged results (Gaumond et al., 2014; Wu and Porté-Agel, 2015; Antonini et al., 2019). Nevertheless, this approach is arguable not the most efficient while other methods, such as polynomial chaos, have become a promising alternative to reduce the number of deterministic evaluations as it has been shown in CFD in other fields (Han et al., 2012; Gorlé et al., 2016; Karimi et al., 2019).

1.4 Summary, aims and objectives of this work

This introductory chapter described the big picture of wind energy and the challenges ahead. Wind power will be crucial for decarbonising the energy sector, reducing GHG emissions, limiting the increase in global mean temperature, and as a consequence, mitigating the negative impacts of climate change.

The wind energy system is very complex and chaotic in nature and involves physical phenomena across a wide range of time and length scales, and even though, the wind energy industry has relied in simple engineering tools for many years, as the wind turbines and wind farms increase in size, and as wind power continue to increase its participation in the electrical system, new engineering tools are needed to address the challenges ahead.

New engineering tools are needed to improve our understanding of the atmospheric flows and its interactions with the new generation of wind turbines and wind farms. Turbulence at all scales needs to be understood and modelled, and even though there are well developed models at different scales (e.g. weather prediction models, wind turbine aeroelastic models, etc), the problem is how to combine them, how to determine what simplifications are feasible and what sources of uncertainty are introduced by such simplifications (van Kuik et al., 2016). More importantly is to identify whether there are 'missing' environmental factors that impact power generation and structural safety that are not present in current standards (van Dijk et al., 2016; Veers et al., 2019).

Furthermore, uncertainty quantification is highlighted as a key research challenge as uncertainties are an inherent part of wind power generation, and as more accurate estimates are needed.

1.4.1 Main objective

The present work aims to develop an efficient computational framework to systematically assess the influence of different sources of uncertainties in offshore wind farms using CFD simulations.

The main objective of this framework is to increase the information obtained from CFD models by providing not only a single value answer to a specific problem, but a probability distribution function of any quantity of interest being analysed.

In general, uncertainty quantification involves two main steps. In the first place, there is a need to identify and characterise the different sources of uncertainty (uncertainty characterisation); and secondly, these uncertainties are propagated using stochastic computational models to assess their influence on the response of the system (uncertainty propagation). The computational cost of these algorithms depends on two main aspects: the cost of the deterministic models used and the number of deterministic evaluations required.

This work focuses on the uncertainty propagation step. Therefore, one of the key considerations is keeping a balance between model accuracy and computational cost. For this reason, Reynolds Averaged Navier-Stokes (RANS) will be used as governing equations and polynomial chaos as the propagation algorithm. For now, polynomial chaos should be understood as a regression algorithm that finds the response of a system under uncertainty with a reduced number of deterministic evaluations. Chapter 3 is dedicated to present the polynomial chaos method in detail.

1.4.2 Specific objectives

The specific objectives are:

1. To implement and validate a CFD model that captures the main physics and flow features in a wind farm. The model is implemented in OpenFOAM, which is an open source multi-physics C++ library widely used for Computational

Fluid Dynamics (The OpenFOAM Foundation, 2020). The CFD model implemented consists of two main components:

- The wind turbine model that accounts for wind turbine aerodynamics where loadings are calculated, and;
- The atmospheric boundary layer model that aims to reproduce a horizontally homegeneous boundary layer free of streamwise gradients.

2. To implement and validate a library for the polynomial chaos algorithm. This is done in Python, an open source high-level and general purpose programming language (Python, 2020).
3. To construct the computational framework for uncertainty quantification by integrating the OpenFOAM CFD model and Python polynomial chaos algorithm.

1.5 Thesis structure

The thesis is organised in 6 additional chapters. Chapter 2 presents the literature review and theoretical background. It describes the main physical aspects of wind turbines and wind farms including the atmospheric boundary layer, wake effects, wind farm control and computational models. It highlights some of the key challenges in wind energy and the role of CFD models and uncertainty quantification to face them.

Each of the following three chapters is overall self-contained describing the different components of the computational framework implemented. Chapter 3 presents the fundamental concepts of uncertainty quantification and in particular, provides a description of the generalised polynomial chaos (gPC) method and how it has been implemented in a Python library. Some simple examples to test its capabilities and limitations are shown and discussed. Chapter 4 deals with the CFD model of wind turbine rotors. Here, a RANS-BEM non-axisymmetric actuator disk model (ADM) has been implemented in OpenFOAM. This chapter gives a detailed description of the ADM implemented and presents the validation against experimentals test cases such as NREL-Phase-VI and MEXICO experiments. Chapter 5 presents the modelling of the atmospheric boundary layer (ABL) under neutral stratification and the implementation of a new set of boundary conditions that are appropriate to sustain a horizontally homogeneous boundary layer (e.g. without streamwise gradients).

In Chapter 6, the three components are integrated to create the uncertainty quantification framework. The polynomial chaos library, the actuator disk model, and the atmospheric boundary layer model are combined in a single system capable of propagating uncertainties for uncertainty quantification studies and sensitivity analyses. In this chapter, the framework is tested with some simple wind turbine arrays to determine how efficient the method is and under what circumstances its appropriate.

Finally, Chapter 7 presents the discussion and conclusions of this work. It discusses the advantages and limitations of the framework implemented and all the possibilities and opportunities to improve the system as a whole, as well as suitable ways to take advantage of its capabilities for future studies.

Chapter 2

Literature Review and Background Theory

2.1 Introduction

This chapter presents a literature review on wind energy research and the appropriate background theory for this thesis. It is separated into four main sections. The first section describes the wind energy physical system, including wind turbine aerodynamics, wake effects and their interaction with atmospheric boundary layer flows and the role of atmospheric stability. The second section reviews computational models for wind turbines. Particular emphasis is given to computational fluid dynamics and actuator disk models widely used in the literature. The third section presents important research topics on wind farm optimization and active control strategies. These areas use these models to study methods that can potentially increase the efficiency of new and existing wind farms. The fourth section discusses a key point of this thesis: uncertainty quantification. This section highlights wind power high variability and low predictability as one of its main disadvantages. It identifies the current gaps between CFD modelling techniques and uncertainty quantification, which is the central topic of this thesis. It also points out the challenges ahead in wind energy research and the role of CFD models to improve our understanding of physical phenomena and the need to address uncertainty quantification to increase the accuracy and confidence in the predictions. Finally, an additional section summarises the main ideas and their relevance for this work.

2.2 Wind energy physical system

Wind energy is the outcome of a very complex physical system that integrates several phenomena across a wide range of time and length scales. The physical system includes the mesoscale atmospheric flows, the atmospheric boundary layer and its interaction with wind turbines and wind farms, the dynamic response of the rotor blades, supporting structures and electrical systems to changing inflow conditions and wake effects, and the control system that integrates the electric power to the grid ensuring its stability and reliability. All this makes wind power an extremely complex and challenging multidisciplinary subject. This section describes the most relevant features of the wind energy system to understand the challenges ahead and put in context the work presented in this thesis.

2.2.1 Atmospheric boundary layer

The atmospheric boundary layer (ABL) is the lowest part of the atmosphere directly in contact with the ground and sea surfaces and affected by frictional forces. Above the ABL the frictional forces become negligible and therefore is called *free atmosphere*. In the free atmosphere, the balance between pressure gradients and Coriolis forces drive the geostrophic wind G, which can be thought of as the reservoir of wind energy.

Across the ABL occurs the transport of momentum, heat and moisture between the free atmosphere and the ground and oceans, playing an essential role in the atmospheric conditions, the weather and the climate. Some studies suggest that more than half of the atmosphere kinetic energy is lost in the ABL (Garratt, 1994). The kinetic energy carried by the geostrophic wind is transported across the ABL down to the surface, where a wind farm eventually will use it to generate electricity at a rate that will be limited by the transport mechanisms across the ABL (Stevens and Meneveau, 2016).

The ABL extends from the ground surface up to around 1 km depending on the stability conditions (i.e. thermal stratification). It can be subdivided into two different layers, the *Surface Layer* and the *Ekman Layer*. The *Surface Layer*, also known as the Prandtl layer, inertial sub-layer or constant flux layer, is immediately above the ground and it is primarily affected by frictional forces. In this region, the wind profile follows a log law and its height varies with time of the day and atmospheric stability from less than 50 m up to around 200 m. On the other hand, the *Ekman Layer* (or outer region of the ABL) is immediately above the surface layer and is characterised by the influence not only of the frictional forces, but also the pressure gradients and the Coriolis force (Landberg, 2016).

It is important to note that in some cases, considering the growing size of wind turbines, parts of these can eventually be outside the surface layer, where Coriolis turning effects appear. These heights might be viewed as a relatively unexplored area in the sense that is too high for other technologies currently operating on the sea, or too low for weather forecast expert or the aviation industry (van Kuik et al., 2016).

2.2.2 Atmospheric stability

Atmospheric stability is one of the most relevant characteristics of the atmospheric boundary layer since it affects the transport mechanisms across it. It depends on the balance between buoyancy and inertial forces. For example at high wind speeds buoyancy effects become negligible compared to inertial forces, and the ABL is said to be on neutral stability. Generally speaking, atmospheric stability can be classified into three categories: neutral, stable and unstable conditions, although up to seven stability classes have been used in the literature (Barthelmie, 1999; Gryning et al., 2007; Holtslag et al., 2017). The height of the atmospheric boundary layer depends on the stability conditions, Garratt (1994) suggest that under strong unstable conditions the ABL can extend even further up to about 5 km and the opposite, with very stable conditions up to no more than a few hundred meters, particularly over open oceans.

From the wind energy point of view, atmospheric stability will contribute to the wind shear profile, the turbulence intensity, and the evolution of the wind turbines wakes, playing a major role in the performance and lifetime of wind farms. For example, it has been shown that the power deficit produced by wake effects is more significant under stable atmospheric conditions (Hansen et al., 2012). And, depending on the wind speed distribution at a given specific site, turbines might be operating near the cut-in speed for a significant part of the time, where stability effects become more relevant (Barthelmie, 1999).

The atmospheric stability is closely related to thermal stability, and therefore one way of defining atmospheric stability conditions is based on the gradient of *potential temperature* θ.

$$\theta = T \left(\frac{\mathrm{p}_0}{\mathrm{p}} \right)^{R/c_p} \tag{2.1}$$

where T is the temperature, p_0 is the pressure at the surface, p is the pressure at the same height as T, R is the gas constant and c_p the specific heat. The potential temperature might be thought of as a property that also includes variation in pressure, remaining unchanged in a moving air parcel, if no heat is transferred through its boundaries.

In a neutrally stratified atmosphere the potential temperature does not change with altitude, thus $d\theta/dz = 0$. If θ decreases with altitude, $d\theta/dz < 0$, the atmosphere is in unstable condition, and if θ increases with altitude, $d\theta/dz > 0$, the atmosphere is in stable stratification.

Alternatively, atmospheric stability may also be defined based on the surface heat flux H_s (which indeed depends on the temperature gradients). If it is considered positive the heat flux going from the ground into the atmosphere, then a positive heat flux $H_s > 0$, leads to unstable conditions; and a negative heat flux, $H_s < 0$, to stable conditions; and zero heat flux, $H_s = 0$, to neutral conditions.

However, the most common way to characterize atmospheric stability in the literature is through the Obukhov length L, first proposed by Alexander Obukhov (1946).

$$L = -\frac{u_*^3 \bar{\theta}_v}{\kappa g (\overline{w'\theta_v'})_s} \tag{2.2}$$

Where u_* is the friction velocity, κ the von Karman constant, g the gravitational acceleration, $\bar{\theta_v}$ is the mean virtual potential temperature (which essentially represent a similar quantity as the potential temperature but it also takes into account humidity), and $(\overline{w'\theta_v'})_s$ is the surface flux of virtual temperature. Similarly to the heat flux H_s mentioned above, when the surface flux of virtual temperature $(\overline{w'\theta_v'})_s$ is positive, L will be negative, and the atmosphere is in unstable conditions; and when the flux of virtual temperature is negative, L is positive, and the atmosphere is under stable stratification. If the virtual temperature flux is zero, then L will be infinite and the atmosphere will be in neutral conditions. Usually, to avoid an infinite number, the stability parameter is represented as $\zeta = z/L$.

However, it is not easy to measure the parameters exactly as they appear in Eq. 2.2, and different methods have been proposed to estimate the Obukhov length L from more simple measurements. Some approaches calculate the friction velocity u_* by using stability corrected wind shear profiles (see Section 2.2.3.3) and wind speed measurements; while the heat flux is estimated by temperature gradients (Beljaars and Holtslag, 1990; Barthelmie, 1999).

Another way to determine L is based on the Monin-Obukhov Similarity Theory (MOST). This approach consists in finding a functional dependence between the stability parameter ζ and the bulk Richardson number Ri_b. This method was proposed by Grachev and Fairall (1997) and it has been used in wind energy studies (Hansen et al., 2012).

$$Ri_b = \frac{g}{T} \frac{(\Delta T/\Delta_{z,T}) + \gamma_l}{(U/z_U)^2} \tag{2.3}$$

In Eq. 2.3, g is the acceleration of gravity, T is the absolute temperature, $\Delta T/\Delta_{z,T}$ is the measured temperature gradient in the vertical direction, U/z_U is the ratio between the horizontal mean wind speed and the height at which it was measured, and γ_l is the lapse rate. Depending on the value of Ri_b, different expresions are used to determine the stability parameter ζ.

$$\zeta = \frac{z}{L} = \begin{cases} 10Ri_b & \text{if } Ri_b < 0 \text{ (unstable)} \\ \dfrac{10Ri_b}{1-5Ri_b} & \text{if } Ri_b > 0 \text{ (stable)} \end{cases} \tag{2.4}$$

It is important to remark that the applicability of the MOST theory is limited to Ri_b below a critical value Ri_{cr}, and even though there is not a clear established limits, values of around 0.2 to 0.25 are accepted (Grachev et al., 2013).

2.2.3 Wind shear profiles

In the *surface layer* the flow is affected by frictional forces generating velocity gradients or *wind shear*. These vertical gradients of wind speed characterise the loading on the turbines as the blades rotate from higher velocities above the hub height to lower velocities below. Wind shear is also the primary source of turbulence generation impacting the wind farm performance.

Wind shear profiles represent the vertical variation of averaged horizontal wind speeds, and rarely an instantaneous picture of the actual wind profile (at any given instant) will fit into one of these averaged curves. However, wind profiles are useful to estimate the horizontal mean wind speed at different altitudes, when measurements are available at one or more specific heights. A typical example is when wind speed from 10 m height meteorological masts are used to estimate wind speeds at hub height.

The most common vertical wind profiles are the logarithmic profile and the power law profile. Nevertheless, as it is described in the following sections, the wind shear depends on many other parameters, such as surface roughness, wind direction, and atmospheric stability.

2.2.3.1 Logarithmic profile

The logarithmic wind profile is a widely used semi-empirical relation to describe the variation of horizontal mean wind speeds with height depending on the aerodynamic roughness. It is described by Eq.2.5.

$$U(z) = \frac{u_*}{\kappa} ln\left(\frac{z}{z_0}\right) \tag{2.5}$$

Where u_* is the friction velocity $\sqrt{\tau/\rho}$, with τ as the surface shear stress, ρ the air density, κ is the von Karman constant, and z_0 is the aerodynamic roughness.

The aerodynamic roughness represents the presence of obstacles in the ground or sea surface. Inland, typical values of z_0 vary between 10^{-3} m for smooth surfaces like snow or sand, up to 1 m for cities or forests. In contrast, in offshore sites it is usually much smaller being approximately 0.0001 m at the sea surface with small waves (Troen and Lundtang Petersen, 1989), but it also depends on the wind speed, which increases the wave size and consequently the roughness of the sea surface. Charnock (1955) proposed a relationship (Eq. 2.6) between the friction velocity u_* and the aerodynamic roughness z_0, which also includes the acceleration of gravity and an empirical parameter known as the *Charnock-parameter* α_{ch}. A brief summary of different values of α_{ch} proposed by other studies is given in Türk and Emeis (2010).

$$z_0 = \frac{\alpha_{ch} u_*^2}{g} \tag{2.6}$$

2.2.3.2 Power law profile

Another wind profile widely used is the power law (e.g. IEC 61400 standards), given by the following equation.

$$U(z) = U_{ref}\left(\frac{z}{z_{ref}}\right)^{\alpha_P} \tag{2.7}$$

Where U_{ref} is the reference wind speed at the reference height z_{ref}, and α_P is the power law exponent, also known as *wind shear coefficient*, which is usually considered as 1/7 for neutral atmospheric conditions. However, wind shear will vary depending on atmospheric conditions and consequently the power law exponent will also change. Typical offshore values observed in the North Sea and western Atlantic are between 0.06 and 0.16, on the other hand values between 0.14 to 0.30 are expected inland (Bailey, 2016).

2.2.3.3 Wind shear profiles and atmospheric stability

It is known that wind shear increases for stable stratification and decreases for unstable atmospheric conditions. To account for the influence of the atmospheric stability, additional wind profiles have been developed, where a correction function Φ has been added to the logarithmic profile creating what is known as the diabatic or stability correct profile (see Eq.2.8).

$$U(z) = \frac{u_*}{\kappa}\left(ln\left(\frac{z}{z_0}\right) - \Phi\left(\frac{z}{L}\right)\right) \tag{2.8}$$

There are many functions Φ that have been proposed. Landberg (2016) pointed out that a widely used set of correction functions Φ, known as the Businger-Dyer profiles, are given by equations Eq. 2.9 (Businger et al., 1971; Dyer, 1974).

$$\Phi = \begin{cases} -5\left(\frac{z}{L}\right) & \text{if } z/L > 0 \text{ (stable)} \\ 0 & \text{if } z/L = 0 \text{ (neutral)} \\ 2\ln\left(\frac{1+x}{2}\right) + \ln\left(\frac{1+x^2}{2}\right) - 2\tan^{-1}(x) + \frac{\pi}{2} & \text{if } z/L < 0 \text{ (unstable)} \\ \quad \text{with } x = \left(1 - 16\frac{z}{L}\right)^{1/4} & \end{cases} \tag{2.9}$$

2.2.3.4 Wind profiles above the surface layer

As it was mentioned before, it is important to have in mind that the size of modern wind turbines is increasing and it is expected that at least part of the rotor will operate above the surface layer (Ekman layer or outer region of the ABL, particularly under stable conditions), where Coriolis forces are no longer negligible producing turning of the wind along the vertical axis (Wind veer). Therefore a more detailed understanding of the vertical structure of the boundary layer is required to describe their impact in wind turbine performance (Emeis, 2014; Landberg, 2016; Holtslag et al., 2017).

The description of the horizontal mean wind speeds by the log law or a power law described above, is limited to the surface layer region. However, Gryning et al. (2007) and Holtslag et al. (2017) have proposed more advanced wind profiles for the entire boundary layer under different stability conditions. The details about those models are beyond the scope of this work, but reader can find them in the given references.

2.2.4 Offshore wind climate

2.2.4.1 Stability conditions offshore

In onshore sites, unstable conditions occur typically on sunny days when the ground is hotter than the upper air, or by top-cloud radiative cooling, where buoyancy forces will raise air parcels from lower levels increasing the mixing with upper layers. In contrast, under stable conditions, at nights with a cooler ground surface, buoyancy forces will enhance the stability, reducing the mixing between upper and lower layers. Neutral conditions are found typically in cloudy days or with strong winds, or around sunrise and sunset, where buoyancy forces are not predominant.

In offshore sites, the thermo-physical properties of the sea surface are different. Temporal and spatial variability of atmospheric stability in offshore sites has been analysed by Barthelmie (1999), Barthelmie et al. (2005), Motta et al. (2005), and

Hansen et al. (2012). First of all, it was found that diurnal variability was smaller compared with inland sites which are strongly influenced by variation in the ground surface temperature between day and night. Secondly, stability also varies depending on the wind direction due to changes in aerodynamic roughness and thermal characteristics of the ground surface. In fact, depending on the wind direction and distance to shore, coastal effects have an impact in the offshore stability. Thirdly, as the wind speed increases, near-neutral conditions are predominant, and it is concluded that stability effects on wind farms are particularly important for wind speeds between the cut-in and rated values.

An example of variability of stability classes is shown in Figure 2.1 for a meteorological mast located at Rødsand in the Baltic Sea (Denmark). It is shown diurnal and seasonal changes in atmospheric stability, as well as the influence of wind speed and wind direction. Note how for wind speeds greater than 10 to 12 m/s neutral conditions are predominant.

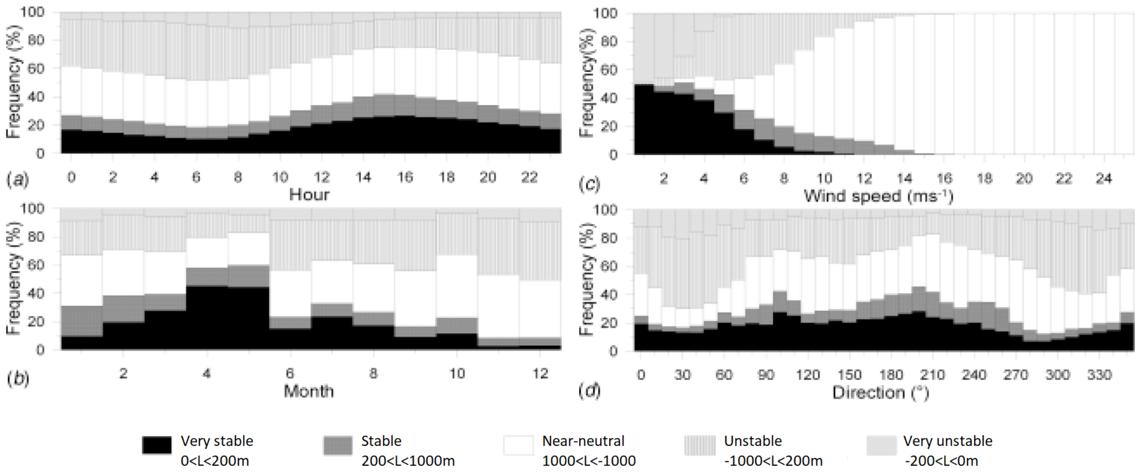

Figure 2.1: Variability of stability at Rødsand mast in the baltic sea between 2002 and 2003. (a) Hourly, (b) Monthly, (c) as a function of wind speed at 48 m height, and (d) as a function of wind direction. Figure adapted from Barthelmie et al. (2005).

2.2.4.2 Turbulence characteristics

Understanding the turbulence in the ABL is essential to achieve optimum designs and durability of turbines components and wind farms. In addition to wind shear profiles, turbulence intensity profiles are useful to estimate the loads and predict the evolution of wakes. It is known that the power output and the structural loads increase as the turbulence intensity increases (Türk and Emeis, 2010; Barthelmie and Jensen, 2010).

Turbulence is generated by wind shear and by thermal instability. At higher wind speed thermal instability becomes negligible and wind shear is the dominant source of turbulent kinetic energy, and at low speed, buoyancy forces also contribute to either increase or reduce turbulence levels, depending on the atmospheric stability condition.

The particular characteristics of offshore wind turbulence as a function of the wind speed have been analysed by Barthelmie et al. (2005) and Türk and Emeis (2010). Barthelmie et al. (2005) plotted the turbulence intensity against the wind speed using 10 minute averaged data measured offshore with a 48 m height meteorological mast at Rødsand, between 2002 and 2003 (see Figure 2.2). The left plot shows that for low wind speeds (2 m/s) the turbulence intensity is around 10 %, and as the wind speed increases it goes down to its minimum values (6 and 8% at 48 m and 8 m height respectively) at $10-13$ m/s, and as the wind speed is further increased the turbulence intensity also increases continuously to values above 12 % for wind speeds higher than 25 m/s at 8 m height. In addition, turbulence levels are higher at lower altitudes, which is also shown in the plot to the right, where a linear relationship between mean turbulence intensity values and height is observed. Note also that, at lower wind speed the differences with height are not very significant.

A similar analysis was presented by Türk and Emeis (2010), based on empirical measurements from the platform FINO1 (Forshung in Nord- und Ostsee 1) located in the North Sea. The results are shown in Figure 2.3 and follow the same trend. The turbulence intensity drops quickly as the wind speed is increased from 1 m/s up to around 4 m/s, then, it decreases gradually to the minimum values at wind

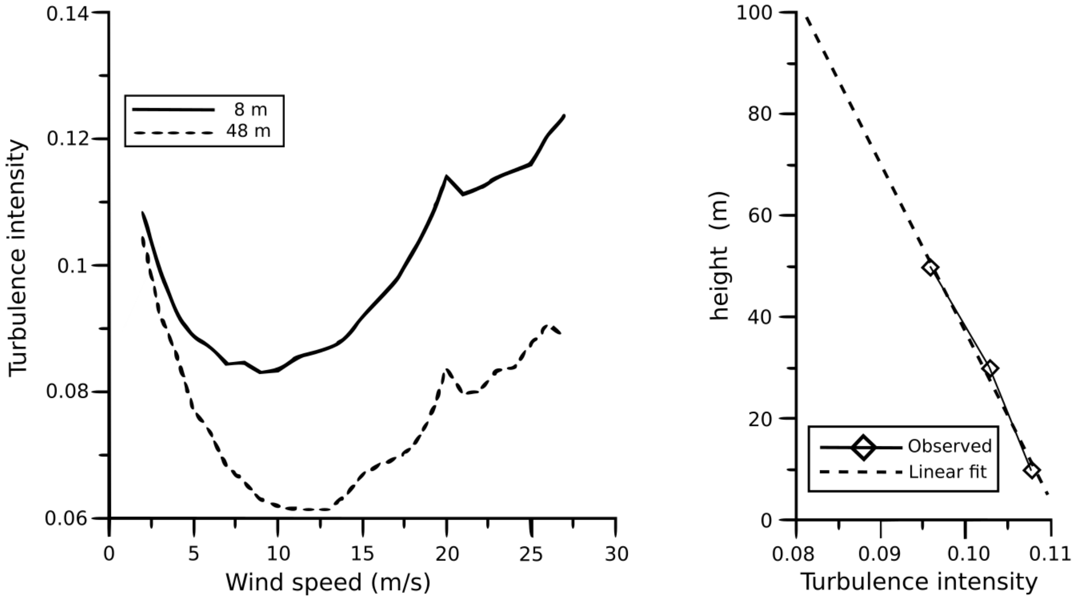

Figure 2.2: Turbulence intensity from Rødsand mast in the Baltic Sea between 2002 and 2003. Data correspond to 10 minute averaged values. (left) Turbulence intensity vs wind speed at 48 m and 8 m height (right) Mean turbulence intensity vs height. Figure adapted from Barthelmie et al. (2005).

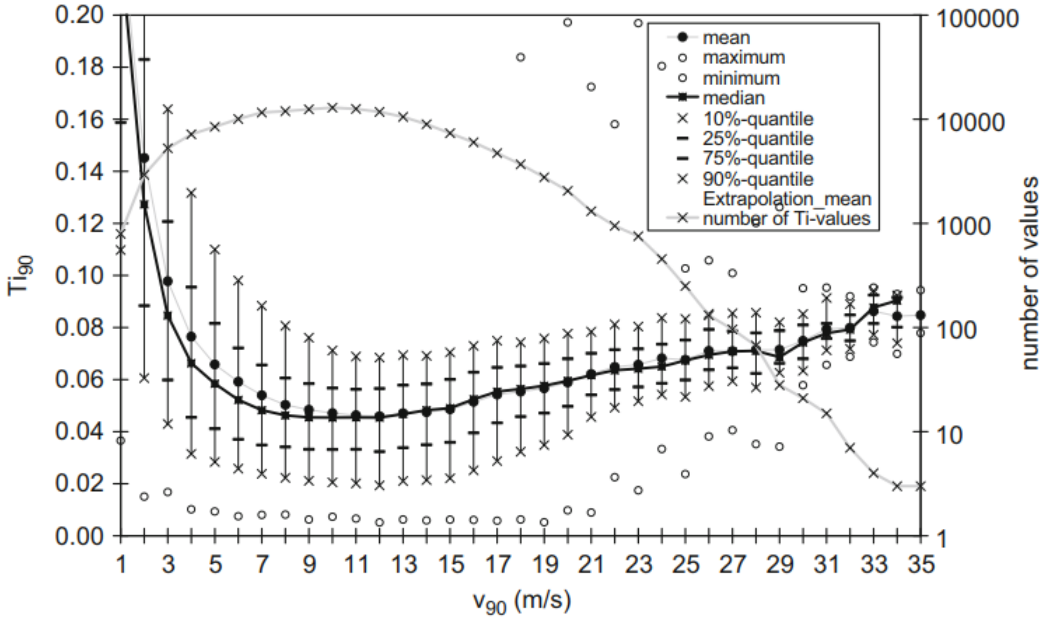

Figure 2.3: Turbulence intensity against wind speed from FINO1 in the North Sea. Data correspond to 10 minute averaged values from September 2003 to August 2007 (Türk and Emeis, 2010).

speeds of around 9 to 12 m/s, and finally, as the wind speed is further increased, the turbulence level goes up again almost linearly with wind speeds. Comparing the turbulence level at different heights, it was also found that higher turbulence intensities are predominant at lower altitudes.

Furthermore, it was reported that it is possible in some situations, for very stable atmospheric conditions, to have very low turbulence intensity (the minimum values measured of around 1 %) even at high wind speeds (up to 20 m/s). Similar results reported by Hansen et al. (2012), suggest that both stable and unstable conditions can be observed for wind speed up to 15 m/s, and moreover, that the stability is also dependent on the wind direction. Nevertheless, it is difficult to maintain unstable or stable condition at higher speeds (over 15 m/s), and that neutral conditions are predominant (Barthelmie and Jensen, 2010).

2.2.5 Wake effects

2.2.5.1 Wind Turbine Wakes

One of the main characteristics of the flow field through a wind turbine is the wake generated downstream of the rotor. As the turbine extracts kinetic energy from the wind to generate electricity, the wind speed decreases across the rotor area. This reduction in wind speed is accompanied by an expansion of the wake, and as the turbine exerts a rotational force, part of the energy in the flow is converted into angular momentum (wake rotation). The velocity deficit creates a high shear layer with the free flow increasing the turbulence generation.

The wake can be separated into two zones (see Figure 2.4), the near wake immediately after the rotor up to $2D$ to $4D$ rotor diameters downstream (Katic et al., 1986; Ainslie, 1988), where it is possible to observe complex turbulent structures, such as tip and root vortices which are highly dependent on the turbine geometry and the operating conditions (Troldborg et al., 2009), and the far wake, which starts around $5D$ downstream (Fitch et al., 2012), and it is not very dependent on the rotor geometry, but on the environmental conditions such as turbulence intensity and atmospheric stability.

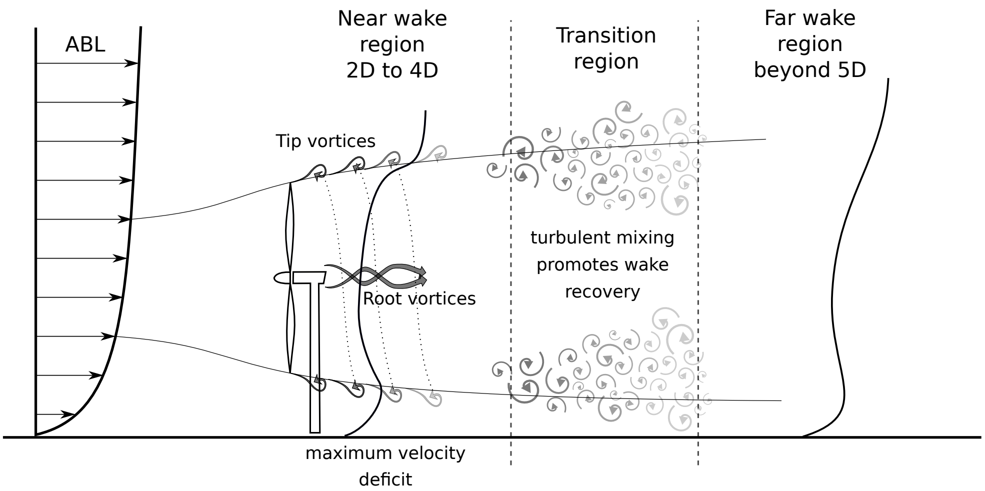

Figure 2.4: Schematic representation of a turbine wake showing the near and far wake regions.

Wakes are important because they impact the performance of downstream turbines, which is particularly important in large wind farms. Barthelmie et al. (2009) estimated that wake effects produce power losses between 10 to 20%. In addition, higher turbulence levels increase fatigue loads reducing the lifetime of turbines. Note that turbulence also dissipates kinetic energy from the wind as heat (Corten, 2000).

Wake rotation reduces the efficiency. From a pure aerodynamic point of view, this can be minimised by increasing the angular speed, but there are other technical issues such as noise levels and mechanical resistance of the blades that limit the tip speed ratio TSR (See Section 2.4). Besides, as the wake rotates in the sheared atmospheric boundary layer flow, high velocity air parcels move downwards in one side of the wake, and low velocity air parcels move upwards in the other side, producing a skewed wake. This asymmetry increases with the distance downstream (Troldborg et al., 2009). Some studies have analysed the effects in the overall performance of wind farms and wind turbines using counter-rotating rotors. A good summary of some alternatives, such as wind farms with alternate rows of clockwise and counter-clockwise rotating wind turbines; or dual counter-rotating wind turbines has been recently presented by Vasel-Be-Hagh and Archer (2016). They analysed these alternatives using LES simulations with actuator line models and showed an increase of 1.4 % in power using alternate rows, and up to 22.6 % with dual rotor turbines.

It is known that the wake characteristics and the power deficit they produce will depend on the wind speed, the turbulence levels and the stability conditions. Higher turbulence mixing promotes a quicker recovery of the wind speed by transfer of momentum from higher wind speed layers. Barthelmie and Jensen (2010) studied the power losses of the Nysted offshore wind farm in Denmark, concluding that the wind farm efficiency is most strongly affected by the wind speed, and also, but as second order effects, by the wind direction, the atmospheric stability and the turbulence intensity. Therefore seasonal variations in wind speed are also reflected in changes in the overall efficiency along the year. As an example, in the study case at the Nysted offshore wind farm in Denmark, it was reported that wake losses were around 10% higher in summer than in winter.

The large scale movement of a wind turbine wake is known as wake meandering, this phenomenon is believed to be dependent on large scale turbulence in the environment. It is known that wake meandering has significant effects in the loading of downstream turbines since the wake moves in and out of the rotor continuously. Partial wake overlap increases considerably the asymmetric loading in downstream turbines van Dijk et al. (2016). Wake meandering also reduced the mean wind speed deficit and therefore any model that neglect this phenomenon will overpredict the power deficit. Ainslie (1988) said that under stable atmospheric conditions wakes can be modelled as stationary, but under neutral and unstable conditions a proper treatment of wake meandering needs to be considered.

2.2.5.2 Wind farm wakes

Wind farm wake also are becoming increasingly important. Until this point, wakes has been described as a single wind turbine phenomenon that has an impact on the performance and durability of downstream turbines. However, wind farm arrays themselves produce a wake at a mesoscale level as a superposition of all the individual wind turbine wakes. Wind farm wakes can affect the performance of other wind farms nearby, and therefore, the interaction between wind farm wakes is gaining importance particularly in offshore sites as in the North Sea, where the number and the size of wind farms is increasing.

Christiansen and Hasager (2003) using satellite and airborne synthetic aperture radars (SAR) measurements at Horns Rev I, concluded that the wind farm wake deficits were up to 10% and that persists at least 10 km downstream. More recently, Hasager et al. (2015) observed wind farm wakes in the North Sea captured by satellite measurements reporting that the most prolonged wake observed extended up to approximately 55 km in the open sea.

2.2.5.3 Wind Turbine Array Boundary Layer

Another interesting phenomenon that arises by superposition of single wakes is known as the Wind Turbine Array Boundary Layer (WTABL), which is an internal boundary layer that starts to develop at the first row of turbines upstream. If the array is large enough, whose length is greater than the ABL height (Calaf et al., 2010), a fully developed WTABL could be achieved, where streamwise gradients are no longer significant, and the vertical transport of mean kinetic energy from upper layers (geostrophic wind) become relevant for wind energy generation. This phenomenon was studied by Calaf et al. (2010) and Calaf et al. (2011) through LES simulations, and it was also observed experimentally in wind tunnel test by Chamorro and Porté-Agel (2011).

2.2.6 Time and length scales

Wind energy is the outcome of a very complex physical system that integrates several phenomena across a wide range of time and length scales. The time scales involved range from less than a second for turbulent fluctuations to decades that characterise climate processes. At time-scales of the order of minutes to hours, local conditions (e.g. the presence of clouds, rain or waves) will determine variations such as the atmospheric stability and turbulence intensity during the day. Diurnal cycles are related to changes in thermal exchanges between the atmosphere and the earth surface, and seasonal variations during the year due to changes in atmospheric conditions, vegetation or land use. On the other hand, length scales vary from thousands of kilometers (synoptic and global scales) that will determine the weather patterns, and therefore the wind energy resource, down to the smallest scales of the order of millimetres that will determine the turbulence characteristics of the boundary layer at the blades. In the order of decades long-term climate processes occur, for example, Earl et al. (2013), mentioned a couple of studies where a decline in mean wind speed have been observed from meteorological stations surface data, across most areas of the world, including Europe. This process was called *global stilling* and it was attributed to changes in land biomass.

2.3 Computational models

The wind flow through wind farms in the atmospheric boundary layer is characterised by a high Reynolds number of the order of $Re \sim 10^7$. Thus, there is a wide range of turbulent time and length scales, from large eddies comparable to the characteristic length scale of the atmospheric boundary layer to the smallest eddies where dissipation takes place. From the computational fluid dynamics (CFD) point of view, this makes it prohibitively expensive to solve all the length scales through Direct Numerical Simulation (DNS).

Large Eddy Simulations (LES) resolve the large turbulent structures and model sub-grid scale eddies providing greater insight into the flow physics compared to Reynolds Averaged Navier Stokes equations (RANS). For this reason, LES is used to study the flow in wind farms (Jimenez et al., 2007; Sanderse et al., 2011; Wu and Porté-Agel, 2011; Afgan et al., 2013; Porté-Agel et al., 2014; Mehta et al., 2014; Stevens et al., 2017). Nevertheless, LES is still far more expensive than RANS models and is unsuitable for uncertainty propagation studies. Therefore, following the objectives of this work, this section presents an overview of RANS models used in the literature for simulations of the atmospheric boundary layer, wind turbines and wind turbine wakes.

CFD plays a critical role in the design of wind turbines and in increasing the understanding of wind turbine aerodynamics, reducing the costs and the need for large scale experiments. However, CFD is still considerably expensive and the aerodynamic design of wind turbines and wind farms still relies on simplified models such as 1D momentum theory and the Blade Element Momentum (BEM) method. Besides, considering that actuator models described later are based on these fundamental concepts, the first following sections will present them.

Then, the RANS equations will be introduced along with some widely used eddy viscosity models. The models presented are primarily two-equations linear eddy viscosity models. A specific subsection discusses the application of eddy viscosity models to wind farms, highlighting some of their disadvantages and the attempts that have been made to improve their accuracy for wind turbine wakes. Then, a brief overview of actuator methods for modelling wind turbines is presented, such as actuator disk and actuator line models. Actuator disk models in particular offer a good balance between accuracy and cost for the objectives of this work. Chapter 4 will be dedicated to the implementation and validation of an ADM in OpenFOAM.

As a closing remark, due to the complexity of the physical system and the wide range of time and length scales involved, different computational models coexist, with different level of complexities, and all of them have their role. Here engineering wake models widely used for wind farm optimizations are not included but more detail can be found in Jensen (1983), Ainslie (1988) and Larsen (2009).

2.4 1D Momentum theory

The most simple model for a horizontal axis wind turbine is the 1D momentum theory, which fundamentally is a balance of momentum in the axial direction under idealised conditions: incompressible, inviscid and stationary flow, with no variation in internal energy between the inlet and outlet (see Figure 2.5). The turbine is assumed as an ideal zero thickness permeable disk without frictional or rotational forces. When the flow passes through the disk, the pressure drops Δp, and the axial velocity decreases from the free stream velocity U_0 to U_W further downstream. Under the idealised conditions, Bernoulli's equation leads to:

$$\Delta \mathrm{p} = \frac{1}{2}\rho\left(U_0^2 - U_W^2\right) \tag{2.10}$$

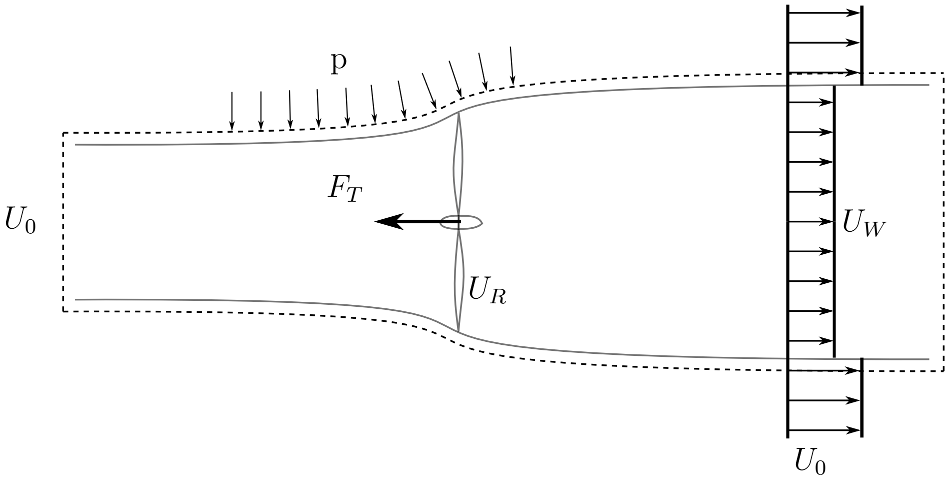

Figure 2.5: Control volume for momentum balance in the axial direction. Figure adapted from Hansen (2008).

Using Eq. 2.10 into the momentum equation leads to:

$$F_T = \rho U_R A\left(U_0 - U_W\right) \tag{2.11}$$

and,

$$U_R = \frac{1}{2}\left(U_0 + U_W\right) \tag{2.12}$$

where U_R is the axial velocity at the rotor and F_T is the thrust force. On the other hand, using the energy equation the power extracted P can be written as:

$$P = \frac{1}{2}\rho U_R A\left(U_0^2 - U_W^2\right) \tag{2.13}$$

Introducing axial induction factor a, which represent the fractional decrease of velocity from the free stream U_0 to axial velocity at the rotor U_R. U_R and U_W can written as:

$$U_R = U_0(1-a) \tag{2.14}$$

$$U_W = U_0(1 - 2a) \tag{2.15}$$

Which allows to rewrite the power P and thrust F_T as a function of the axial induction factor a.

$$P = 2\rho U_0^3 a(1 - a)^2 A \tag{2.16}$$

$$F_T = 2\rho U_0^2 a(1 - a)A \tag{2.17}$$

Defining the power coefficient C_P as the fraction of the available power, and the thrust coefficient C_T as:

$$C_P = \frac{P}{\frac{1}{2}\rho A U_0^3} \tag{2.18}$$

$$C_T = \frac{F_T}{\frac{1}{2}\rho A U_0^2} \tag{2.19}$$

Combining Eq.2.16 and Eq.2.17 with Eq.2.18 and Eq.2.19 respectively, the following relations can be written.

$$C_P = 4a(1 - a)^2 \tag{2.20}$$

$$C_T = 4a(1 - a) \tag{2.21}$$

From this equations it can be obtained that the maximum C_P is 16/27 when the axial induction factor is $a = 1/3$. This correspond to the maximum theoretical power that can be extracted from the flow by an ideal turbine, known as the Betz's Limit (Betz, 1920).

Looking at Eq.2.15 it is possible to see that for an axial induction factor $a > 0.5$, the axial velocity in the wake U_W becomes negative. In reality, it is known that this simplified model is valid for axial induction factors lower than 0.4, after this value the flow becomes very unstable and entrainment from outer layers introduces additional mass and momentum and the model is no longer valid.

Also, a tangential induction factor a' can be defined, and the absolute tangential velocity of the flow at the rotor plane $U_{\theta,R}(r)$ at radial distance r can be written as:

$$U_{\theta,R}(r) = a'\omega r \tag{2.22}$$

where ω is the rotor angular speed. Note that the tangential velocity relative to the blades will be:

$$U_{\theta,R,rel}(r) = (1 + a')\omega r \tag{2.23}$$

In general, the tangential velocity component of the wake can be reduced by increasing the angular speed of the rotor (see Figure 2.6), hence improving the efficiency. Nevertheless, this is limited by the maximum TSR allowed, either by mechanical resistance of the blades or the noise levels produced.

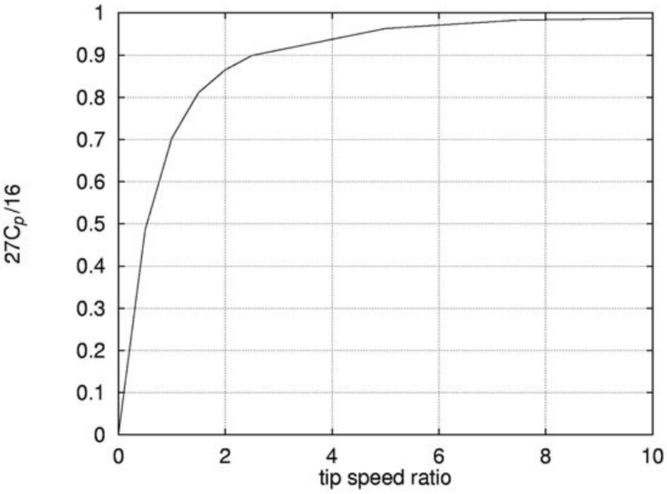

Figure 2.6: Maximum C_P including wake rotation compared to the Betz's limit 16/27 as a function of the tip speed ratio (TSR). Figure taken from Hansen (2008).

2.5 Blade Element Momentum method

The Blade Element Momentum method was first proposed by Glauert (1935). This approach takes the fundamental principles of the 1D momentum theory but includes rotation and the effects produced by the actual turbine geometry, such as lift and drag forces from 2D airfoil data, number of blades, and operating conditions such as angular speed and pitch angle.

The momentum balance is performed in a discrete number of annular tubes, as the one shown in Figure 2.7. The annular control volumes are considered in such a way that their boundaries follow streamlines, and therefore there is no flow across them, and consequently, they can be assumed to be independent of each other. The turbine rotor is correspondingly represented as annular elements, and the thrust dF_T and tangential dF_θ forces are calculated separately for each one of them from linear and angular momentum balance respectively (see Eq. 2.24 and Eq. 2.25). These forces are assumed to be constant and uniformly distributed across each annular element.

$$dF_T = 4\pi r \rho U_0^2 a(1-a)dr \tag{2.24}$$

$$dF_\theta = 4\pi r^3 \rho U_0 \omega (1-a)a' dr \tag{2.25}$$

Also, the thrust dF_T and tangential dF_θ forces can be calculated as a decomposition of the lift dF_L and drag dF_D forces as shown in Figure 2.8 (see Eq. 2.26 and Eq. 2.27). Note that a the sub-index $_1$ has been introduced to indicate that these are the contributions from one single blade element.

$$dF_{T,1} = dF_L \cos\phi + dF_D \sin\phi \tag{2.26}$$

$$dF_{\theta,1} = dF_L \sin\phi - dF_D \cos\phi \tag{2.27}$$

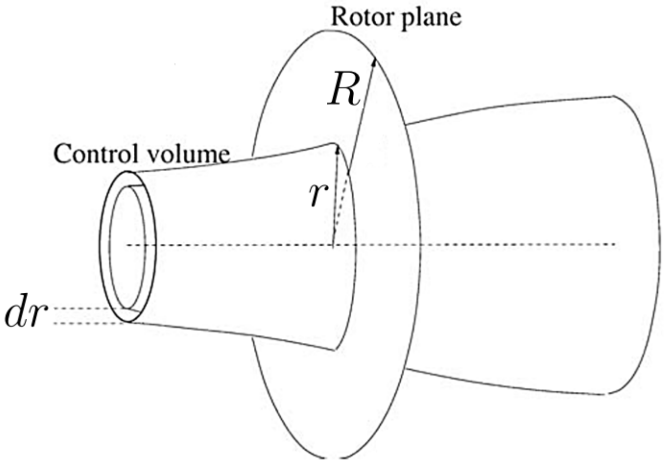

Figure 2.7: Control volume for momentum balance in the Blade Element Momentum (BEM) method. Figure adapted from Hansen (2008).

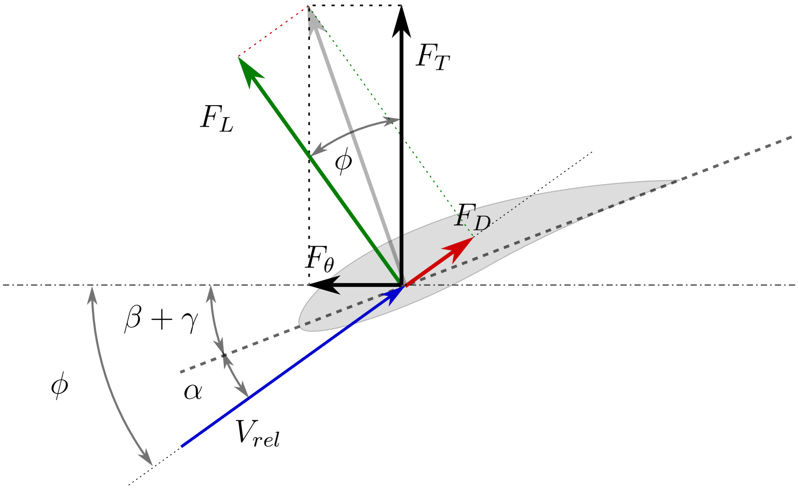

Figure 2.8: Lift and drag decomposition into thrust and torque.

The lift and drag forces can be derived from 2D airfoil tabulated data for lift and drag coefficients C_L and C_D, knowing the geometry of the rotor, pitch angle θ_p, angular speed ω, using Eq. 2.28 and 2.29 .

$$dF_L = \frac{1}{2}\rho\, V_{rel}^2\, c\, C_L\, dr \tag{2.28}$$

$$dF_D = \frac{1}{2}\rho\, V_{rel}^2\, c\, C_D\, dr \tag{2.29}$$

where, $c(r)$ is the chord length, V_{rel} is the velocity relative to the blade that can be calculated from the velocity triangle shown in Figure 2.9, using Eq. 2.30; and C_L and C_D are the lift and drag coefficient respectively. Note that in this case, the relative velocity V_{rel} is calculated based on the 1D momentum theory (see also Eq. 2.14 and Eq. 2.23), but this is not always suitable, particularly when modelling wakes interactions, where the free stream velocity is also unknown.

To extract C_L and C_D from tabulated data it is necessary to know the local angle of attack α, which can be calculated using Eq. 2.31, where the flow angle ϕ can be obtained with Eq. 2.32, the twist angle γ and the pitch angle β. Note that both, the axial induction factor a and the tangential induction factor a' are required to compute the lift and drag forces, but at the same time these values depend on the unknown thrust and tangential forces. Therefore, this method needs to be solved iteratively initializing the values of a and a' and updating them in every iteration until they converge.

$$V_{rel} = \sqrt{U_R^2 + U_{\theta,R,rel}^2} = \sqrt{\left(U_0(1-a)\right)^2 + \left(\omega r(1+a')\right)^2} \tag{2.30}$$

$$\alpha = \phi - (\beta + \gamma) \tag{2.31}$$

$$\tan(\phi) = \frac{U_0(1-a)}{\omega r(1+a')} \tag{2.32}$$

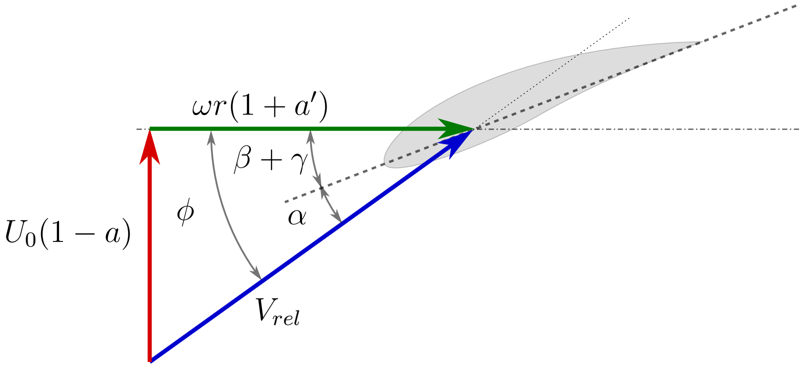

Figure 2.9: Velocity triangle at airfoil section.

Introducing the number of blades B and combining Eq. 2.26 and Eq. 2.27 with Eq. 2.28 and Eq. 2.29, it is possible to write the total thrust force and torque contributions for each annular element as:

$$dF_T = \frac{1}{2}\rho B \frac{U_0^2(1-a)^2}{\sin^2\phi} cC_t dr \tag{2.33}$$

$$dF_M = \frac{1}{2}\rho B \frac{U_0(1-a)\omega r(1+a')}{\sin\phi\cos\phi} cC_m r dr \tag{2.34}$$

where

$$C_t = C_L \cos\phi + C_D \sin\phi \tag{2.35}$$

$$C_m = C_L \sin\phi - C_D \cos\phi \tag{2.36}$$

Then, combining 2.33 and 2.34 obtained from airfoil data, with Eq. 2.24 and Eq. 2.25 from linear and angular momentum balance, expressions to update the value of a and a' are obtained as follow.

$$a = \frac{1}{\dfrac{4\sin^2\phi}{sC_t} + 1} \tag{2.37}$$

$$a' = \frac{1}{\dfrac{4\sin\phi\cos\phi}{sC_m} - 1} \tag{2.38}$$

$$\sigma_s(r) = \frac{Bc(r)}{2\pi r} \tag{2.39}$$

The total Thrust F_T and Torque F_M can be obtained by adding together the contributions $dF_{T,i}$ and $dF_{M,i}$ for each annular element in the rotor disk.

$$F_T = \sum_i dF_{T,i} \tag{2.40}$$

$$F_M = \sum_i dF_{M,i} \tag{2.41}$$

Similarly, since the angular speed is known, the shaft power P, and the total electric power P_e can be calculated as:

$$P = \omega F_M \tag{2.42}$$

$$P_e = P\eta \tag{2.43}$$

where η is the efficiency for the conversion process of angular momentum at the rotor shaft into electrical power.

The BEM method described above needs to include two corrections to improve its accuracy. The first one is known as Prandtl's tip loss correction. Prandtl introduced the concept of tip loss by looking at the flow circulation and the differences between a finite number of blade turbine or propeller compared with an infinite number of blades actuator disk representation. Glauert (1935) introduced this correction to BEM. In a real rotor with a finite number of blades, the local blade induction factors are different from the averaged values obtained from 1D momentum theory and they need to be corrected before reading tabulated airfoil data. The second correction has to do with equation Eq.2.21. When the axial induction factor $a > 0.5$ the rotor enters into a turbulent wake state and the basics assumptions in 1D momentum theory are no longer suitable. Thus, the thrust coefficient in equation Eq.2.21 needs to be corrected. This type of correction is known as Glauert correction and essentially it uses an empirical fit for C_T for values of $a > 0.4$ (Buhl Jr, 2005; Chapman et al., 2013).

2.5.1 Reynolds Averaged Navier Stokes (RANS) Equations

The Reynolds Averaged Navier Stoke equations for a steady and incompressible flow are written in tensor notation as:

$$\frac{\partial U_i}{\partial x_i} = 0 \tag{2.44}$$

$$U_j \frac{\partial (U_i)}{\partial x_j} = -\frac{1}{\rho}\frac{\partial p}{\partial x_i} + \frac{\partial}{\partial x_j}\left(2\nu S_{ij} - \overline{u_i u_j}\right) + \frac{S_M}{\rho} \tag{2.45}$$

where p is the pressure, ν the kinematic viscosity, S_M represents a momentum source term, S_{ij} the mean rate of strain tensor:

$$S_{ij} = \frac{1}{2}\left(\frac{\partial U_i}{\partial x_j} + \frac{\partial U_j}{\partial x_i}\right) \tag{2.46}$$

and $\overline{u_i u_j}$ is Reynolds stress tensor which add siz addional unknowns (symmetric tensor) and that needs to be modelled with a turbulence closure model.

2.5.1.1 Linear eddy viscosity models

The most common turbulence closure model is the Boussinesq hypothesis that assumes a linear relationship between the Reynolds stress tensor and the mean strain rate tensor introducing the concept of *eddy viscosity* ν_t as:

$$\overline{u_i u_j} = \frac{2}{3} k \delta_{ij} - 2\nu_t S_{ij} \tag{2.47}$$

where δ_{ij} is the Kronecker delta and k the turbulent kinetic energy. This simplified model implies that the eddy viscosity is isotropic which is not true, particularly in sheared flows such as the atmospheric boundary layer. Nevertheless, this reduces the problem to find an appropriate model for the eddy viscosity ν_t, which is commonly done using two-equations turbulence models.

2.5.1.2 The $k-\varepsilon$ model

The Standard $k-\varepsilon$ model developed by Jones and Launder (1972) and Launder and Sharma (1974) is a two-equation model that add a transport equation for the turbulent kinetic k energy and turbulence dissipation rate ε.

$$\frac{Dk}{Dt}=P_k-\varepsilon+\frac{\partial}{\partial x_j}\left[\left(\nu+\frac{\nu_t}{\sigma_k}\right)\frac{\partial k}{\partial x_j}\right] \tag{2.48}$$

$$\frac{D\varepsilon}{Dt}=C_{\varepsilon 1}\frac{\varepsilon}{k}P_k-C_{\varepsilon 2}\frac{\varepsilon^2}{k}+\frac{\partial}{\partial x_j}\left[\left(\nu+\frac{\nu_t}{\sigma_\varepsilon}\right)\frac{\partial \varepsilon}{\partial xj}\right] \tag{2.49}$$

with

$$P_k=-\overline{u_i u_j}\frac{\partial U_i}{\partial x_j} \tag{2.50}$$

Where the standard values for model constants are $C_\mu=0.09$, $C_{\varepsilon 1}=1.44$, $C_{\varepsilon 2}=1.92$, $\sigma_k=1.0$, and $\sigma_\varepsilon=1.3$.

2.5.1.3 $k-\omega$ model

Wilcox (1988) proposed to solve an equation for $\omega \equiv \varepsilon/k$ instead of ε.

$$\frac{Dk}{Dt}=P_k-\beta' k\omega+\frac{\partial}{\partial x_j}\left[\left(\nu+\frac{\nu_t}{\sigma_{kw}}\right)\frac{\partial k}{\partial x_j}\right] \tag{2.51}$$

$$\frac{D\omega}{Dt}=C_{\omega 1}\frac{\omega}{k}P_k-C_{\omega 2}\omega^2+\frac{\partial}{\partial x_j}\left[\left(\nu+\frac{\nu_t}{\sigma_\omega}\right)\frac{\partial \omega}{\partial x_j}\right] \tag{2.52}$$

With model constants $C_{\omega 1}=5/9$, $C_{\omega 2}=5/6$, $\beta'=0.09$, and $\sigma_k=\sigma_\omega=2$.

2.5.1.4 The $k-\omega-SST$ model

The $k-\omega-SST$ was proposed by Menter (1992) and it was designed to combine the best of both the $k-\varepsilon$ and the $k-\omega$ model. Thus, it retains the near wall behaviour of the ω equations and remove the sensitivity to the free stream turbulence as the $k-\varepsilon$ model. It does so by including blending functions F_1 that switches from one to another. The detailed formulation can be found in Menter (1994) and also in Menter and Esch (2001).

2.5.2 Turbulence Modelling for Wind Farms

The linear eddy viscosity models described above are isotropic, and therefore they are not suitable to capture the turbulence anisotropy that characterises the turbine wakes and the shear flow in the atmospheric boundary layer. Nevertheless, they can still be useful to predict the velocity field and determine the power deficit in wind farm arrays at relatively low cost compared with non-linear eddy viscosity models or LES simulations. However, it is known that the standard turbulence models underestimate the power deficit. The high-velocity gradients increase the eddy viscosity, leading to a fast wake recovery, resulting in an over-estimation of wake velocities. In this context, different studies have introduced modifications to the standard turbulence models to improve their accuracy for modelling wakes.

Secondly, changes in model coefficients have been applied to make the models suitable for atmospheric flows. Crespo et al. (1986) used a parabolic boundary layer approximation for modelling turbine wakes in the ABL with the two equations $k-\varepsilon$ closure model introducing changes in the model coefficients for neutral stability conditions. Similarly, Prospathopoulos et al. (2008) used alternative model coefficients for the $k-\varepsilon$ and $k-\omega$ model for atmospheric boundary layer flows. In particular, the model coefficients proposed by Crespo et al. (1986) have been widely used (see for instance, El Kasmi and Masson (2008) and van der Laan et al. (2015a)). More about modelling the atmospheric boundary layer will be discussed in Chapter 5, where a horizontally homegenous boundary layer is simulated using the standard

$k - \varepsilon$ and the $k - \omega - SST$ models.

El Kasmi and Masson (2008), apart from using the model coefficients from Crespo et al. (1986), proposed to add an additional term to turbulent dissipation rate equation in the $k - \varepsilon$ model to improve the prediction of the flow field in the near and far wake of wind turbine simulations, based on the work from Chen and Kim (1987). The additional term is applied to a local region around the rotor, increasing the dissipation of turbulent kinetic energy, where the production of turbulent kinetic energy is high, reducing the turbulent mixing and retarding the wake recovery. Their results showed an improvement in the prediction of the velocity deficit in the wake. Later, Prospathopoulos et al. (2011) used the same approach as El Kasmi and Masson (2008), but with the $k - \omega$ model, and it was concluded that the model needs to be calibrated for each test case since the model constant in the additional term varies considerable from one case to another. A similar conclusion was obtained by Shives and Crawford (2016). Also, the approach from El Kasmi and Masson (2008) requires the definition of the region around the rotor, where the model is applied, adding an additional parameter that needs to be defined.

van der Laan et al. (2015c) developed a turbulence model specifically designed to predict the wake deficit, named the $k - \varepsilon - f_P$ model, based on a non-linear eddy viscosity model. The model introduced a variable C_μ which decrease the eddy viscosity in regions with high velocity gradients, improving the accuracy of the wake deficit compared to the standard $k - \varepsilon$ model. Good agreement with measurements and LES was obtained. One advantage of the $k - \varepsilon - f_P$ model is that is applied to the entire domain, and it is not necessary to prescribed the region as in the model from El Kasmi and Masson (2008).

van der Laan et al. (2014) also assessed non-linear eddy viscosity models (NLEVMs) for wind turbines wake modelling, and experienced numerical instability issues, particularly when using higher order NLEVMs, small grid spacing and small values of C_μ. It was concluded that the quadratic NLEVMs are the most promising alternatives for wake modelling because they improve the prediction of the turbulence anisotropy, but without impacting significantly the numerical stability as higher order NLEVMs, which showed high instability when simulating the ABL even without turbines.

Shives and Crawford (2016) simulated model-scale tidal turbines using the approach from El Kasmi and Masson (2008) and Menter's SST model (Menter, 1992). It was found that even though these model improve the predictions of the velocity in the near wake, they underestimate the turbulent kinetic energy. They stated that this occurs because the AD approach is not solving the tip vortices, and therefore it cannot capture the production of turbulence as a result of the breakdown of these structures, and therefore this process needs to be modelled to improve the accuracy. To this end, they proposed to add an additional source term into the k equation of the SST model, that essentially increases the production of turbulent kinetic energy in a cylindrical region behind the rotor. The additional term is a percentage of the standard production rate that needs to be prescribed, and accounts for the breakdown of larger eddies into smaller ones. Also, two additional parameters are needed to determine the size of the cylindrical region where the turbulent kinetic energy is augmented, which will vary from case to case. Their results showed good prediction of velocities and turbulent kinetic energy. Finally, Shives and Crawford (2016) also implemented the $k-\varepsilon-f_P$ model from van der Laan et al. (2015c), and found that it was significantly increased the decay rate of turbulent kinetic energy when modelling the empty water-tunnel.

2.5.3 Wind turbine CFD models

The most accurate approach to simulate a wind turbine using CFD is by fully solving the flow field around the blades, with a very fine mesh that captures the boundary layers at the walls. These simulations, commonly known as full rotor simulations (FRS), are computationally expensive (Gómez-Iradi et al., 2009; Afgan et al., 2013; Herráez et al., 2014; Abdulqadir et al., 2016). Occasionally, a uniform inflow is used, where the flow can be assumed axisymmetric, to further reduce the domain size and computational cost. This limitation has encouraged researchers to develop alternative numerical models that are less expensive than FRS but more accurate than BEM.

One example is actuator models, where the Navier-Stokes equations are solved and the turbine rotor is modelled by actuator points that act as additional source/sink terms in the momentum equations (See Eq.2.45). Two such methods, actuator disk models (ADM) and actuator line models (ALM) are widely used in the literature. These methods, apart from reducing considerably the computational cost of fully resolved CFD simulations, simplify considerably the mesh generation process allowing the change of the turbine geometry parameters easily.

2.5.3.1 Actuator line models (ALM)

The actuator line models (ALM), first developed by Sørensen and Shen (2002) combined with LES simulation, is intrinsically unsteady and non-axisymmetric. Here, each blade is replaced by a line of actuator points. Each actuator point represents a sink of momentum produced by a blade element. The loading at each actuator point is calculated from the local flow field, the turbine geometry and the airfoil data. Integrating these individual contributions the torque and thrust can be calculated. If the grid is fine enough, this method can reproduce complex flow features such as tip and root vortices, producing in general good predictions in the near wake region. Actuator line models have been used in several studies Troldborg et al. (2009), Porté-Agel et al. (2011), Troldborg et al. (2011), Lu and Porté-Agel (2011), Troldborg et al. (2015), Sørensen et al. (2015) and Baba-Ahmadi and Dong (2017a), Apsley et al. (2018), Apsley and Stansby (2020) among many others. However, the computational cost is still significantly high (compared to actuator disk models (ADM)) considering that the time step is determined by the mesh resolution at the tip of the blade and the blade tip speed. Sanderse et al. (2011) pointed out that most LES simulations of wind farms were performed using ADM.

2.5.3.2 Actuator disk models (ADM)

Actuator disk models (ADM) are significantly cheaper, particularly if they are used in combination with RANS equations and simple eddy viscosity models. There are different ways of implementing them. The simplest actuator disk model is known as the Rankine-Froude actuator disk and is also the basis of the 1D momentum theory. In this model, the turbine geometry is replaced by a disk of zero thickness with uniformly distributed acting force and without rotation. However, here we use ADM to refer to more general types of models, that follow essentially the same principles as the ALM models described above. Thus, the Navier Stokes equations are solved to determine the flow field, and the forces acting on blade elements are calculated and distributed across a disk of actuator points.

Several studies have used actuator disks and in general two main approaches are found in the literature. The first and simplest form introduces a drag force proportional to the square of the unperturbed velocity at the disk centre using the turbine thrust coefficient (Jimenez et al., 2007; Prospathopoulos et al., 2011; Cabezon et al., 2011; Porté-Agel et al., 2011; El-Askary et al., 2017; Antonini et al., 2019). This method ignores the geometric details of the turbine and the tangential forces that induce wake rotation. The second approach is based on Blade Element theory, which requires the specification of the turbine geometry and tabulated airfoil data (Mikkelsen, 2003; Wu and Porté-Agel, 2011; Porté-Agel et al., 2011; Wu and Porté-Agel, 2013; Porté-Agel et al., 2013; Tossas and Leonardi, 2013; Shives and Crawford, 2016).

ADMs simplify considerably the flow field through the rotor and therefore they do not capture some complex flow features such as tip and root vortices. The intrinsic unsteadiness of the flow field is lost in a rotor with a virtually infinite number of blades. Thus, ADM predictions are not expected to be accurate in the near wake region, but they still produce good prediction in the far wake. Troldborg et al. (2015) compared full rotor simulations with ALM and ADM and concluded that even though full rotor simulations produce a more turbulent wake, ADM is as accurate as the ALM to study the turbine wakes (far wake region). Consequently, considering that they are significantly cheaper, they are a good choice to model wind farms. Chapter 4 will describe the ADM model implemented in OpenFOAM, which is one of the main components of the framework for uncertainty quantification being developed.

2.5.3.3 Correction factors and 3D effects

As described in Section 2.5 the Blade Element Momentum theory requires two types of corrections: The Prantl's tip loss correction to account for the infinite number of blade representation and the Glauert correction to account for the breakdown of underlying assumptions of 1D momentum theory when the axial induction factor $a > 0.5$. On the other hand, the actuator models described above solve the velocity field from first principles, nevertheless, they still might need additional corrections to account for rotational effects.

ADMs, in particular, lack the discrete number of blades and therefore need to add a sort of Prandtl tip loss correction but in a different way (Shen et al., 2005a). Mikkelsen (2003) and Shen et al. (2005b) proposed that the tip loss correction should be used as a relaxation parameter when solving Navier-Stokes. Thus, applying the correction to the axial and tangential induction factors before reading airfoil data. Furthermore, ADMs cannot resolve tip and root vortices and need an additional correction for pressure equalisation at the tip of the blades (Shen et al., 2005b; El Kasmi and Masson, 2008). Usually, these models neglect the radial velocity component. Depending on the operating conditions, this might be a good approximation in the mid-span. However, near the tip and the root of the blades, this radial component becomes more significant. Tip vortices will drop the lift generated and change the airfoil polar curves. This correction reduces the loading towards the tip and is done by applying a Prandtl tip loss correction to the 2D airfoil data.

ALMs, on the other hand, can capture tip and root vortices and pressure equalisation develops naturally and in principle, there is no need for tip loss corrections (Tossas and Leonardi, 2013; Apsley and Stansby, 2020). However, tip loss corrections have also been used with ALM to correct loading when using 2D airfoil data that is not consistent with the local flow conditions (Shen et al., 2005b). Shen et al. (2012) and Baba-Ahmadi and Dong (2017b) used the ALM with tip loss correction proposed by Shen et al. (2005b). Blondel et al. (2017) used the ALM implemented in SOWFA (Simulator fOr Wind Farm Applications) developed by the US National Renewable Energy Laboratory that also gives the option to include tip loss corrections. Wimshurst and Willden (2017) compared an ALM with Full Rotor Simulations (FRS) and showed that the Shen et al. (2005b) correction does improve the loading prediction of the ALM, but the correction model coefficients need tunning.

Finally, real rotors under dynamic inflow conditions experience other phenomena such as stall delay, rotational augmentation and dynamic stall (Snel et al., 1993; Schreck and Robinson, 2002; Larsen et al., 2007; Schepers et al., 2014). 2D airfoil data does not account for these phenomena and additional models are used to correct them. Herráez et al. (2014) derived 3D airfoil data from blade resolved simulations to use as an alternative to 2D airfoil data, but they will be valid only at the operating conditions at which they were obtained. Dynamic stall models, in particular, might be required when analysing active pitch control strategies and more accurate loading on the blades are needed. Nevertheless, the present work focuses primarily on wake interaction and dynamic stall models will be not further discussed.

2.6 Wind farm optimization

The primary objective of any wind farm is to produce the maximum amount of energy at the minimum LCOE. This optimization process can be analysed from many different perspectives and wind turbine aerodynamics is only one of many aspects to consider along the entire lifespan of a wind farm. This section describes some of the fundamental aspects to be considered for wind farm optimization at the design and operation phases (i.e. micrositing and control respectively).

2.6.1 Micrositing

Micrositing consists in determining the exact position of the turbines (and turbine model) based on the characteristics of the wind at a particular location. The main objective is to minimize power losses and reduce structural loads. In one hand, turbines should be placed well separated to reduce wake interactions, but close enough to reduce installation, operation and maintenance costs. An optimum balance that minimize the LCOE has to be found.

Barthelmie and Jensen (2010) found that larger turbine spacing increases the wind farm efficiency up to velocities of the order of 15 m/s (in this particular study), over which no significant effect of turbine spacing was observed. Thus, over a certain wind speed, turbine spacing becomes less relevant for the overall wind farm efficiency. Similarly, increasingly large wind turbines have also a positive impact in reducing wake losses. Since the power output increases with the square of the rotor diameter and the wake losses decrease linearly with turbine spacing, for a given area and power rating for a wind farm, large wind turbines will increase the turbine spacing reducing wake losses Barthelmie et al. (2011).

In practical situations relatively simple wake models are used to simulate several turbine arrays under the local wind characteristics. However, it is known that these simple engineering wake models underpredict wake losses in large wind farms (Gaumond et al., 2014). Moreover, Bleeg et al. (2018) showed the importance of wind farm scale blockage using field measurements and RANS simulations, and how traditional wake superposition methods only consider the effects of wind turbines on downstream turbines is not suitable. Therefore, as the understanding of wind farm flow physics improves, and computational resources increase, better engineering tools will be developed.

2.6.2 Active wake control

During operation, however, the turbine position is fixed and now the control system is in charge of develivering the maximum power. In general, there are two different approaches for wind farm power control. The first and more conventional method is to optimise each turbine in a wind farm individually (single turbine control), maximizing power generation and minimizing structural loads. The second approach is to pursue the same objectives but considering the entire wind farm as a whole using smart control strategies (van Dijk et al., 2016; Boersma et al., 2017). This latter approach is known as wind farm active control or active wake control, and it might need that some turbines operate under sub-optimal conditions to improve the total performance of the wind farm. These smart control strategies are typically separated in two groups, axial induction control and wake steering. Both methods aim to control the turbine wakes and reduce loads and losses, and they will be briefly described in the following subsections. Note that with the development of floating offshore wind turbines, in the future it might be also possible to control the position of turbines (Boersma et al., 2017).

2.6.2.1 Axial induction control

The main idea behind axial induction control is to reduce the axial induction of the upstream turbines, such that the turbine in the wake have more kinetic energy available, increasing the total power generation and reducing the loadings. This idea can be traced back to Corten (2000). An actuator disk not only extracts momentum from the wind mean kinetic enery as useful power, but also dissipates some of this wind kinetic energy as heat. Corten (2000) showed from 1D momentum theory that when operating two or more turbines aligned along the wind direction, it is also important to minimize this energy loss in upstream turbines. Thus, by reducing the axial induction of the first turbine, the power reduction will be over-compensated by an increase in power generation in downstream turbines, as less wind kinetic energy is lost into heat, increasing the overall wind farm efficiency. Later, Corten and Schaak (2003, 2004b) found through simulations that the reduction of the axial induction produced an additional effect (which they named *flux*) that had to do with the expansion of wake. Lower axial inductions resulted in a reduced wake expansion and an increased momentum flux for the downstream turbine. As such, they called this control strategy *Heat and Flux*, currently known as axial induction control. They also confirmed their finding in wind tunnel tests where a 4.6% increase in power was achieved (Corten and Schaak, 2003), and applied for US patent (Corten and Schaak, 2004a).

Machielse et al. (2007) and Barthelmie et al. (2011) presented the results of a real scale experimental work where the 'Heat and Flux' approach was applied. Full scale turbines at the Energy Research Centre of the Netherlands (ECN) Wind Turbine Test Station Wieringermeer (EWTW) were tested. The turbines had a rated power of 2.5 MW and a hub height of 80 m separated by 3.8D (Schepers, 2007). First of all, it was found that effectively a power increase is achieved by reducing the axial induction factor in the first turbine and that the gain in power is dependent on the wind speed. The greatest gain was obtained at lower wind speeds, which was close to the cut in speed and therefore the reduction in the wake effect has a considerable effect in power generation of downstream turbines, and as the wind speed was increased the gain in power decreases continuously up to near zero for the rated wind speeds. In general, it was reported that the total gain should be around 0.5% or less which was considered significant since it comes at a very low additional cost. More recently, van der Hoek et al. (2019) conducted a similar field test to assess the effects of axial induction control and they estimated an energy increase of around 0.37% for the Goole Fields onshore wind farm. They found an increase of 3.3% of energy for a specific wind direction sector, where five turbines are aligned and separated between 2.3D and 3.1D. It is important to note that these experimental studies were carried out using SCADA datasets using 10 minute averaged values with a margin of ±10 degrees, and as it was showed by Gaumond et al. (2014), the high variability of wind directions is not well captured within these averaged values.

Furthermore, Annoni et al. (2016) showed that running simulations using low-order engineering wake models result effectively in an increase in power production when using axial induction control, but high order simulations (LES) lead to different conclusions challenging previous results. Annoni et al. (2016) analysed this control method simulating two turbines in a row using a high order wind farm model (SOWFA: Simulator fOr Wind Farm Applications developed at the US National Renewable Energy Laboratory NREL) and found that the second turbine was unable to capture the power lost on the first turbine by reducing the axial induction, resulting overall in a reduction of the total power. They emphasize that the simulated conditions, with low turbulence levels and large wake losses, represent an ideal case for axial induction control (i.e. inflow at 8 m/s with $TI = 6\%$). Their analysis shows that the additional power resulting from the reduced axial induction spreads out of the rotor region as the wake expands. Thus, the turbine downstream is not able to recapture it unless it is located within 1D downstream, which is of course unrealistic.

Further research is needed to fully understand under what circumstances axial induction control has a benefit. It has been observed the greatest gain in terms of power occurs at wind speeds lower than the rated wind speed, under strong wake interaction, with little wake recovery and reduce turbine spacing. Nevertheless, even if the total power generation is not increased, the structural loads might be reduced significantly for the same power output (Boersma et al., 2017).

2.6.2.2 Wake steering

Wake steering in another interesting control method that aims to increase the power production of a wind farm by reducing wake losses. The concept is essentially to deflect a turbine wake away from downstream turbines by yaw misalignment. If the flow is not perpendicular to the rotor plane, it will experience a lateral thrust force changing the flow direction (Note that this could be achieved also by tilting the rotor). As a consequence, the misaligned turbine will produce less power, while the turbine downstream could compensate this power loss as it is no longer under full wake. To the best of the author knowledge, this idea was presented for the first time by Parking et al. (2001) at a conference in Gottingen, Germany. Later, one of the co-authors of this conference paper (Medici, 2005), states in his PhD thesis that the original idea of Active Wake Control by yaw misalignment was from J.A. Dahlberg, and estimated that 4% power increase could be achieved. Corten et al. (2004) were granted a patent for a series of methods to arrange wind turbines based on the wake steering principle with both yaw and tilt angles.

A field test showed no clear effect on wake redirection (Machielse, 2011; Wagenaar and Schepers, 2012). On the other hand, simulations have demonstrated the wake steering effect (Jiménez et al., 2009). Churchfield and Fleming, P Bulder, B White (2015) studied yaw-misalignment as a control strategy in LES simulations combined with actuator line models (ALM) and found an increase in the efficiency with yaw angles in the order of 20°. Some studies have estimated an increase of 3.7% of the AEP (Gebraad et al., 2017), but depending on the models and the assumptions the benefits this could be anywhere between 0.5% to 6% (Knudsen et al., 2015). More recently, Kanev et al. (2018) concluded that wake steering could regain between 4% to 6% of wake losses, and that it could actually reduce loads and increase the lifespan of turbines by 1.5%. Nevertheless, it might also occur that if the wake is not completely redirected away from the downstream rotor, an increase in fatigue loads will be produced van Dijk et al. (2016).

Certainly, further research is needed to establish more precisely the potential benefits of wake steering under a wide range of operating conditions, and to develop improved models for wind farm control. And, even though currently the wind turbine tilt angle is fixed, understanding the effects of tilt steering could potentially improve wind farm designs (Fleming et al., 2014).

2.7 Uncertainty quantification in wind energy

So far, this chapter described the main physical aspects of wind turbines, wakes and their interaction with the atmospheric boundary layer. It presented the role of computational models with particular emphasis on RANS-BE actuator methods to model turbine rotors. And the last section discussed some interesting research topics of wind farm optimization that essentially use CFD models to enhance our understanding and provide new insights to make wind energy more efficient.

According to Veers et al. (2019), the three major challenges ahead for wind energy research are: (i) to increase our understanding of the physics of atmospheric and wind farm flows, (ii) to improve modelling tools and materials for the design of the new generation of larger and more flexible wind turbines and wind farms, and (iii) the optimization and control strategies for the integration of the increasingly large number of wind turbine and wind farms to the electrical grid. Note that all these challenges are interrelated. More knowledge about the physical processes can improve the computational models, and better models can enhance the comprehension of the physics and improve wind farm optimization and control strategies. As such, this work directs attention to the modelling tools emphasising the need for uncertainty quantification in CFD computations.

2.7.1 Uncertainty quantification in wind energy

In engineering, uncertainties that are beyond our understanding end up behind a rather conservative safety factor. A typical example of uncertainty quantification in wind energy is the estimation of the annual energy production (AEP). Long term measurements are used to characterise the wind resource and simplified engineering wake models (and experience) are used to quantify wake effects and predict the performance of a wind farm. Nevertheless, the wind energy industry is moving fast into increasingly large (and more flexible) wind turbines and wind farms where there is no or little experience increasing the risks and leading to inappropriate decision making.

One example comes from one of the challenges mentioned before: our lack of a complete understanding of the interaction between large wind farms and the atmospheric boundary layer. Bleeg et al. (2018) showed the importance of wind farm scale blockage using field measurements and RANS simulations, and how traditional wake superposition methods, that only consider the effects of wind turbines on downstream turbines, are not suitable. Later in 2019, Ørsted was forced to update its long-term financial targets after realizing that their offshore productions forecast were underestimating the negative impact of wakes and blockage effects (Ørsted, 2019). This example also highlights the value of computational fluid dynamics.

Uncertainty quantification was described as a key research challenge for wind energy by the European Academy of Wind Energy (EAWE) (van Kuik et al., 2016). Uncertainty quantification involves two main tasks: uncertainty characterisation where the sources of uncertainties are identified and described statistically using probability density functions, and uncertainty propagation where the uncertainties are propagated to determine the response of the system. These topics will be discussed in more details in Chapter 3. As such, the wind industry must characterise and quantify the impact of different sources of uncertainties not only in experiments and field measurements but also in the computational models used in the design and operation of wind farms.

A review of uncertainty quantification in wind energy is given by van den Bos and Sanderse (2017). Although there are several studies dealing with uncertainty quantification and optimization in wind energy applications, many of which use low-cost wake models and Monte Carlo simulation methods to propagate uncertainties (Lackner et al., 2007; Marmidis et al., 2008; Hrafnkelsson et al., 2016; MirHassani and Yarahmadi, 2017), here the attention is on CFD models and what has been done to quantify the impact of uncertainties.

One topic that has been analysed in the literature is wind direction uncertainty. Barthelmie et al. (2009) compared measured and computed power losses at Horns Rev offshore wind farm using different engineering wake models and CFD simulations. They observed that the wake models tend to overpredict the power losses, particularly when narrow wind direction sectors were compared, and that for wider direction sectors up to ±15°, better predictions were obtained. Later, Gaumond et al. (2014) found that the main reason for the discrepancies between measured power losses and predicted values by wake models, are due to the variability in measured wind directions, which is not captured by the 10 min averaged values obtained from measurements. Thus, narrow wind sectors in 10 min averaged data are very likely to include moments where the wind direction is outside the narrow wind sector, with only partial or without wake interaction recording higher power outputs. They performed computation for a wide range of wind directions every 0.5 degrees and calculated the power using weighted averages using the wind direction probability density function. Wu and Porté-Agel (2015) studied this problem by running LES simulations with the ADM. They simulated the entire wind farm under nearly neutral stability conditions running simulations for wind sectors with increments of 1° and 2° and then averaged the results to obtain a more representative power deficit. They found that their simulation predicted more accurately the power deficit even for narrow wind direction sectors of ±1° and ±3°, although the same trend was found, the narrower the sector the greater the power deficit. A similar approach was followed by van der Laan et al. (2015b) and Antonini et al. (2019) who used RANS simulations with weighted averages to include wind direction uncertainties.

Both studies used ADM and performed simulations every 3° and 2.5° respectively.

All these studies have made an effort in propagating wind direction uncertainty but arguable not in the most efficient way. For instance, Wu and Porté-Agel (2015) ran sixteen LES simulations to capture the wind direction uncertainty for half of a wind sector (because it was assumed that the response was symmetric on the other half) and van der Laan et al. (2015b) used seventeen RANS simulations for a wind sector. However, CFD models are relatively expensive and the number of simulations should be reduced as much as possible. A more efficient alternative method is the so-called Polynomial Chaos (gPC), which reduces considerably the number of deterministic evaluations needed being very attractive to propagate uncertainties in CFD applications.

2.7.2 Polynomial Chaos

Generalized Polynomial Chaos methods have been used to perform uncertainty quantification analysis in a wide variety of problems. Murcia et al. (2015) presented a study, where polynomial chaos was applied to estimate the annual energy production in wind farms using simple engineering wake models. The aim was to reduce the number of evaluations compared with traditional methods based on trapezoidal and Simpson's integration rules. The wind speed and wind direction were taken as random variables following Weibull and Von Misses probability density functions respectively. A multi-element approach was used to separate the integration regions in small-sub-regions (defined as wind directions bins), where the wind speed and the wind direction can be assumed to be independent. Different Weibull parameters were determined for each wind direction sector. They capture the power response surface of horns rev using 288 simulations and compared very well with a more detailed and more traditional method that used 30960 simulations. Similarly, Padrón et al. (2016) presented a wind farm layout optimisation method based on polynomial chaos. In this study, a stochastic computation of the AEP as a function of the wind speed and wind direction, taken as random variables, was performed. The turbines position x and y were the design optimisation variables. An engineering wake model was used to determine the wake deficit, together with the turbine characteristics such as the power curve. The optimization model was run several times varying the positions of 60 turbines, calculating each time the AEP. The optimized layout was then compared with a square grid-like layout, the original layout, and a randomly generated layout. It was found that the more grid-like the layout is, the more is the variability of the power output as a function of the wind direction, being the optimized layout not only the one that maximizes the AEP but also the one that has lower variability. These two studies proposed methods for wind farm layout optimization, where thousands of simulations are required to test different turbine configurations under different operating conditions. Although polynomial chaos reduces significantly the number of simulations, simplified engineering wake models are still needed because CFD models remain too expensive for this purpose.

As mentioned before, CFD models at the moment have a different role by enhancing our understanding of the flow physics in wind turbines and wind farms. Nonetheless, as all computational models, CFD models themselves have intrinsic sources of uncertainty due to the simplifications introduced in the mathematical formulations (e.g. turbulence models) and the numerical discretisation (See Chapter 3). Moreover, several phenomena contribute to the uncertainty in the response of the system such as 3D effects, dynamic effects, stall, yaw misalignment (Schepers et al., 2018), as well as the uncertainty in the inflow conditions. Therefore, it is important to close the existing gap between CFD and uncertainty quantification mainly due to the high computational cost. In this way, CFD would provide greater insights into the physical processes increasing the accuracy and the confidence in the predictions.

Fortunately, there are good examples of the application of polynomial chaos to CFD computations. Han et al. (2012) determined the response of a laminar flow past a flat plate with uncertainty in the inflow conditions using direct numerical simulations (DNS) and a bivariate polynomial expansion with 49 simulations in total. García-Sánchez et al. (2014) and Gorlé et al. (2016) presented an uncertainty quantification study for CFD simulations of the wind flow within downtown Oklahoma City using a non-intrusive Polynomial Chaos expansion and the two equations $k-\varepsilon$ turbulence model. They considered three inflow parameters as random variables: wind speed, wind direction, and aerodynamic roughness. In total 729 RANS simulation were performed (with 9 quadrature points in each direction). Daróczy et al. (2016) used polynomial chaos to analyse the performance of a vertical axis wind turbine H-Darrieus running bivariate cases with 36 simulations for each TSR with CD-Adapco StarCCM+. Karimi et al. (2019) applied polynomial chaos to a gas turbine vane using ANSYS Fluent R18.2.

This thesis aims to develop a computational framework for uncertainty quantification in wind turbines and wind farms using CFD. This will allow us to enhance our understanding of the physical interaction between wind turbine arrays and the atmospheric boundary layer and contribute to the major challenges in wind energy research.

2.8 Summary and Conclusions

This chapter presented the literature review and theoretical background with the most relevant concepts for wind energy from the aerodynamic perspective as well as the challenges of wind energy research and the role of uncertainty quantification.

It was described the fundamentals characteristics of the wind energy physical system pointing out the complex interaction between wind farms and the atmospheric boundary layer and the wide range of time and length scales involved. The energy that can be harvested by a wind farm is limited by the transport mechanisms of momentum across the ABL, between the geostrophic wind in the free atmosphere (wind energy reservoir) and the ground surface. Atmospheric stability is one of the most important characteristics of the atmospheric boundary layer. Stability conditions determine the height of the ABL, the shape of the wind shear profiles, and the turbulence intensity. At higher wind speeds (above rated wind speeds) buoyancy forces become negligible and neutral conditions are predominant. Besides, wake effects account for up to 10 to 20% of power losses while increasing the fatigue loadings and reducing the lifespan of wind turbines. Consequently, minimizing their impact is one of the primary tasks during the design and operation of a wind farm.

Over the last decades, there has been an increasing interest in active wake control strategies, that aim to improve the performance of wind farms as a whole, rather than optimizing the performance of individual turbines. There are two main methods: axial induction control, and wake steering. Axial induction control aims to reduce wake losses by reducing the axial induction in upstream turbines (by pitching the blades), reducing the losses of kinetic energy into heat, so that downstream turbines increase their power generation compensating the power loss in the upstream turbine. Wake steering, on the other hand, aims to redirect the wakes out of downstream turbines by yawing the rotor. However, these control strategies require a deep understanding of the physics of the wakes and how they interact with each other, and with downstream turbines, the intrinsic variability, so that control algorithms are capable of effectively maximise the benefits. Wakes are hard to control, particularly under unstable conditions (Boersma et al., 2017).

This chapter also presented the computational models used with an emphasis on RANS CFD models and actuator models. There is a wide range of modelling tools used in wind energy varying in complexity, costs and accuracy, and each one of them plays an important role. The optimization of the wind farm layout, and the control algorithms, rely on simplified engineering models that are based on fundamental physical principles and empirical observations, because of their low computational cost. Nevertheless, as the size of wind turbines and wind farms increases, the underlying assumption in such models are no longer suitable.

With the growth of computational power, CFD models are helping to increase our understanding of the physical processes involved. One example is wind farm blockage effects, which have shown that turbines not only affect downstream turbines. Actuator line (ALM) and actuator disk models (ADM) have proven to be good alternatives to more expensive blade resolved computations. While ALM can solve some turbulent structures in the near wake region, ADM can be good at predicting the main flow features in the far wake region at a much lower cost. RANS models also reduce the cost compared to LES but the widely used linear eddy viscosity models are not able to capture turbulence anisotropy that characterises such flows. Model improvements have been proposed (El Kasmi and Masson, 2008; van der Laan et al., 2015b; Shives and Crawford, 2016), but some require additional model parameters. Besides, CFD models are still relatively expensive and little has been done in uncertainty quantification since several simulations are required. Polynomial chaos has been used successfully to propagate uncertainties in CFD applications increasing the level of information and the confidence in the predictions. This offers an opportunity to address uncertainty quantification in wind farms using CFD and reduce the number of simulations that are needed to propagate uncertainties.

Finally, as a closing remark, it is expected that this overview can help to understand the advantages, disadvantages, and limitations of the methods used in the current work.

BLANK PAGE

Chapter 3

Uncertainty Quantification

3.1 Introduction

In the previous chapter, some of the physical aspects of offshore wind environment and its relationship with the performance of wind farms were described. It was established that the physical system is very complex and chaotic, limiting the predictability of the performance of wind farms (e.g. Power output, Levelised cost of energy (LCOE)).

To analyse such a complex system, it would be ideal to carry out extensive measuring campaigns that collect high fidelity data at a high spatial and temporal resolution, but unfortunately, that is technically and economically impossible. With limited resources engineers need to develop simplified mathematical models to make predictions of an outcome given certain conditions and to improve the understanding of that physical phenomenon.

Computational resources have significantly increased over the past decades making computational models a fundamental tool in engineering design and optimisation. In particular, computational fluid dynamics (CFD) has proven to be a powerful tool to solve many scientific and engineering problems, reducing the need to carry out extensive and expensive experimental work. Nevertheless, it is important to understand its limitations such as the underlying simplification introduced in the mathematical formulation of the models, and the errors introduced in the numerical approximation of a solution. Also, CFD models are deterministic and their output will depend on the input data provided (e.g. initial and boundary conditions), which in reality is somewhat uncertain.

In chaotic systems, small uncertainties in input data grow exponentially in time, increasing the complexity of creating mathematical models that can predict, for instance, how the weather is going to be the next day, how windy is going to be, or what is going to be the power output of a wind farm. It can be argued then, that wind power output should be analysed as a stochastic process due to its inherent variability.

Therefore, uncertainties should be identified, characterised and quantified. This process is known as uncertainty quantification (UQ), and it is a crucial component of engineering development. It provides valuable information to manage and reduce the risk in decision making to achieve the required levels of performance, reliability and safety.

In this work, a framework for uncertainty quantification for wind turbine arrays has been developed, which integrates CFD modelling with the generalised polynomial chaos. This chapter presents the main concepts behind this framework, the polynomial chaos method, how it has been implemented, along with some examples that illustrates its advantages and disadvantages.

3.2 Uncertainty quantification

In general, UQ involves the following aspects: uncertainty characterisation; verification and validation of the computational models to reduce or eliminate errors; and the propagation of uncertainties to determine how a quantity of interest responds under those uncertainties.

The validation of the computational model is achieved by comparing the model predictions with experimental measurements. In this context UQ could also help to make a fair comparison between experimental data and model predictions. More about the validation of the CFD models used in this work will be presented in Chapter 4. In this section the focus is on the uncertainty characterisation and uncertainty propagation parts. In particular, the propagation through generalised polynomial chaos (GPC) expansions.

3.2.1 Uncertainty characterisation

Uncertainty characterisation aims to establish the state of knowledge of every source of uncertainty in the system. In other words, every source of uncertainty should be identified and modelled as a random variable with a given probability density function. Nevertheless, in practice it might be impossible to account for all sources of uncertainties and a sensitivity analysis could be used to determine if a parameter should or not be considered. If the parameter shows a significant effect in the response of the quantity of interest, it should be considered as a source of uncertainty. This can help to reduce the number of uncertainties or input random variables, which is a critical aspect of uncertainty propagation.

Generally speaking, uncertainties can be classified in two groups: epistemic uncertainties that might be controlled and reduced, and aleatoric uncertainties (also known as stochastic uncertainties) that can never be eliminated and are understood as the natural variability of a system. Each source of uncertainty can be modelled as purely aleatoric, purely epistemic or a mixture of both (Roy and Oberkampf, 2011).

Alternatively, the sources of uncertainties, in the context of computational fluid dynamics, can be categorized in:

- **Model uncertainty:** which includes all the underlying assumptions and simplifications introduced in the mathematical description of the physical system (e.g. incompressibility, eddy viscosity). Note that, increasing the complexity of the models, capturing more physical aspects, will not necessarily reduce the uncertainty, particularly when the uncertainty in the measurements is high. Since it is not possible to include all the physical variables in mathematical models, the questions are which ones are the most relevant parameters and how sensitive is the quantity of interest on other variables, which might even be unknown.

- **Numerical uncertainty:** which correspond to the numerical errors added by the spatial and temporal discretization of the system of equations and the finite representation of numbers in computers. This in theory can be reduced by refining the computational mesh, but this increases the computational cost.
- **Data uncertainty:** related to all the input parameters that are required to close the system of equations (e.g. inflow and boundary conditions, geometries) and other model coefficients that are determined experimentally, and that may not be suitable for all applications, or that are simply affected by experimental errors.

Some uncertainties might be completely unknown, or if they are known the effects they produce in the output of interest might not be completely understood. In these cases, a common engineering practice is to add safety factors. However, one of the aims of uncertainty quantification is to reduce these uncertainties and increase the knowledge of the system. In general, knowledge from computational models and experimental measurements, which costs time and resources, can help to reduce epistemic uncertainties and allow a better characterisation of aleatoric uncertainties.

3.2.2 Uncertainty propagation

After the uncertainty characterisation process, the source of uncertainties can be arranged in a set of N random variables $\boldsymbol{\xi} = \{\xi_1, ..., \xi_N\}$, with their respective probability density functions $p_i(\xi_i)$ for $i = 1, .., N$, representing the uncertainty in the system. The next step is to propagate this uncertainty to determine how the system responds, or in other words to quantify the effect of the uncertainty on any quantity of interest $s(\boldsymbol{\xi})$. Note that here, the quantity of interest $s(\boldsymbol{\xi})$ represents the deterministic model, but since $\boldsymbol{\xi}$ is a set of input random variables, $s(\boldsymbol{\xi})$ is also a random variable. The goal of uncertainty propagation is to determine the probability density function of this model response. To this end, different methods exist, in this chapter two of them are described: Monte Carlo Sampling and Polynomial Chaos.

3.2.3 Monte Carlo propagation

Monte Carlo propagation is perhaps the simplest approach to propagate uncertainties, which consists in random sampling $\boldsymbol{\xi}$ and evaluating the deterministic model $s(\boldsymbol{\xi})$ as shown in Figure 3.1. This process is repeated several times until the probability density function of the quantity of interest is determined. The statistic of the model output converges after a large number of deterministic realizations of the model (The Law of Large Numbers). This is probably fine for relatively simple models, but certainly will not be appropriate for most CFD applications, where a single simulation has a relatively high computational cost.

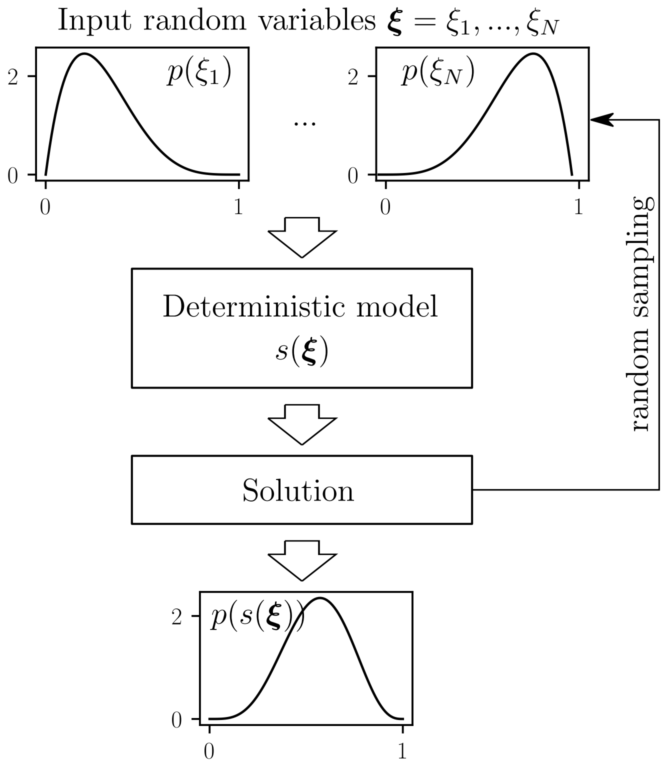

Figure 3.1: Schematic representation of Monte Carlo approach for uncertainty propagation.

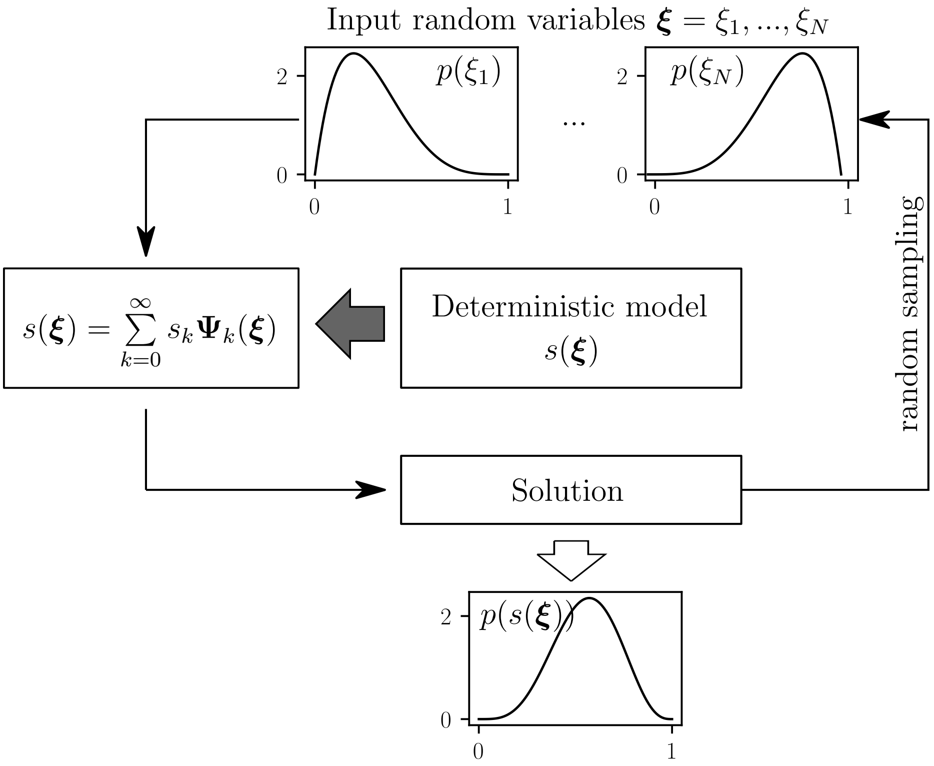

Figure 3.2: Schematic representation of spectral methods approach for uncertainty propagation.

3.2.4 Spectral methods for uncertainty propagation

When the deterministic model is expensive, an alternative approach is to use so called spectral methods for uncertainty quantification (see Figure 3.2). Here the idea is to reconstruct the functional dependence from the model solution $\boldsymbol{s}(\boldsymbol{\xi})$ on the input independent random variables $\boldsymbol{\xi}$ in a series expansion (Eq.3.1).

$$s\left(\boldsymbol{\xi}\right) = \sum_{k=0}^{\infty} s_k \boldsymbol{\Psi}_k(\boldsymbol{\xi}) \tag{3.1}$$

Where $\boldsymbol{\Psi}_k$ are a set of selected functionals of the random variables, and s_k are deterministic coefficients, where information from the actual deterministic model is passed to the series expansion. Therefore, the main task in spectral methods is finding both the functionals $\boldsymbol{\Psi}_k$ and the expansion coefficients s_k. In this case, the deterministic model is used to construct the spectral expansion, but with considerably fewer evaluations than Monte Carlo propagation, being much more appropriate for CFD applications. One of such methods is called *Polynomial Chaos*, described in the following section. A detailed description of spectral methods for stochastic computations is given by Le Maître and Knio (2010), and in particular, for polynomial chaos expansion, is given by Xiu (2010).

3.3 Generalised Polynomial Chaos

Generalized Polynomial Chaos (GPC) is a method to find an approximation of a random variable through a series expansion as in Eq.3.1, where the functionals $\boldsymbol{\Psi}_k$ are determined using families of orthogonal polynomials, and the deterministic coefficients $\boldsymbol{s}_k$ are found from deterministic evaluations of the model.

The polynomial family for each random variable should be chosen based on the shape of the response surface, which is of course unknown. The idea is that choosing the appropriate polynomial family will improve the convergence of the method and reduce the number of deterministic evaluations. In practice, the polynomial families are chosen based on the probability density function of the input random variables, even though this does not always guarantee an optimal convergence. For instance, Legendre polynomials are used when the random variable is uniformly distributed, and Hermite polynomials are more suitable when the variable follows a Gaussian distribution.

In this section is outlined how the generalised polynomial chaos expansion of a random variable is obtained. This is based on the more complete descriptions in Le Maître and Knio (2010) and Xiu (2010).

Let $s(\boldsymbol{\xi})$ be a deterministic model of the quantity of interest s as a function of N independent random variables $\boldsymbol{\xi} = \{\xi_1, ..., \xi_N\}$, where $\xi_i \in \mathbb{R}$ is defined in a probability space $(\Theta_i, \Sigma_i, P_i)$, with a known probability density function $p_i(\xi_i)$. Note that $s \in \mathbb{R}$ is itself a random variable that maps $\boldsymbol{\xi} \in \Theta_1 \times ... \times \Theta_N \mapsto s(\boldsymbol{\xi}) \in \mathbb{R}$.

The idea is to find the PC expansion of the random variable $s(\boldsymbol{\xi})$. In general, the polynomial chaos of order p consists of all polynomials of order p, with all the possible combinations of the random variables ξ_i as:

$$\Gamma_p = \left\{ \bigcup_{\gamma \in \lambda_p} \prod_{\lambda_1}^{\lambda_N} \psi_{\gamma_i}(\xi_i) \right\} \tag{3.2}$$

where λ_p is a set of multi-indices $\gamma = \gamma_1, ..., \gamma_N$ for N independent random variables given by:

$$\lambda_p = \left\{ \gamma : \sum_{j=1}^{N} \gamma_i = p \right\} \tag{3.3}$$

and ψ_{γ_i} is the orthogonal polynomial of order γ_i from the corresponding polynomial family (See Appendix A), which is chosen according to the probability density function of each random variable.

As an example, consider the case with $N = 2$ random variables uniformly distributed and polynomials up to order $p = 3$. The first step is to construct the set of multi-indices λ_p for $p = 0, 1, 2, 3$ (from Eq.3.3).

$$\lambda_0 = \{\{0,0\}\} \tag{3.4}$$

$$\lambda_1 = \{\{1,0\},\{0,1\}\} \tag{3.5}$$

$$\lambda_2 = \{\{2,0\},\{1,1\},\{0,2\}\} \tag{3.6}$$

$$\lambda_3 = \{\{3,0\},\{2,1\},\{1,2\},\{0,3\}\} \tag{3.7}$$

Then Eq.3.2 can be expanded. The terms in Γ_p of order p can be expanded as follows:

$$\Gamma_0 = \psi_0(\xi_1)\psi_0(\xi_2) \tag{3.8}$$

$$\Gamma_1 = \psi_1(\xi_1)\psi_0(\xi_2) + \psi_0(\xi_1)\psi_1(\xi_2) \tag{3.9}$$

$$\Gamma_2 = \psi_2(\xi_1)\psi_0(\xi_2) + \psi_1(\xi_1)\psi_1(\xi_2) + \psi_0(\xi_1)\psi_2(\xi_2) \tag{3.10}$$

$$\Gamma_3 = \psi_3(\xi_1)\psi_0(\xi_2) + \psi_2(\xi_1)\psi_1(\xi_2) + \psi_1(\xi_1)\psi_2(\xi_2) + \psi_0(\xi_1)\psi_3(\xi_2) \tag{3.11}$$

Finally, the polynomial chaos expansion of order $p = 3$ of the random variable $s(\boldsymbol{\xi})$ with $N = 2$ is given by:

$$\begin{aligned} s(\xi_1, \xi_2) \approx\ & s_0\psi_0(\xi_1)\psi_0(\xi_2) \\ & + s_1\psi_1(\xi_1) + s_2\psi_1(\xi_2) \\ & + s_{11}\psi_2(\xi_1)\psi_0(\xi_2) + s_{12}\psi_1(\xi_1)\psi_1(\xi_2) + s_{22}\psi_0(\xi_1)\psi_2(\xi_2) \\ & + s_{111}\psi_3(\xi_1)\psi_0(\xi_2) + s_{112}\psi_2(\xi_1)\psi_1(\xi_2) + s_{122}\psi_1(\xi_1)\psi_2(\xi_2) \\ & + s_{222}\psi_0(\xi_1)\psi_3(\xi_2) \end{aligned} \tag{3.12}$$

where the indexing in the expansion coefficients s_x represent the order of the polynomial in each random variable. For instance, s_{112} indicates that is second order in ξ_1 and first order in ξ_2, since 1 is repeated twice and 2 only once. The polynomials $\psi_p(\xi_i)$ can then be substituted with Legendre polynomials, since the random variables are uniformly distributed, leading to:

$$\begin{aligned} s(\xi_1, \xi_2) \approx\ & s_0 \\ & + s_1\xi_1 + s_2\xi_2 \\ & + s_{11}\,\frac{1}{2}\left(3\,\xi_1^2 - 1\right) + s_{12}\,\xi_1\xi_2 + s_{22}\,\frac{1}{2}\left(3\,\xi_2^2 - 1\right) \\ & + s_{111}\,\frac{1}{2}\left(5\,\xi_1^3 - 3\,\xi_1\right) + s_{112}\,\frac{1}{2}\left(3\,\xi_1^2 - 1\right)\,\xi_2 + s_{122}\xi_1\,\frac{1}{2}\left(3\,\xi_2^2 - 1\right) \\ & + s_{222}\,\frac{1}{2}\left(5\,\xi_2^3 - 3\,\xi_2\right) \end{aligned} \tag{3.13}$$

To simplify the notation given in Eq.3.12, each term is writen as $s_k \boldsymbol{\Psi}_k(\xi_1, \xi_2)$ where s_k are the expansion coefficients and :

$$\boldsymbol{\Psi}_k(\xi_1, \xi_2) = \prod_{i=1}^{2} \psi_{\alpha_i^k}(\xi_i) \tag{3.14}$$

Here, α_i^k represent the same set of multi-indices λ_p but conveniently organised to have a single-index k corresponding to each term (See Table 3.1).

Table 3.1: Single- and multi-indexing correspondence in 2 dimensions

p	multi-index λ_p	single-index k
0	$\{0,0\}$	0
1	$\{1,0\}$	1
	$\{0,1\}$	2
2	$\{2,0\}$	3
	$\{1,1\}$	4
	$\{0,2\}$	5
3	$\{3,0\}$	6
	$\{2,1\}$	7
	$\{1,2\}$	8
	$\{0,3\}$	9

For the general case, with N independent random variables, the $p-$order PC expansion can be written as a series expansion with $P+1$ terms (See Eq.3.15). Note that the infinite series in Eq.3.1 has been truncated leaving an error $\epsilon(N,p)$. $\boldsymbol{\Psi}_k(\boldsymbol{\xi})$ for $k = 0, ..., P$ form an orthogonal basis of the polynomial chaos expansion. All that is left it to find the expansion coefficients s_k, which in the present work is done using what is called Non-Intrusive Spectral Projection described in the next section.

$$s\left(\boldsymbol{\xi}\right) = \sum_{k=0}^{P} s_k \boldsymbol{\Psi}_k(\boldsymbol{\xi}) + \epsilon(N,p) \tag{3.15}$$

$$\boldsymbol{\Psi}_k(\xi_1, \xi_2, ..., \xi_N) = \prod_{i=1}^{N} \psi_{\alpha_i^k}(\xi_i) \tag{3.16}$$

$$P + 1 = \frac{(N+p)!}{N!p!} \tag{3.17}$$

3.3.1 Non-Intrusive Spectral Projection (NISP)

There are different methods to determine the expansion coefficients s_k in Eq.3.15. They can be classified into intrusive and non-intrusive methods. The latter approach is the most attractive for CFD applications since the deterministic solver is taken as a black box, and there is no need to modify the model as it is the case for intrusive methods. Note that introducing changes in the model might be problematic considering that most of the available CFD solvers have been optimised, and any modification is very likely to impact the stability and convergence of the solver. However, non-intrusive methods are computationally expensive if the model, being considered as a black box, is expensive as well (Le Maître and Knio, 2010).

One of these non-intrusive methods is known as Non-Intrusive Spectral Projection (NISP), which aims to determine the expansion coefficients as an orthogonal projection (Eq. 3.18) of the model output s on the polynomial chaos expansion basis $\mathbf{\Psi}_k$.

$$s_k = \frac{\langle s, \mathbf{\Psi}_k \rangle}{\langle \mathbf{\Psi}_k, \mathbf{\Psi}_k \rangle} \tag{3.18}$$

This spectral projection uses the inner product defined as a multi-dimensional integral:

$$\langle u, v \rangle = \int_{N-dim} u(\boldsymbol{\xi}) v(\boldsymbol{\xi}) p_{\boldsymbol{\xi}}(\boldsymbol{\xi}) d\boldsymbol{\xi} \tag{3.19}$$

Where $p_{\boldsymbol{\xi}}(\boldsymbol{\xi})$ is the joint probability density function, which for independent random variables can be written as follows:

$$p_{\boldsymbol{\xi}}(\boldsymbol{\xi}) = \prod_{i=1}^{N} p_i(\xi_i) \tag{3.20}$$

Note that the denominator in Eq. 3.18 only depends on the orthogonal basis and can be calculated since the functionals $\boldsymbol{\Psi}_k$ have already been determined. Using the definition of the inner product in Eq. 3.19, the numerator in Eq.3.18 can be written as follow.

$$\langle s, \boldsymbol{\Psi}_k \rangle = \int_{N-dim} s(\boldsymbol{\xi}) \boldsymbol{\Psi}_k(\boldsymbol{\xi}) p_{\boldsymbol{\xi}}(\boldsymbol{\xi}) d\boldsymbol{\xi} \tag{3.21}$$

Note however, this multidimensional integral requires the solution of the model $s(\boldsymbol{\xi})$ that is being approximated, which remains unknown. This is where the deterministic CFD model is used to pass information to the PC expansion, or in other words, where deterministic simulations are required.

There are two types of techniques to estimate the multi-dimensional integral, ones are based on pseudo-random sampling strategies, and others based on cubature methods. An example in the latter case is the Gauss-Legendre quadrature, which is used in the present work (See Eq. 3.22). Here the multi-dimensional integral is approximated using a number N_q of deterministic realizations of the model $s(\boldsymbol{\xi})$ at specific values of $\boldsymbol{\xi}^j$ (known as nodes or quadrature points) and using the weights W^j. Note that the total number of deterministic evaluation $N_q = n_{q_1} \times ... \times n_{q_N}$, scales exponentially with the number of of random variables (i.e. $N_q = n_q^N$ if $n_{q_1} = ... = n_{q_N} = n_q$).

$$\langle s, \boldsymbol{\Psi}_k \rangle \approx \sum_{j_1=1}^{n_{q_1}} ... \sum_{j_N=1}^{n_{q_N}} s(\xi^{j_1}, ..., \xi^{j_N}) \boldsymbol{\Psi}_k w_{q_1}^{j_1} ... w_{q_N}^{j_N} = \sum_{j=1}^{N_q} s(\boldsymbol{\xi}^j) \boldsymbol{\Psi}_k(\boldsymbol{\xi}^j) W^j \tag{3.22}$$

3.3.2 Expected Value and Variance

Having found the polynomial expansion or order p with N random variables:

$$s\left(\boldsymbol{\xi}\right) = \sum_{k=0}^{P} s_k \boldsymbol{\Psi}_k(\boldsymbol{\xi}) \tag{3.23}$$

the expected value of s is given by:

$$E[s] = \langle s(\boldsymbol{\xi})\rangle = \langle \boldsymbol{\Psi}_0 s(\boldsymbol{\xi})\rangle = \sum_{k=0}^{P} s_k \langle \boldsymbol{\Psi}_0, \boldsymbol{\Psi}_k\rangle = s_0 \tag{3.24}$$

Note that by construction $\boldsymbol{\Psi}_0 = 1$ and because of orthogonality $\langle \boldsymbol{\Psi}_0, \boldsymbol{\Psi}_k\rangle$ is only non-zero for $k = 0$.

Similarly, the variance can be calculated by:

$$\begin{aligned} \mathrm{var}(s) = \sigma_s^2 = E[(s - E[s])^2] &= E\left[\left(\sum_{k=0}^{P} s_k \boldsymbol{\Psi}_k - s_0\right)^2\right] \\ &= E\left[\left(\sum_{k=1}^{P} s_k \boldsymbol{\Psi}_k\right)^2\right] = \sum_{k=1}^{P} s_k^2 \langle \boldsymbol{\Psi}_k^2\rangle \end{aligned} \tag{3.25}$$

3.3.3 Convergence of L^2Norm

To assess the convergence of the gPC expansions, the truncation error ϵ (see Eq.3.15) can be normalised with the L^2Norm as (Han et al., 2012):

$$\frac{\epsilon_2(s)}{\mathrm{var}_2(s)} = \sqrt{\frac{\int_\Theta \left[\sum\limits_{k=P+1}^{\infty} s_k^2 \boldsymbol{\Psi}_k^2\right]^2 d\boldsymbol{\xi}}{\int_\Theta [\mathrm{var}(s)]^2 d\boldsymbol{\xi}}} \tag{3.26}$$

In practice, no exact solution exists for the variance and therefore the variance computed with highest number of quadrature points (p, max) is used to estimate the L^2Norm for the gPC expansion of order p as:

$$L^2\mathrm{Norm}|_p = \frac{\epsilon_2(s,p)}{\mathrm{var}_2(s,p)} = \sqrt{\frac{|A_{p,max} - A_p|}{A_{p,max}}} \quad \text{with} \quad A_p = [\mathrm{var}(s)]_p^2 \tag{3.27}$$

3.3.4 Sobol's indices

Sobol indices can also be computed for sensitivity analysis as:

$$S_i = \frac{\sum\limits_{k \in I} s_k^2 \langle \mathbf{\Psi}_k^2 \rangle}{\mathrm{var}(s)} \tag{3.28}$$

where I is the subset of indices of polynomials of the orthogonal basis $\mathbf{\Psi}_k$ that are function only of the random variable ξ_i.

3.4 Implementation and examples

3.4.1 Polynomial chaos library - gpcPy

The formulation of the GPC described in this chapter was implemented in a python library named `gpcPy`. The library is quite simple, it reads information about the input random variables $\boldsymbol{\xi}$ from text file dictionary called `gpcDict.py` (e.g. number of random variables N, order of polynomial expansion p, probability density functions $p_i(\xi_i)$ and the number of quadrature points n_q), and it generates a list with the specific evaluation points needed to calculate the expansion coefficients s_k in another text file named `gpcList`. This file is later used to run the model as a black box and calculate one outcome for each quantity of interest at each quadrature point. Once the model evaluations are finished, `gpcPy` will construct the gPC expansion selecting the orthogonal families accordingly, creating the orthogonal basis $\mathbf{\Psi}_k$, and calculating the expansion coefficients s_k using NISP. Once the gPC expansion is created, `gpcPy` produce plots for the response surfaces and calculates the statistical parameters of the quantities of interest. In Chapter 6, it will be described how `gpcPy` is integrated with the CFD models implemented in OpenFOAM.

3.4.2 Examples

In this section, some examples are presented to see how well a PC expansion approximates a random variable, here simple bivariate functions are used as the deterministic model. The exact solution of these simple functions is known and so the `gpcPy` library can be validated. In all the examples, two input random variables ξ_1 and ξ_2 are considered uniformly distributed in the range $[-1, 1]$.

Before the PC expansions are calculated, it is necessary to define a measure to assess how well these expansions compare with the exact solution. To this end a relative difference is defined as:

$$RD(\xi_1, \xi_2) = \frac{|GPC(\xi_1, \xi_2) - s(\xi_1, \xi_2)|}{\max(s(\xi_1, \xi_2))|_{(\xi_1,\xi_2)\in\Theta_1\times\Theta_2} - \min(s(\xi_1, \xi_2))|_{(\xi_1,\xi_2)\in\Theta_1\times\Theta_2}} \times 100 \quad (3.29)$$

RD represents the relative difference between the PC expansion and the exact solution compared to the difference between the maximum and minimum values of $s(\xi_1, \xi_2)$ within the parameter space $\Theta_1 \times \Theta_2$.

To find the PC expansion then, the first step is to choose the order p at which the polynomial chaos expansion will be truncated, and the number of deterministic evaluations or quadrature points n_q for each random variable. In these examples, different values for p and n_q are tested. For simplicity, both variables will have the same number of quadrature points.

3.4.2.1 Example 1

In the first example, the function $s(\xi_1, \xi_2) = \xi_1 \sin(\xi_2)$ is used as a deterministic model. Figure 3.3 shows both the surface and contour plots of this function. These can be thought as the deterministic evaluation of every possible realisation (ξ_1, ξ_2) in the random space spanned by the two random variables.

Figure 3.6 shows three different PC approximations varying the order of the poly-

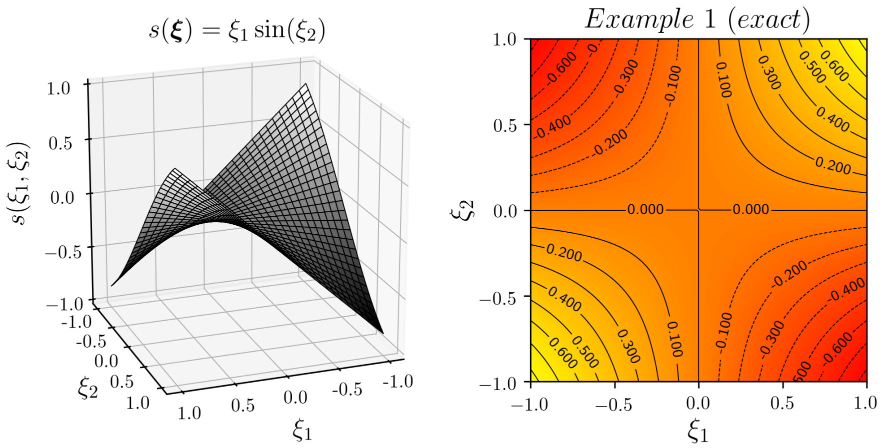

Figure 3.3: Left: Example 1 surface plot. Right: contour plot used for comparison with PC expansions in Figure 3.6.

nomial expansion p and the number of quadrature points n_q. For this model, which has a relatively simple response surface, a polynomial expansion of order $p = 3$ and only $n_q = 4$ quadrature points in each dimension, approximates very well the exact function with $RD < 5\%$ across the entire random space. Increasing the order of the polynomial to $p = 4$ and the number of quadrature points to $n_q = 5$ in each direction, decreases the RD to less than 0.1%. In other words, with only 25 deterministic evaluations the response surface is approximated very accurately. Finally, if the order p and number of quadrature points n_q is further increased, as expected the RD becomes negligible.

3.4.2.2 Example 2

In example 2, the function $s(\xi_1, \xi_2) = \cos(2\xi_1) + \sin(2\xi_2)$ is used as a deterministic model. Figure 3.4 shows the surface and contour plots of this function. As before, Figure 3.7 shows three different PC approximations varying the order of the polynomial expansion p and the number of quadrature points n_q. It is evident that a higher order polynomial will fit better the exact solution. Using four quadrature point in each direction (only 16 deterministic evaluations) leads to a $RD < 5\%$ within the parameter space, and it is reduced even further with 36 and 64 evaluations.

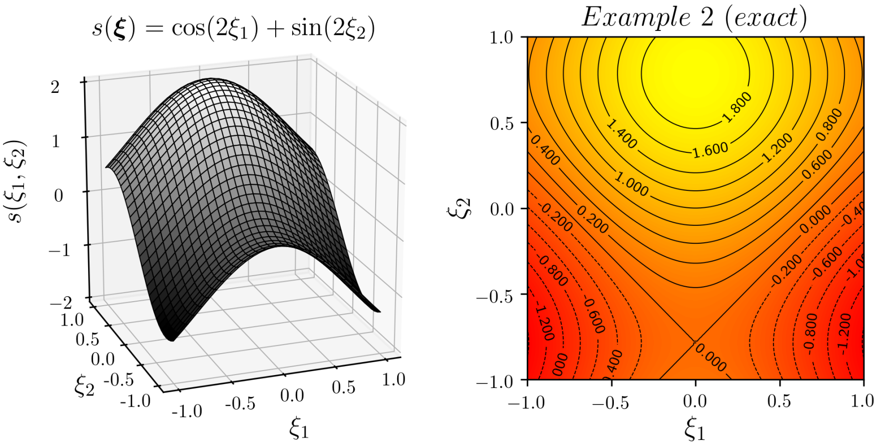

Figure 3.4: Left: Example 2 surface plot. Right: contour plot used for comparison with PC expansions in Figure 3.7.

3.4.2.3 Example 3

In this last example the function $s(\xi_1, \xi_2) = \sin(\pi\xi_1)\sin(\pi\xi_2)$ is used. This function is slightly more complicated in the sense that higher order polynomials are required to approximate its response surface (See Figure 3.5). Figure 3.8 shows the PC expansions and their respective RD. In all cases, the largest RD values occur at the corners of the random space. For order $p = 6$ and $p = 7$ the contour plots appear skewed compared to the exact one shown in Figure 3.5. In these cases, even though is not completely clear from the figures, the maximum RD values lie in the range $20\% - 50\%$. However, it is less than 5% across most of the random space. On the other hand, with order $p = 8$ and $n_q = 9$ the maximum RD is less than 5% at the corners, with RD values less than 0.5% across most of the random space.

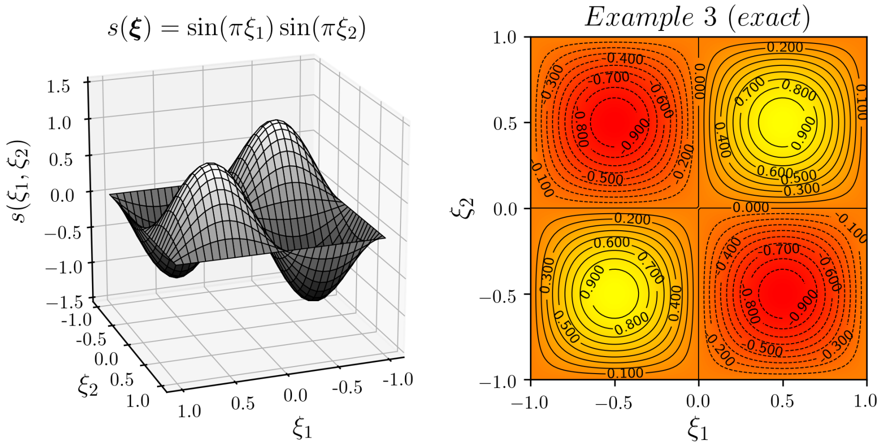

Figure 3.5: Left: Example 3 surface plot. Right: contour plot used for comparison with PC expansions in Figure 3.8.

3.5 Advantages and limitations of gPC

The main advantage of polynomial chaos is that a significantly lower number of deterministic evaluations are needed to capture the response surface of the quantity of interest. For instance, in Example 1, only 25 deterministic evaluations were sufficient to determine the response surface with a relative difference of less than 0.1% (5 quadrature points in each dimension of the random space). Nevertheless, to determine the polynomial chaos expansion some rather arbitrary choices were made, namely the order p and the number of quadrature points n_q. As shown in the previous examples, this choice depends on the characteristics of the response surface, which in a practical application is the unknown.

In principle, gPC expansion can be build with increasing order p (and number of quadrature points n_q) to assess the convergence of the response surface using the L^2Norm. However, it is important to note that when changing the number of quadrature points, their location in the random also change. This means that all the simulations have to be carried out again.

Finally, and probably the greatest disadvantage of this method, is that the number of deterministic evaluations required increases exponentially with the number of random variables (or uncertainties) being considered. This is often referred to as

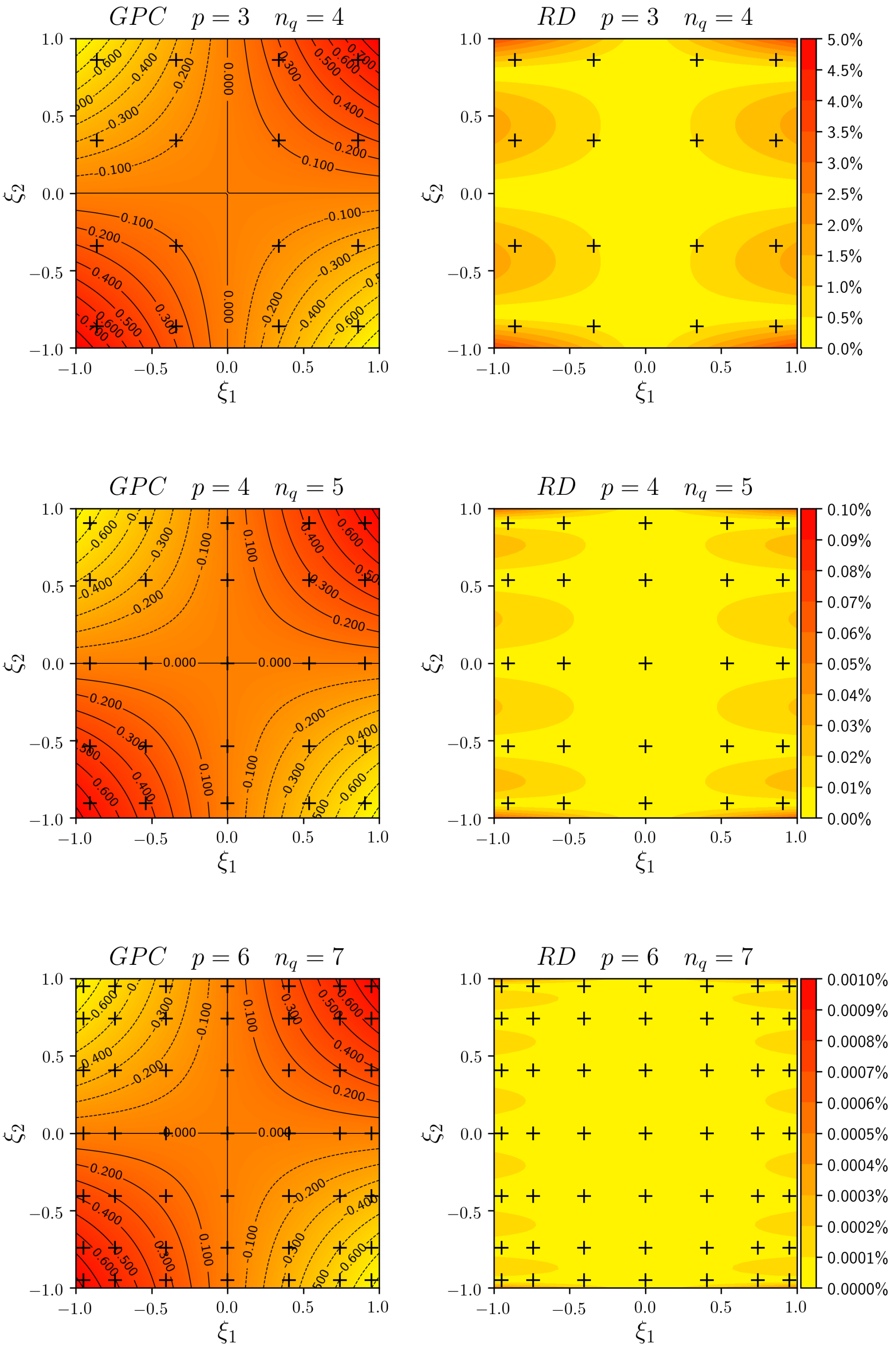

Figure 3.6: Example 1 - Left: PC chaos expansion of $s(\xi_1, \xi_2) = \xi_1 \sin(\xi_2)$ varying the order of the polynomial expansion p, and the number of quadrature points n_q. Right: RD to assess how well the PC expansion approximates the contour plot in Figure 3.3 (See Eq.3.29). The black crosses + indicate the quadrature points (ξ_1, ξ_2) where a deterministic model evaluation was obtained.

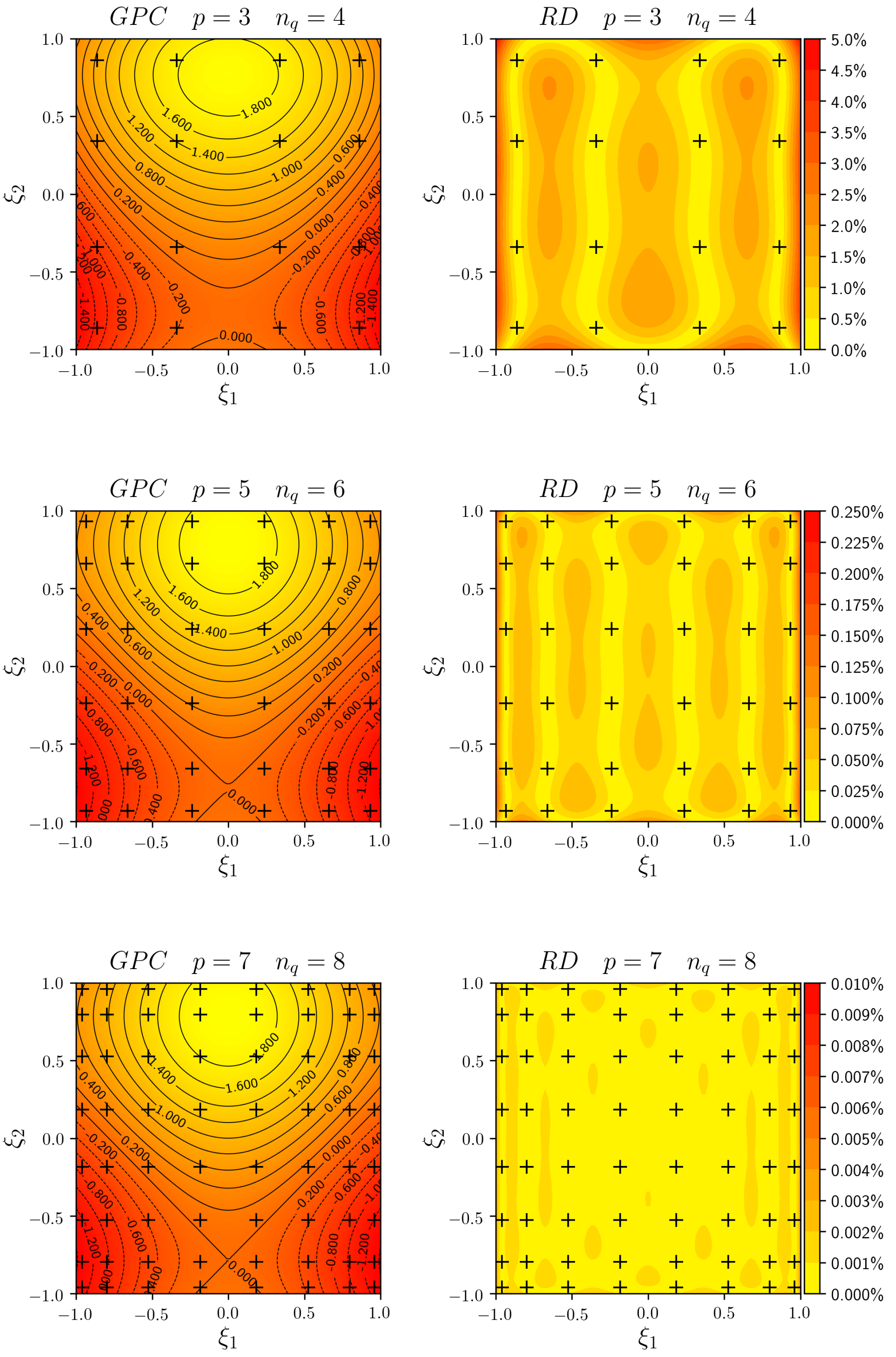
$GPC \quad p=3 \quad n_q=4$

$RD \quad p=3 \quad n_q=4$

$GPC \quad p=5 \quad n_q=6$

$RD \quad p=5 \quad n_q=6$

$GPC \quad p=7 \quad n_q=8$

$RD \quad p=7 \quad n_q=8$

Figure 3.7: Example 2 - Left: PC chaos expansion of $s(\xi_1, \xi_2) = \cos(2\xi_1) + \sin(2\xi_2)$ varying the order of the polynomial expansion p, and the number of quadrature points n_q. Right: RD to assess how well the PC expansion approximates the surface plot in Figure 3.4(See Eq.3.29). The black crosses $+$ indicate the quadrature points (ξ_1, ξ_2) where a deterministic model evaluation was obtained.

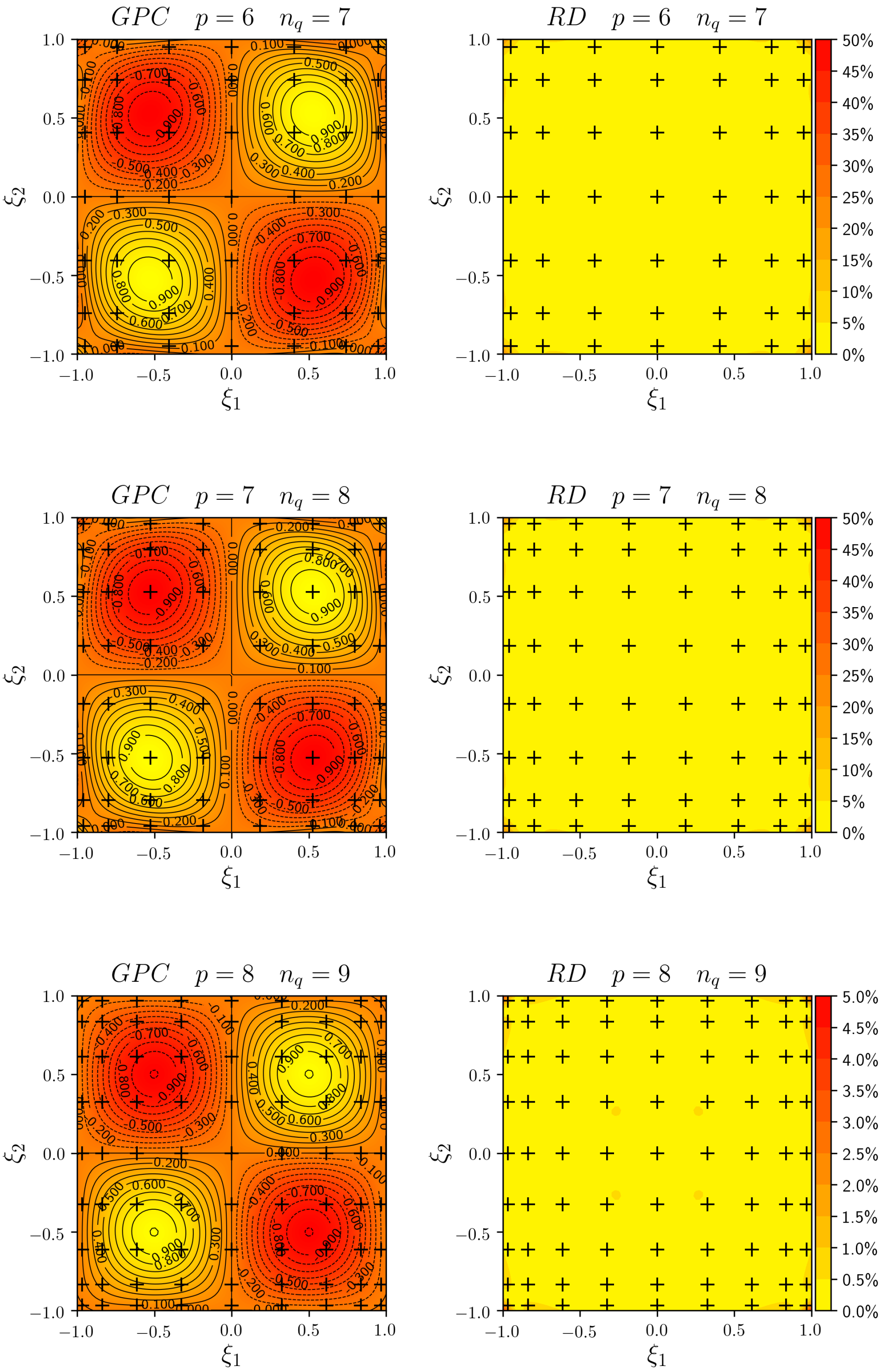

Figure 3.8: Example 3 - Left: PC chaos expansion of $s(\xi_1, \xi_2) = \sin(\pi\xi_1)\sin(\pi\xi_2)$ varying the order of the polynomial expansion p, and the number of quadrature points n_q. Right: RD to assess how well the PC expansion approximates the surface plot in Figure 3.5(See Eq.3.29). The black crosses + indicate the quadrature points (ξ_1, ξ_2) where a deterministic model evaluation was obtained.

the curse of dimensionality. There are strategies to improve this, such as adaptive choice of the polynomial basis, adaptive element selection in multi-element GPC, and adaptive sparse grid collocation which are described in more detail in Xiu (2010).

3.6 Summary and conclusions

Polynomial chaos is used to propagate uncertainties reducing the number of deterministic evaluations required compared with sampling methods such as Monte Carlo, which makes it attractive for CFD applications. However, the number of model evaluations grows exponentially with the number of random variables analysed, which is the main limitation. For instance, García-Sánchez et al. (2014) and Gorlé et al. (2016) presented an uncertainty quantification study for CFD simulations of the wind flow in an urban area using GPC performing 729 RANS simulations (three random variables with nine quadrature point each). Even though there are ways of reduce even further the number of simulations, such as sparse polynomial chaos, the CFD model should balance the accuracy with the computational resources available.

This chapter described how polynomial chaos expansion work and how they have been implemented in a Python library named `gpcPy`. This library was validated using simple bivariate functions comparing the polynomial expansions with the exact solutions. It has been shown that some rather arbitrary choices are made, such as the order of the polynomial expansion p, which depends on the shape of the response surface. However, in more practical application this is unknown and convergence studies should be carried out to determine if the appropriate order was chosen. In the next chapters 4 and 5, the focus will be on the implementation of the CFD models of wind turbines and the atmospheric boundary layer respectively. Later in Chapter 6, `gpcPy` will be integrated with those CFD models.

Chapter 4

Wind turbine rotor modelling

4.1 Introduction

The previous chapter described the polynomial chaos expansions and how they can be used to propagate uncertainties using a computational model as a black box. This chapter, following the review of wind turbine CFD models in Chapter 2, describes the implementation and validation of a non-axisymmetric actuator disk model for wind turbine rotors in OpenFOAM. This model, together with the atmospheric boundary layer models described in the next chapter, will be used as the black-box model, and it represents the core of the polynomial chaos framework for uncertainty quantification developed in this thesis.

4.2 ADM Implementation in OpenFOAM

4.2.1 Overview

A new library named `turbineDisk` was implemented in `OpenFOAM v.6`, to model a wind turbine as an actuator disk. Figure 4.1 shows the overall structure of `turbineDisk` (right hand side) and how it is integrated with the solver (left hand side). The model is implemented using the `fvOptions` dictionary, which allows to easily add source terms to the governing equations, without the need of changing the source code. When the solver is executed, if the `fvOptions` dictionary is present, it will run the additional code specified by the user to calculate the source terms required. Here is when the new implemented `turbineDisk` library is used to compute additional source terms applied to the momentum equations. In principle, `turbineDisk` is independent of the solver being used, however in the present work, the steady-state incompressible solver for turbulent flows `simpleFoam` is used.

The `fvOptions` dictionary contains all the input parameters needed to determine the source terms. This includes the turbine characteristics such as the location (x, y, z coordinates in the domain), the turbine diameter D, the number of blades B, the blade geometry and airfoil data, as well as the operating conditions (e.g. pitch, rotational speed).

When the `turbineDisk` library is called, the `fvOptions` dictionary is read and a series of initialization tasks are performed. These tasks are used to determine which cells will be affected by the additional source terms, as well as to calculate parameters that will not change on run-time (e.g. the smearing factor to spread the forces that will be described later). After that, on run-time, information is shared between the solver and the library through the `fvOptions` system. This allows reading the local velocity vector at the actuator points from the solver to determine the relative velocity (respect to the blade elements), the local angle of attack (AOA or α) and chord-based Reynolds number Re_c. Then, the airfoil coefficients are interpolated and used to compute the loadings which are sent back to the solver after the correction factors are applied (e.g. tip correction). Finally, The `addSup()` function is used to pass the momentum source terms to the solver and the entire process is repeated until convergence.

To close this section, please note that the implementation of `turbineDisk` was inspired in an existing library named `rotorDiskSource`, implemented by Wahono (2013) to model the helicopter rotor downwash, which is contained in the standard `OpenFOAM` release.

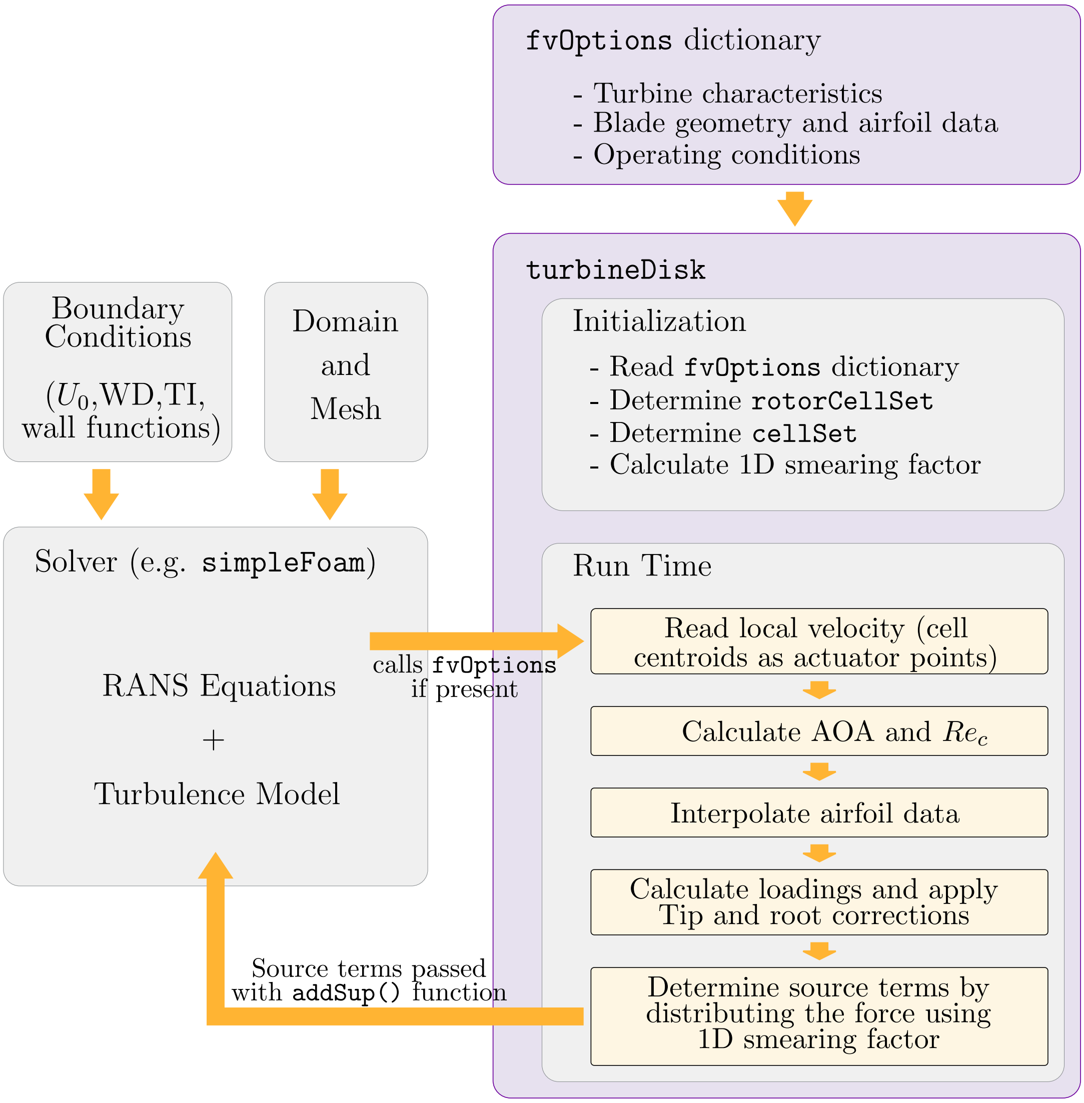

Figure 4.1: Flow diagram showing how `turbineDisk` works.

4.2.2 Model description

Figure 4.2 shows a schematic representation of how `turbineDisk` works. First of all, note that the 3D turbine geometry shown here is for reference only, since this is replaced by actuator points acting as sinks of momentum. Secondly, there are two sets of cells used in `turbineDisk`: the `rotorCellSet` and the `cellSet`. The `rotorCellSet` is the set of cells whose centroid is closest to the rotor, representing the actuator disk, it has a single cell thickness in the $x-$direction, and it is depicted as a purple disk in Figure 4.2. The loadings are calculated at each cell centroid within the `rotorCellSet`. On the other hand, the `cellSet`, is a larger set of cells contained in a cylinder of the same diameter as the turbine, that goes from $1D$ upstream to $1D$

downstream (shown as a grey cylinder, this distance can be modified). This cell set is defined in the `topoSetDict` dictionary and it is used to distribute the forces along the $x-$direction (using a smearing factor as it will be discussed). In addition, three coordinate systems are considered. A global cartesian coordinate system (x, y, z), a blade local cartesian coordinate system (r, θ, a) (i.e. radial, tangential, and axial directions respectively) and an airfoil chord based 2D coordinate system (n, t) (i.e. normal and tangential to the chord line).

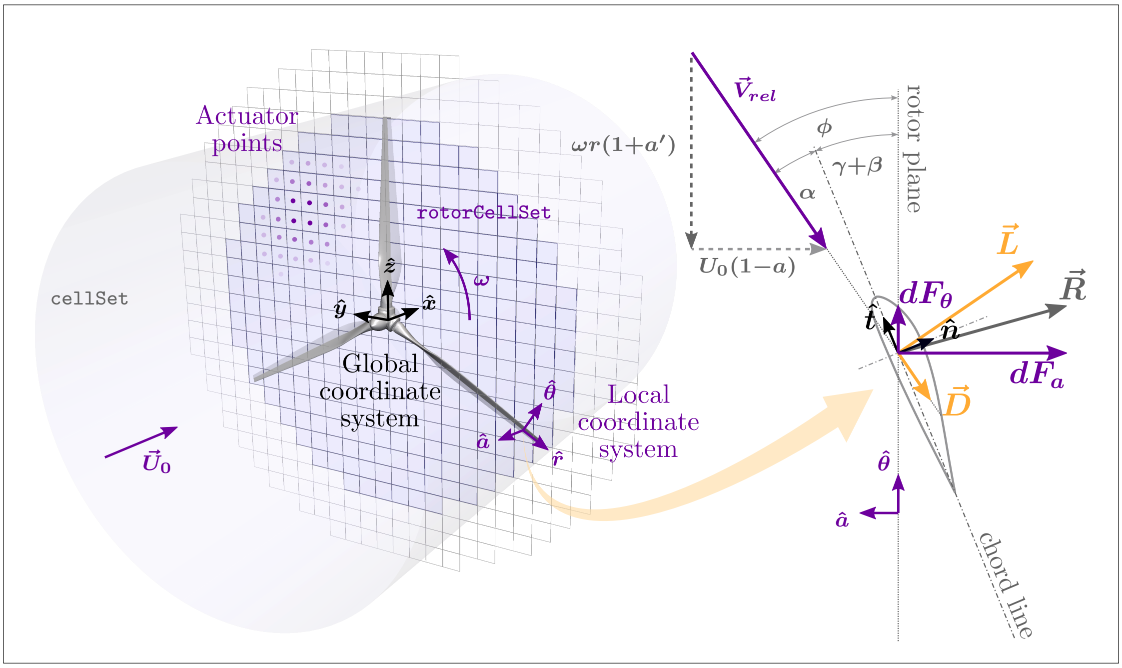

Figure 4.2: Actuator disk schematic representation

For each cell in the `rotorCellSet` a force contribution $d\vec{F}_i$ is calculated based on the local flow velocity $\vec{U}_i = \vec{U}(x_i, y_i, z_i)$ (i.e. at the cell centroid) and the local blade geometry (i.e. airfoil, chord length, twist angle). First, the velocity $\vec{U}_i$ is transformed from global to local coordinate system into $\vec{V} = (V_r, V_\theta, V_a)$. Then, the relative velocity $\vec{V}_{rel}$ is determined by adding the rotational speed of the blade and by neglecting the radial component as follows.

$$\vec{V}_{rel} = (0 \quad , \quad V_\theta - \omega r \quad , \quad V_a) \tag{4.1}$$

Here it is possible to calculate the axial and rotational induction factors a and a' as:

$$|V_a| = U_0(1-a) \quad \Rightarrow \quad a = 1 - (|V_a|/U_0) \tag{4.2}$$

$$|V_\theta - \omega r| = \omega r(1+a') \quad \Rightarrow \quad a' = (|V_\theta|/\omega r) - 2 \tag{4.3}$$

The angle of attack α and the Reynolds number based on the local chord length $Re_c = |\vec{V}_{rel}|\, c/\nu$ are needed to calculate the forces acting on the blade element. From Figure 4.2 is clear that:

$$\alpha = \phi - (\gamma + \beta) \tag{4.4}$$

$$\phi = \tan^{-1}(V_a/(V_\theta - \omega r)) \tag{4.5}$$

where α is the angle of attack, ϕ is the incidence angle relative to the rotor plane, γ is the local twist angle, and β is the pitch angle.

Once the AOA and the Re_c are calculated, the lift and drag coefficient C_l and C_d are interpolated from tabulated airfoil data. The `turbineDisk` can use airfoil data for single and multiple Reynolds numbers. If tabulated data for multiple Reynolds number is provided, it will interpolate the lift and drag coefficients to the local Reynolds number.

The lift and drag forces acting on a blade element of length dr are given by:

$$L = \frac{1}{2}\rho\, V_{rel}^2\, c(r)\, C_l\, dr \tag{4.6}$$

$$D = \frac{1}{2}\rho\, V_{rel}^2\, c(r)\, C_d\, dr \tag{4.7}$$

Where ρ is the air density, $c(r)$ is the chord length which depends on the radial distance and it is interpolated from the blade geometry.

The resulting force $\vec{R} = \vec{L} + \vec{D}$ can be decomposed in the local coordinate system into an axial force dF_a and a tangential force dF_θ that contribute to the total thrust and torque respectively.

$$dF_a = \frac{1}{2}\rho V_{rel}^2 c(r) C_a dr \tag{4.8}$$

$$dF_\theta = \frac{1}{2}\rho V_{rel}^2 c(r) C_\theta dr \tag{4.9}$$

where the coefficients C_a and C_θ are calculated as follows.

$$C_a = C_l \cos\phi + C_d \sin\phi \tag{4.10}$$

$$C_\theta = C_l \sin\phi - C_d \cos\phi \tag{4.11}$$

Note that in Equations 4.8 and 4.9, the blade element length dr needs to be determined. Typically, in BEM based methods the number of blade elements and their lengths dr are prescribed, however, `turbineDisk` works differently. To explain this, consider the diagrams shown in Figure 4.3.

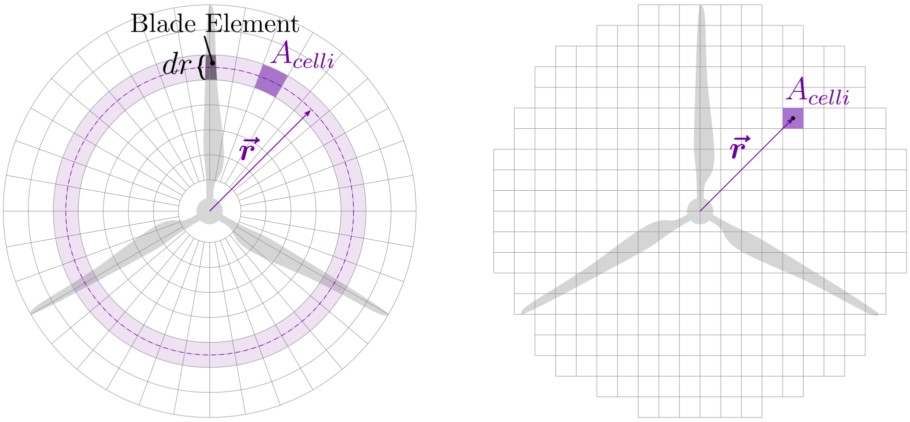

(a) BEM (b) ADM

Figure 4.3: Schematic representation of a key difference between standard ADM models based on BEM and the `turbineDisk` ADM. While BEM based methods typically prescribed the number of blade elements, the ADM computes an equivalent blade element contribution based on its cell face area A_i.

In the left hand side (Figure 4.3(a)), the BEM based approach consists in prescribing the number of blade elements (number of annulus across the disk), calculating the total force acting on each annulus, multiplying Eq.4.8 and Eq.4.9 by the number of blades B (assuming a uniform inflow), and then distributing these forces uniformly to each cell in the annulus proportionally to the cell face area A_{celli} as:

$$dF_{a,celli} = \frac{1}{2}\rho V_{rel}^2 c(r) C_a dr\, B\, \frac{A_{celli}}{2\pi r dr} \tag{4.12}$$

$$dF_{\theta,celli} = \frac{1}{2}\rho V_{rel}^2 c(r) C_\theta dr\, B\, \frac{A_{celli}}{2\pi r dr} \tag{4.13}$$

In these equations, it is observed that the blade element length dr is simplified as it appears in the numerator and denominator leading to:

$$dF_{a,celli} = \frac{1}{2}\rho V_{rel}^2 c(r) C_a\, B\, \frac{A_{celli}}{2\pi r} \tag{4.14}$$

$$dF_{\theta,celli} = \frac{1}{2}\rho V_{rel}^2 c(r) C_\theta\, B\, \frac{A_{celli}}{2\pi r} \tag{4.15}$$

And the total force contribution acting on the flow at each cell in the `rotorCellSet` can be written as:

$$d\vec{F}_{celli} = (0 \quad , \quad -dF_{\theta,celli} \quad , \quad dF_{a,celli}) \tag{4.16}$$

In Eq.4.14 and Eq.4.15, the blade element length dr was simplified under the assumption of a cylindrical grid under uniform inflow conditions. In `turbineDisk`, however, there is not a blade element length defined (Figure 4.3(b)). Therefore the same equations are used, but the interpretation of them is slightly different. Here, `turbineDisk` is calculating at each cell of the `rotorCellSet`, the contribution of all the blades elements passing through it, considering the local flow conditions, regardless if the inflow is uniform or not. This approximation might seem not very accurate, but at the same time gives the ADM the ability to work under sheared inflow conditions which is an important advantage of the model as a whole, because it does not assume that the inflow is axi-symmetric and in contrast it will use the local inflow at each actuator point to compute the loadings.

Finally, the integral loads such as the total thrust, torque and power, as well as their non-dimensional coefficients are calculated as follows:

$$Thrust = \sum_{celli} dF_{a,celli} \tag{4.17}$$

$$Torque = \sum_{celli} dF_{\theta,celli}\, r_{celli} \tag{4.18}$$

$$Power = Torque \cdot \omega \tag{4.19}$$

$$C_P = \frac{Power}{\frac{1}{2}\rho A U_o^3} \tag{4.20}$$

$$C_T = \frac{Thrust}{\frac{1}{2}\rho A U_o^2} \tag{4.21}$$

4.2.3 Tip and root corrections

Prandtl introduced the concept of tip loss looking at the flow circulation and the differences between a finite number of blade turbine or propeller compared with an infinite number of blades actuator disk representation. Glauert (1935) used this concept to correct induced velocities in BEM. This is known as Prandtl's correction for an infinite number of blades. However, there is another type of correction needed in low order models based on BEM theory that use 2D airfoil data, which accounts for pressure equalisation in the outboard sections of the blades, which is commonly known as the tip-loss correction. Usually, these models neglect the radial velocity component, which depending on the operating conditions, might be a good approximation in the mid-span. However, near the tip and the root of the blades, this radial component becomes more significant being a critical aspect of tip losses. Tip and root vortices will drop the lift generated, which is more significant at the tip, that contributes the most to torque and thrust.

Note that, when solving the Navier-Stokes equations, the infinite number of blades correction is not needed, since the kinematics is solved from first principles (Shen et al., 2005a). Tip-loss corrections, on the other hand, are needed. However, there is not a consensus on how the tip-loss corrections should be applied (Wimshurst, 2018). Mikkelsen (2003) suggested that the Glauert corrections should be used as a relaxation parameter when solving Navier-Stokes. Thus, applying the correction to the axial and tangential induction factors before reading tabulated 2D airfoil data.

In `turbineDisk`, the correction factor F is applied to the lift coefficient in Eq.4.10 and Eq.4.11, similar to the approach followed by Shen et al. (2005a), who applied the correction to the loading coefficients, resulting in:

$$C_a = FC_l \cos\phi + C_d \sin\phi \tag{4.22}$$

$$C_\theta = FC_l \sin\phi - C_d \cos\phi \tag{4.23}$$

with,

$$F = F_{tip} \cdot F_{root} \tag{4.24}$$

where F_{tip} and F_{root} are the tip a root correction factors respectively. Two types of tip corrections factors F_{tip} and one type of root correction factor F_{root} are implemented in `turbineDisk`.

4.2.3.1 Prandtl's Tip Correction

In this work, the Glauert formulation of Prandtl's tip-loss correction is used, given in Eq. 4.25, where B is the number of blades, R is the rotor radius, r the local radial distance and ϕ the local angle of incidence shown in Figure 4.2.

$$F_{tip} = \frac{2}{\pi} cos^{-1}\left[exp\left(-\frac{B}{2}\frac{R-r}{rsin\phi}\right)\right] \tag{4.25}$$

4.2.3.2 Shen tip correction

Another tip correction was proposed by Shen et al. (2005a) given by the following equation.

$$F_{tip} = \frac{2}{\pi} cos^{-1}\left[exp\left(-G\frac{B}{2}\frac{R-r}{rsin\phi}\right)\right] \tag{4.26}$$

where,

$$G = exp[-c_1(B\lambda - c_2)] \tag{4.27}$$

Here c_1 and c_2 are calibration factors which were proposed as 0.125 and 21 respectively, based on experimental data of the NREL experiment and a Swedish WG500 rotor at TSR (λ) of 3.79 and 14.

4.2.3.3 Root correction factor

A similar expression can be used for root losses. As reported by El Khchine and Sriti (2017), one of such corrections is known as Buhl correction and it is expressed by the following equation.

$$F_{root} = \frac{2}{\pi} cos^{-1}\left[exp\left(\frac{B}{2}\frac{r-r_{hub}}{rsin\phi}\right)\right] \tag{4.28}$$

4.2.4 Force distribution

When modelling wind turbines with actuator disk and actuator line models, the calculated forces need to be distributed smoothly within the computational domain to avoid numerical stability issues. This is typically done using a gaussian smearing function.

For the actuator disk model (ADM), the forces is smoothed along the axial direction by the convolution between the annular force F_i and the 1D regularization kernel η_ϵ^{1D} Mikkelsen (2003).

$$d\vec{F}_\epsilon = d\vec{F}_{celli} \otimes \eta_\epsilon^{1D} \tag{4.29}$$

$$\eta_\epsilon^{1D}(d) = \frac{1}{\epsilon \pi^{1/2}} exp \left[- \left(\frac{d}{\epsilon} \right)^2 \right] \tag{4.30}$$

where d is the distance between the cells centres and the blade element, and ϵ is the smearing parameter that allows to adjust the force distribution.

Smearing factor in `turbineDisk`

In particular, in the `turbineDisk` library, the source term in Eq. 4.16 is calculated for each cell in the `rotorCellSet` (See Figure 4.2), which has a single cell thickness in the $x-$direction. Applying this forcing term in the momentum equation only at these cells produces a discontinuity and unphysical behaviour of the flow field at the rotor area, leading to inaccurate results. Therefore, the 1D approach from Mikkelsen (2003) was adopted.

A smearing factor η_ϵ, given by equation 4.30, was introduced to spread the forcing term along the $x-$direction across the cells in `cellSet`. This distributing mechanism adds another model parameter (ϵ) that can be arbitrary to some extent. Figure 4.4 shows an example of the shape of the smearing factor η_ϵ varying ϵ.

Different values for ϵ have been used in the literature. Sørensen et al. (1998) analysed the influence of ϵ using values based on the mesh cell size (i.e. $\epsilon = 1\Delta x$, $\epsilon = 2\Delta x$ and $\epsilon = 1\Delta x$) with an actuator disk model reporting smooth variations of the velocity at the tip as ϵ is increased, but finally choosing $\epsilon = 1\Delta x$. Mikkelsen (2003) also reported that the values should be $1\Delta x < \epsilon < 4\Delta x$. Wu and Porté-Agel (2011), following Mikkelsen (2003), used $\epsilon = 1\Delta x$. Sarmast et al. (2016) used $\epsilon = 2.5\Delta x$ with the finest cells size of about $\Delta x \sim D/80$. Tossas and Leonardi (2013) modelled the NREL-5MW reference turbine using a uniform grid with 30, 60 and 120 cells per rotor diameter with ϵ values ranging from $0.0333D - 0.0833D$ (i.e $4.2 - 10.5$ m or between $1\Delta x - 10\Delta x$ depending on the mesh resolution). This study showed that the predicted power output becomes more sensitive to the cell size the smaller ϵ is. For a high value of $\epsilon = 10.5$ m $= 0.0833D$ the predicted power increases slightly as the mesh resolution is increased.

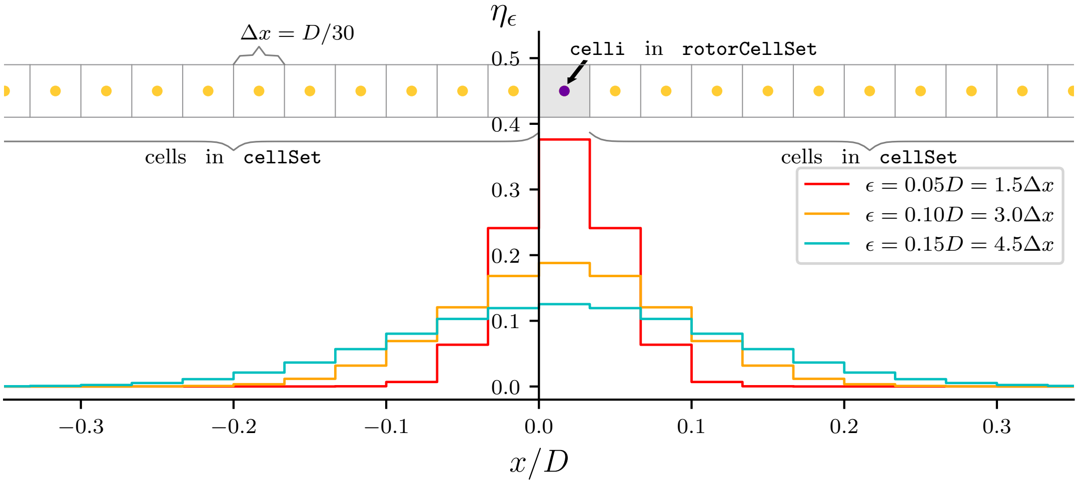

Figure 4.4: Smearing factor η_ϵ as a function of ϵ. Here, as an example, the cell size correspond to a uniform grid with 30 cells per rotor diameter. The loading is calculated a `celli` in `rotorCellSet` (in gray with purple centroid) and it is spread along the axial direction along the cells in the `cellSet` (with yellow centroid).

The behaviour of ϵ within the `turbineDisk` library is assessed in detail in Appendix D (See Section D.2). Five ϵ values were used from $\epsilon = 0.025D = 0.75\Delta x$ to $\epsilon = 0.2D = 6\Delta x$ with a uniform grid with 30 cells per rotor diameter ($\Delta x = D/30$). This resolution was chosen based on the mesh sensitivity analysis also described in Appendix D. The New-MEXICO experiment was chosen because there is more data available, including radial and axial velocity profiles. It was concluded that the $\epsilon = 0.1D = 3\Delta x$ produces reasonable accuracy. Higher values under-predict radial velocities and smooth out the velocity decay across the rotor, whilst smaller values decrease considerably the predicted power. Therefore, all the simulations in the following use $\epsilon = 0.1D$. Note that here the ϵ values are given in terms of the rotor diameter D instead of the cell size Δx since this allows a fair comparison when doing mesh sensitivity analysis. Nevertheless, when possible, their corresponding values in mesh cell size is also given.

4.2.5 Nacelle and Hub Modelling

The purpose of the ADM implemented in `turbineDisk` is to have a low-order model that captures the main flow characteristics with a reduced computational cost. Therefore, the computational grids used are relatively coarse offering a modelling tool that can be used to simulate wind turbine arrays. In Appendix D, as it will be discussed in the following section (ADM Validation), it is shown that using even 20 cells per rotor diameter results in reasonable good predictions of the main flow features and the integral quantities. This makes the model very attractive for simulations of wind turbine arrays. However, as a result, the mesh resolution in the inner part of the blade is too coarse to capture the complex flow features in this region. Therefore, even though it is possible to add the nacelle and hub geometries, it is considered not appropriate for the purpose intended of the present work since it will require higher mesh resolution. Furthermore, Sarmast et al. (2016) showed that the presence of the hub and nacelle geometry has a negligible effect in the loading and overall wake behaviour.

Nevertheless, since `turbineDisk` is designed to add source terms to specific cells, it is simple to have some sort of hub-nacelle model by adding a drag force in the cells at the center. This was done by setting lift and drag coefficients to $C_l = 0$ and $C_d = 2$ respectively. This is a coarse approximation which essentially avoids an acceleration of the flow field through the rotor centre. Also, it requires that the hub or nacelle diameter be specified as an additional element in the blade geometry as shown in Appendix B. Moreover, this will be sensitive to the mesh resolution, for instance, in a coarse mesh, if the cell centroid of the cell closest to the rotor-axis lies outside the hub-nacelle diameter specified, then the source term will be computed as the corresponding blade element and not as a hub element.

4.3 ADM Validation

In this section, the ADM is validated by comparing its predictions against wind tunnel experiments and other state of the art codes from other institutions. The experiments used are the NREL Unsteady Aerodynamics Experiment (UAE) Phase VI, and the Model Experiment in Controlled Conditions (MEXICO, and New-MEXICO). These experiments have been developed over decades to enhance the understanding of wind turbine aerodynamics and improve computational models under a wide range of operating conditions. As such, they are unique and have already been used in several studies to test and validate a variety of computational models (Schepers et al., 2012, 2014, 2018; Plaza et al., 2015; Sarmast et al., 2016; Sørensen et al., 2016). Some of these models will be included in comparison plots by extracting their data series from the literature (e.g. digitising plots) and will be referred to as benchmark models.

The experiments and the benchmark models are described in the following subsections. Then, the cases of interest for each experiment are listed along with the simulation setup used. And finally, the results are presented and discussed.

4.3.1 Wind tunnel experiments

4.3.1.1 NREL UAE Phase VI (NREL-VI)

The National Renewable Energy Laboratory (NREL) conducted a series of field tests using a horizontal axis wind turbine since 1987 in a project known as the Unsteady Aerodynamics Experiment (UAE). The objective was to increase the understanding of the three-dimensional aerodynamic behaviour of full-scale turbines, under atmospheric inflow conditions (Simms et al., 1999). However, the intrinsic variability of the atmospheric wind introduced a great deal of uncertainty (Schreck, 2008). This led to the UAE Phase VI experiment (Hand et al., 2001), where the 10 m test turbine was operated in a large wind tunnel facility at the NASA Ames Research Centre, at Moffett Field, California (See Figure 4.5a), the world's largest wind tunnel.

The UAE turbine is 10 m diameter with 2 blades, stall-regulated, with a full-span pitch control mechanism (See Figure 4.5b). The nominal rotational speed is 72 rpm and the rating power 20 kW. The blades are twisted and use the S809 airfoil from root to tip. The turbine could be configured to operate in upwind or downwind positions. Wind tunnel blockage was found to be less than 1% is most of the tests and less than 2% in all cases. For simplicity, the NREL UAE Phase VI experiment is referred to as NREL-VI.

(a) (b)

Figure 4.5: (a) Wind tunnel, NASA Ames Research Centre, Moffett Field, California (Image taken from https://upload.wikimedia.org/) (b) NREL UAE Test Turbine (Image taken from Schreck (2008)).

Notes on NREL-VI experimental data

The experimental normal and tangential forces are determined from pressure measurements distributed around five airfoil sections along the blade. The pressure is linearly interpolated and at the trailing edge is estimated as the average between the extrapolated pressure in both the pressure and suction sides. Schepers et al. (2014) showed that this data reduction process lead to underestimation in blade loadings.

4.3.1.2 MEXICO and New-MEXICO Experiments

The Model Experiments in Controlled Conditions, also known as MEXICO experiment, is probably the most detailed wind turbine experiment. It was carried out in the Large Scale Low-Speed Facility (LLF) of the German-Dutch Wind Tunnel Organisation (DNW) in 2006 (See Figure 4.6a). The wind tunnel was operated in an open configuration with a nozzle and a collector. In this ways the blockage was estimated to be less than 1% (Schepers et al., 2012).

The main objective of MEXICO was to reduce uncertainties in model predictions, which at that moment was estimated to be around 10 to 20% for performance, and 30% for dynamic loads (Schepers and Snel (2007)). Therefore, this experiment produced a significant amount of data used for validation of lifting line codes and more advanced CFD codes by several researchers Schepers et al. (2012).

A 4.5 m diameter model rotor with three blades was designed and manufactured. The design considered three airfoil sections: DU 91-W2-250, RISOE A1-21 and NACA 64-418 (See Figure 4.6b). The design conditions of MEXICO rotor are a tip speed ratio of 6.67, with a rotational speed of 424.5 rpm, thus with an inflow velocity of $U_0 = 15$ m/s. It was implemented with a speed controller and pitch actuator. Pressure taps were distributed around 5 sections of the blades. A tripping tape was used at 5% of the chord length to avoid laminar separation. Also, strain gauges and a six-component wind tunnel balance was used to measure bending moments, total forces and moments. Furthermore, a unique aspect of MEXICO is that Particle Image Velocimetry (PIV) was used to measure the flow field close to the rotor (upstream and downstream) (Schepers and Snel, 2007). The experiment also intended to be a complement of NREL-Phase-VI, a successor of IEA Wind Task 20 (Schepers et al., 2012).

New-MEXICO

Measured data from MEXICO was extensively used to compare with a wide variety of computational models in what was called IEA Task 29 Mexnext. In this

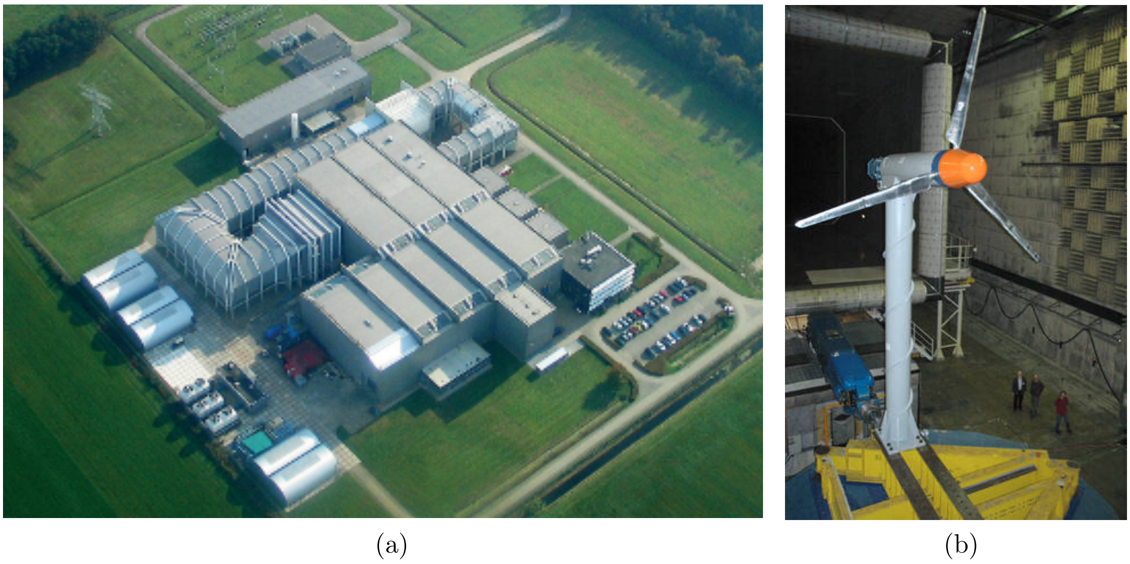
(a) (b)

Figure 4.6: (a) DNW Large Scale Low-Speed Facility (LLF) (b) MEXICO Rotor (Image taken from https://www.mexnext.org/).

project, a total of 20 organisations from 11 countries were involved. Even though this experiment provided a signficant amount of data that contributed to enhance the understanding of wind turbine aerodynamics, it was reported that blade loadings were consistently over-predicted by computational models Schepers et al. (2012), as well as discrepancies between loads and induced velocities. Boorsma and Schepers (2014) found that the wind tunnel velocities were underestimated by 0.2 to 0.3 m/s. Also, other unexplained phenomena were noticed such an apparent vortex shedding at the inner part of the blade and a lateral force that scales with wind speed and pitch angle under axial inflow conditions (Schepers, 2007). Trying to get more insights and solve these issues, the Mexnext project was extended by comparing the models with other existing experiments, such as the NREL-Phase-VI (Schepers et al., 2014), and also by carrying out new measurements of the MEXICO rotor. This measuring campaign is known as New-MEXICO and was carried out in 2014. This time the loads and velocities fulfilled the momentum balance, giving a better agreement with model predictions and solving some of the issues found in the original experiment Schepers et al. (2018). For all these reasons, in the present work, the experimental values from New-MEXICO are used instead of the original MEXICO experiment.

Notes on New-MEXICO experimental data

All the loads are derived from pressure distributions measured by pressure taps around the airfoil sections at five radial positions assuming zero loads at the blade root and tip. A linear variation is assumed between pressure sensors, and therefore the accuracy is limited by the number of pressure taps. Also, in this process, the frictional forces are ignored, which can be a significant contribution to the tangential force F_t.

The New-MEXICO experiment also provided valuable velocity traverses using PIV. Axial and radial traverses for the three velocity components (axial U_a, radial U_r and tangential U_t) are presented in Schepers et al. (2018). Note, however, there is an important difference between axial and radial traverses. Firstly, the radial traverses are presented as azimuthal averages at two locations: upstream ($x = -0.3$ m) and downstream ($x = 0.3$ m). In contrast, the axial traverses are measured at a specific azimuthal position (when blade one is pointing upwards, 0° azimuth, with the PIV sheets located at 270° azimuth (at 9 o'clock)), at two radial distances ($r = 0.5$ m and $r = 1.5$ m). Finally, in the present work the radial traverses at the two locations are used, but only the axial traverse at $r = 1.5$ m is considered, since the values at $r = 0.5$ m are highly affected by complex flow phenomena (high variability) that is not captured by the ADM being validated.

4.3.2 Benchmark Models

The NREL-VI and MEXICO experiments have been widely used to assess the performance of a variety of computational models; from simple models based on Blade Element Momentum (BEM) theory and 1D momentum theory, low order models such as actuator disk (ADM) and actuator line models (ALM), to full rotor simulations (FRS). As part of the mexnext project (Schepers et al., 2011, 2014, 2018), several participants have provided their simulation results. Some of those model predictions are included in this chapter to have a better picture of how `turbineDisk` compares not only with the experimental measurements but also with different mod-

Table 4.1: Summary list of benchmark models used as comparison in the validation of the ADM in `turbineDisk`. The data series have been digitised from plots in the literature as indicated with numerals in the table footnote.

Benchmark Model	Short description[1]	Experiment
Uppsala-AD [2]	ADM in EllipSys3D (LES)	New-MEXICO
ECNAero-BEM[3,4]	BEM in ECN Aero Module	NREL-VI, New-MEXICO
DTU-BEM[3]	BEM from DTU	NREL-VI
DTU-HAWC2[3,4]	ADM based on BEM and 1D momentum theory	NREL-VI, New-MEXICO
DTU-AL[4]	ALM in EllipSys3D (LES)	New-MEXICO
DTU-EllipSys3D[3,4]	FRS at DTU	NREL-VI, New-MEXICO
CENER-CFD[3]	FRS CENER and University of Liverpool	NREL-VI

[1] In Appendix C a full description of the model is given with the corresponding references.
[2] Data series digitised from Sarmast et al. (2016).
[3] Data series digitised from Schepers et al. (2014).
[4] Data series digitised from Schepers et al. (2018).

elling techniques. The models chosen are listed in Table 4.1, and they are described in more details in Appendix C.

4.3.3 Cases of Interest for Validation

NREL-VI

The NREL-VI experiment performed an extensive set of tests aiming to emulate field operation and to study specific flow phenomena. The full details can be found in Hand et al. (2001). In the present work, however, only 4 tests are considered (See Table 4.2). These cases have been compared to a variety of computational models in Schepers et al. (2014), offering a good resource to validate the ADM under a few different operating conditions (e.g. angles of attack and induction factors), and an opportunity to compare the ADM with other codes. All these cases consider a uniform inflow velocity with zero yaw angle.

Table 4.2: Cases of interest for validation NREL-VI. All these cases have a uniform inflow with 0° yaw angle. rotational speed of 425.1 rpm, pitch angle of $-2.3°$, and 0° yaw angle.

Case Name	U_0 [m/s]	pitch β [°]	Rotational speed [rpm]	[1]$\text{AOA}_{80\%R}$ [°]	[2]a [-]	ρ [kg/m^3]	TSR [-]
I05	5.08	0	71.7	4.5	0.21	1.2245	7.43
X05	5.02	3	90.2	1.5	0.20	1.2253	9.46
X10	10.04	3	90.9	8.0	0.15	1.2228	4.77
X12	12.02	3	91.6	10.0	0.11	1.2228	4.01

[1] Estimated angles of attack at 80% span by Schepers et al. (2014).
[2] Estimated rotor averaged axial induction by Schepers et al. (2014).

New-MEXICO

The New-MEXICO campaign produced a large amount of data covering a wide range of operating conditions (Schepers et al., 2018). Wind tunnel speeds varying from 10 to 20 m/s at two rotational speeds of 324.5 and 424.5 rpm, resulting in tip speed ratios ranging from 3.3 to 10. Different yaw and pitch angles were also tested. However, here we consider only the three cases shown in Table 4.3 because they cover different loading conditions and are widely studied in the literature.

Table 4.3: Cases of interest for validation New-MEXICO. All these cases have a rotational speed of 425.1 rpm, pitch angle of $-2.3°$, and 0° yaw angle.

Case Name	U_0 [m/s]	ρ [kg/m^3]	TSR [-]
MEX1	10.05	1.197	9.97
[1]MEX2	15.06	1.191	6.65
MEX3	24.05	1.195	4.16

[1] Design operating conditions.

4.3.4 Simulations Setup

The simulations are performed using a structured grid with uniform cells across the rotor with 30 cells per rotor diameter, following the mesh resolution sensitivity analysis in Section D.1 from Appendix D. Also in this appendix, in Section D.2, a similar study is carried out to find out what the optimal value of the smearing parameter ϵ is, and therefore here $\epsilon = 0.1D = 3\Delta x$ is used here. The blade geometry and airfoil data for each experiment are shown in Appendix B.

The lift and drag coefficients for the S809 airfoil (NREL-VI) are interpolated not only for the angle of attack α but also for the local Reynolds number Re_c (See Table B.2 and Table B.3 in Appendix B. Note that two series of lift and drag coefficients are provided for the S809 airfoil at $Re_c = 1 \times 10^6$ obtained by the Ohio State University (OSU) and the Delft University of Technology (DUT).

On the other hand, for the New-MEXICO experiment, the loading coefficients are only interpolated to the local angle of attack since airfoils change along the blade (See Table B.6, Table B.7, Table B.8 and Table B.9). Boorsma and Schepers (2014) reported two sets of coefficients, clean and rough (i.e. without and with a tripping tape mechanism). The New-MEXICO in particular used tripping tape only in the inboard sections (DU91-W2-250 and RISØ A1-21) and a clean surface in the outboard section (NACA-64-418).

For each case, the uniform inflow velocity U_0, the rotational speed ω and the pitch angle of the blades β are set according to Table 4.2 and Table 4.3 for the NREL-VI and MEXICO experiments respectively. The Shen et al. (2005a) tip loss correction is applied with default coefficients $c_1 = 0.125$ and $c_2 = 21$. The turbulence intensity is set to a very small value ($TI = 0.1\%$) and the $k - \omega - SST$ eddy viscosity model is used (Menter, 1994; Menter and Esch, 2001), as implemented in OpenFOAM v6, with the incompressible OpenFOAM solver `simpleFoam`. Some tests with $k-\varepsilon$ model showed overprediction of velocities which was in agreement with observations made by Antonini et al. (2019), who also found that the $k-\omega-SST$ model was consistently more accurate than $k-\varepsilon$ and $k-\omega$ models when using an ADM. Similarly, Troldborg et al. (2015) and Réthoré et al. (2014) also used the $k - \omega - SST$ with both ADM and ALM with good accuracy. Shives and Crawford (2016) argued that the SST limiter for adverse pressure gradient help to predict wake velocity profiles quite well, but this results in under predicting the turbulence intensity. In addition, previous studies have shown that the turbulent model used has small influence on the loadings of isolated rotors and that this impacts primarily the evolution of wakes Apsley et al. (2018).

4.3.5 Results and Discussion

The results are presented separately for the NREL-VI and New-MEXICO experiments. In each case, comparisons are made for the performance (e.g. power and thrust), blade loadings (F_n and F_t) and induced velocities (axial induced velocity U_{ai}, tangential induced velocity U_{ti} and angle of attack α. In addition, for the New-MEXICO experiments, axial and radial traverses of velocity components are included.

4.3.5.1 NREL-VI

Two ADM results are included which use different airfoil data at $Re_c = 1 \times 10^6$ (See Table B.2 and Table B.3), ADM-1 uses the values obtained at the Ohio State University (OSU) and ADM-2 uses the values obtained at the Delft University of Technology (DUT). The coefficients at other Re_c remain equal.

Performance

In Figure 4.7 the power and thrust predicted by the ADM are compared to experimental values and benchmark models. The plots at the top show the absolute values, while the two at the bottom show the relative error compared to the experiments. Note that, since the data points from benchmark-model were digitised from other plots, they are likely to include an additional human error, which can be negligible in absolute the values but might be amplified in the error plots. This is particularly important in the cases I05 and X05 because their absolute values are small.

In general, the ADM predictions are comparable with the experiments and other modelling techniques. The relative errors are within 15% to 20%, except for case X12 with higher angles of attack were it reaches up to about 30%. Interestingly, the models that deviate more from experimental torque in X12 are the FRS (DTU-EllipSys3D and CENER-CFD). Note that X10 and X12 cases have flow separation (Schepers et al., 2014), and are quite challenging for full rotor simulations. However,

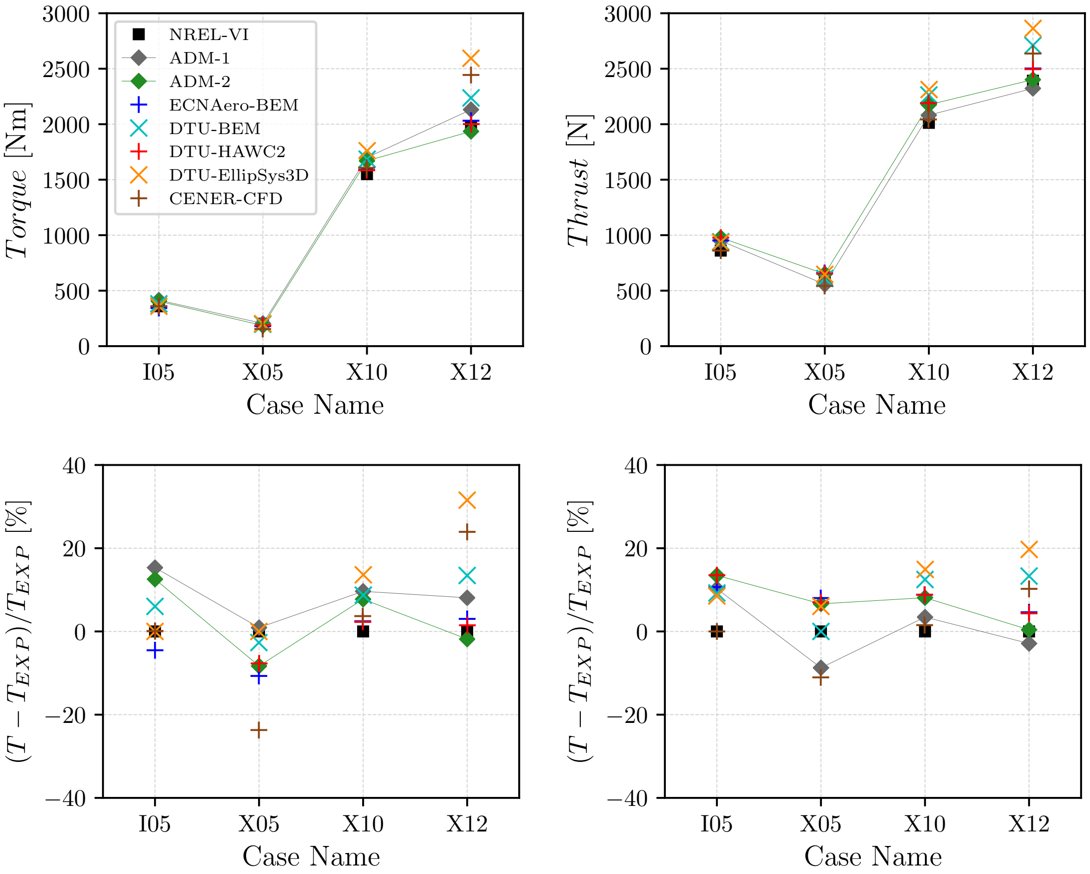

Figure 4.7: Torque and thrust predictions of the four cases compared to experimental data and other benchmark models. At the top the absolute values. At the bottom the error relative to experimental values. ADM-1 uses lift and drag coefficients at Re_c obtained by Ohio State University (OSU) and ADM-2 those obtained at the Delft University of Technology (DUT).

it is also important to consider here that the limited number of pressure taps (spanwise and chordwise) also plays a role in the integral loads calculated. Schepers et al. (2014) analysed this by integrating the pressure distributions from DTU-EllipSys3D using different resolutions, with the lower resolution being comparable to the experimental setup. This analysis showed that the reduced number of pressure sensors results in an underestimation of the thrust and torque up to 17% and 25% respectively, depending on the case.

Now, in terms of the airfoil data used, significant differences are observed, particularly at case X05 and X12. Figure 4.8 shows the chord based Reynolds number along the blades for the four cases considered. It is noted that $Re_c > 0.75 \times 10^6$ in most cases and the values go up to around 1.25×10^6 in the outer region. Thus, changes in lift and drag coefficients at $Re_c = 1 \times 10^6$ do have a great impact in overall predictions, but more importantly, and additional set of coefficient at $Re_c = 1.25 \times 10^6$ should be included since most of the contribution comes from this outer region.

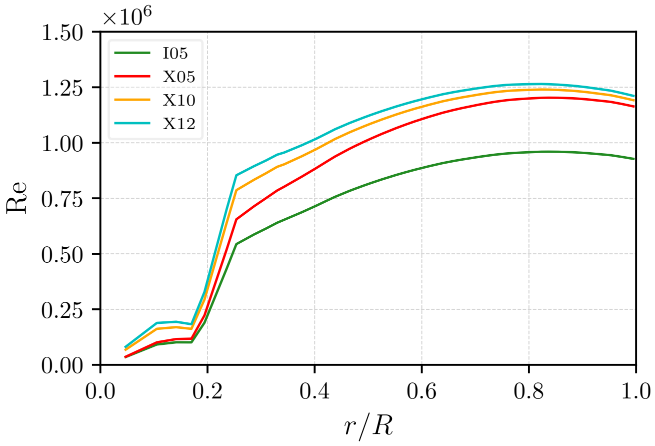

Figure 4.8: Reynolds number Re_c along the blades NREL-VI.

Loadings

Figure 4.9 shows the normal and tangential forces along the blades. In general, the ADM overpredicts the loads towards the tip, which might be due to wrong Re_c airfoil coefficients, and to some extend, to the Shen et al. (2005a) tip correction factor coefficients c_1 and c_2. On the other hand, towards the inner region, the ADM underpredicts the loads in the separated flow cases (X10, X12). This is related to 3D effects, which are not modelled, but Schepers et al. (2014) showed that adding 3D corrections to airfoil data does improve the results.

An important observation, and somewhat expected, is that all the simulations based on BEM that use essentially the same 2D airfoil follow the same trend in all four cases. The same is true for FRS, which are better capturing 3D effects in the separated flow cases. But note that the choice of airfoil data impacts significantly the tangential force F_t in case X05, where using coefficients from OSU leads to similar results to those obtained from FRS EllipSys3D, while using DUT coefficients gives results that fit better other BEM based models.

Induced velocities

Looking now at Figure 4.10, that shows the angle of attack and induced velocities compared to the BEM based benchmark models, it is noted that the angle of attack α increases significantly towards the tip. In this region, the axial and tangential inductions are gradually decreased by the application of the tip-loss correction, which leads to higher angles of attack and loading coefficients. Note that the smearing factor η_ϵ also plays a role, as discussed in Appendix D, where it was shown that larger ϵ lead to smoother gradients of velocity towards the tip. This might result in higher axial velocities U_x and angles of attack α towards the tip.

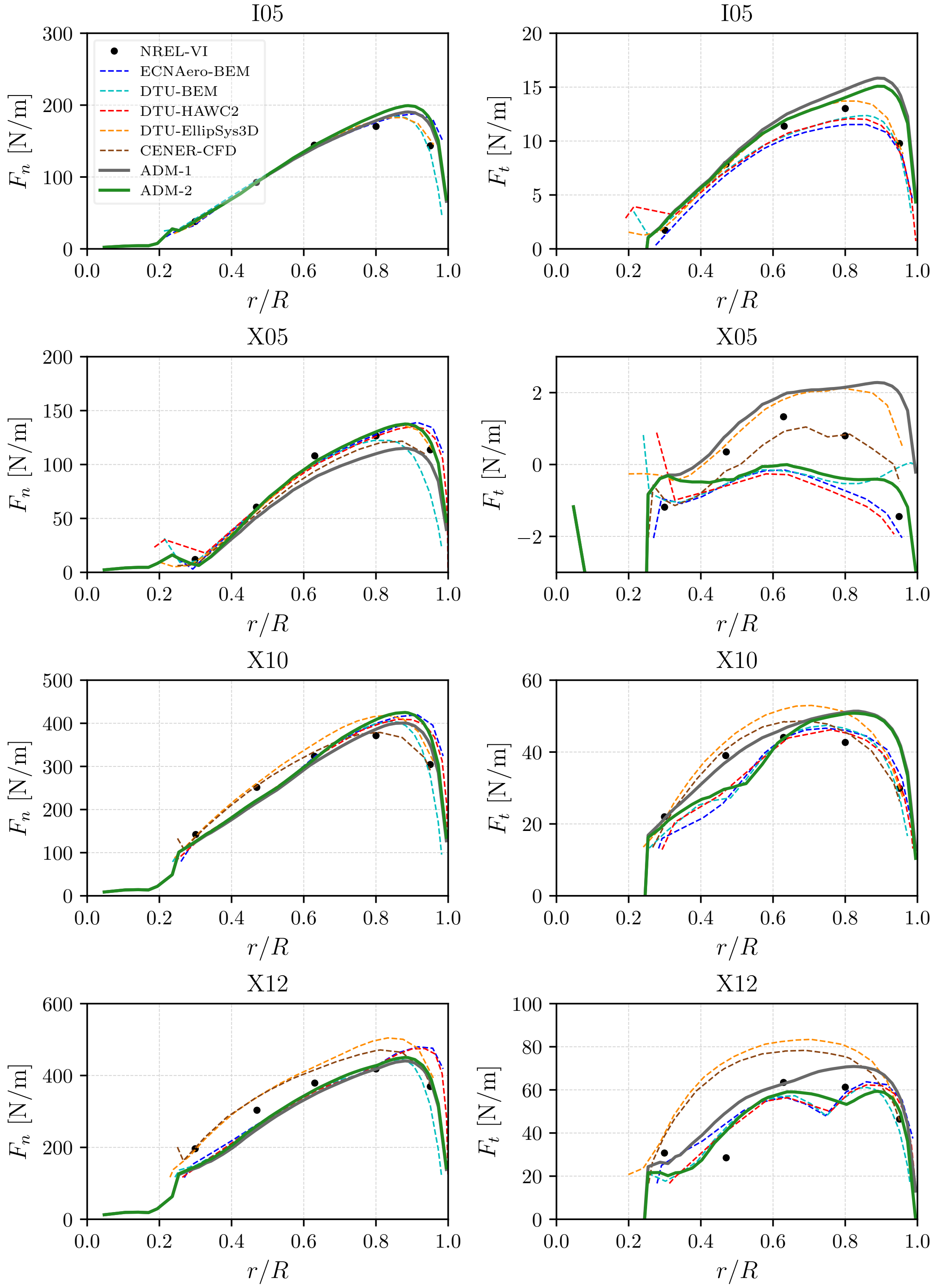

Figure 4.9: Normal and tangential forces along the blades. The legend box at the top applies to all the plots. Experimental values (•) and benchmark models (dashed lines) were digitised from Schepers et al. (2014). Benchmark models are described in Appendix C.

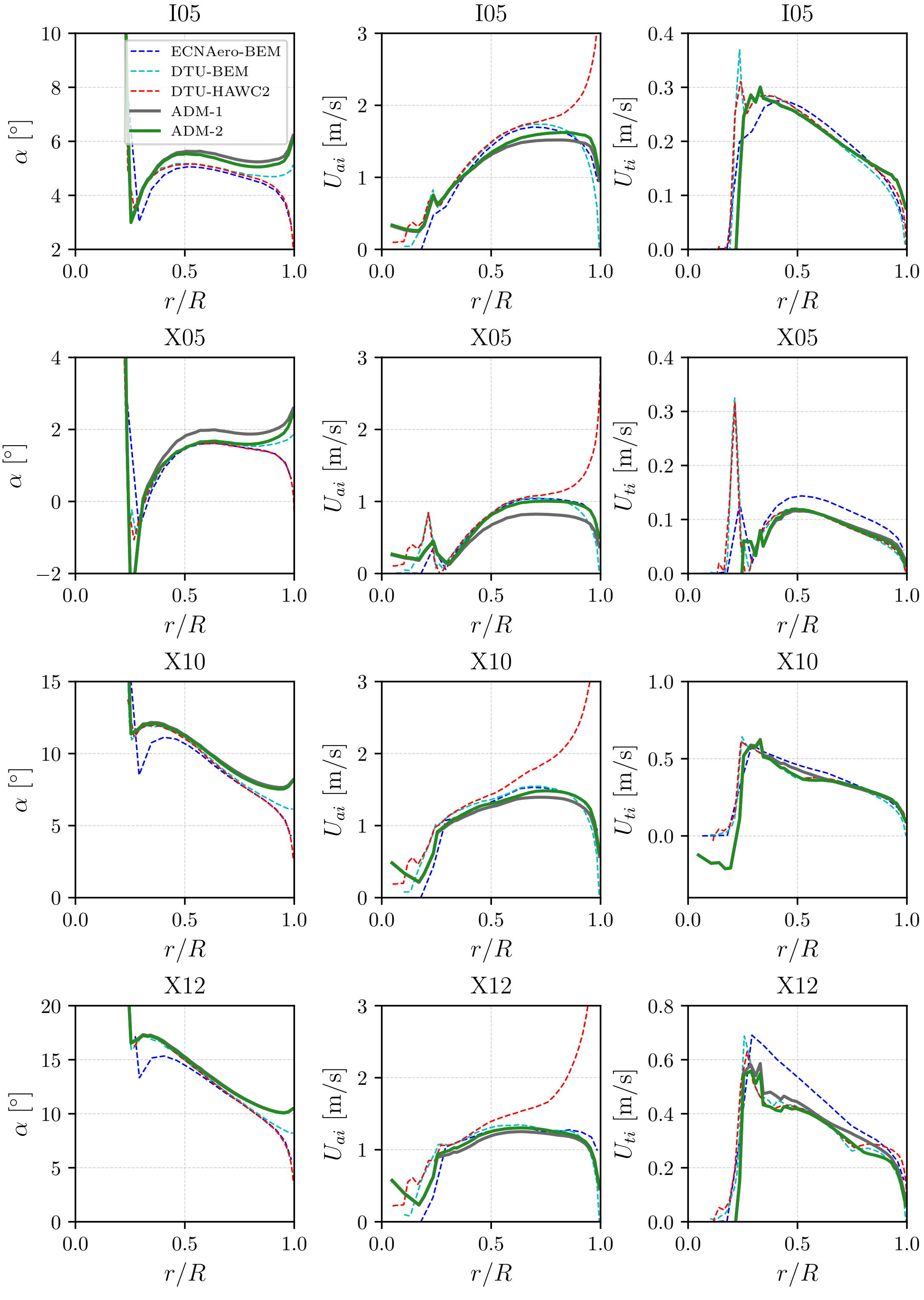

Figure 4.10: Angle of attack α and induced velocities (axial U_{ai} and tangential U_{ti}) along the blades compared to other benchmark models which provided such information. Values were digitised from Schepers et al. (2014).

4.3.5.2 New-MEXICO

In this section, the ADM is compared with the New-MEXICO experiment and some of the benchmark models listed in Table 4.1. One of the advantages of New-MEXICO is that Particle Image Velocimetry (PIV) was used to measure the flow field near the rotating blades which are also compared with the ADM. Furthermore, the tripping tape to avoid laminar separation was not installed in the outer section of the blades using the NACA 64-418 airfoil. This was done to reduce uncertainties when comparing experimental values with tripping tape with CFD simulations without them (Boorsma and Schepers, 2014). Therefore, two series of ADM results are presented here, one considering actual clean configuration used in the experiment (ADM-c, using airfoil coefficients in Table B.8) and another one using the rough configuration (ADM-r, which uses the coefficients in Table B.9).

Additionally, note that the three cases here cover a wide range of operating conditions, the design condition with $TSR = 6.65$ and $U_0 = 15$ m/s, a separated flow condition with $TSR = 4.16$ and $U_0 = 24$ m/s, and a turbulent wake state condition with $TSR = 9.97$ and $U_0 = 10$ m/s.

Performance

Figure 4.11 shows the Power and Thrust coefficients (C_P, C_T) as a function of the tip speed ratio TSR, including the experimental values obtained from pressure sensors and the benchmark models for the three cases of interest. In particular, special attention should be paid to the Uppsala-AD model, which in principle is the most similar modelling technique compared to the ADM in `turbineDisk`. The simulations results from ADM-c and ADM-r include additional TSR points to have a complete picture. It is observed that the ADM predictions are comparable in accuracy to other models. Nevertheless, there is significant variability in power predictions which is higher in off-design operating conditions.

The Uppsala-AD model tends to overpredict C_P significantly at $TSR = 9.97$ (turbulent wake state), this is rather unexpected since the same airfoil data is used.

Similarly, the EllipSys3D (FRS) model also overpredicts the power at this TSR, but as mentioned before, the limited number of pressure sensors (and the linear interpolation) also underestimate the experimental loadings. Besides, this turbulent wake state was also harder to converge with the ADM.

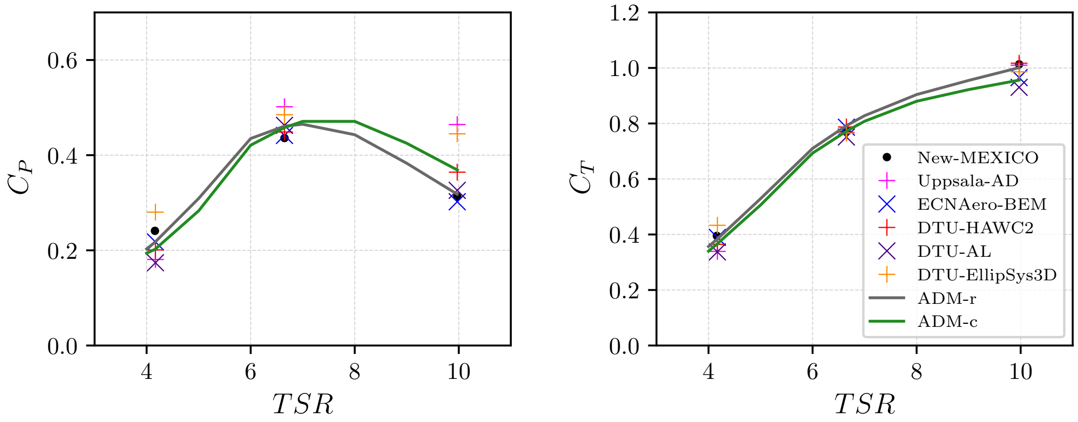

Figure 4.11: Power an Thrust coefficients (C_P, C_T) as a function of the tip speed ratio (TSR).

Loadings

Figure 4.12 shows the blade loadings. Overall, the ADM behaves similarly to other models, though the normal force F_n is consistently underpredicted towards the tip, particularly when using the clean configuration (ADM-c). In this region, the tip-loss correction might be tuned to improve the fit to experimental values. In the midsection, it is noticeable the transition between different airfoils. On the other hand, the tangential forces F_t shows much more variability between models, this can be explained as a result of having much smaller absolute values where changes in loading coefficients become more significant. The bigger differences arise in the turbulent wake state (10 m/s) and the separated flow case (24 m/s).

Induced velocities

Figure 4.13 presents the induced velocities and local angle of attack. Similar to the NREL-VI case, the axial induction for the ADM is reduced towards the tip, which is consistent with the underpredicted normal forces. This is compensated by larger angles of attacks towards the tip which lead to larger loadings. As mentioned before, the smearing factor η_ϵ also impacts the velocity gradients near the tip, which combined with the rather coarse mesh might be leading to these inaccuracies. However, the mesh sensitivity analysis in Appendix D shows that the differences between 30 and 60 cells per rotor diameter are minimal. Nevertheless, the prediction tends to agree better with the DTU-ALM. Tangential induced velocities, on the other hand, seem to be more in agreement with other BEM based models, excepting at the separated flow case ($U_0 = 25$ m/s) where greater discrepancies are found, even with a sign change in the case of DTU-AL model.

Axial traverses

Axial traverses of the three velocity componentes (axial U_x, radial U_r and tangential U_t) are shown in Figure 4.14. The axial traverses are located at $r = 1.5$ m and go from $1D$ upstream to $1.5D$ downstream. Overall the ADM model does capture the main flow features. Differences between the rough and clean configurations are only noticeable in the turbulent wake state case ($U_0 = 10$ m/s). Under this condition the numerical simulation was more unstable and took longer to converge, particularly for the clean configuration ADM-c, which shows some strange behaviour. The Uppsala-AD is only shown for the design operating conditions ($U_0 = 15$ m/s) and compared well with ADM results, though, the velocity changes are underpredicted. DTU-AL and EllipSys3D models, as expected, are much better capturing the complex flow features in the near wake region.

Radial traverses

Finally, radial traverses of velocity components just upstream ($x = -0.3$ m) and downstream ($x = 0.3$ m) of the rotor are shown in Figure 4.15 and 4.16. The axial velocity component U_x is in good agreement with experimental observations and benchmark models, in particular in the upstream location, whereas in the downstream position the ADM predict smoother transitions near the tip, which is consistent with loads underpredictions in the outer region. The radial component U_r

shows larger deviation towards the root which is explained by the lack of the nacelle and hub in ADM but it still compares well with Uppsala-AD which does not include the nacelle either. Also, the ADM underpredicts the peak in radial velocities at the tip, which in part it is associated with the missing nacelle structure that would increase the radial velocity, but it is also influenced by the smearing parameter ϵ that smooth out velocity gradients at the tip. Lastly, the tangential velocity components U_t show the largest variability, particularly at the upstream location and towards the root. In Appendix D it is showed that the tangential velocity is very sensitive to the smearing parameter ϵ, larger values determine how far upstream the flow *feels* the presence of the turbine through sink of momentum terms. This is particularly important for the tangential force components since essentially the spreading occurs by translating a fraction of the force vector in the axial direction without correcting the moment introduced by this translation. As a result, the larger ϵ is, the sooner the flow starts to rotate. Furthermore, the behaviour downstream shows that the ADM, as well as the DTU-AL and Uppsala-AD, fail to capture the complex flow features towards the root at stall condition ($U_0 = 24$ m/s, which are well captured by EllipSys3D). One reason for this is that all these model rely on the same 2D airfoil data, but more importantly in the case of the ADM, the mesh resolution is relatively coarse (particularly in the inner region), and these flow features are beyond the capabilities of such a low order model. Still, the ADM does capture the main flow features.

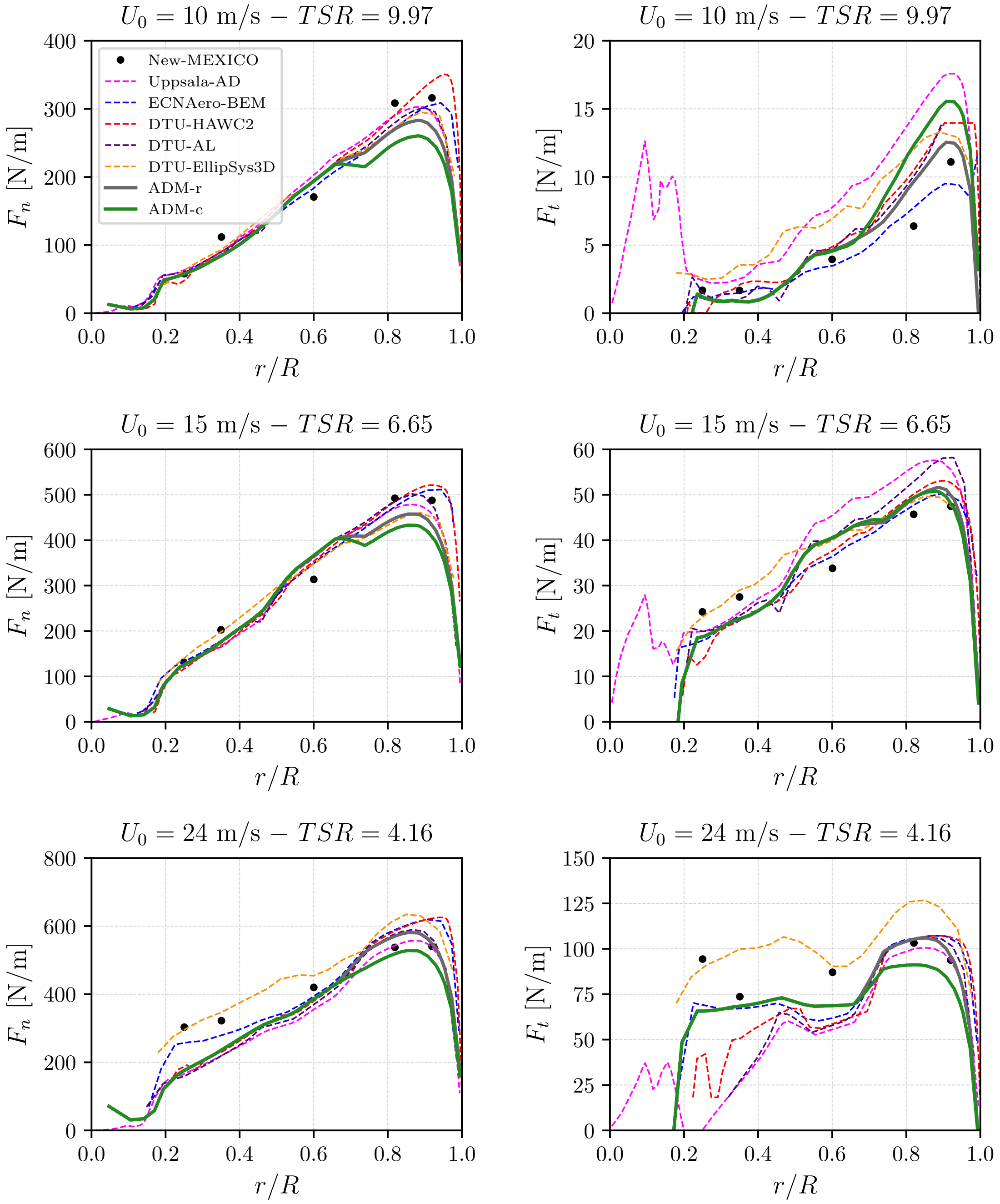

Figure 4.12: Normal and tangential forces along the blades. Continuous lines represent the ADM simulations. ADM-r and ADM-c correspond to the rough and clean configurations using NACA 64-418 airfoil data from Table B.9 and Table B.8 respectively (See Appendix B). Dashed lines are used for benchmark models (See Table 4.1).

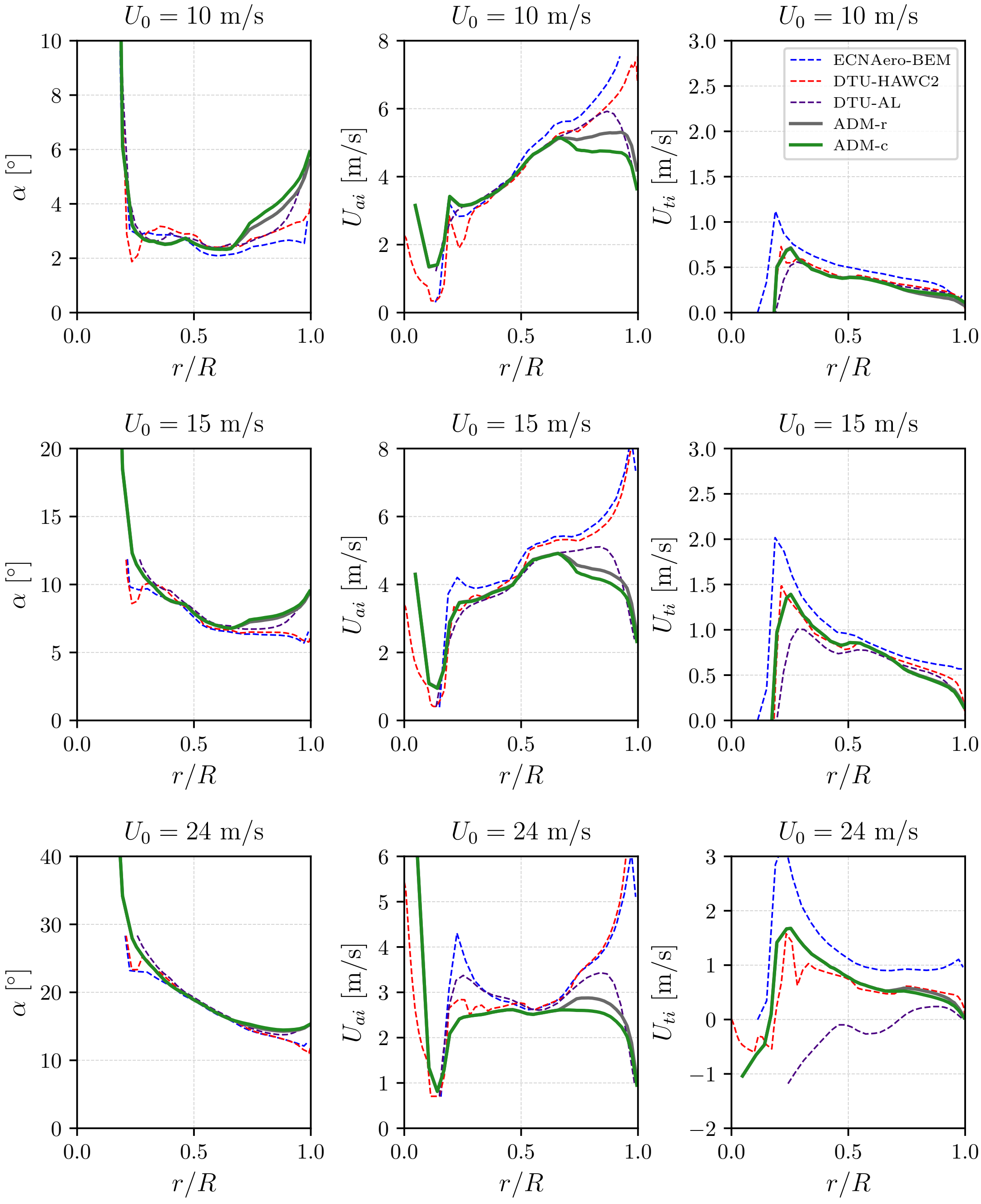

Figure 4.13: Angle of attack α and induced velocities (axial U_{ai} and tangential U_{ti}) along the blades. Dashed lines show benchmark models and continuous lines ADM results for rough and clean configurations.

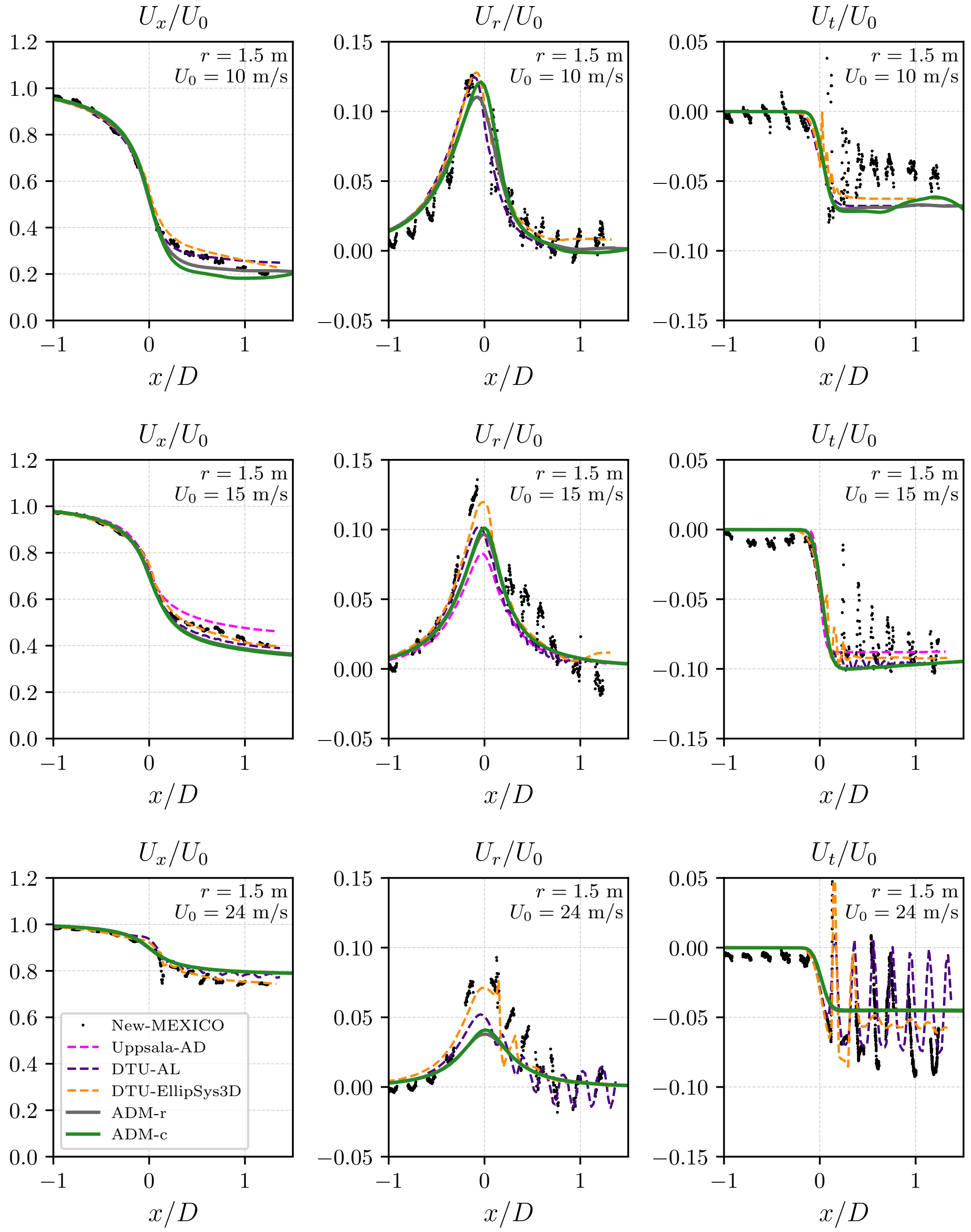

Figure 4.14: Axial traverses for axial (U_x), radial (U_r) and tangential (U_t) velocity components. The traverse line is located at a radius $r = 1.5$ m and goes from $1D$ upstream to $1.5D$ downstream. The values are normalised with free flow velocity U_0. Experimental values were digitised from Schepers et al. (2018), and are measured at specific azimuthal position (0° azimuth). Benchmark model data is digitised as indicated in Table 4.1.

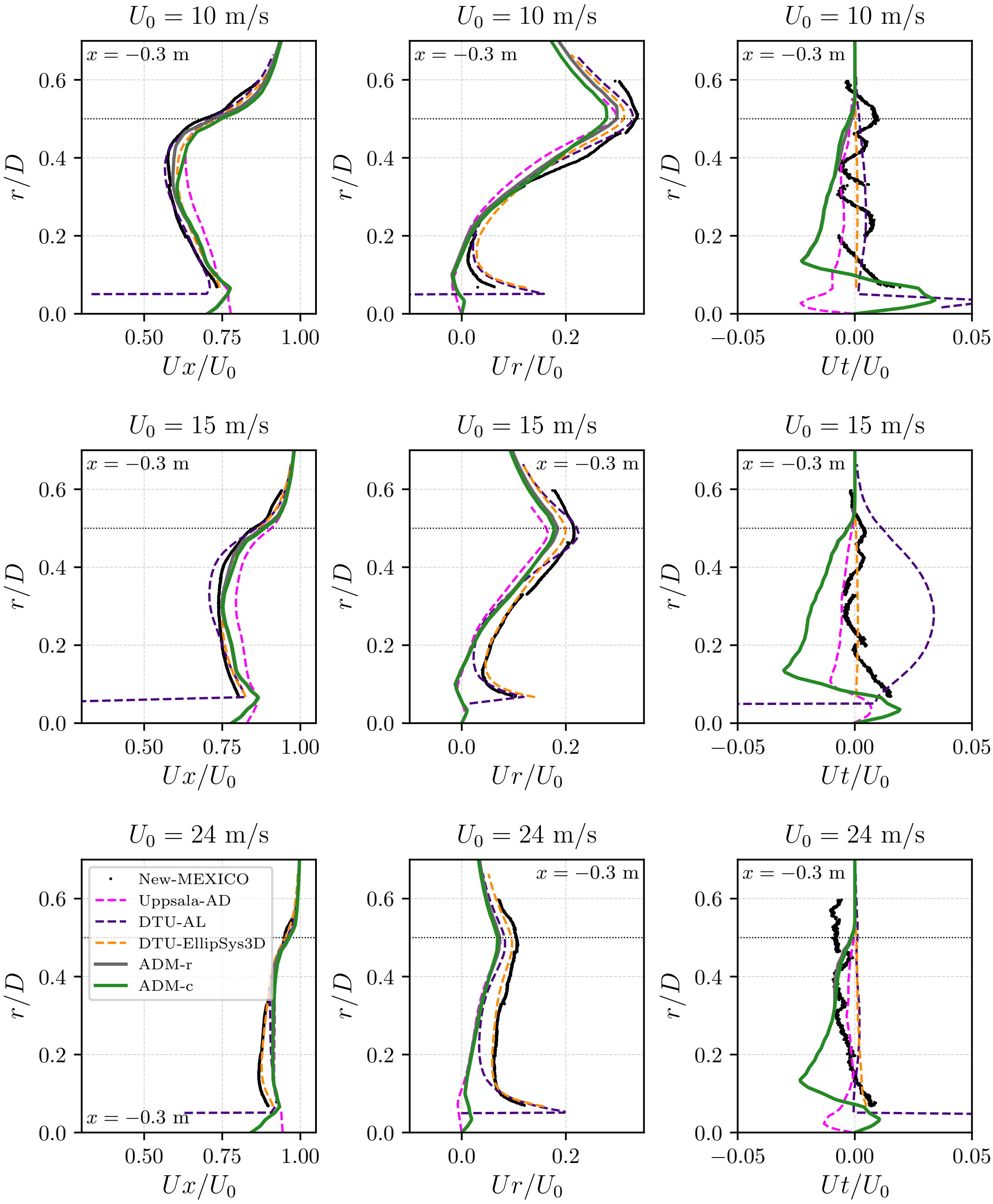

Figure 4.15: Upstream radial traverses of velocity components at $x = -0.3$ m (axial U_x, radial U_r and tangential U_t velocity components from left to right). Values are normalised with free flow velocity U_0. Experimental values are azimuthal averages and were digitised from Schepers et al. (2018). Benchmark models data digitised as indicated in Table 4.1.

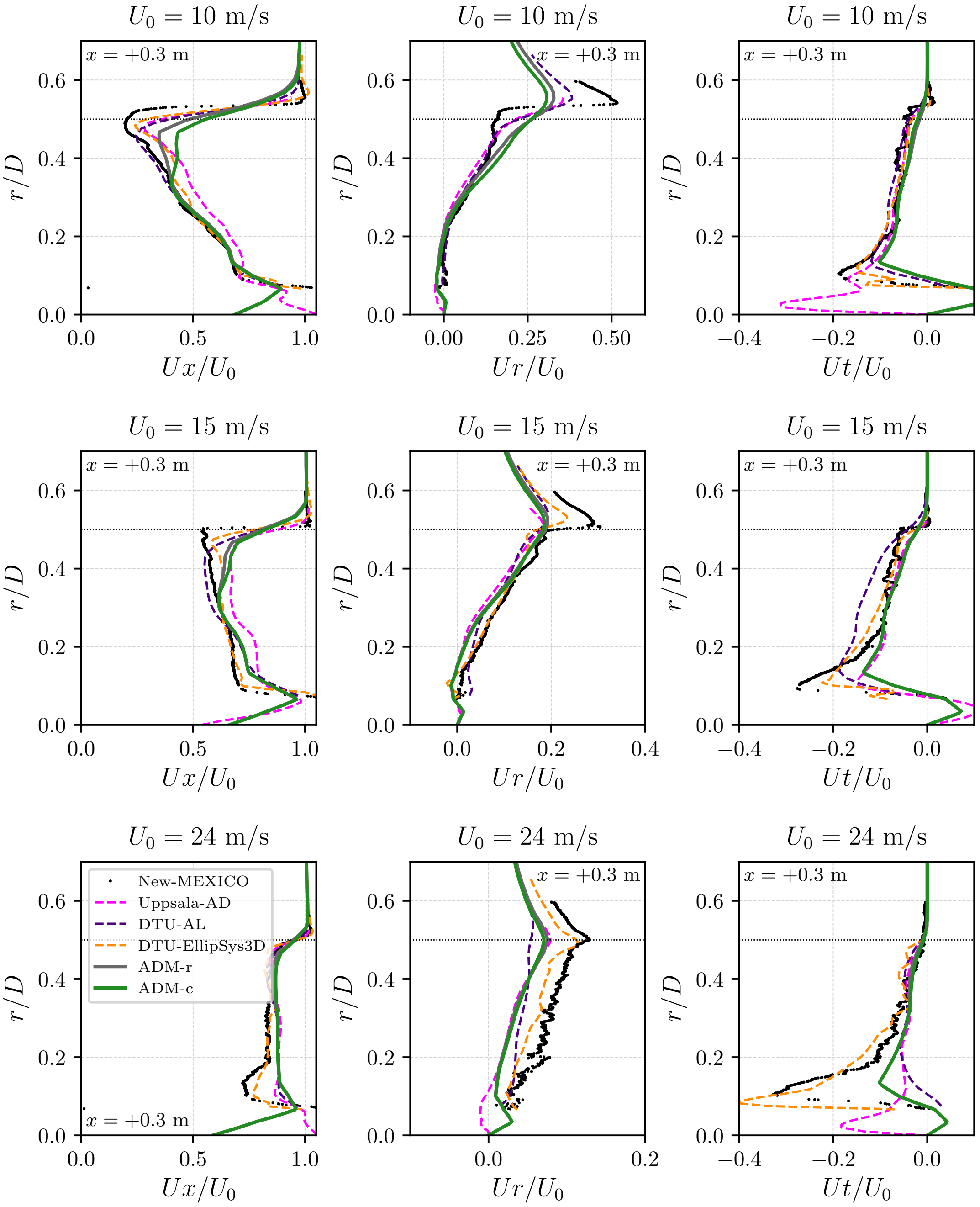

Figure 4.16: Downstream radial traverses of velocity components at $x = 0.3$ m (axial U_x, radial U_r and tangential U_t velocity components from left to right). Values are normalised with free flow velocity U_0. Experimental values are azimuthal averages and were digitised from Schepers et al. (2018). Benchmark models data digitised as indicated in Table 4.1.

4.4 Summary and Conclusions

This chapter described how a new `OpenFOAM` library was implemented to model wind turbines as an actuator disk based on blade element momentum theory (BEM). The model is used in combination with RANS equations which are solved for steady incompressible flow. The $k-\omega-SST$ turbulence model was used since it was found to give better predictions than the standard $k-\varepsilon$ model. This is in agreement with other studies (Shives and Crawford, 2016; Antonini et al., 2019). This ADM model aims to capture the main flow features at a low computational cost, since uncertainty propagation requires several simulations. Therefore, capturing the complex flow features in the near wake region is beyond the scope of this work. Nevertheless, comparisons with experimental measurements of the NREL-VI and MEXICO experiments, as well as other state of the art codes, have revealed that the ADM here implemented is reasonable accurate both in terms of loadings and flow features at a very low computational cost. Power predictions are within 15% error (in NREL-VI cases), which is comparable to other benchmark models, and which is reasonable good considering that experimental values of integral quantities might be underestimated because of the limited number of pressure sensors as shown by Schepers et al. (2014), introducing a rather large experimental uncertainty.

One of the main features of this ADM is that it uses local inflow conditions at each actuator point, making it suitable for non-uniform inflow conditions (no axial symmetry is assumed), taking into account the rotation of the wake. The model makes use of tabulated airfoil data that is linearly interpolated at the local AOA and Re_c. The loads are calculated at the cell centroids of the cells at the rotor disk, and they are corrected applying tip and root corrections. Also, the forces are spread in the axial direction, introducing an additional model parameter ϵ, to avoid unphysical behaviour of the flow. However, since ϵ determines how far upstream the flow `feels` the presence of the turbine, large values of ϵ lead to smoother velocity gradients at the rotor because there has been more spreading. Nevertheless, even though these effects are observed particularly in velocity components in the outer sections, the net impact in integral quantities such as power and thrust is very limited. For instance, using $\epsilon = 0.1D$ ($3\Delta x$ when using 30 cells per rotor diameter) and $\epsilon = 0.2D$ ($6\Delta x$) results in a variation of power and thrust lower than 0.9% and 0.4% respectively. On the other hand, if the value is too small ($\epsilon < 1.5\Delta x$) results in unphysical behaviour with major errors in power and thrust going up to about 12% and 4% respectively.

The model may also be useful to simulate large wind farms. To model wind turbine arrays in the atmospheric boundary layer, the simplest approach is to have a uniform structured grid (ignoring some details such as the nacelle and tower). Therefore all the test included in this work use such computational grids. It has been shown that using at least 20 cells per rotor diameter does allow to capture the main flow features, which in terms of power and thrust, and compared with the same setup but using 60 cells per rotor diameter, results in relative errors of less than 0.9% and 0.15% respectively. However, a uniform coarse mesh has a noticeable drawback, they are too coarse in the inner section of the rotor limiting its accuracy in this region. This is not a significant problem considering that this is a low order model that is not intended to be accurate in the near wake region.

Finally, the there are two main limitation of the model that can be improved in a future work. The first one is that the operating conditions such as pitch and rotational speed are prescribed, and it would be better to add a control system that adjust these parameters based on the flow conditions at the each specific turbine. The second is that the model is not capable of simulating yawed or tilted rotors, primarily because of the way the code takes advantage of the structure grid to compute and applied the source terms. Yawed rotors can still be tested by changing the wind directions, but as mentioned before, currently the forces are spread along the axial direction, and in the yaw misalignment is too big, then this would be unphysical. No proper validation has been made for yawed inflow. Furthermore, it would be ideal to control the yaw angle of each turbine separately, regardless of the grid, so active wake control strategies could be tested. Besides, implementing this feature will require further validations tests and usually is not easy to find complete experimental data sets, and probably higher order models might be needed to assess the accuracy.

Chapter 5

Atmospheric Boundary Layer Model

5.1 Introduction

This chapter describes the model used to simulate the atmospheric boundary layer flow, which together with the ADM model presented in the previous chapter, constitute the deterministic CFD model that will be used to model wind turbine arrays and propagate uncertainties through polynomial chaos expansion.

In Chapter 2 the main features of the atmospheric boundary layer(ABL) were described. It was shown that wake effects are impacted by the wind shear, the turbulence intensity and the atmospheric stability. Therefore accurate modelling of the ABL is a key element for wind farms simulations. However, as it will be discussed, this is not as straightforward as one might expect, as the inflow conditions should be consistent with the top and the ground boundary conditions, to avoid streamwise gradients (horizontal homogeneity) that may change the evolution of wakes. Furthermore, stability effects increase even more the complexity of the models adding buoyancy effects. For now this work focuses only on neutral stability conditions.

The simplest ideal case of a atmospheric boundary layer flow is a horizontally homogeneous atmospheric boundary layer (HHABL) under neutral stratification.

Richards and Hoxey (1993) proposed a set of inflow profiles to model a HHABL using the standard $k-\varepsilon$ turbulence model (Launder and Sharma, 1974). They proposed these boundary conditions to eliminate streamwise gradients that they observed in previous studies. Nevertheless, Hargreaves and Wright (2007) showed that these BCs were only partially adopted by commercial CFD packages leading to decay in turbulence and velocity profiles.

In this chapter, a comprehensive set of numerical experiments is carried out to determine the right set of boundary conditions to model a HHABL that eliminate or reduce streamwise gradients. The simulations are performed using OpenFOAM v.6, using a existing library and implementing new boundary conditions. RANS equations are solved using both, the standard $k-\varepsilon$ and the $k-\omega-SST$ model. In addition, the new set of BCs are tested using structured grids with different resolution, and also, varying the inflow conditions (velocity and aerodynamic roughness). Finally, a test is carried out with an unstructured non-conformal grid ,that allows to reduce significantly the number of cells when modelling wind turbines, to see how it behaves compared with a simple structured grid.

5.2 Modelling neutral ABL

In a HHABL the buoyant effects and streamwise gradients are negligible, with a constant shear stress (which drives the flow), zero pressure gradient and zero vertical velocities. Under these assumptions, the incompressible momentum equation is reduced to:

$$\nu_t \frac{\partial U}{\partial z} = \frac{\tau_w}{\rho} = u_\tau^2 \tag{5.1}$$

where molecular viscous effects are negligible in atmospheric flows $\nu_t \gg \nu$, τ_w is the wall shear stress and u_* is the friction velocity. Similarly, the turbulent kinetic energy and turbulent dissipation rate equations from the standard $k-\varepsilon$ model (Launder and Sharma, 1974) are reduced to:

$$\frac{\partial}{\partial z}\left(\frac{\nu_t}{\sigma_k}\frac{\partial k}{\partial z}\right) + P_k - \varepsilon = 0 \tag{5.2}$$

$$\frac{\partial}{\partial z}\left(\frac{\nu_t}{\sigma_\varepsilon}\frac{\partial \varepsilon}{\partial z}\right) + C_{\varepsilon 1} P_k \frac{\varepsilon}{k} - C_{\varepsilon 2}\frac{\varepsilon^2}{k} = 0 \tag{5.3}$$

$$P_k \;=\; -\overline{u_i u_j}\frac{\partial U_i}{\partial x_j} \;=\; \frac{\tau_{turb}}{\rho}\frac{\partial U}{\partial z} \;=\; u_\tau^2\frac{\partial U}{\partial z} \tag{5.4}$$

Richards and Hoxey (1993) derived a set of inflow boundary conditions that satisfy the above equations.

$$U(z) = \frac{u_\tau}{\kappa}\ln\left(\frac{z+z_0}{z_0}\right) \tag{5.5}$$

$$k = \frac{u_\tau^2}{\sqrt{C_\mu}} \tag{5.6}$$

$$\varepsilon = \frac{u_\tau^3}{\kappa(z+z_0)} \tag{5.7}$$

Where z_0 is the aerodynamic roughness. If the boundary conditions at the top and ground boundaries are not consistent with such inflow profiles, they will decay to adapt themselves to the new forcing conditions. These inlet profiles only satisfy the transport equations if the following relationship between model coefficient is also satisfied.

$$\sigma_\varepsilon = \frac{\kappa^2}{(C_{\varepsilon 2} - C_{\varepsilon 1})\sqrt{C_\mu}} \tag{5.8}$$

It must also be noted that $C_\mu = (\overline{uv}/k)^2$ is typically given a value of 0.09, which is appropriate for channel flows and boundary layer flows (justified by DNS-data), but not for atmospheric flows where values around 0.03 seem to be more suitable according to field measurements (Richards and Hoxey, 1993). Also, it is common practice to change C_μ to adjust the turbulence intensity (van der Laan et al., 2015c), but care must be taken to ensure that other model coefficients are adjusted accordingly.

To be consistent with the inflow profiles, a constant shear stress ρu_τ^2 should be specified at the top boundary. Similarly, an equal stress in the opposite direction should be prescribed at the ground through a wall function. The values for k and ε at the near ground cell should be specified as:

$$k = \frac{u_{\tau P}^2}{\sqrt{C_\mu}} \qquad ; \qquad \varepsilon = \frac{\sqrt{C_\mu}\, k\, u_{\tau P}}{\kappa(z_P + z_0)} \tag{5.9}$$

where $u_{\tau P}$ is the friction velocity computed locally with the velocity at the cell centroid U_P using Eq.5.5, and z_P as the distance from the wall to the near wall cell centroid.

Nevertheless, standard wall near wall treatment in most used CFD packages are not consistent with inflow profiles described above resulting in undesired streamwise gradients, particularly when modifications to source code are not possible or when the appropriate boundary conditions are simple neglected (Hargreaves and Wright, 2007; Blocken et al., 2007; Richards and Norris, 2011).

Yang et al. (2009), following a similar approach to Richards and Hoxey (1993), proposed a set of more general inflow conditions to model horizontally homogeneous atmospheric boundary layer with the standard $k-\varepsilon$ model. In this study, an analytical solution for the k-equation was used to determine the inflow profiles for k and ε, although the latter was only an approximate solution of the ε-equation. Their results showed an improvement in maintaining the inlet conditions through the domain, even without the shear stress at the top boundary where a free slip condition was considered.

Richards and Norris (2011) extended the work from Richards and Hoxey (1993) to other turbulence models such as the standard $k-\omega$ model, the RNG $k-\varepsilon$ model, and the LRR QI Reynolds Stress Model. However, although in all cases the streamwise gradients are reduced, they are not completely removed.

O'Sullivan et al. (2011) proposed a different approach by computing fully developed profiles running simulations with periodic boundary conditions between the inlet and the outlet to determine the inflow profiles, so they are consistent with the boundary conditions applied and in this way removing completely the streamwise gradients. In this study, the top boundary condition was also a shear stress, prescribed as a constant gradient for streamwise velocity, as well as for the turbulent kinetic energy and the turbulent dissipation rate, that were calculated from the profiles given by Richards and Hoxey (1993). One of the main advantages of this approach is that the standard wall functions can be used without modifications. Another advantage compared to Richards and Hoxey (1993) is that the turbulence profile develops naturally to a more realistic one, where turbulence decreases with height. However, this approach will require that every time the inflow change, a new set of fully developed profiles should be generated. While this is in principle possible, because of the way the uncertainty propagation framework described in Chapter 6 was created, it was considered a more general approach to have a fixed model where parameters can be change to initialize the cases rather than running pre-simulations that may apply only in some situations.

5.3 OpenFOAM boundary conditions

OpenFOAM implemented the inflow profiles from Richards and Hoxey (1993) shown in Eg.5.5, Eg.5.6 and Eq.5.7 within a library named `libatmosphericModels.so`, which also includes an appropriate wall function to get the right wall shear stress τ_w at the ground by correcting the eddy viscosity at the near wall cell. The implementation of these boundary conditions can be found in the following files and their respective header files:

- `atmBoundaryLayer.C`
- `atmBoundaryLayerInletVelocity.C`
- `atmBoundaryLayerInletK.C`
- `atmBoundaryLayerInletEpsilon.C`
- `nutkAtmRoughWallFunction.C`

5.3.1 Wall function for momentum equation

OpenFOAM, as other codes when using eddy viscosity models, in order to get the right wall shear stress at the walls for the momentum equation, it uses a corrected eddy viscosity at the walls such that using a linear variation to compute the gradient (Eq.5.10), can still reproduce the same shear stress that will occur in the actual non-linear velocity profile (Eq.5.12).

$$\frac{\tau_w}{\rho} = \nu_{eff} \frac{U_P - U_W}{z_P} \tag{5.10}$$

where ν_{eff} is the effective viscosity that results from adding the laminar viscosity ν and the corrected turbulent viscosity $\nu_{t,c}$.

$$\nu_{eff} = \nu_{t,c} + \nu \tag{5.11}$$

$$\frac{\tau_w}{\rho} = u_\tau^2 = \frac{u_\tau U_P}{\frac{1}{\kappa} \ln(Ey^+)} \tag{5.12}$$

Combining equations Eq.5.10, Eq.5.11 and Eq.5.12 the corrected turbulent viscosity can be prescribed as Eq.5.14.

$$\nu_{eff} = \frac{\nu \kappa y^+}{\ln Ey^+} \tag{5.13}$$

$$\nu_{t,c} = \nu \left(\frac{\kappa y^+}{\ln(Ey^+)} - 1 \right) \tag{5.14}$$

OpenFOAM includes slightly different forms of wall functions to correct the turbulent viscosity for both smooth and rough walls, based on either the velocity at the near wall cell U_P (Eg.5.15) or the turbulent kinetic energy at the near wall cell k_P (Eg.5.16) to determine the friction velocity.

$$u_\tau = \sqrt{\frac{\tau_w}{\rho}} = \frac{U_P \kappa}{\ln(Ey^+)} \tag{5.15}$$

$$u_* = C_\mu^{1/4} k_P^{1/2} \tag{5.16}$$

Details of their implementation can be found in the following files and respective header files:

- `nutUWallFunction.C`
- `nutURoughWallFunction.C`
- `nutkWallFunction.C`
- `nutkRoughWallFunction.C`

Velocity based wall functions are implicit and solved iteratively. For rough walls the roughness parameter E is modified using sand-grain roughness height based on the experimental work by Nikuradse (1933).

Nikuradse (1933) adjusted the law of the wall for the flow in rough pipes. Uniform sand grain particles where attached to the internal walls to represent the wall roughness, where the roughness height K_s was varied by changing the particle size. It was determined that the law of the wall should be corrected by a function ΔB that depends on the roughness height K_s (or, in non-dimensional form, $K_s^+ = K_s u_\tau/\nu$).

$$U^+ = \frac{1}{\kappa}\ln(Ey^+) - \Delta B \tag{5.17}$$

$$\Delta B = \begin{cases} 0 & K_s^+ < 2.25 \\ \frac{1}{\kappa}\ln\left(\frac{K_s^+ - 2.25}{87.75} + C_s K_s^+\right)\sin(A) & 2.25 \le K_s^+ < 90 \\ A = 0.4258\left[\ln K_s^+ - 0.811\right] & \\ \frac{1}{\kappa}\ln\left(1 + C_s K_s^+\right) & 90 < K_s^+ \end{cases} \tag{5.18}$$

Surfaces with $K_s^+ < 2.25$ are considered as aerodynamically smooth while those with $K_s^+ > 90$ are considered as fully rough. Atmospheric flows in general can be considered as fully rough, since typically the roughness elements are large compared to the viscous sub-layer which is virtually suppressed, becoming independent of the molecular viscosity (Blocken et al., 2007). As an example, Richards and Hoxey (1993) showed that the ratio between the turbulent and laminar viscosity was $\nu_t/\nu \approx 172$, at a height of 10 mm using wind velocity measurements at Silsoe Research Institute. Note that 10 mm was equivalent to the calculated aerodynamic roughness z_0 at that location with the measured wind profile.

One of the main difficulties of the sand-grain roughness height approach in atmospheric flows is that the distance from the near wall cell centroid to the wall has to be larger than K_s (i.e. it would not be consistent to have cells smaller than the roughness elements, otherwise it would be more appropriate to fully solve those elements with a finer mesh). The K_s height is approximately $30z_0$ (Blocken et al., 2007), then, if the aerodynamic roughness is $z_0 = 0.1$ m the near wall cell height should be around 6 m (or even higher for larger aerodynamic roughness). This mesh resolution would not allow to solve some flow features near the ground and it will also results in high y^+ values at the near wall cells, even above 10.000 (Blocken and Carmeliet, 2004). Fortunately, for wind energy applications this is not necessarily a problem, a very fine grid will increase considerably the computational cost and in contrast with other wind engineering applications, it is not needed to solve flow features at ground level, providing that an appropriate wall function is used to determine the correct wall shear stress at the boundary.

OpenFOAM has a specific boundary condition to correct ν_t that was implemented with Richards and Hoxey (1993) inflow profiles named `nutkAtmRoughWallFunction`. This boundary condition is implemented as in Eq.5.19.

$$\nu_{t,c} = \nu \left(\frac{\kappa y^+}{\ln\left(\frac{z_P + z_0}{z_0}\right)} - 1 \right) \tag{5.19}$$

with y^+ calculated based on the turbulent kinetic energy at the cell centroid k_P.

$$y^+ = \frac{u_* z_P}{\nu} = \frac{C_\mu^{1/4} k_P^{1/2} z_P}{\nu} \tag{5.20}$$

Note that the inflow velocity profile in Eq.5.5, uses $y^+ = u_\tau z_P/\nu$, with u_τ based on the velocity as in Eq.5.15. However, in this simple ABL model, both Eq.5.15 and Eq.5.16 are equivalent (See also Eq.5.6). The advantage of k based friction velocity is that the turbulent viscosity ν_t does not vanish when the velocity is zero (e.g. separation, impingement). Nevertheless, as it will be discussed later, over-prediction of k_P may lead to wrong estimations of $\nu_{t,c}$.

5.3.2 Wall functions for turbulent quantities

For the turbulent kinetic energy equation, the standard approach is to set a zero gradient boundary conditions at the wall for k, and prescribing both the production and dissipation of turbulent kinetic energy to be equal $P_k = \varepsilon$, so that there is a balance between these two when the k equation is solved at the near wall cell. In OpenFOAM this boundary condition is called `kqRWallFunction`.

For the turbulent dissipation rate ε on the other hand, a different approach is used. In this case, the ε is not solved at the near wall cell, and the value of ε is set at the cell centroid (Eq.5.21). This is done through the `epsilonWallFunction`, which also compute the production of turbulent kinetic energy P_k to keep the balance (Eq.5.22).

$$\varepsilon_P = \begin{cases} \dfrac{2 k_P \nu}{z_P^2} & y^+ < \texttt{yPlusLam} \\[2ex] \dfrac{C_\mu^{1/4} k_P^{1/2}}{\kappa z_P} & y^+ > \texttt{yPlusLam} \end{cases} \tag{5.21}$$

$$P_k = (\nu + \nu_t) \left| \frac{\partial U}{\partial y} \right| \frac{C_\mu^{1/4} k_P^{1/2}}{\kappa z_P} \tag{5.22}$$

Thus, the ε equation is solved for the internal field, the values of ε and P_k at the wall boundary cells are prescribed, and then the k equation is solved. Note that equation Eq.5.22 is equivalent to Eq.5.4 having:

$$\frac{\tau_{turb}}{\rho} = (\nu + \nu_t) \left| \frac{\partial U}{\partial z} \right| \tag{5.23}$$

$$\frac{\partial U}{\partial z} = \frac{u_*}{\kappa z_P} \tag{5.24}$$

However, it is important to remark that $|\partial U/\partial z|$ in `epsilonWallFunction` (Eq.5.22) is approximated using a linear fit between cell centroid values with the `snGrad()` function.

5.4 Neutral HHABL test cases

In this section, the results of a set of numerical experiments to determine the best set of boundary conditions to model HHABL in OpenFOAM are presented. Different grids, turbulence models, and inflow wind shear profiles are tested (e.g. varying wind speed U and aerodynamic roughness z_0). To this end, new boundary conditions are implemented in OpenFOAM, which are tested with the standard $k - \varepsilon$ (Launder and Sharma, 1974) and $k - \omega - SST$ (Menter and Esch, 2001) turbulence models.

5.4.1 Domain and grids

In order to make a comprehensive set of test cases, two types of grids are used: structured and non-conformal. The non-conformal will be referred to as *SnappyMesh* because it is generated using an OpenFOAM application called `snappyHexMesh`, that generates semi structured non-conformal grids that snap to surface objects. Nevertheless, its detailed description will be given later in Section 5.7.

A set of structured grids were generated using python scripts, varying the total

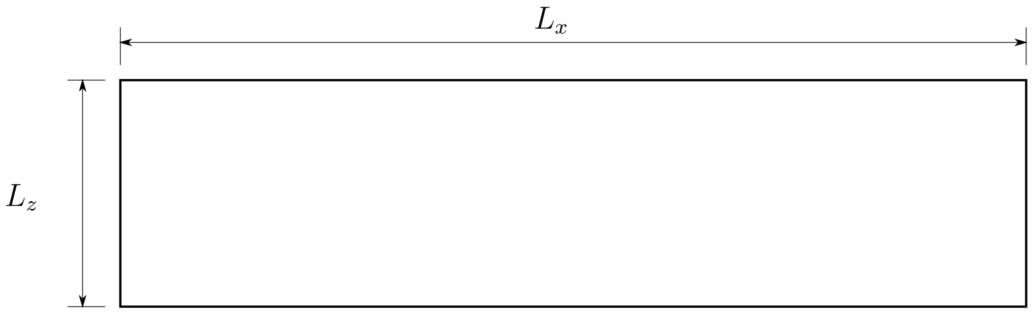

Figure 5.1: Schematic representation of the domain for structured grids.

domain length, the vertical refinement (particularly in the near wall region) and also the horizontal resolution. In Figure 5.1, a schematic representation of the domain for structured grids is shown. The python scripts are created to generate grids to model wind turbines, and therefore all the dimensions are parameterised using the turbine diameter D, and the hub height H_{hub}. In all simulations, the NREL-5MW turbine rotor with a diameter $D = 126$ m and $H_{hub} = 90$ m is used as a reference. Two domains of length of $L_x = 10D$ and $L_x = 100D$ (e.g. 1260 m and 12.6 km respectively) are used, which will be referred to as the *short mesh* (SM) and *long mesh* (LM) respectively. The height is kept constant in both cases with $L_z = 6D$, and although the flow is essentially two dimensional the width is set to $0.3D$ with 3 cells in the spanwise direction. This is is because the same mesh generating algorithm as the one used in Chapter 4 was used. Thus, the domain is split in three blocks in the spanwise direction to refine the grid gradually towards the rotor, and in this particular case at least one cell per block has to be used. The short domain allows to reduce the computational time, and the long domain allows to verify if an appropriate set of boundary conditions allow to sustain the inflow profiles across long distances.

The near wall refinement is key to optimize the computational cost when running 3D simulations of turbine arrays. As discussed before, sand-grain roughness approach can lead to very high y^+ values, beyond the limits $30 < y^+ < 300$ usually recommended where the logarithmic law of the wall holds. Nevertheless, the underlying assumptions in Richards and Hoxey (1993) inflow profiles assume a constant shear stress across the entire domain, thus imposing a logarithmic profile. Three different near wall refinement will be tested with y^+ values around 500, 2000 and 10000 based on a reference velocity of 10 m/s at 90 m height, with aerodynamic roughness $z_0 = 0.001$ m and von Karman constant $\kappa = 0.41$. The three refinements will be referred to as Y1, Y2 and Y3 respectively.

Table 5.1: Meshing details specifying the domain length, horizontal resolution Δx, near wall refinement [1] y^+ and the total number of cells[3].

Mesh Name	L_x	Δx	[1]$\sim y^+$	N Cells
LMX4Y1[2]	$100D$	$D/2$	500	50400
LMX4Y2	$100D$	$D/2$	2000	36600
LMX4Y3	$100D$	$D/2$	10000	25200
SMX1Y1	$10D$	$D/20$	500	50400
SMX2Y1	$10D$	$D/10$	500	25200
SMX3Y1	$10D$	$D/5$	500	12600
SMX4Y1	$10D$	$D/2$	500	5040
SMX1Y2	$10D$	$D/20$	2000	36600
SMX2Y2	$10D$	$D/10$	2000	18300
SMX3Y2	$10D$	$D/5$	2000	9150
SMX4Y2	$10D$	$D/2$	2000	3660
SMX1Y3	$10D$	$D/20$	10000	25200
SMX2Y3	$10D$	$D/10$	10000	12600
SMX3Y3	$10D$	$D/5$	10000	6300
SMX4Y3	$10D$	$D/2$	10000	2520

[1] Approximated y^+ for a reference velocity of 10 m/s at 90 m height, with $\kappa = 0.41$ and $z_0 = 0.001$ m.
[2] SM: Short Mesh $L_x = 10D$ & LM: Long Mesh $L_x = 100D$. X1,X2,X3,X4 determines Δx and Y1,Y2,Y3 the near wall refinement y^+ values.
[3] Note that the total number of cells includes the 3 cells across the spanwise direction.

On the other hand, the streamwise refinement is intended to give insights on the influence that cells with high aspect ratio near the wall have on the results. As it will be discussed later, a peak of turbulent kinetic energy near the ground when modelling atmospheric boundary layer has been reported in the literature (Hargreaves and Wright, 2007; Richards and Norris, 2011). Then, it is intended to see if varying the horizontal grid spacing has an impact in this peak of turbulent kinetic energy k. Four different horizontal cell sizes will be tested, $\Delta x = D/20$, $\Delta x = D/10$, $\Delta x = D/5$ and $\Delta x = D/2$ which will be referred to as X1, X2, X3 and X4 respectively.

Table 5.1 shows a summary of all the meshes generated. The grids were named using the above mentioned references. For instance the mesh LMX4Y1 is a long mesh with $\Delta x = D/2$ and $y^+ \sim 500$. In addition, Figure 5.2 shows sections of the finest ($\Delta x = D/20$ and $y^+ \sim 500$) and coarsest ($\Delta x = D/2$ and $y^+ \sim 10000$)

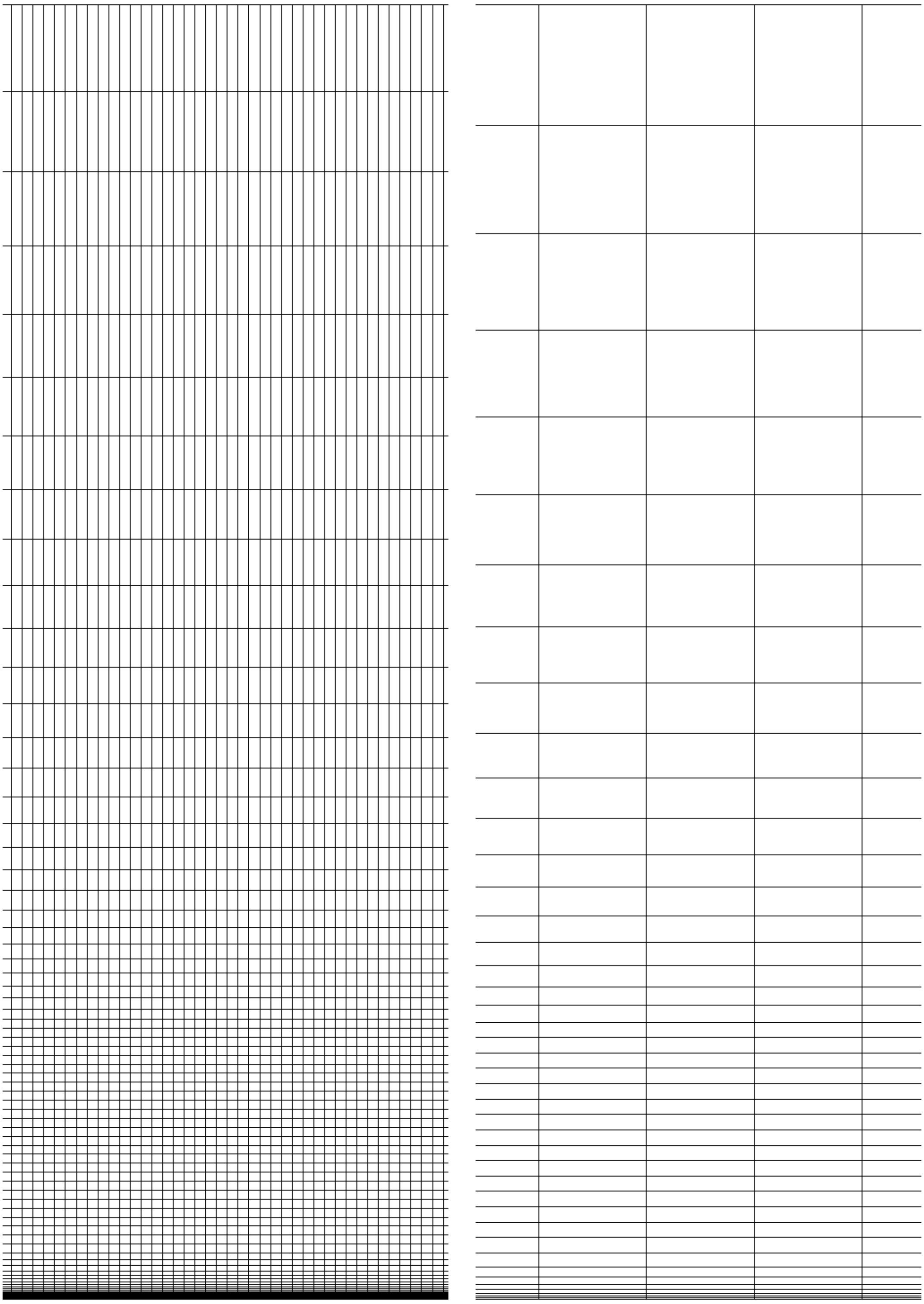

Figure 5.2: Mesh sections showing the horizontal and near wall refinement. Left: $\Delta x = D/20$ (X1) and $y^+ \sim 500$ (Y1). Right: $\Delta x = D/2$ (X4) and $y^+ \sim 10000$ (Y3). Note that y^+ are approximated for a reference velocity of 10 m/s at 90 m height, with $\kappa = 0.41$ and $z_0 = 0.001$ m. See Table 5.1 for more details.

combinations.

5.4.2 Standard $k-\varepsilon$ base case

The first test case aims to see how well the existing OpenFOAM libraries, including `libatmosphericModels.so`, can model a HHABL under neutral stratification. In this case a reference velocity of $U_{ref} = 10$ m/s at $z_{ref} = 90$ m height, with aerodynamic roughness of $z_0 = 0.001$ m and $\kappa = 0.41$ is used as a base case. Table 5.2 summarizes the boundary conditions chosen using standard OpenFOAM v.6 libraries. The standard $k-\varepsilon$ turbulence model was used (Launder and Sharma, 1974). The long domain mesh LMX4Y1 has been used in this case (See Table 5.1). This case is named *Base-ke*.

The results in Figure 5.3 show the vertical profiles of streamwise velocity component U_x, turbulent kinetic energy k and turbulent dissipation rate ε at different positions along the domain ($1D$, $50D$ and $99D$ downstream), along with the error when comparing with the prescribed inlet profiles. Here the inlet profiles are sampled at $1D$ downstream from the inlet because of interpolation errors that occur if profiles are sampled at $0D$.

It is observed that effectively, the inflow profiles decay along the domain. The velocity increases around $\sim 1.5\%$ at hub height after ~ 12.5 km ($99D$). At the top boundary the `slip` boundary condition is unable to maintain the velocity, reducing the shear with a consequent decay in turbulent kinetic energy and turbulent dissipation rate for up to $20-30\%$ in the upper half of the domain. Close to the ground, increasing velocities and gradients enhance the production of turbulent kinetic energy k and therefore the turbulence dissipation rate ε is also increased.

It is believed that the OpenFOAM wall function `nutkAtmRoughWallFunction` (See Eq.5.19) over-predicts the wall shear stress τ_w, and the corrected turbulent viscosity at the wall ν_t, increasing P_k (See Eq.5.22). In addition, since ν_t is calculated using the cell centroid value of turbulent kinetic energy k_P for the friction velocity, high turbulent generation rates will feed back again into higher ν_t values, reaching a point where the excess k is diffused to the upper layers. This point will be addressed again later.

Table 5.2: Base case for testing boundary conditions for ABL model

Field	Patch	Boundary Conditions
U	Inlet	`atmBoundaryLayerInletVelocity`[1]
	Ground	`fixedValue (0,0,0)`
	Outlet	`zeroGradient`
	Top/Sides	`slip`
ν_t	Inlet	`calculated`
	Ground	`nutkAtmRoughWallFunction`[4]
	Outlet	`calculated`
	Top/Sides	`slip`
k	Inlet	`atmBoundaryLayerInletK`[2]
	Ground	`kqRWallFunction`
	Outlet	`zeroGradient`
	Top/Sides	`slip`
ε	Inlet	`atmBoundaryLayerInletEpsilon`[3]
	Ground	`epsilonWallFunction`
	Outlet	`zeroGradient`
	Top/Sides	`slip`
p	Inlet	`zeroGradient`
	Ground	`zeroGradient`
	Outlet	`fixedValue 0`
	Top/Sides	`slip`

[1] As Richards and Hoxey (1993) given in Eq.5.5

[2] As Richards and Hoxey (1993) given in Eq.5.6

[3] As Richards and Hoxey (1993) given in Eq.5.7

[4] As given in Eq.5.19

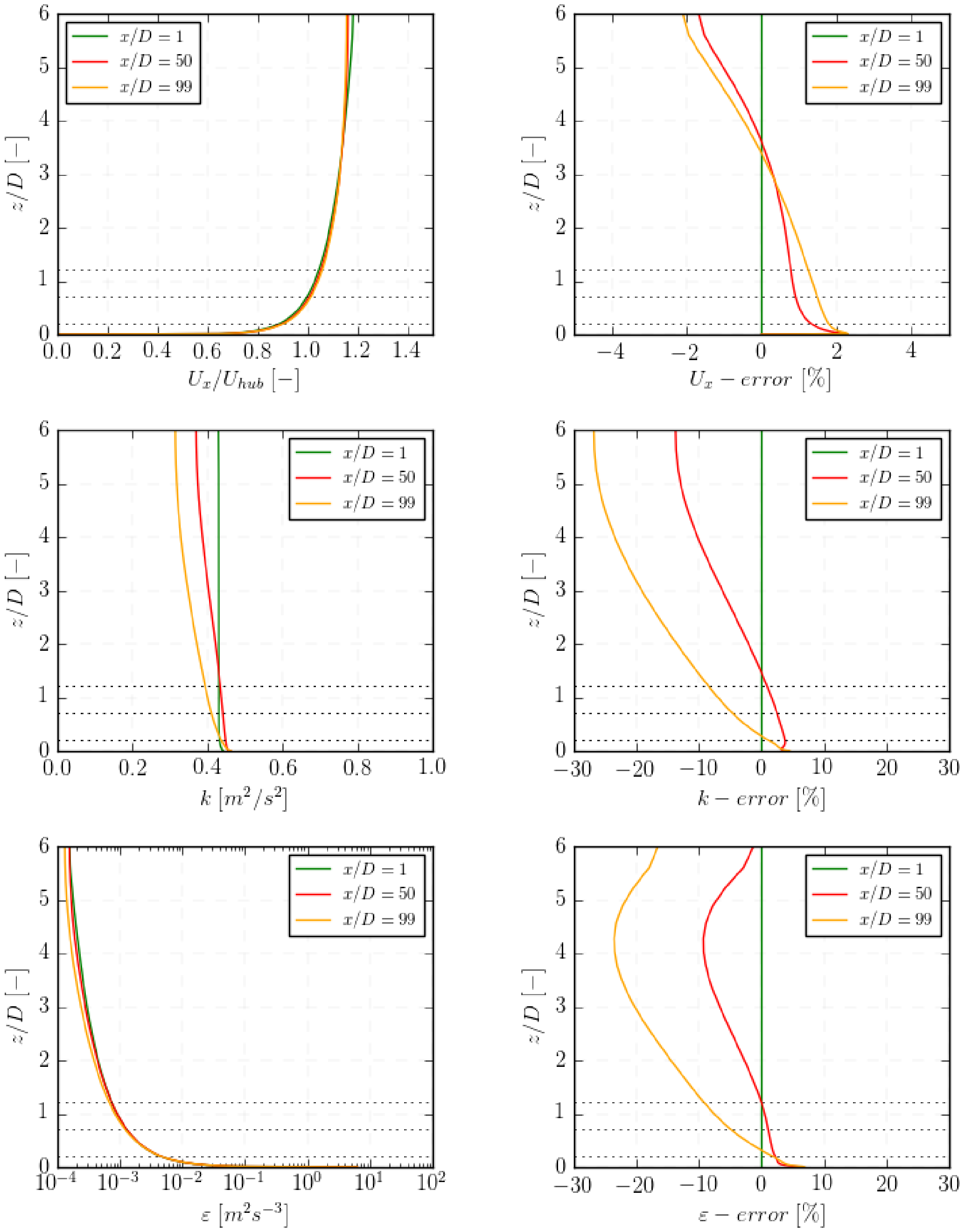

Figure 5.3: Vertical profiles of streamwise velocity U_x, turbulent kinetic energy k and turbulent dissipation rate ε at different positions along the domain (1, $50D$ and $99D$ downstream). Plots in the right hand side show the *error* of the profiles compared to the inlet prescribed values calculated as $100(X - X_{inlet})/X_{inlet}$, where X_{inlet} is taken at $1D$ from the inlet. Horizontal dotted lines represent the top, hub and bottom height of the NREL-5MW reference turbine.

5.4.2.1 Fixing the top boundary condition

One of the underlying assumption for deriving the inlet profiles from Richards and Hoxey (1993), is a constant shear stress across the boundary layer. In the base case described above (*Base-ke*), a slip condition was applied at the top boundary for all fields including the momentum equation. Therefore, new boundary conditions were implemented to be consistent.

Firstly, a new boundary condition was created, named `myABLTopFixedShearStress`, to set a constant shear stress at the top wall as $\tau = \rho u_\tau^2$, where u_τ is calculated using Eq.5.5 replacing the given reference velocity U_{ref} at reference height z_{ref}. Secondly, based on the observations of the results in the *Base-ke* case, another alternative was implemented to set a constant velocity at the top boundary using Eq.5.5. This boundary condition was named `myAtmBoundaryLayerTopVelocity`. The rationale is simple, if the top velocity is kept constant, by continuity, it will avoid an acceleration near the ground and changes in the vertical velocity gradients across the domain.

Both boundary conditions were tested using exactly the same setup as in *Base-ke*, but changing the top boundary condition for U field from `slip` to either `myABLTopFixedShearStress` or `myAtmBoundaryLayerTopVelocity`. These cases are named *Base-ke-TopTau* and *Base-ke-TopU* respectively.

In Figure 5.4 a comparison between these two cases and the base case *Base-ke* is made. This time only the error profiles at $50D$ and $99D$ are shown. First of all, it is noted that both new boundary conditions improve significantly the vertical profiles of the streamwise velocity U_x across the domain except close to the ground (below hub height $z_{ref} = 90$ m) where the error reaches a maximum value of around 1.5% very close to the ground, but it is much smaller at hub height compared with the base case. k profiles reduced the error from $\sim 30\%$ to less than 10% after ~ 12.5 km. On the other hand, ε passes from being under-predicted across the top half of the domain to be over-predicted.

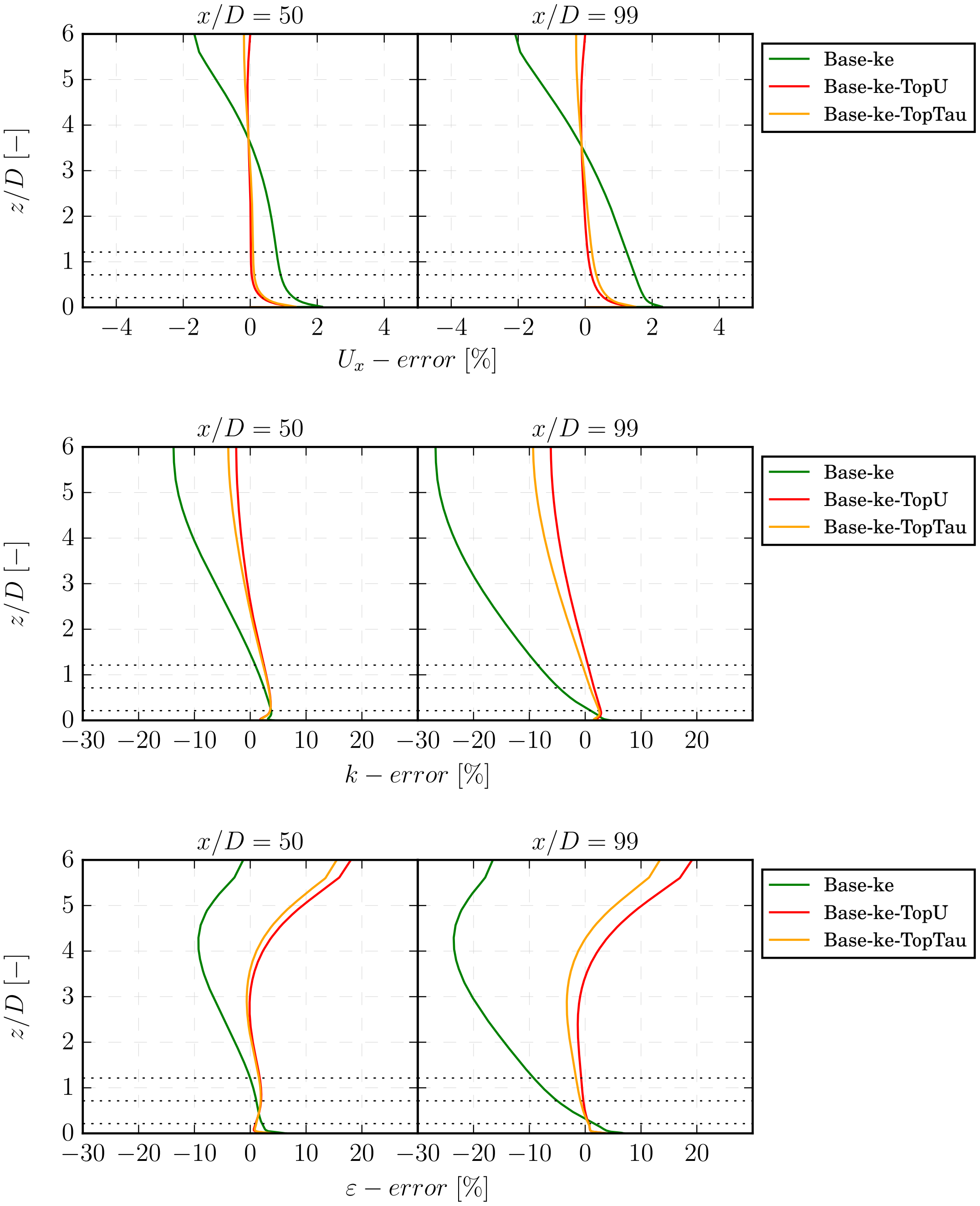

Figure 5.4: Influence of top boundary condition for momentum equation. Plots show error between vertical profiles of U_x, k and ε, at $50D$ and $99D$ downstream compared to the inlet prescribed values calculated as $100(X - X_{inlet})/X_{inlet}$, where X_{inlet} is taken at $1D$ from the inlet. Horizontal dotted lines represent the top, hub and bottom height of the NREL-5MW reference turbine.

5.4.2.2 Constraining turbulent quantities at the top boundary

The following step taken was to constraint the turbulent quantities at the top boundary. In other words, to prescribe a fixed value at the top boundary using the inlet profiles equations from Richards and Hoxey (1993). Therefore, two new boundary conditions were implemented: `myAtmBoundaryLayerTopK` and `myAtmBoundaryLayerTopEpsilon`, that calculate and set the values of k and ε at the top boundary using Eq.5.6 and Eq.5.7 respectively.

These two boundary conditions were tested using exactly the same setup as in the previous simulations (*Base-ke-TopTau* and *Base-ke-TopU*), but adding this new constrains for k and ε. These two cases are referred to as *Base-ke-TopTauke* and *Base-ke-TopUke* and their results are compared with previous cases in Figure 5.5 (at $50D$ and $99D$ downstream). The errors in k and ε were reduce below 5% across the entire domain. In addition the streamwise velocity was also improved.

5.4.2.3 Modifying ground boundary conditions

So far, improvements were achieved in reducing the streamwise gradients. Nevertheless, it is observed that the larger errors occur close to the ground, where the velocity increases compared to the values prescribed at the inlet. In addition, the turbulent kinetic energy k is also over-predicted close to the ground. As it was discussed earlier, the corrected turbulent eddy viscosity $\nu_{t,c}$ is calculated using a friction velocity based on the value of turbulent kinetic energy at the near wall cell k_P (See Eq.5.19 and Eq.5.20). Therefore, an over-prediction of k leads to incorrect values of wall shear stress, increasing the velocity gradients, and therefore the velocity magnitude close to the ground. To test this, the `nutkAtmRoughWallFunction` was modified into a new boundary condition named `myNutUAtmRoughWallFunction`, which uses the near wall cell velocity to determine the friction velocity (Eq.5.15) and y^+ in Eq.5.19.

In Figure 5.6 the effect of this new U based ν_t wall function is compared with the existing k based approach. Two cases were run using both the fixed shear stress

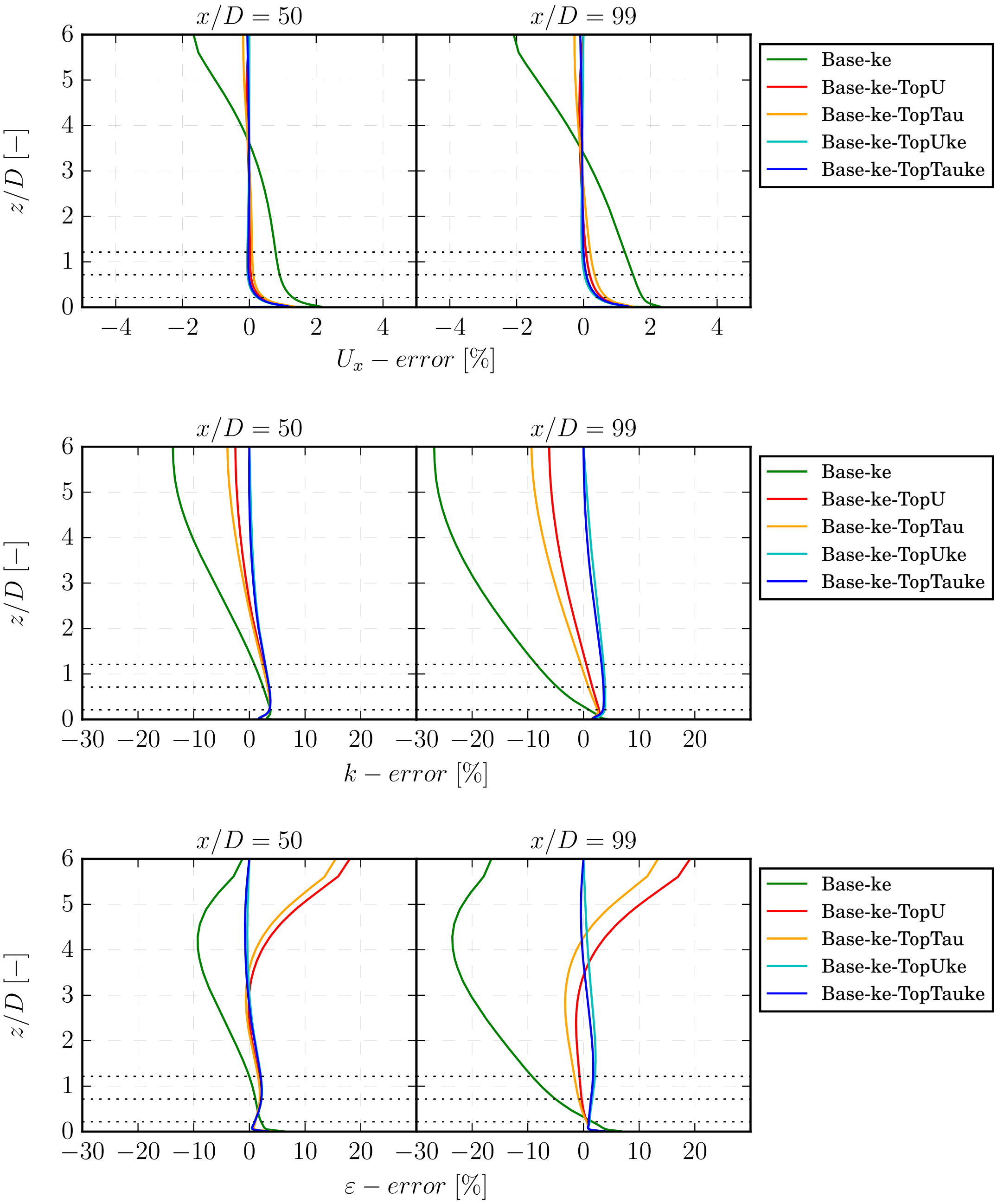

Figure 5.5: Effect of prescribing fixed values k and ε at the top boundary. Plots show the error between vertical profiles of U_x, k and ε, at $50D$ and $99D$ downstream compared to the inlet prescribed values calculated as $100(X - X_{inlet})/X_{inlet}$, where X_{inlet} is taken at $1D$ from the inlet. Horizontal dotted lines represent the top, hub and bottom height of the NREL-5MW reference turbine.

and the fixed velocity at the top boundary (*Base-ke-TopTauke-nutU* and *Base-ke-TopUke-nutU*). The only difference with the previous two cases *Base-ke-TopTauke* and *Base-ke-TopUke* is the used of `myNutUAtmRoughWallFunction` instead of the original `nutkAtmRoughWallFunction`. Note that for a better visualization, this time the plots show only the error profiles close to the ground from $z = 0$ to $z = 0.5D$. It is observed that regardless the top boundary condition used, the U based ν_t wall function reduces the errors for k and ε, however right at the wall the error profile are practically the same. Furthermore, a slight increase in the streamwise velocity error is observed, but it is considered to be too small to be significant. Overall, the U based ν_t wall function reduce the streamwise gradients across the domain and the fixed shear stress at the top boundary gives the smallest error in k at $99D$ downstream.

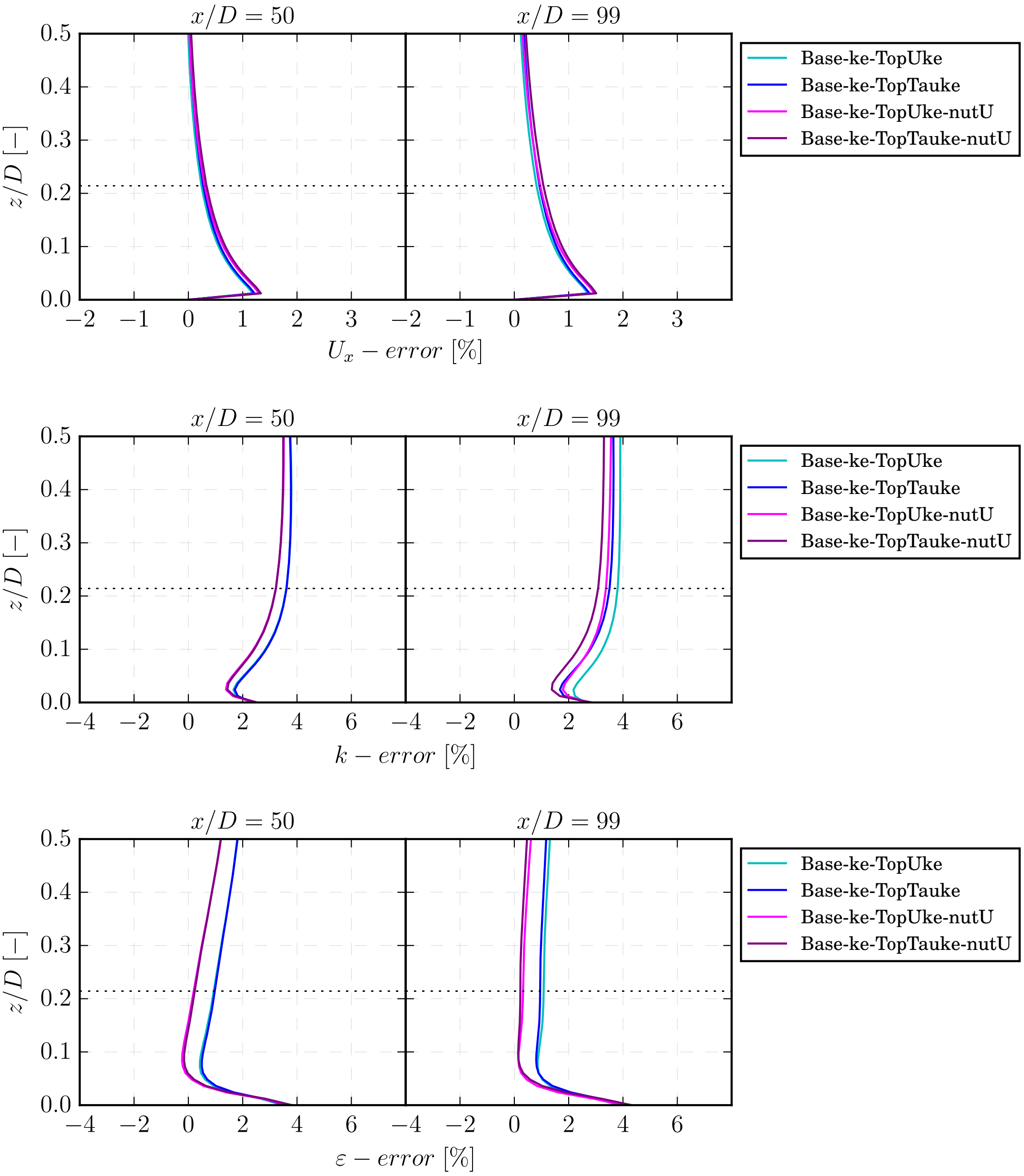

Figure 5.6: Effect of U based friction velocity to calculate the corrected eddy viscosity $\nu_{t,c}$. Plots show the error between vertical profiles of U_x, k and ε, at $50D$ and $99D$ downstream compared to the inlet prescribed values calculated as $100(X - X_{inlet})/X_{inlet}$, where X_{inlet} is taken at $1D$ from the inlet. Horizontal dotted lines represent the top, hub and bottom height of the NREL-5MW reference turbine.

5.4.3 $k - \omega - SST$ base case

As discussed in Chapter 4, the $k-\omega-SST$ model (Menter, 1993; Menter and Esch, 2001) have shown more accurate predicions of wind turbine wake velocities than the standard $k - \varepsilon$ model (Shives and Crawford, 2016; Antonini et al., 2019), and therefore it seems reasonable to test the same set of boundary conditions with the $k - \omega - SST$ model. To do this, new ω boundary conditions were implemented: `myAtmBoundaryLayerInletOmega` and `myAtmBoundaryLayerTopOmega`. The former prescribe the inlet vertical profile for ω and the latter prescribe a fixed value at the top boundary. These boundary conditions are equivalent to `atmBoundaryLayerInletEpsilon` and `myAtmBoundaryLayerTopEpsilon` that use the inflow profiles from Richards and Hoxey (1993), but using $\varepsilon = C_\mu k\omega$.

Four test cases were run. In all of them fixed values for k and ω were set at the top boundary. The first two cases, use the original `nutkAtmRoughWallFunction` formulation (k based $\nu_{t,c}$ correction), one with a fixed velocity at the top boundary (`myAtmBoundaryLayerTopVelocity`) and the other with a fixed shear stress at the top boundary (`myABLFixedShearStress`). These case were named *Base-kwsst-TopUkw* and *Base-kwsst-TopTaukw* respectively. The last two cases, correspond to exactly the same conditions, but using the U based $\nu_{t,c}$ correction `myNutUAtmRoughWallFunction`. These last two cases therefore were named *Base-kwsst-TopUkw-nutU* and *Base-kwsst-TopTaukw-nutU*.

The results are shown in Figure 5.7. It is observed that the U based $\nu_{t,c}$ correction `myNutUAtmRoughWallFunction` has a significant impact reducing the streamwise gradients of U_x, k and ω, much more significant than it was for the standard $k - \varepsilon$ model. Another difference is that the original formulation `nutkAtmRoughWallFunction` leads in this case to a decay in the turbulent kinetic energy of up to 16% close to the ground, except right at wall where k is indeed over-predicted (Not very clear in these plots). This confirms that a U based $\nu_{t,c}$ correction produce more accurate results reducing the streamwise gradients.

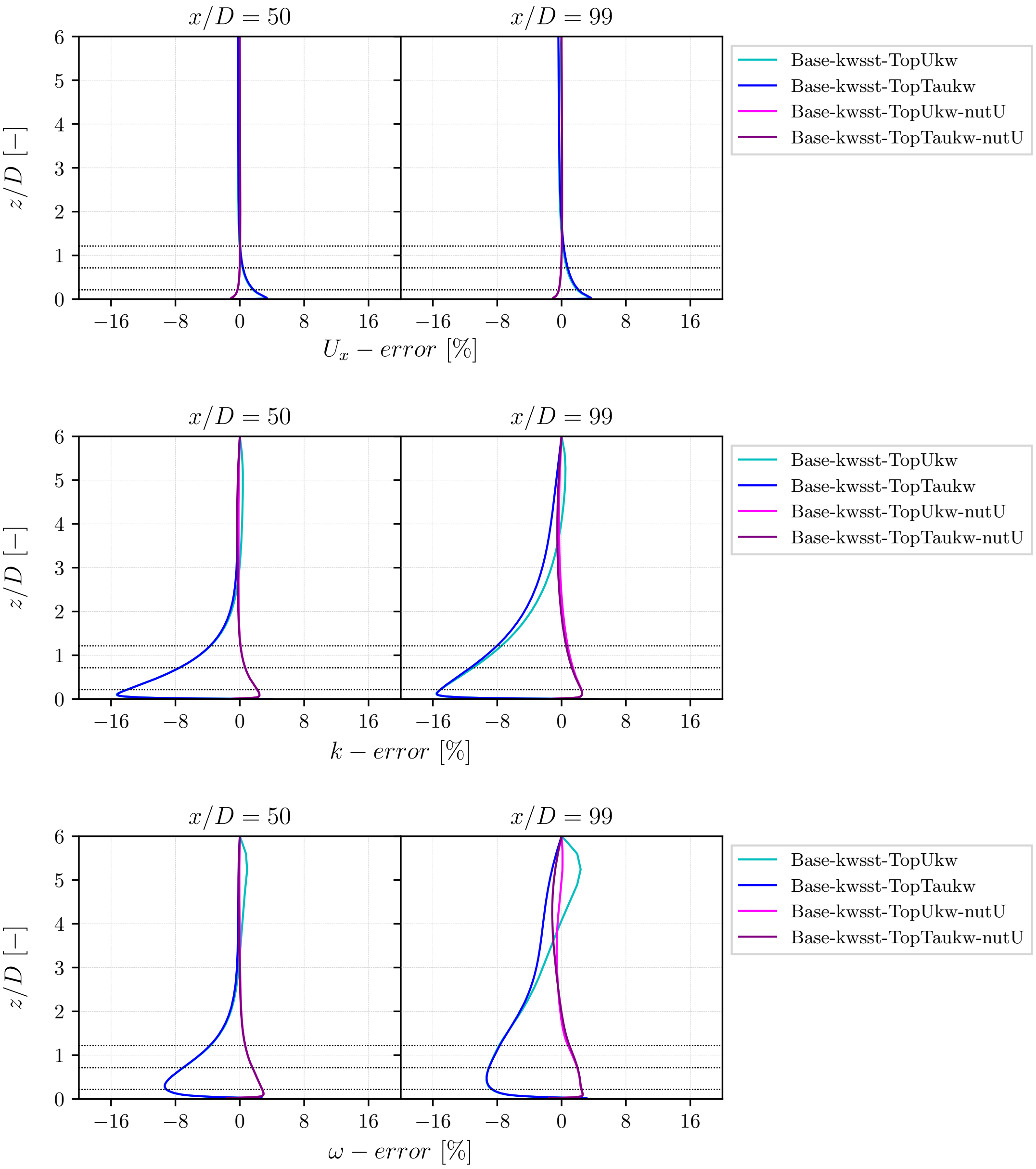

Figure 5.7: Test cases using the $k - \omega - SST$ model. Plots show the error between vertical profiles of U_x, k and ω, at $50D$ and $99D$ downstream compared to the inlet prescribed values calculated as $100(X - X_{inlet})/X_{inlet}$, where X_{inlet} is taken at $1D$ from the inlet. Horizontal dotted lines represent the top, hub and bottom height of the NREL-5MW reference turbine.

5.4.4 Summary of new BCs implemented

New boundary conditions were implemented in OpenFOAM to model a horizontally homogeneous atmospheric boundary layer under neutral stratification, reducing the streamwise gradients that arise when inconsistent boundary conditions are applied. Table 5.3 shows a list of all boundary conditions implemented. These new boundary conditions were tested with both the standard $k-\varepsilon$ and the $k-\omega-SST$ turbulence models. Streamwise gradients were significantly reduce by applying these set of boundary conditions. In particular, the U based $\nu_{t,c}$ corrections leads to significant improvements. The original implementation based on the turbulent kinetic energy at the near wall cell over-predict the wall shear stress at the wall in a positive feedback loop.

Table 5.3: New boundary conditions implemented

Boundary Condition	Details
`myAtmBoundaryLayerTopVelocity`	Fixed velocity at the top boundary (Eq.5.5)
`myABLFixedShearStress`	Fixed shear stress at the top boundary $\tau = \rho u_\tau^2$
`myAtmBoundaryLayerTopK`	Fixed turbulent kinetic energy at the top boundary (Eq.5.6)
`myAtmBoundaryLayerTopEpsilon`	Fixed turbulent dissipation rate at the top boundary (Eq.5.7)
`myAtmBoundaryLayerTopOmega`	Fixed specific turbulence dissipation at the top boundary (Eq.5.7 with $\varepsilon = C_\mu k\omega$)
`myAtmBoundaryLayerInletOmega`	Inlet profile for specific turbulence dissipation (Eq.5.7 with $\varepsilon = C_\mu k\omega$)
`myNutUAtmRoughWallFunction`	Corrected ν_t at the ground based on local velocity U_P

It has been observed a peak in turbulent kinetic energy near the ground by several authors (Blocken et al., 2007; Hargreaves and Wright, 2007; Richards and Norris, 2011). Hargreaves and Wright (2007) attributed the peak of TKE near the ground to an over-production of turbulent kinetic energy near the ground. Later, Richards and Norris (2011) pointed out that the peak in k is due to discretization errors in the P_k term, where the turbulence viscosity is taken at the cell centroid, while the velocity gradient is taken from cell face values. A more detailed explanation can be found in Norris et al. (2011), where a new discretazation approach is proposed that allows to eliminate completely the peak in the turbulent kinetic energy. With that in mind, using the U based $\nu_{t,c}$ correction improve the results. Note however, that one of the main drawbacks of this approach is that the wall shear stress becomes zero if the velocity at the near wall cell is zero (e.g. separation, impingement). This will be particularly important when modelling bluff bodies such as buildings, but not as important to model wind turbines since no such flow features are expected.

Finally, in Figure 5.8, as a summary, vertical profiles of U_x, ν_t and k are presented for both, the standard $k-\varepsilon$ and the $k-\omega-SST$ turbulence models along with the error profiles. The error in the streamwise velocity after 12.5 km is kept around 1% only close to the ground (below hub height $y_{ref} = 90$ m). The $k-\omega-SST$ shows smaller errors for ν_t and k, below 1% and 3% respectively. On the other hand, the $k-\varepsilon$ model show larger errors for ν_t at about 7%.

What is left is to test how these boundary conditions behave by changing the grid resolution and the inflow wind shear profile (U and z_0). In addition, it also important to run a test with the *SnappyMesh*, since it allows to reduce significantly the computational cost but reducing the accuracy. These aspects will be addressed in the following sections.

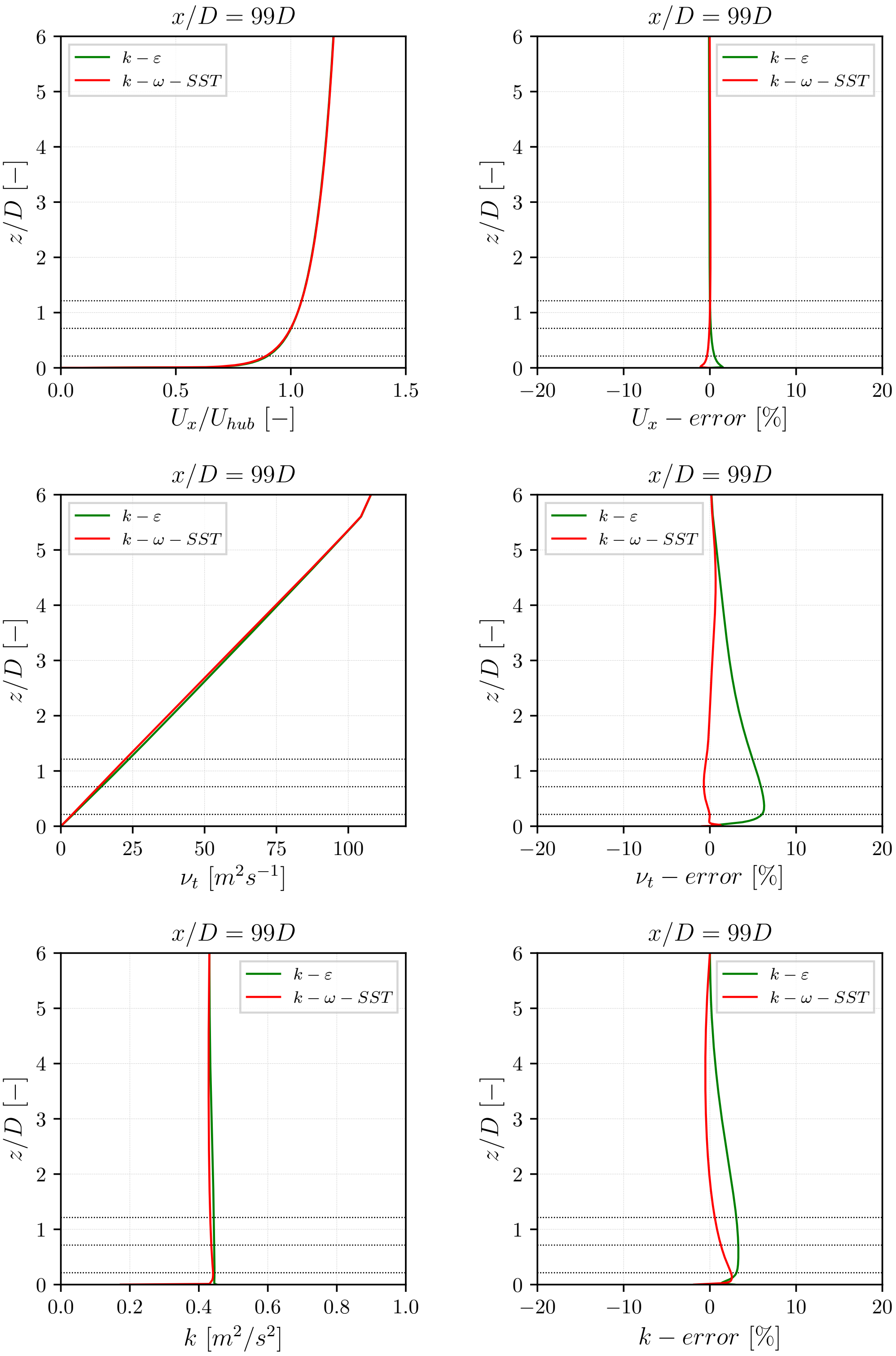

Figure 5.8: HHABL modelled with Richards and Hoxey (1993) inflow profiles and new implemented boundary conditions using both, the standard $k-\varepsilon$ model and the $k-\omega-SST$ model. Vertical profiles are shown at $99D$ downstream. Error values are calculated as $100(X - X_{inlet})/X_{inlet}$, where X_{inlet} is taken at $1D$ from the inlet.

5.5 Mesh sensitivity analysis

Mesh sensitivity was analysed by changing the near wall refinement and the horizontal resolution. All cases in this sections are run with the $k-\omega-SST$ model, using Richards and Hoxey (1993) inflow profiles, and the new implemented boundary conditions: fixed shear stress at the top for the momentum equation, fixed values for k and ω at the top boundary, and U based $\nu_{t,c}$ correction at the wall.

5.5.1 Near wall refinement

First of all, to assess the influence of the near wall refinement, three grids were used: SMX4Y1, SMX4Y2 and SMX4Y3 (See Table 5.1). The error profiles this time compare the values at $9D$ downstream with the inlet profiles at $1D$ downstream (See Figure 5.9). Using a coarser resolution near the ground reduces the maximum error, but this is spread to slightly higher altitudes. Nevertheless, the differences are not considered significant. In any case the errors are kept below 3% for k, ν_t and ω, and more importantly, below 1% for the streamwise velocity. This is particularly important considering that the near wall refinement is key to reduce the computational cost.

5.5.2 Horizontal Resolution

To analyse the influence of the horizontal resolution, four grids were used: SMX1Y1, SMX2Y1, SMX3Y1 and SMX4Y1 (See Table 5.1). Note that the grid SMX4Y1 has the same resolution as the mesh used in the base case LMX4Y1, but this time only $10D$ long. In Figure 5.10 it is noted that the horizontal mesh resolution has an almost negligible effect in the error profiles. This is not surprising, since streamwise gradients are expected to be zero, and therefore the horizontal grid resolution should not be important except for numerical errors since coarser horizontal resolution implies cells with high aspect ratio which could lead to numerical instabilities. However, it is noted that the finer grid shows the largest errors for k and ν_t. This might be explained because a finer grid also implies a larger number of cells through which numerical errors can propagate.

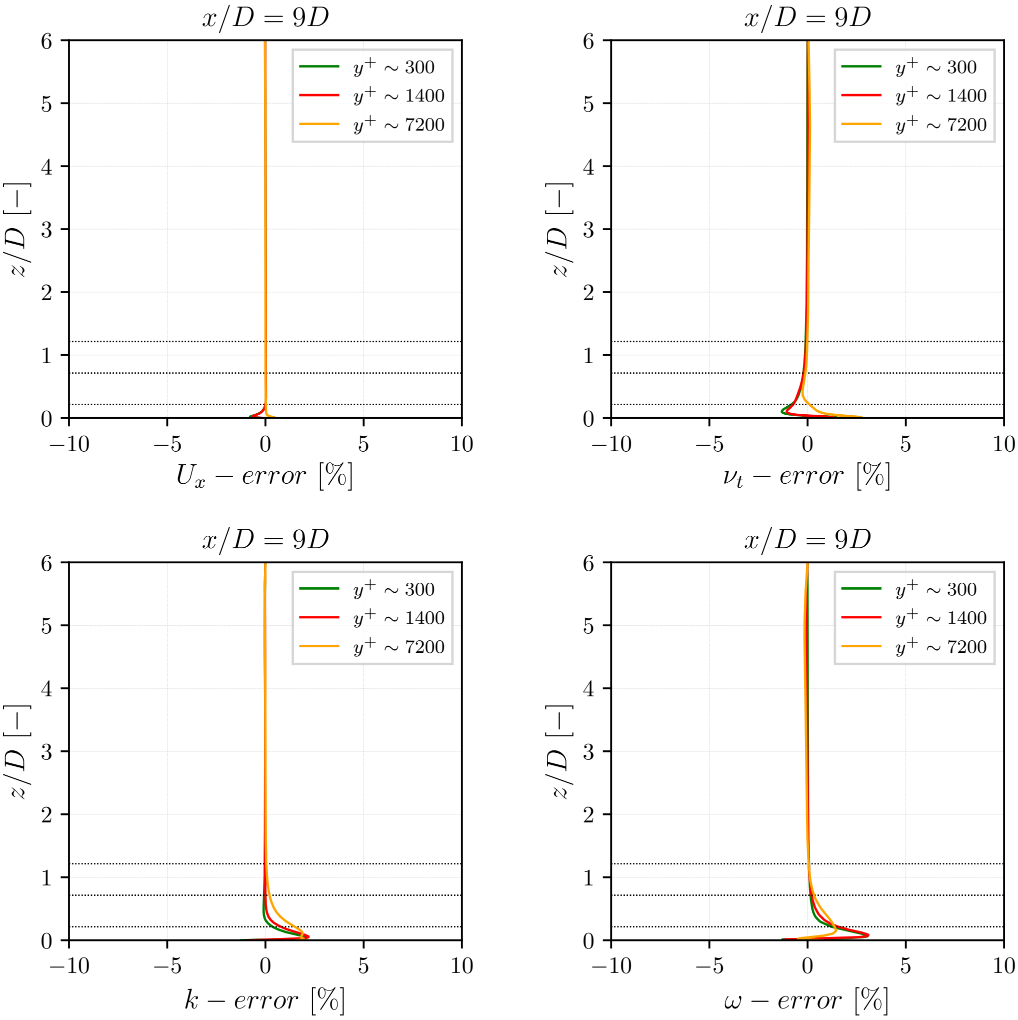

Figure 5.9: Effect of the near wall refinement in streamwise gradients. Error profiles are calculated as $100(X - X_{inlet})/X_{inlet}$, where X_{inlet} is taken at $1D$ from the inlet. Note that y^+ are slightly different to those reported in Table 5.1 that were obtained with the standard $k - \varepsilon$ model. Meshed used are SMX4Y1, SMX4Y2 and SMX4Y3 (See Table 5.1).

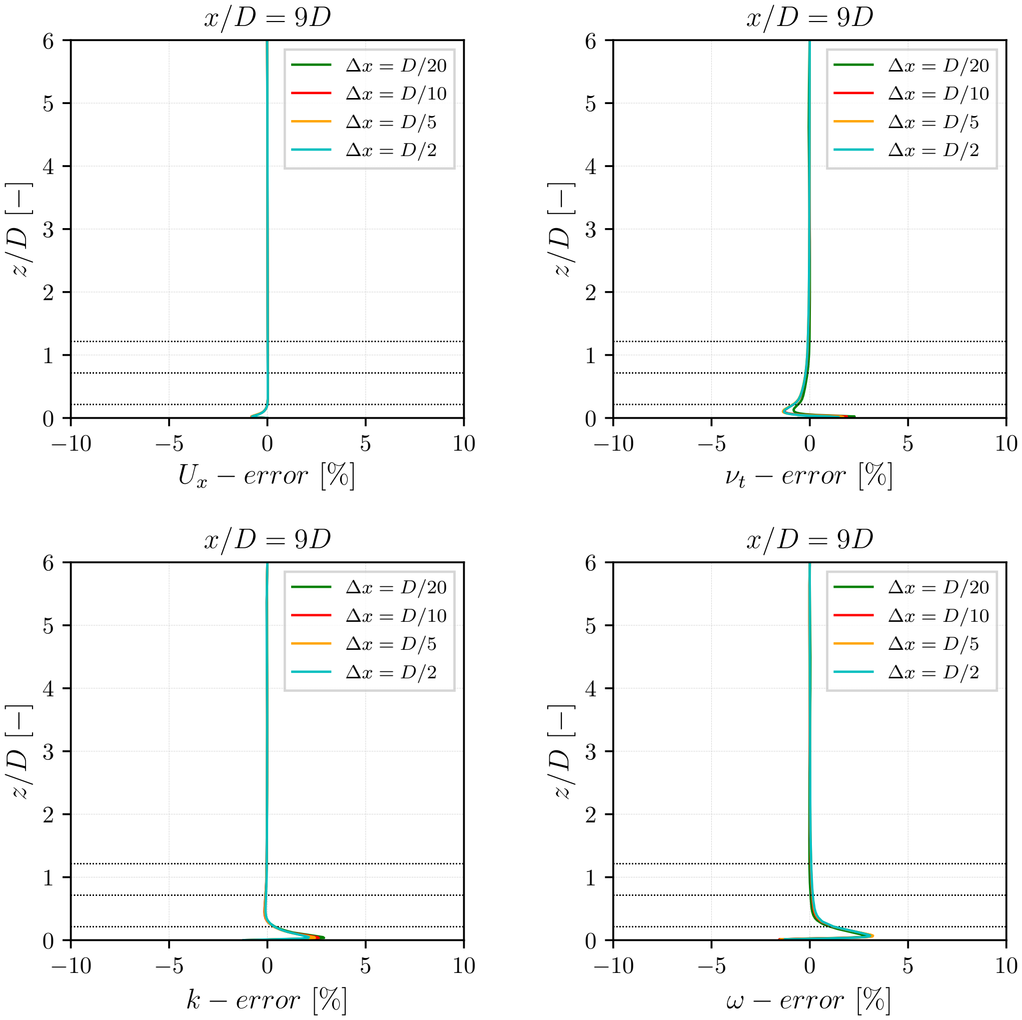

Figure 5.10: Effect of the horizontal resolution in streamwise gradients. Error profiles are calculated as $100(X - X_{inlet})/X_{inlet}$, where X_{inlet} is taken at $1D$ from the inlet. Meshes used are SMX1Y1, SMX2Y1, SMX3Y1 and SMX4Y1 (See Table 5.1).

5.6 Reference velocity and aerodynamic roughness

In this section, the boundary conditions are tested under different wind shear profiles. Thus, changing the reference velocity U_{ref} and the aerodynamic roughness z_0. In total six test cases are presented , three velocities (6, 10 and 14 m/s) for a fixed aerodynamic roughness $z_0 = 0.001$ m; and three aerodynamic roughness (0.001, 0.01 and 0.1 m) for a fixed reference velocity $U_{ref} = 10$ m/s. Reference velocities U_{ref} are given at $z_{ref} = 90$ m. All cases use a fixed shear stress at the top boundary for the momentum equation and fixed values for k and ω. At the ground, the U based $\nu_{t,c}$ correction `myNutUAtmRoughWallFunction`. Finally, the coarsest long structured mesh was used (LMX4Y3, see Table 5.1).

5.6.1 Changing the inflow reference velocity

The influence of the reference velocity is shown in Figure 5.11. As expected the dimensionless shear profile U_x/U_{hub} does not change because the roughness is kept constant. And certainly, k and ω profiles are determined by the inflow conditions from Richards and Hoxey (1993). However, the streamwise gradients (error profiles) appear to be independent of the reference velocity even after $\sim$ 12.5 km.

5.6.2 Changing the aerodynamic roughness

Finally, Figure 5.12 shows the effect of changing the aerodynamic roughness for a fixed reference velocity. The error profiles here do change, becoming larger as the aerodynamic roughness is increased, but they still smaller than roughly 3% even after $\sim$ 12.5 km. Note that typical values for aerodynamic roughness in offshore environment are as low as $z_0 = 0.0001$ m.

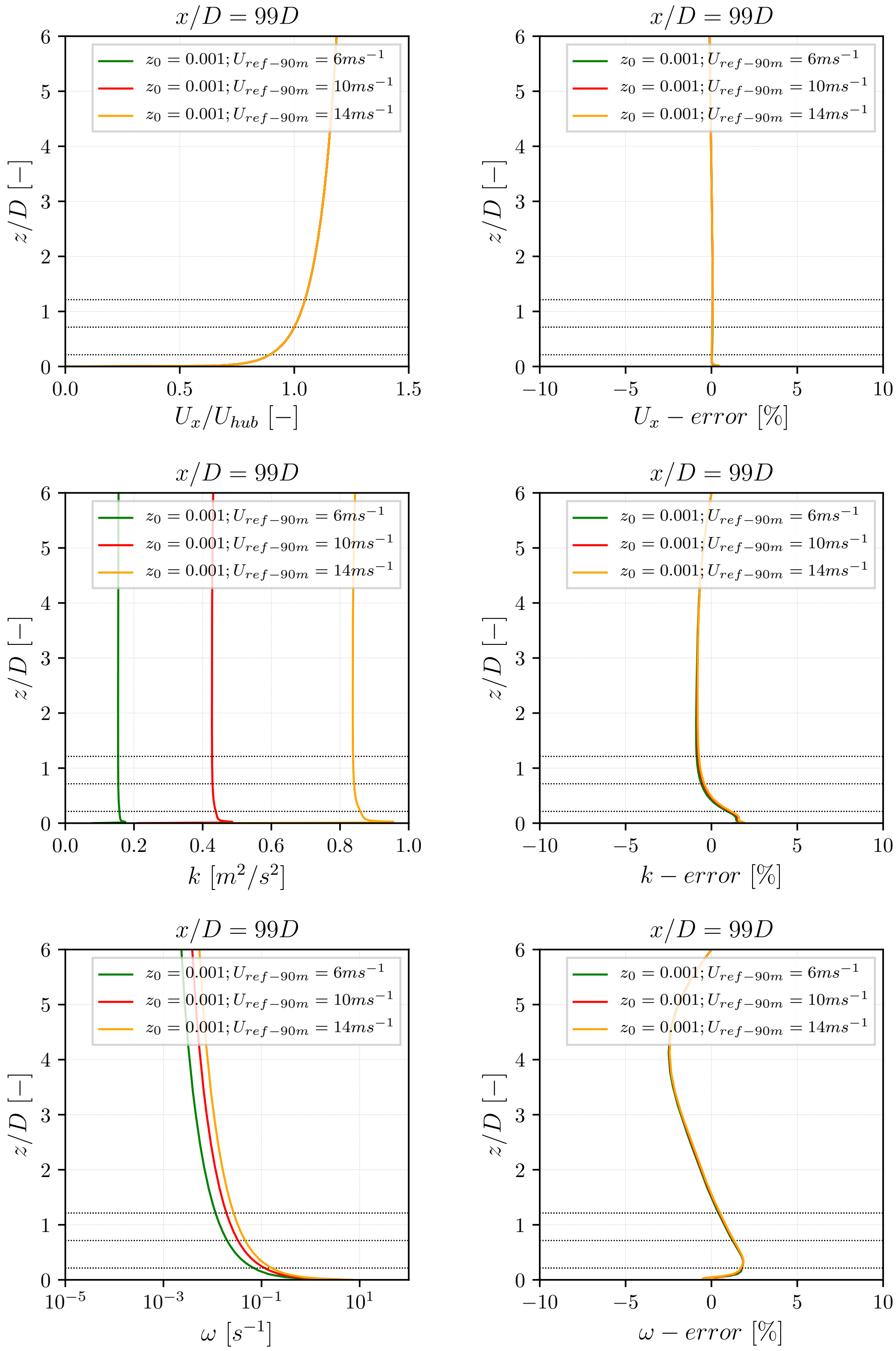

Figure 5.11: Influence of the inflow reference velocity U_{ref} (6, 10 and 14 m/s at $z_{ref} = 90$ m) keeping the same aerodynamic roughness $z_0 = 0.001$ m. Left: vertical profiles of streamwise velocity U_x, turbulent kinetic energy k and ω. Right: error comparing profiles at $99D$ downstream with those at the inlet at $1D$. The grid used is LMX4Y3 (See Table 5.1).

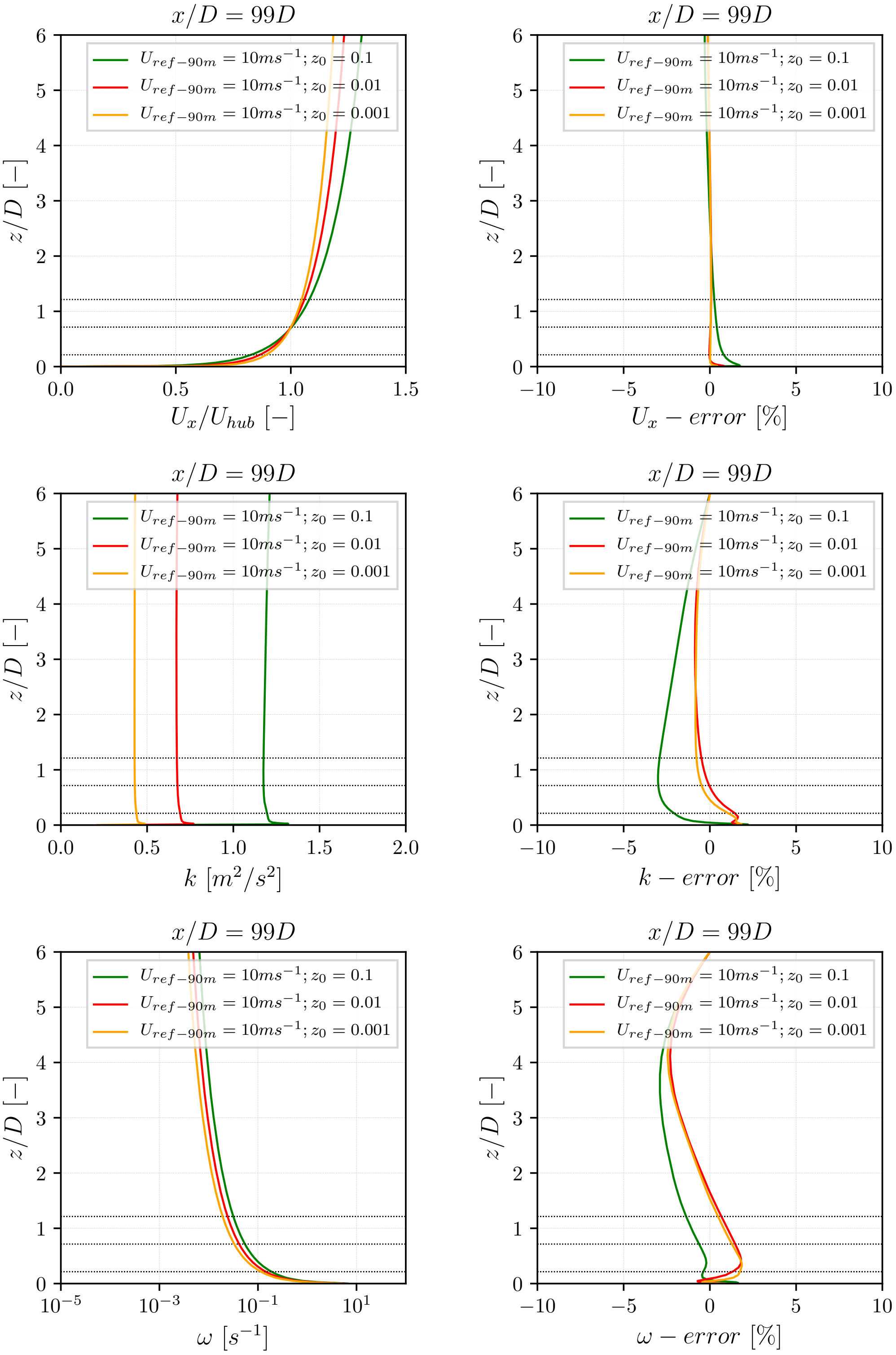

Figure 5.12: Influence of the aerodynamic roughness z_0 (0.1, 0.01 and 0.001 m) keeping the same reference velocity $U_{ref} = 10$ m/s at $z_{ref} = 90$ m. Left: vertical profiles of streamwise velocity U_x, turbulent kinetic energy k and ω. Right: error comparing profiles at $99D$ downstream with those at the inlet at $1D$. The grid used is LMX4Y3 (See Table 5.1).

5.7 Testing SnappyHexMesh grid

One of the main disadvantages of structured grids is that high refinement in the region of interest leads to refine zones where it is not needed increasing considerably the number of cells and the computational cost. It is therefore desirable to have the possibility to refine only those regions where high gradients are expected. In OpenFOAM there is a utility that permit exactly this called `snappyHexMesh`. Firstly, a coarse background mesh is generated using `blockMesh`, then the grid can be refined at specific regions or surfaces specifying the level of refinement. One level of refinements halves the cell size. For instance, if the cell size across the rotor area is required to be $D/30$, with 4 levels of refinement $(D/2)(1/2)^4 = D/32$ is achieved, if the background cell size is $D/2$. In addition, different refinement levels can be used for different regions (e.g. near and far wake regions could have different refinement). This approach allows to reduce significantly the number of cells and the computational cost, which is particularly important if one intend to model wind turbine arrays.

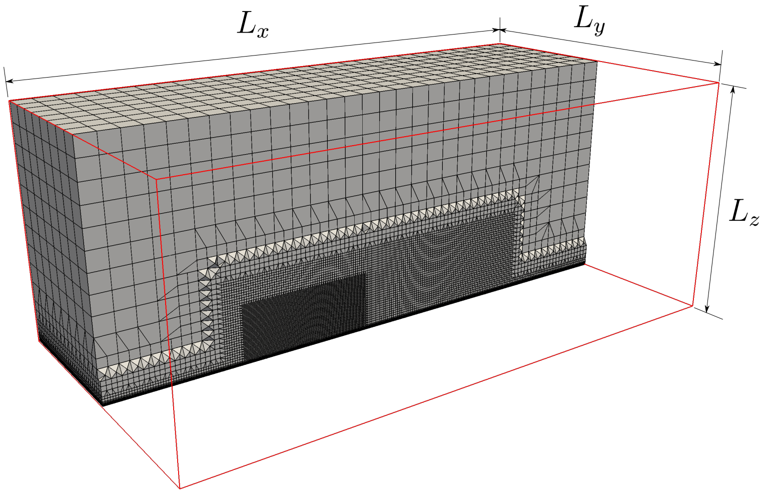

Figure 5.13: Example of *SnappyMesh* generated with `blockMesh`, `snappyHexMesh` and `extrudeMesh`.

However, it is expected that at the interfaces with different levels of refinement numerical errors are introduced reducing the accuracy. In addition, having different levels of refinement across the domain brings another another difficulty close to the ground, where a non-uniform cell height at the wall introduce additional errors when passing from a coarse cell to one that is half the size, producing spurious oscillation in the vertical profiles. One alternative to overcome this issue is to use another application named `extrudeMesh` that allows to add layers to an existing mesh by extruding a patch or surface grid. Thus, the mesh can be generated starting at a higher altitude using `blockMesh`, then refine the mesh at specific places using `snappyHexMesh`, and finally adding the layers at ground using `extrudeMesh`. An example is shown in Figure 5.13 where the total domain length is $L_x = 15D$, the width $L_y = 8D$ and the total height is $6D + \Delta z$, where Δz is thickness of the layers added at the ground. In this case, Δz was set to half the distance between the ground $z = 0$ m and the bottom of the rotor $H_{hub} - D/2$, and the number of layers was set to 10.

In Figure 5.14 a closer look at specific locations along the streamwise direction are shown. (a) shows vertical lines at which the fields are sampled to plot vertical profiles. (b) shows the mesh near the ground at position $x = 1D$ and $14D$, where sudden increase in cell size occurs between the extrude layers (purple) and different refinement levels. (c) shows a much smoother transition at the turbine rotor region at positions $x = 4D$ and $5D$ where 4 levels of refinements are used, and finally (d) shows the transition at positions $x = 8D$ and $10D$.

To assess the behaviour of the *SnappyMesh* the results are compared with those obtained in a structured mesh (LMX4Y1). Using a fixed shear stress at the top wall for the momentum equation, fixed values for k and ω at the top wall, and the U based $\nu_{t,c}$ wall function at the ground, and the $k - \omega - SST$. Figure 5.15 and Figure 5.16 show the comparison between the *SnappyMesh* and the structured mesh for vertical profiles and error profiles respectively. First of all, hardly any difference is observed from Figure 5.15. However, when looking at the error profiles in Figure 5.16, some differences become more clear. It is noted unphysical oscillations in the error values for ν_t and ω. But this seems to be related to the way the values are sampled and also how the error is calculated. The values are sampled interpolating between values at the cell centre, then in the regions with larger cells, the values sampled are not very accurate, particularly in non-linear profiles such as ω, so, when comparing these values with the more refined regions, they appear to be in disagreement. This explains why the error profile for ω at $x = 14D$ is 'smaller', because it is using the same cell size distribution as at the inlet ($1D$).

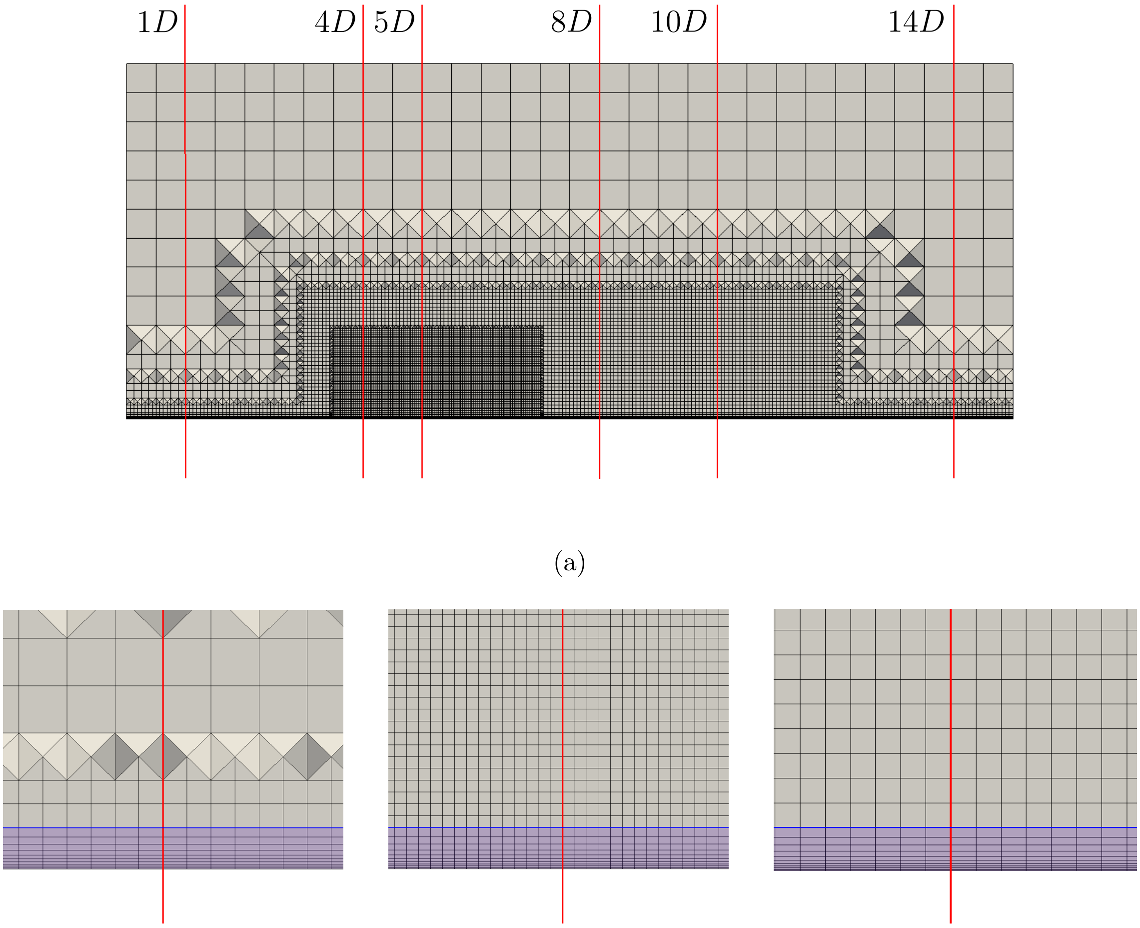

(a)

(b)

(c)

(d)

Figure 5.14: (a) Side view of *SnappyMesh* showing positions at which vertical profiles are sampled ($1D$, $4D$, $5D$, $8D$, $10D$ and $14D$). (b) Zoom in at positions $1D$ and $14D$. (c) Zoom in at positions $4D$ and $5D$. (d) Zoom in at positions $8D$ and $10D$.

Note however, that the largest errors in ν_t occur at $x = 4D$ just after the transition from the coarse to the most refine region (See Figure 5.14.(a)). This suggest that the wind turbine should be located not very close to these transitions. This is taken into account when generating meshes for wind turbine arrays.

In conclusion, the behaviour of the *SnappyMesh* is satisfactory. Streamwise gradients have been reduce significantly, particularly in the streamwise velocity where is lower than 1% after $13D$ (~ 1.6 km). Note also that the y^+ value obtained at the ground was ~ 3200.

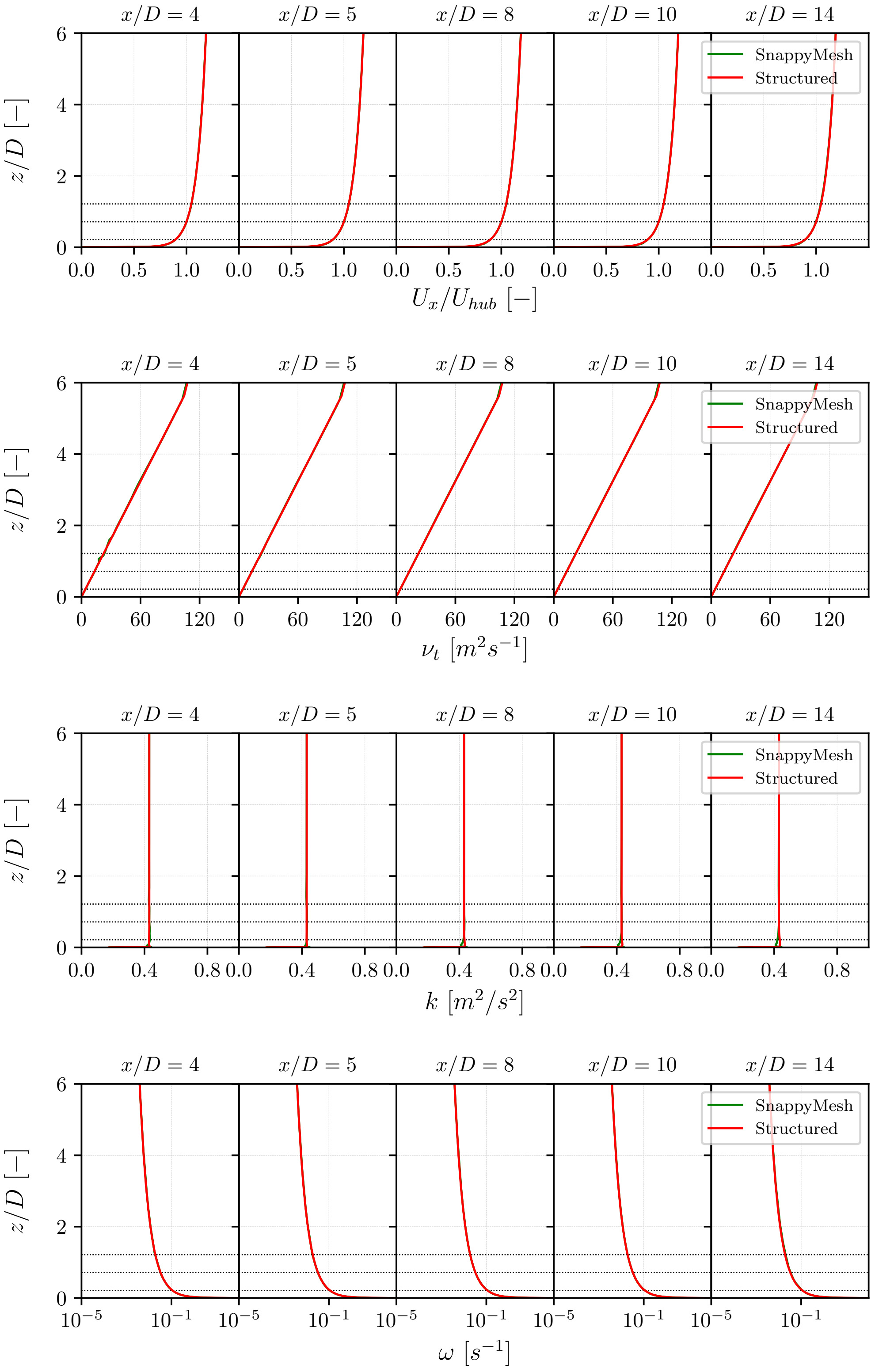

Figure 5.15: Comparison between *SnappyMesh* and structured mesh. Vertical profiles of streamwise velocity U_x, ν_t, k and ω at different positions downstream.

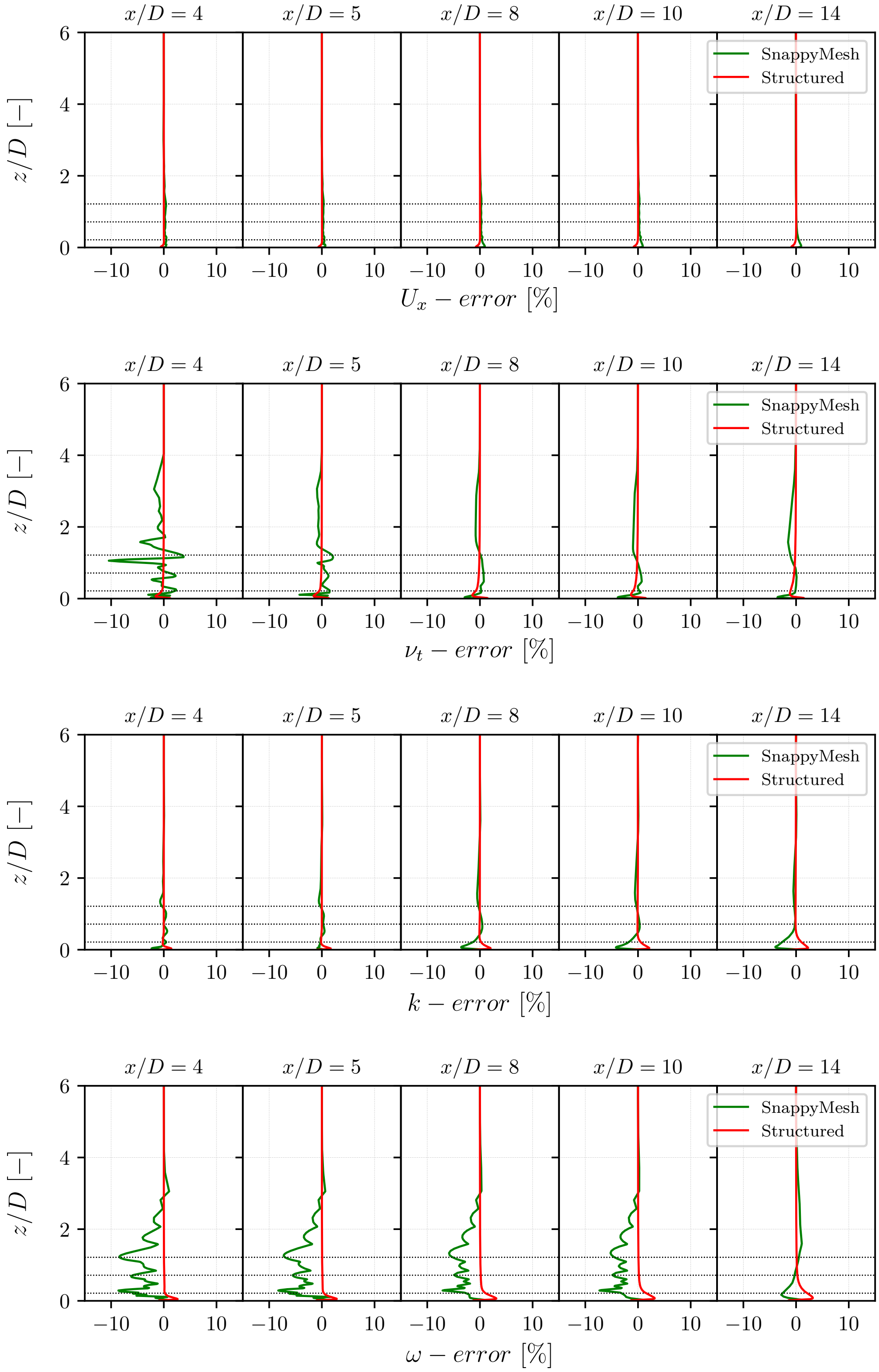

Figure 5.16: Comparison between *SnappyMesh* and structured mesh. Error profiles of streamwise velocity U_x, ν_t, k and ω at different positions downstream.

5.8 Summary and conclusions

New boundary conditions were implemented in OpenFOAM to model HHABL. The inflow profiles from Richards and Hoxey (1993) and Richards and Norris (2011) were used to define fixed value boundary condition for the velocity and turbulence quantities k, ε and ω. For the momentum equation at the top boundary two BCs were implemented, a fixed velocity and fixed shear stress. In addition, a velocity based ν_t correction wall function was implemented, which improves significantly the results. It was found that the standard library in OpenFOAM uses a k based approach to calculate the friction velocity, which results in over-prediction of the wall shear stress in a positive feedback loop. Other authors have reported peak in the turbulent kinetic energy close to the ground (Blocken et al., 2007; Hargreaves and Wright, 2007; Richards and Norris, 2011). Richards and Norris (2011) found that the peak in k occurred at the second cell from the ground, and that reason comes from the discretization of the production term of turbulent kinetic energy P_k. Norris et al. (2011) proposed an alternative discretization method that eliminates the peak in k.

These BCs have been tested with both the standard $k-\varepsilon$ and $k-\omega-SST$ model and the streamwise gradients have been reduce significantly with errors less than 1% for the velocity profiles, and less than 3% for turbulent quantities after $\sim$ 12.5 km. It has been shown that these BCs can be applied for different type of grids, and different inflow conditions, minimizing the streamwise gradients.

However, the atmospheric boundary layer model described here has some limitations. First of all the model is only valid for neutral stability conditions, and as it was discussed in Chapter 2, stability conditions play an important role in the operation and optimization of wind farms, particularly between cut-in and rated wind speeds. Secondly, the turbulence intensity decreases with height and it is not constant as considered in this simplified models. Thirdly, the model assumes that the surface layer (with constant shear) extends all the way up to the top boundary, but it is known that the surface layer height depends on stability conditions. And finally, the turbulence levels depend on the aerodynamic roughness z_0 and C_μ, meaning that to change the turbulent kinetic energy one of these two parameters should be adjusted. Unfortunately, changing C_μ requires to adjust all the other model coefficients and this is not as straightforward when using the $k - \omega - SST$ model, because these models were derived for the standard $k - \varepsilon$ model.

Chapter 6

UQ Framework - gpcADM

6.1 Introduction

A new computational framework for uncertainty quantification in CFD simulatios of wind turbines and wind farms has been created. The framework is used to propagate uncertainties efficiently through the generalised polynomial chaos system (`gpcPy`) described in Chapter 3, reducing significantly the number of deterministic evaluations required compared with other random sampling strategies. This chapter describes how the different components of this framework are integrated, along with some test cases where two turbine arrays were tested considering different input parameters as random variables.

6.2 UQ Framework - gpcADM

The framework is named `gpcADM` since it is built by the integration of `gpcPy` and the `ADM` implemented in OpenFOAM (described in Chapter 4). The atmospheric boundary layer flow is modelled as a HHABL with the appropriate boundary conditions as described in Chapter 5. `gpcADM` is essentially a set of bash and Python scripts that facilitate the pre-processing, running, and post-processing stages of the uncertainty propagation algorithm (see Figure 6.1 where separated boxes indicate each of these three stages). To outline the whole process, the five main bash scripts are described in the following sub-sections (highlighted in dark purple in the flow diagram).

6.2.1 Pre-processing

The first script is named `preGPC.sh` which uses the `gpcPy` library to create a list of quadrature points based on the gpc settings specified in `gpcDict.py`. This list of values is stored in a text file named `gpcList`. As discussed in Chapter 3, the number of quadrature points depends on the order of the expansion chosen. This decision should be based on the shape of the response surface, which is nonetheless generally unknown, and it relies on the user experience with the physical system being analysed. Alternatively, it is possible to construct several gPC expansions increasing the order p and check the convergence of truncation error (see Section 3.3.3) as it will be observed in the test cases in the following sections.

The second script, called `setCase.sh`, it is probably the most interesting one since it is where all the openfoam cases are generated, one for each quadrature point. To understand how the CFD cases are generated, it should be noted that `OpenFOAM` is essentially a very specialized `C++` library where a single OpenFOAM case consist of a single directory containing all the settings needed within text file dictionaries (e.g. models, transport properties, boundary conditions, solver settings, etc), and where all the solution fields are stored after the solver converges. As such, one OpenFOAM case directory should be created for each quadrature point needed in the polynomial chaos expansion. For instance, in a bivariate gPC case with 7 quadrature points in each random variable, a total of 49 OpenFOAM case directories should be created. To this end, a base OpenFOAM case named `./baseCase/` is made, which contains all the specifications that are common for all 49 simulations. This includes the ADM model settings such as the turbine geometry, the airfoil data, the operating conditions, smearing parameter ϵ and tip corrections; as well as the ABL model setting that specify the inflow conditions, such as the aerodynamic roughness z_0 and reference velocity U_{ref} and the reference height z_{ref}. Note that sometimes,

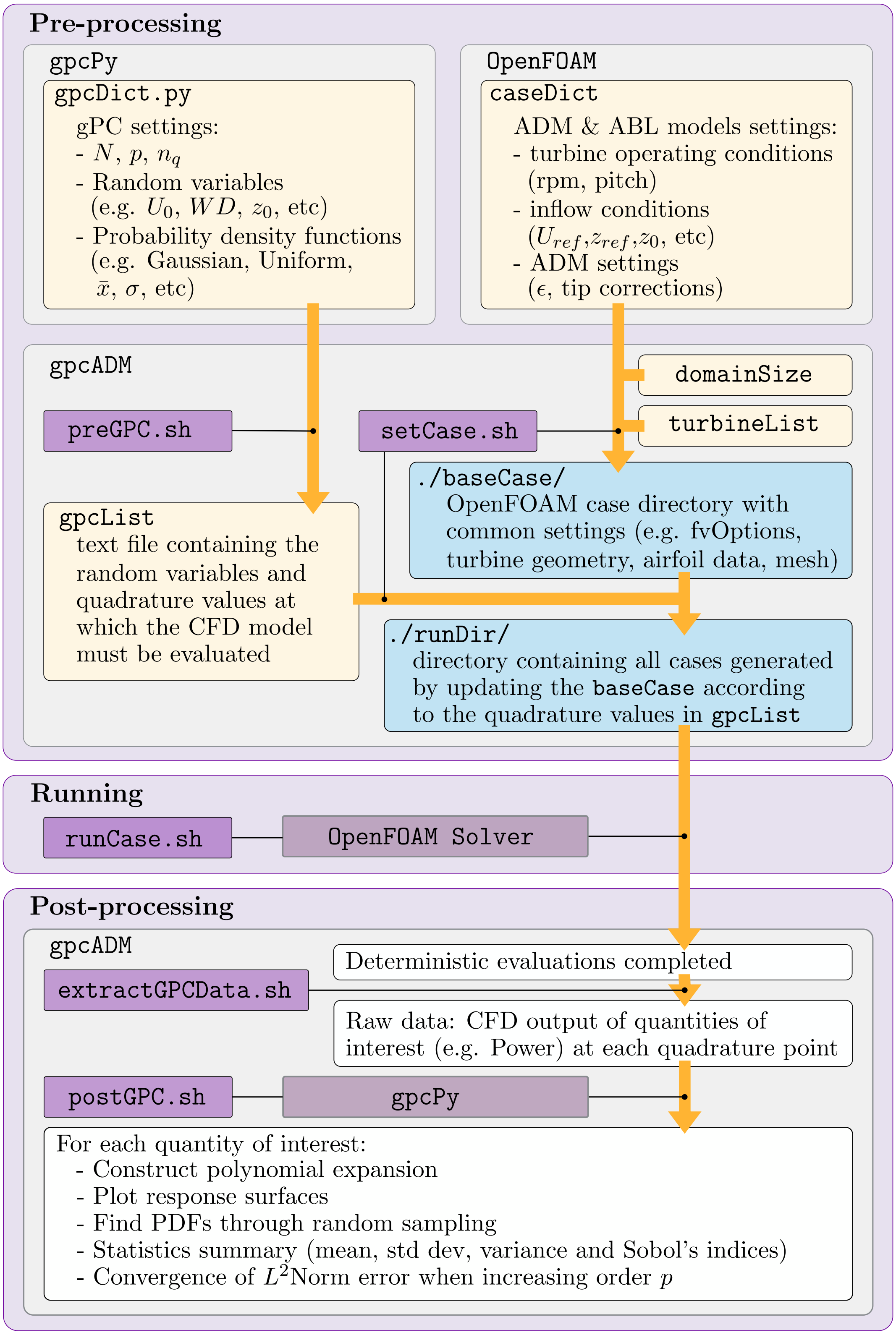

Figure 6.1: Flow diagram showing how `gpcADM` works.

the change in one parameter requires to modify more than a single entry in the OpenFOAM dictionaries. For example, changing the wind direction also requires changing what patches should be considered as inlets or outlets. Therefore, updating the OpenFOAM dictionaries needs an specific implementation (coding) for each parameter that needs to be treated as a random variable, so that every revelant entry is updated accordingly. This is not hard to do, because `gpcADM` contain also some Python scripts that help updating each OpenFOAM dictionary, which were coded to be as general as possible, so more model parameters could be added in the future. Nonetheless, this does require some time, particularly to verify that the code is working properly.

The mesh is also common to all cases, and it is generated using `blockMesh`, `snappyHexMesh` and `extrudeMesh` (OpenFOAM utilities, see also Section 5.7) based on the inputs given in two additional files: `domainSize` and `turbineList`. The `domainSize` file is used to set the overall dimensions of the domain (length, width and height) and set the location of the origin of the (X, Y) cartesian system where by default the first turbine is located. The second file, `turbineList`, is just a list of all the turbines in the array with their corresponding name and (X, Y) coordinate location. Therefore, `setCase.sh` will use this information to construct the mesh and, in particular, it will use `snappyHexMesh` to refine the mesh at the turbines locations. The refinement can be adjusted within the Python script that updated the OpenFOAM dictionary. Note also that, when running in parallel, the domain decomposition is done within the `./baseCase/` using the OpenFOAM `decomposePar` utility.

Once the `./baseCase/` has been created, `setCase.sh` proceeds to generate all the OpenFOAM cases as a copy of the base case and updating the parameters considered as random variables in the OpenFOAM dictionaries according to the values specified in `gpcList`. Since the mesh is the same for all cases, a symbolic link is used as a reference to the mesh location (i.e. the `polyMesh` directory in `./baseCase/`) avoiding duplication of large files and minimizing the storage needed. All the openfoam cases generated are stored in nested directories within the `./runDir/` directory. The nested directories contain as many levels as random variables are used facilitating the coding to access individual cases. With this, the *Pre-processing* stage is finished, and one single OpenFOAM case for each quadrature point in the random space has been created, and it is ready to run.

6.2.2 Running

The third script, `runCase.sh`, is in charge of running the simulations through the OpenFOAM solver. The simulations in this work were performed on the Computational Shared Facility (CSF3) from The University of Manchester. Thus, `runCase.sh` is a CSF job script that uses `job-arrays` to run all cases assigning a task-ID for each quadrature point. Each simulation was run in parallel with 4 cores, which showed to be the most efficient number of cores following a scaling test performed. Note that a small number of cores also reduces the waiting time in the queue for the jobs to find available nodes. In the next section some test cases examples are presented.

6.2.3 Post-processing

Once all the simulations are completed, the `Post-processing` stage starts by running the fourth script named `extractGPCData.sh` which goes through all cases directories and reads the output of the quantities of interest being analysed. All these raw data is organised and exported in text files to be used later to construct the polynomial expansions with the last script called `postGPC.sh`. This last script uses the `gpcPy` library to build the gPC expansion using the Non-Intrusive Spectral Projection and the CFD outputs. With the polynomial expansions created, `postGPC.sh` plots the response surfaces, finds the probability density functions using random sampling (1 million samples are used), and determines the main statistical parameters (i.e. mean, standard deviation, variance and Sobol's indices).

6.3 Test Cases Description

A series of bivariate gPC test cases have been performed for different turbine arrays, varying the order of the polynomial expansion p, the number of quadrature points n_q, and using different input parameters as random variables: the wind speed at hub height U_0, the wind direction WD and the aerodynamic roughness z_0. For simplicity, in this section a description of the different settings of the gpc cases is given, and in the following section the results will be presented and discussed.

6.3.1 Turbine arrays tested

Two small turbine arrays are presented here named $A1$ and $A3$ (See Figure 6.2 and Figure 6.3). The reference turbine NREL-5MW (Jonkman et al., 2009) is used for the simulations. This is a 126 m rotor diameter with a hub height of 90 m. Array $A1$ consists in three turbines (named $T1$, $T2$ and $T3$) fully aligned with a spacing of $7D$ between them with a domain size of $L_x = 26D$ by $L_y = 12D$ (along the streamwise and spanwise directions respectively), and with a total height $L_z = 6D$. On the other hand, Array $A3$ resembles a sub-set of four turbines (named $T1$, $T2$, $T3$ and $T4$) from a grid like pattern of turbines, similar to the ones one might expect in large wind farm arrays. Array $A3$ considers an special situation where turbines $T1$ and $T4$ are completely aligned along the $x-$axis, where a non-symmetric influence from turbines $T2$ and $T3$ is expected in the performance of $T4$. The domain size is $L_x = 27D$ by $L_y = 16D$, with a total height of $L_z = 6D$.

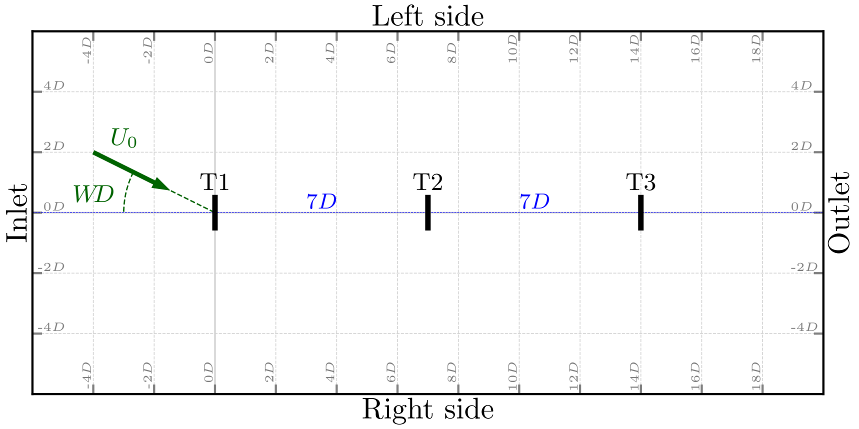

Figure 6.2: Three turbines aligned with spacing = 7D. NREL-5MW Reference Turbine is used. This array is named $A1$.

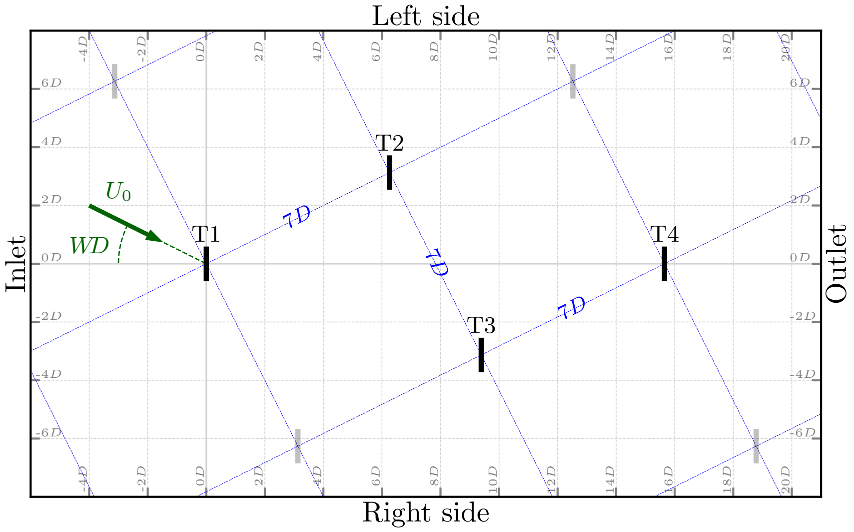

Figure 6.3: Sub-set of four turbines from a grid like pattern with uniform spacing of 7D. NREL-5MW Reference Turbine is used. This array is named $A3$.

6.3.2 Computational meshes

The computational meshes were generated using a set of OpenFOAM utilities such as `blockMesh`, `snappyHexMesh` and `extrudeMesh`. The process starts with `blockMesh` by creating a coarse uniform structured grid based on the domain size specified in a text file named `domainSize`. The dimensiones are paremeterized in terms of the turbine diameter D, so that different turbines sizes can be used. Then, `snappyHexMesh` refines the grid around the turbine locations and near the ground. To this end, the `turbineList` should specify the name and coordinates (X, Y) of each turbine. The refinement is done gradually from the coarse background mesh, by dividing each cell in 8 cells in each level. At the rotor and near wake zones the cell size is $\Delta x = D/32$. Based on the mesh sensitivity analysis from Appendix D, for the ADM implemented, 30 cells per rotor diameter are needed for accurate predictions. Finally, `extrudeMesh` is used at the ground to have uniform cell heights by adding layers decreasing in size. This was found to be more accurate when using wall functions to solve the atmospheric boundary layer model (See Section 5.7 from Chapter 5).

Figure 6.4 shows the details of the mesh around the rotor and close to the ground.

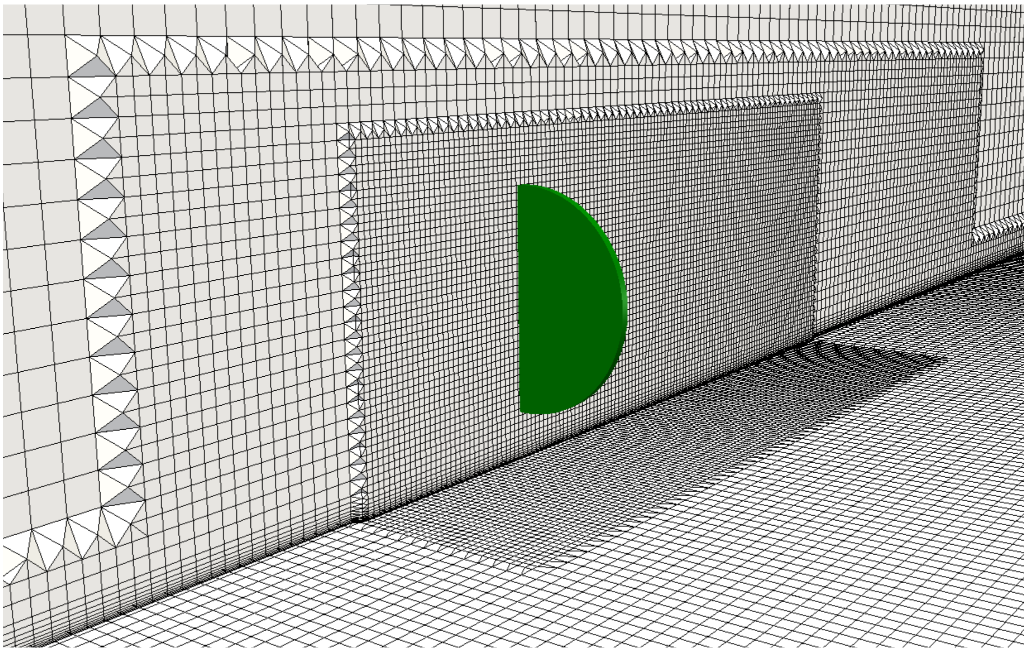

Figure 6.4: Mesh details around the rotor and close to the ground. Green disk represents the location of the turbine.

The finest region goes from $1D$ upstream to $3D$ downsteam, with $3D$ in the spanwise direction, and it extends $0.25D$ above the rotor. This is repeated at each turbine position resulting in the grids used for array $A1$ and $A3$ shown in Figure 6.5 and Figure 6.6 respectively.

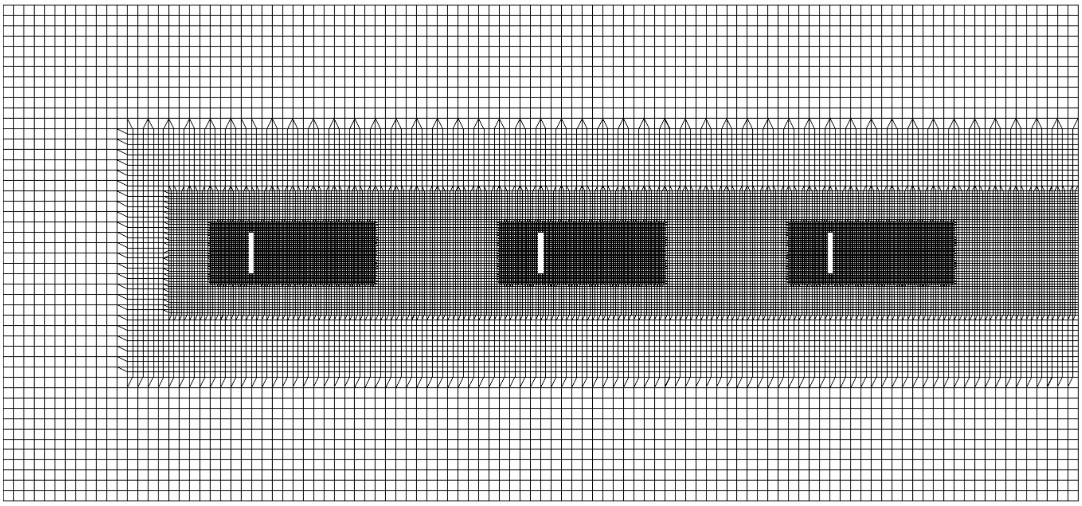

Figure 6.5: Section of computational grid of array $A1$ showing mesh refinement (section made at $z = 138$ m for more clarity)

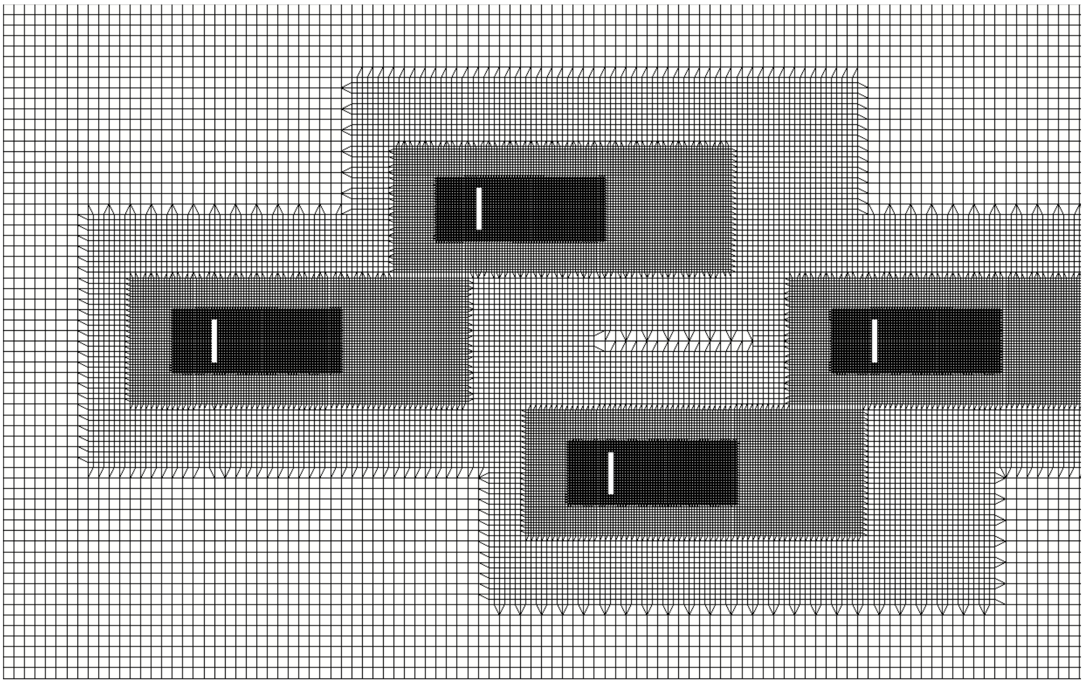

Figure 6.6: Section of computational grid of array $A3$ showing mesh refinement (section made at $z = 138$ m for more clarity)

6.3.3 Random Variables and Operating Conditions

Three input parameters are considered as random variables: the wind speed at hub height U_0, the wind direction WD and the aerodynamic roughness z_0. The wind speed and aerodynamic roughness are input parameters of the neutral atmospheric boundary layer model described in Chapter 5. Note that in this model, z_0 controls the turbulence intensity that is considered uniform across the inlet. Similarly, the wind direction is also assumed constant at the inlet.

In this work, it is assumed that the random variables follow a gaussian probability density function. Table 6.1 shows the mean values $\bar{x}$, the standard deviation σ as well as the random space of possible outcomes (this interval is truncated to $\bar{x} \pm 3\sigma$).

In all cases, the turbine is operated below rated capacity, with a mean wind speed of 8 m/s, at 9.21 rpm and with blade pitch angle of 0° (as in Troldborg et al. (2015); Tossas and Leonardi (2013); Martinez et al. (2016)). The mean wind direction is set to 0° (measured respect to the $x-$axis) with a standard deviation of $\sigma = 3°$. The mean aerodynamic roughness is set to 0.0055 m with a standard deviation of 0.0015 m resulting in an interval that goes from [0.001,0.01]. These values are somewhat arbitrary, but are considered reasonable to test the capabilities of the `gpcADM` framework.

Table 6.1: Random Variables. Three random variables are used in this chapter, the wind speed U_0 and the wind direction WD. However, gpc cases are bivariate and only two of these parameters are used each time. It is assumed that each variable follows a gaussian distribution.

Parameter	$U0$ [m/s]	WD [°]	[2]$z0$ [m]
Mean value ($\bar{x}$)	8	0	0.0055
Standard Deviation (σ)	0.167	3	0.0015
$\bar{x} \pm 3\sigma$[1]	[7.5, 8.5]	$[-9, 9]$	$[0.001, 0.01]$

[1] Note that the random space is truncated to $\pm 3\sigma$.

[2] The aerodynamic roughness z_0 also controls the turbulence intensity TI in the ABL model used, where $k = u_\tau^2/\sqrt{C_\mu}$, $u_\tau = U_{ref}\kappa/\ln((z_{ref} + z_0)/z_0)$, and $TI \approx \sqrt{2k/3}/U_{ref}$. Thus, for $z_0 \in [0.001, 0.01]$, $TI \in [5.35\%, 6.71\%]$ ($U_{ref} = 8$ m/s and $z_{ref} = 90$ m)

6.3.4 gPC Settings

Table 6.2 shows the settings used for the polynomial expansions used. Note that the gPC cases analysed here are bivariate. This means that only two parameters are considered as random variables at a time (N=2), while the third parameter takes a fixed value. Thus, when U_0 and WD are used as random variables, z_0 is set to 0.001 m; and when z_0 and WD are used, U_0 takes its mean value of 8 m/s.

Power and thrust are the quantities of interest for which a polynomial expansion is to be determined. Since the response of such quantities is unknown a priori, the gPC expansion are constructed increasing the polynomial order (i.e. $p = 1, 3, 5, 7$ and 9). In each case, the number of quadrature points is set to $n_q = p + 1$ for each random variable. As a result, the number of CFD simulations start at 4 with $p = 1$ and end with 144 when $p = 11$, resulting in a total of 364 simulation for each series of cases.

Finally, even though it is assumed a Gaussian distribution for the input random variables, Legendre polynomial are used to construct the polynomial expansions since after a few test it was found that they were better at capturing the response surfaces within a truncated random space. The reason for this has to do with the fact that the Gaussian distribution is unbounded and therefore the quadrature points used by the polynomial expansion, when using Hermite polynomial, are also unbounded and in some cases end up outside the truncated random space defined. This not only does not bring any relevant information for the construction of the polynomial expansion, but also may lead to unexpected behaviour of the CFD solver if the input random variables are allowed to take values far outside their truncated intervals.

Table 6.2: gPC settings.

Parameter	Settings
Number of random variables N	2
Quantities of interest	Power,Thrust
Order of polynomial expansion p	$1, 3, 5, 7, 9, 11$
Number of quadrature points $n_q = p + 1$	$2, 4, 6, 8, 10, 12$
Number of simulations n_q^N	$4, 16, 36, 64, 100, 144$
Orthogonal Polynomials	Legendre

[1] Note that in each gpc case series a total of 364 deterministic RANS simulations were performed.

6.3.5 Test Cases Nomenclature

A nomenclature was defined to clearly identify the test cases analysed. All the gPC cases are named with a series of letters as *gPC-AA-F-XXYY*, where AA indicates the turbine array tested ($A1$ or $A3$), F the polynomial family used to construct the gPC expansions(L for Legendre, and H for Hermite), and $XXYY$ the two parameters considered as random variables. For instance, *gPC-A1-L-U0WD* correspond to a gpc case using the turbine array $A1$, with Legendre polynomials L, where U_0 and WD are considered as random variables.

In total, four gpc series are presented in this chapter.The results will be presented in the following sections.

- gPC-A1-L-U0WD
- gPC-A1-L-z0WD
- gPC-A3-L-U0WD
- gPC-A3-L-z0WD

6.4 Results and discussion

6.4.1 Test 1: gPC-A1-L-U0WD

In this gPC series, the array $A1$ is tested with the wind speed at hub height U_0 and wind direction WD as random variables as described in Section 6.3.3.

6.4.1.1 Response Surfaces

The response surfaces for Power and Thrust are shown in Figure 6.7 and Figure 6.8 respectively. In total 9 response surfaces are presented as contour plots with isolines, 3 for each turbine (from left to right) with 3 values of polynomial order $p = 3, 7$ and 11 (from top to bottom).

First of all, note that the overall shape of the response surfaces of Power and Thrust are very similar between them, and therefore the qualitative observations made here are valid in both cases. Turbine $T1$ is in the free stream flow and as such its response is predominantly dependent on the wind speed U_0 (along the $x-$axis). In this case no significant difference is observed when increasing p meaning that 4 quadrature points in each direction are enough to capture the response of Power and Thrust of $T1$ (16 simulations).

However, for turbines $T2$ and $T3$ operating in the wake, the wind direction WD also becomes dominant resulting in a more interesting response surface. For these two turbines, 4 quadrature point are not enough to reproduce the response of the system leading to an over-prediction of power and thrust across the random space. Increasing the polynomial order to $p = 7$ leads to a much more accurate representation with only minor differences respect to the higher order expansion with $p = 11$.

Finally, from these contour plots it is also noticed that the response surfaces are not symmetric respect to the wind direction, which is a known characteristic of a rotating wind turbine wake in a sheared flow.

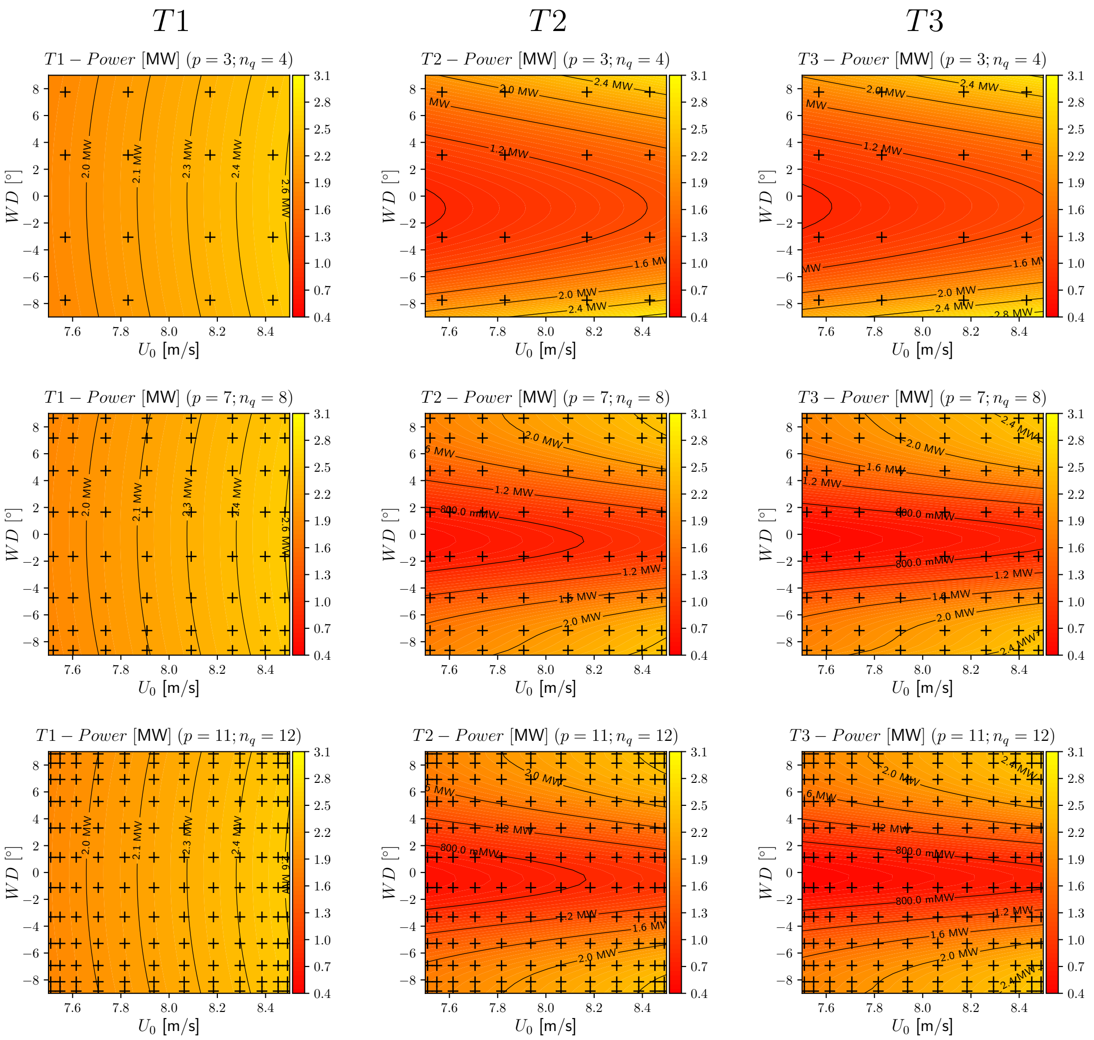

Figure 6.7: Response surfaces of **Power** at each turbine of array $A1$ ($T1$,$T2$ and $T3$ from left to right) increasing polynomial order $p = 3$,7 and 11 from top to bottom (Note: expansions with order $p = 1$,5 and 9 are not shown). The black cross symbols (+) indicate deterministic evaluations.

6.4.1.2 Probability density functions

Polynomial chaos allows to provide a probability density function for any quantity of interest instead of a single value as it is traditionally done in CFD. This is done by random sampling and as described in Section 6.2.3, in this particular case 1 million samples are taken randomly using the Gaussian distribution from the input random variables. Figure 6.9 shows the PDFs for both Power and Thrust, for each turbine, and with increasing order p. As noted before, for turbine $T1$ an expansion with order $p = 3$ is enough to capture its PDFs, while $T2$ and $T3$ require at least $p = 7$ (64 simulations). Smaller values lead to an overprediction of the power and thrust.

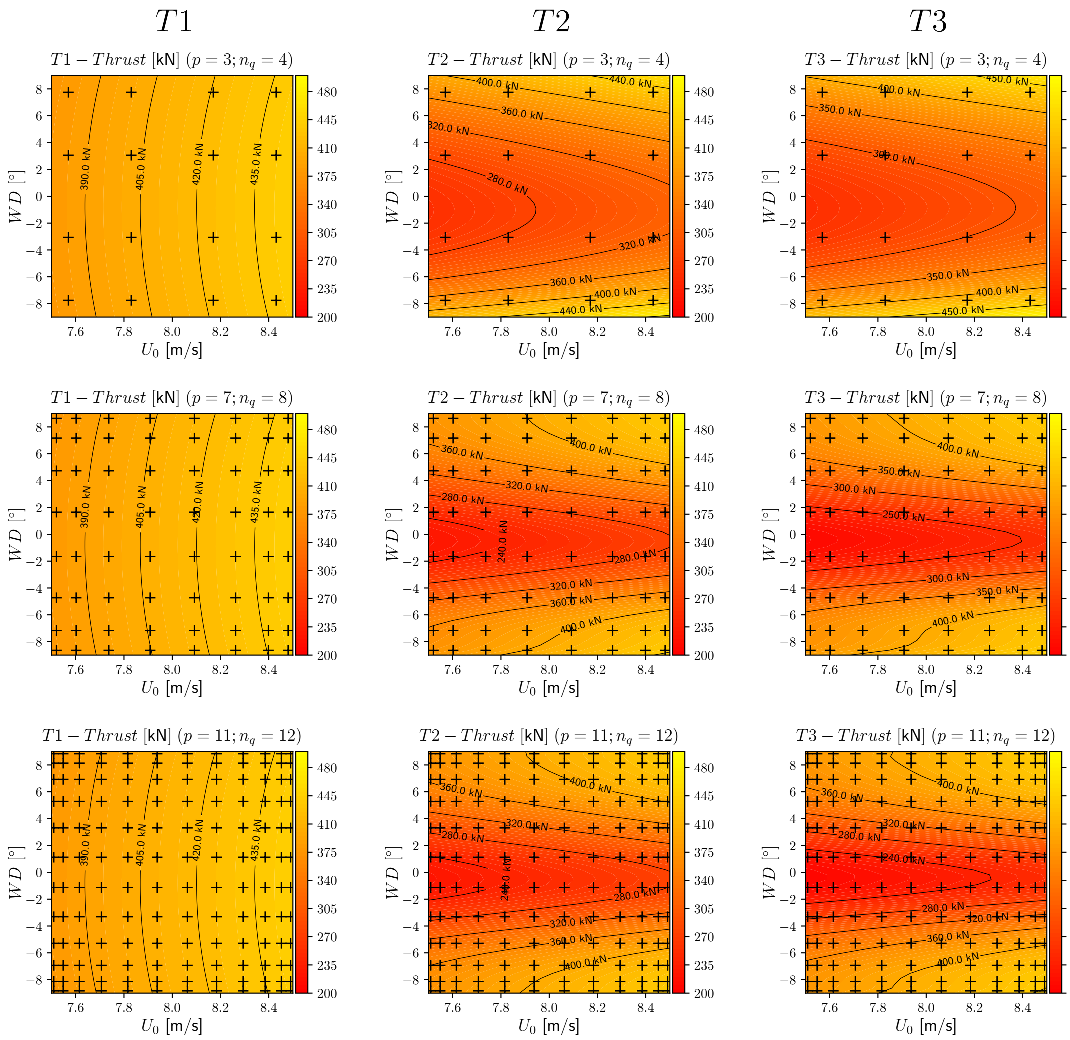

Figure 6.8: Response surface of **Thrust** at each turbine ($T1$,$T2$ and $T3$ from left to right) increasing polynomial order (p = 3,7 and 11 from top to bottom (Note: expansions with order p = 1,5 and 9 are not shown). The black cross symbols (+) indicate deterministic evaluations.

However, using order $p = 5$ gives a relatively good approximation of the PDF, since in this case only 36 simulations are needed, reducing considerably the computational cost.

6.4.1.3 L^2 Norm error

Figure 6.10 shows another perspective of the convergence observed in the PDFs above. Here is plotted the L^2 Norm error for each turbine (See Section 3.3.3 from Chapter 3), for both Power and Thrust, and with increasing order p. At turbine $T1$ the error is relatively low even with order $p = 1$ due to the rather smooth

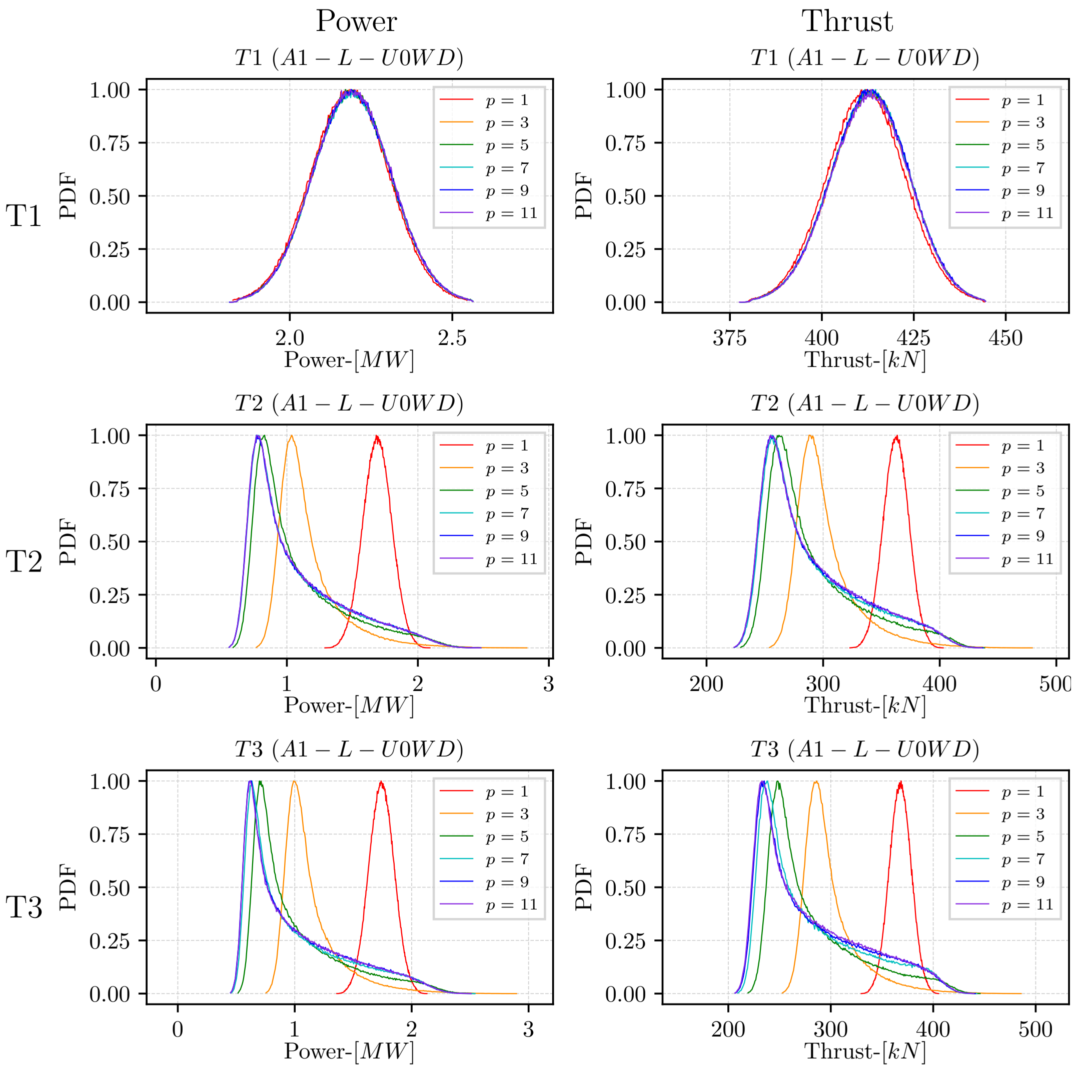

Figure 6.9: Probability density functions for **Power** (left) and **Thrust** (right) at each turbine ($T1$,$T2$ and $T3$ from top to bottom) increasing order $p = 1, 3, 5, 7, 9, 11$.

shape of the response surface that is well approximated by a plane. For turbines $T2$ and $T3$, it appears that the responses have not fully converged yet, but looking at the probability density functions it is considered that more quadrature points will increase the cost with no much difference in the output statistics.

6.4.1.4 Statistics summary

Finally, Table 6.3 summarizes the main statistical parameters such as the mean, variance, standard deviation and Sobol's indices calculated as described in Section 3.3.4 from Chapter 3. All the values are computed using the gPC expansion with the highest order $p = 11$. For $T1$ the sobols indices indicate that wind direction

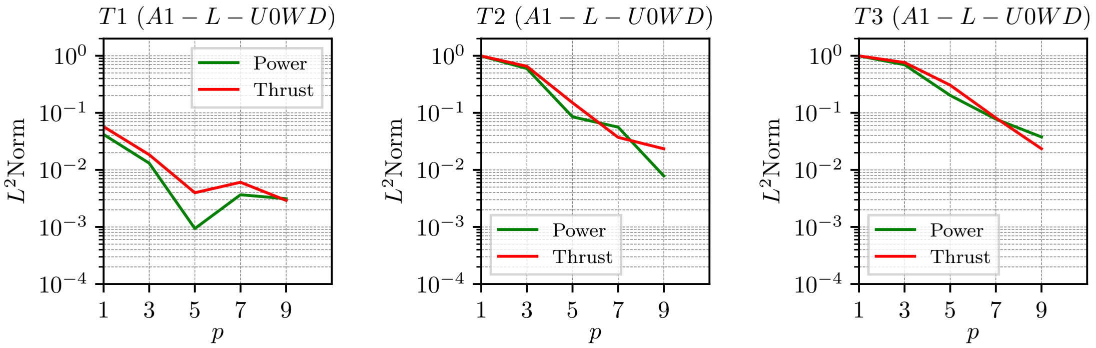

Figure 6.10: Convergence of L^2Norm for **Power** and **Thrust** at each turbine ($T1$,$T2$ and $T3$ from left to right) increasing polynomial order $p = 1, 3, 5, 7, 9$. Variance with $p = 11$ is used as reference.

WD has a very limited contribution to the total variability, while at $T2$ and $T3$ is more significant than wind speed. Note that a gPC expansion for the $Total$ power and thrust were constructed (not shown in above figures), and their statistics added in the table.

Table 6.3: Summary of statistical parameters for gpc case series gPC-A1-L-U0WD.

Turbine	[1]QOI	Mean $\bar{x}$	Variance σ^2	Std. dev. σ	S_{U_0}	S_{WD}	$S_{U_0,WD}$
$T1$	Power [MW]	2.185	$4.342e-2$	$2.084e-01$	$9.966e-01$	$3.364e-03$	$3.818e-05$
	Thrust [kN]	411.945	$3.393e+2$	$1.842e+01$	$9.954e-01$	$4.533e-03$	$1.955e-05$
$T2$	Power [MW]	1.481	$2.674e-1$	$5.171e-01$	$1.032e-01$	$8.926e-01$	$4.195e-03$
	Thrust [kN]	336.573	$3.375e+3$	$5.810e+01$	$9.229e-02$	$9.074e-01$	$3.379e-04$
$T3$	Power [MW]	1.471	$3.356e-1$	$5.793e-01$	$7.509e-02$	$9.193e-01$	$5.640e-03$
	Thrust [kN]	334.167	$4.372e+3$	$6.612e+01$	$6.395e-02$	$9.351e-01$	$9.293e-04$
$Total$	Power [MW]	5.137	$1.356e+0$	$1.164e+00$	$2.095e-01$	$7.862e-01$	$4.243e-03$
	Thrust [MN]	1.083	$1.675e-2$	$1.294e-01$	$1.662e-01$	$8.333e-01$	$5.469e-04$

[1] QOI = Quantity of interest (Power or Thrust).

6.4.2 Test 2: gPC-A1-L-z0WD

The second test case analysed is practically the same as the first one, but using the aerodynamic roughness z_0 instead of the wind speed U_0 as a random variable.

6.4.2.1 Response surfaces

This time only the response surfaces for Power are shown (See Figure 6.11) since, as in the previous case, the Thrust response surfaces are qualitatevly speaking very similar and the observations made here are valid in both cases.

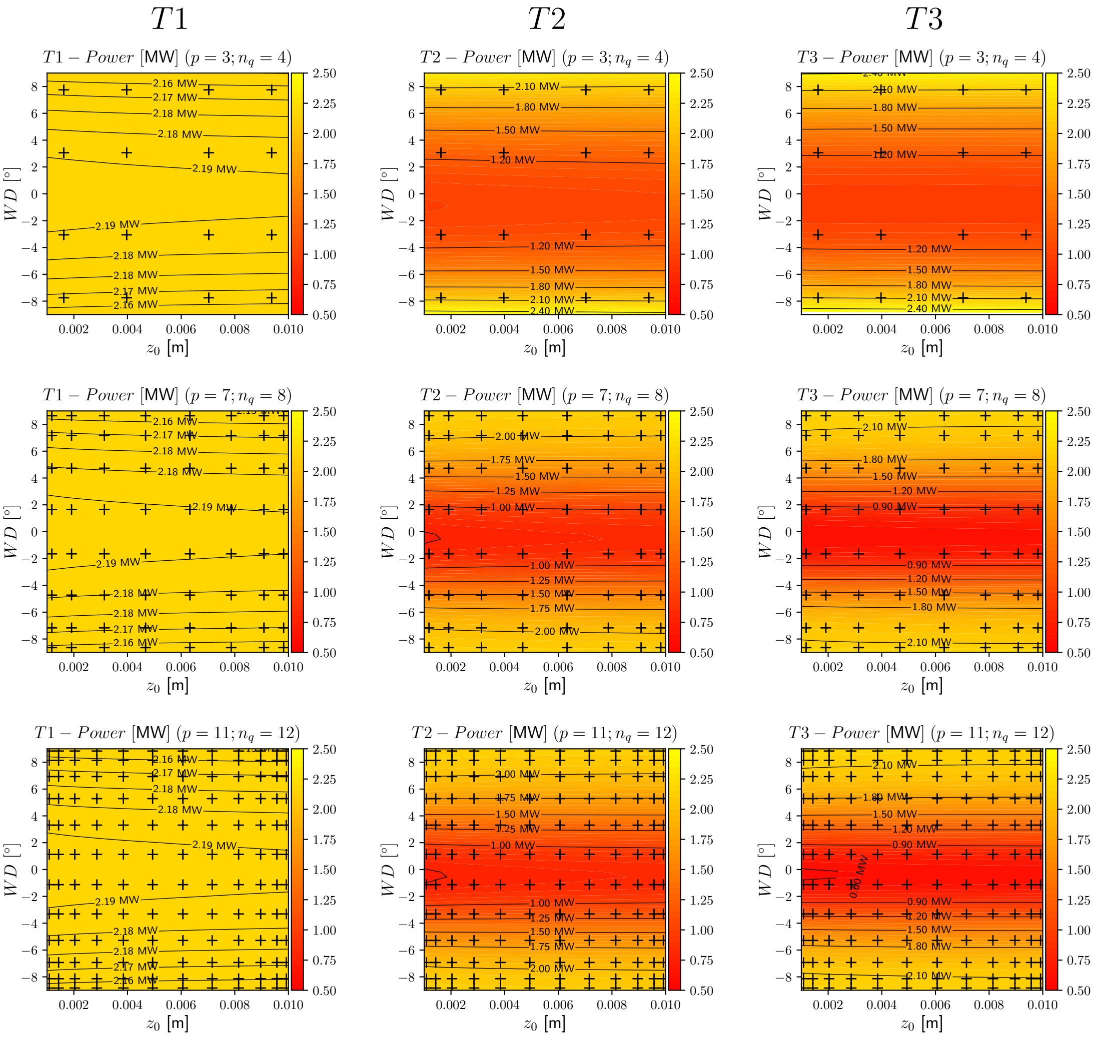

Figure 6.11: Response surface of **Power** at each turbine ($T1$,$T2$ and $T3$ from left to right) increasing polynomial order (p = 3,7 and 11 from top to bottom, Note that expansions with order p = 1,5 and 9 are not shown). The black cross symbols (+) indicate deterministic evaluations.

The first observation is that wind direction WD has a stronger impact compared to the aerodynamic roughness z_0. This is expected, particularly in turbines $T2$ and $T3$ operating in the wake that is strongly dependent on wind direction. Nevertheless, at turbine $T1$ operating in the free stream flow it is observed the effect of the aerodynamic roughness, lower values of z_0 (smoother ground/sea surfaces) result in slightly higher power and thrust for a fixed hub height wind speed. High roughness leads to an increased shear, and for a fixed hub height wind speed, the lower velocities below reduce the total power and thrust. Note that by the shape of the isolines at $T1$, this effect is more significant whit zero yaw misalignment, and becomes negligible in the wake where the wind profile in no longer logarithmic. Here, it is also possible to see that the response is not symmetric respect to the wind direction. Finally, four quadrature points seem to be enough to capture the responses at turbine $T1$, whilst at least 8 are needed for $T2$ and $T3$.

6.4.2.2 Probability density functions

Figure 6.12 shows the PDFs obtained by random sampling of the polynomial chaos expansions. As before, 8 quadrature points ($p = 7$) is good enough capturing the PDFs for turbines $T2$ and $T3$, and only 4 ($p = 3$) for $T1$. This time the PDFs have a sharp spike corresponding to the value at the center of the random space in the response surfaces, the yellow zone for $T1$ and the red zone for $T2$ and $T3$. Note that using an insufficient number of quadrature points leads to an under-prediction of power and thrust for $T1$, while these would be over-predicted for $T2$ and $T3$.

6.4.2.3 L^2 Norm error

Figure 6.13 shows the convergence of the expansion by increasing p. For turbines $T1$ and $T2$ the values seem to reach a plateau between $p = 7$ and $p = 9$ showing good convergence, while for $T3$ it seems that additional quadrature points could improve accuracy. Again, this might be not necessary considering the additional computational cost required.

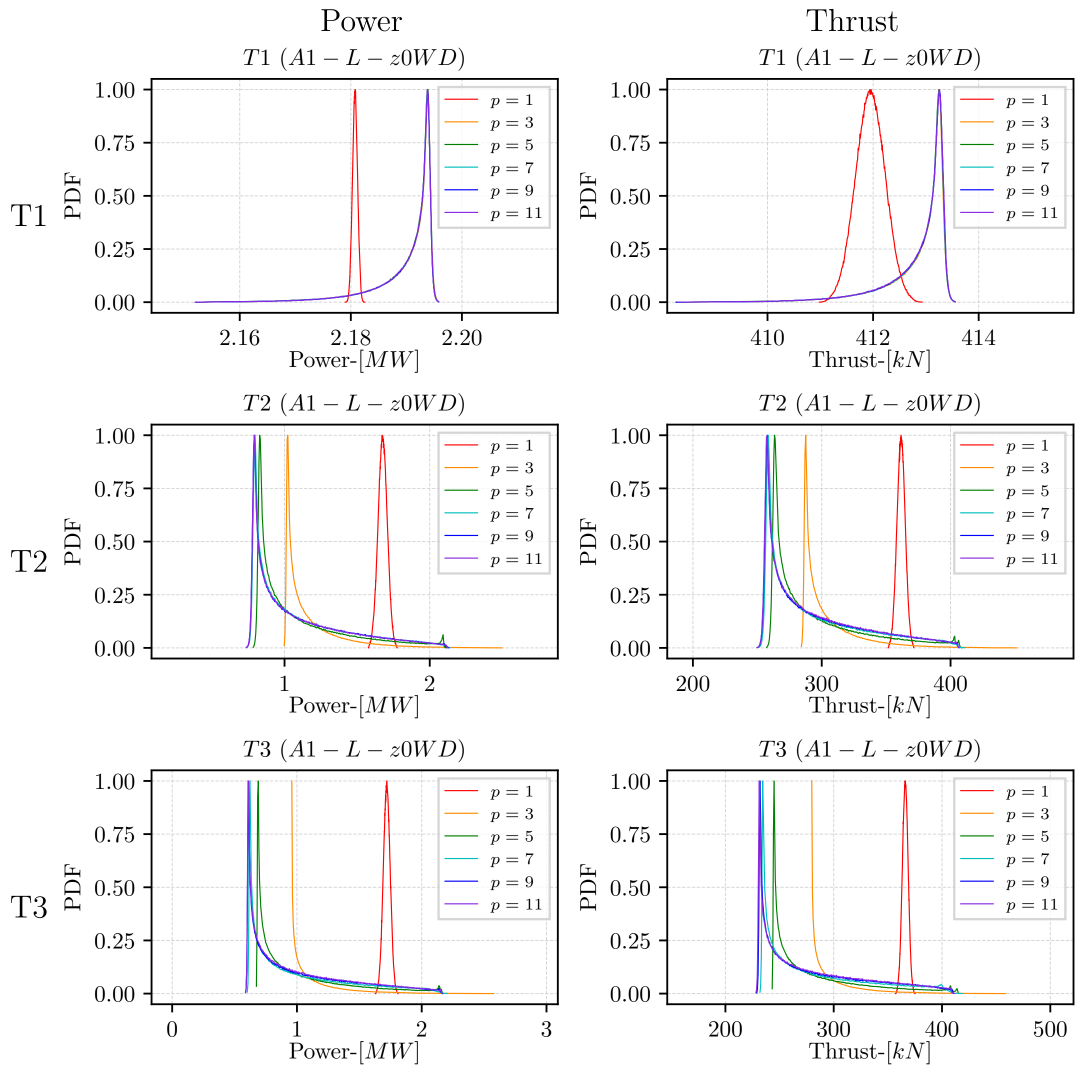

Figure 6.12: Probability density functions for **Power** (left) and **Thrust** (right) at each turbine ($T1$,$T2$ and $T3$ from top to bottom) increasing order $p = 1, 3, 5, 7, 9, 11$.

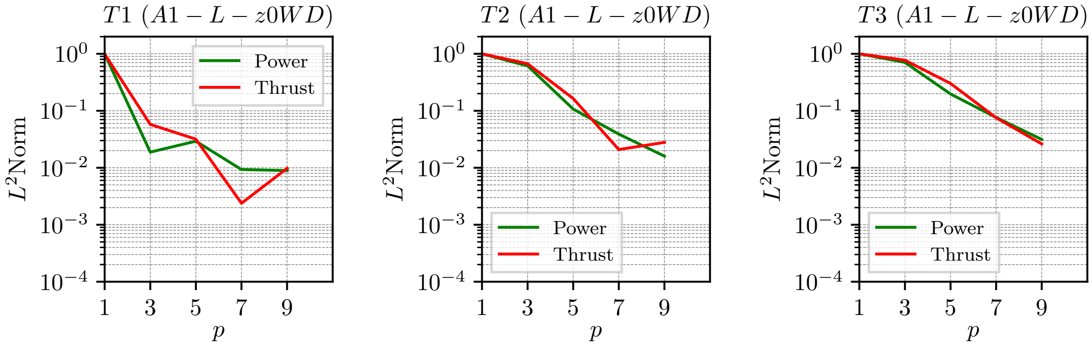

Figure 6.13: Convergence of L^2Norm for **Power** and **Thrust** at each turbine ($T1$,$T2$ and $T3$ from left to right) increasing polynomial order $p = 1, 3, 5, 7, 9$. Variance with $p = 11$ is used as reference.

6.4.2.4 Statistics summary

Finally, Table 6.4 report the summary of statistical parameters. Lookin at the Sobol's indices it is clear that the aerodynamic roughness z_0 has a negligible effect compared to the wind direction WD.

Table 6.4: Summary of statistical parameters for gpc case series gPC-A1-L-z0WD.

Turbine	[1]QOI	Mean $\bar{x}$	Variance σ^2	Std. dev. σ	S_{z_0}	S_{WD}	$S_{z_0,WD}$
$T1$	Power [MW]	2.181	$1.486e-4$	$1.219e-02$	$3.830e-03$	$9.962e-01$	$1.165e-05$
	Thrust [kN]	411.949	$1.645e+0$	$1.283e+00$	$8.276e-03$	$9.912e-01$	$5.688e-04$
$T2$	Power [MW]	1.483	$2.174e-1$	$4.663e-01$	$3.881e-05$	$9.995e-01$	$4.510e-04$
	Thrust [kN]	337.764	$2.763e+3$	$5.256e+01$	$9.421e-05$	$9.993e-01$	$5.705e-04$
$T3$	Power [MW]	1.463	$2.945e-1$	$5.427e-01$	$1.174e-05$	$9.999e-01$	$1.239e-04$
	Thrust [kN]	333.861	$3.909e+3$	$6.252e+01$	$3.540e-06$	$9.999e-01$	$1.298e-04$
$Total$	Power [MW]	5.127	$9.944e-1$	$9.972e-01$	$2.039e-07$	$9.997e-01$	$2.510e-04$
	Thrust [kN]	1.084	$1.297e-2$	$1.139e-01$	$6.020e-06$	$9.997e-01$	$2.923e-04$

[1] QOI = Quantity of interest (Power or Thrust).

6.4.3 Test 3: gPC-A3-L-U0WD

Test 3 and Test 4 are done under the exact same conditions as the Test 1 and Test 2 respectively, but using the wind turbine array $A3$ instead of $A1$ (See Section 6.3.1). This time contour plots of velocity are included to visualize the wake behaviour and better understand the capabilities and limitations of polynomial chaos.

6.4.3.1 Contour plots

Figure 6.14 and Figure 6.15 show contour plots of velocity magnitude and vertical velocity component respectively at hub height (z = 90 m). These plots show the wakes at three different wind directions $-8.834°$, $0°$ and $+8.834°$ (which corresponds to the maximum quadrature value of WD when using a polynomial expansion of order $p = 11$). A solid black line indicating the wind direction passing through each turbine axis has been added to better visualize the wake behaviour.

There are three phenomena that can be observed in these figures: the wake non-axisymmetry, wake steering, and blockage effect. The rotating wake under sheared inflow moves air from higher altitudes (and higher momentum) to one side of the wake, and air from lower altitudes to the other side, resulting in the characteristic non-axisymmetric wakes observed in Figure 6.14 (See blue zones in the near wake region). Wake steering due to yaw misalignment is noticed particularly in Figure 6.15(a) and 6.15(c), where the wake centre line is not aligned with the reference wind direction lines. And finally, blockage effect is particularly clear in Figure 6.14 where downstream turbines influence nearby wakes. For instance, in Figure 6.14(c), the wake of turbine $T1$ is affected by the flow acceleration around $T2$ making it narrower, and further downstream, the wake of $T1$ seems to be affected by turbine $T4$ moving it completely out of the reference direction line.

(a) $WD = -8.834°$

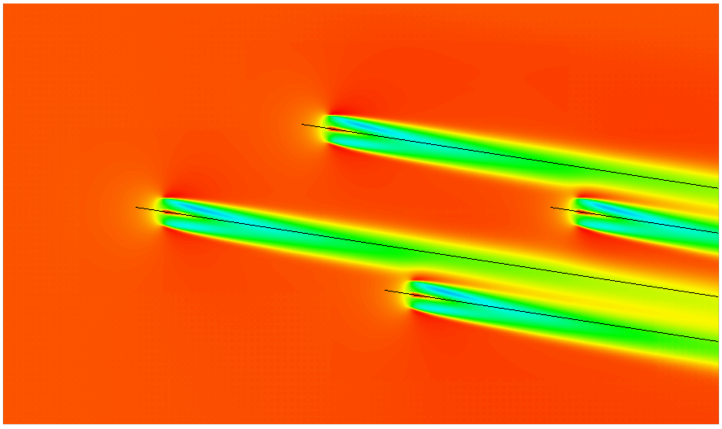

(b) $WD = 0.0°$

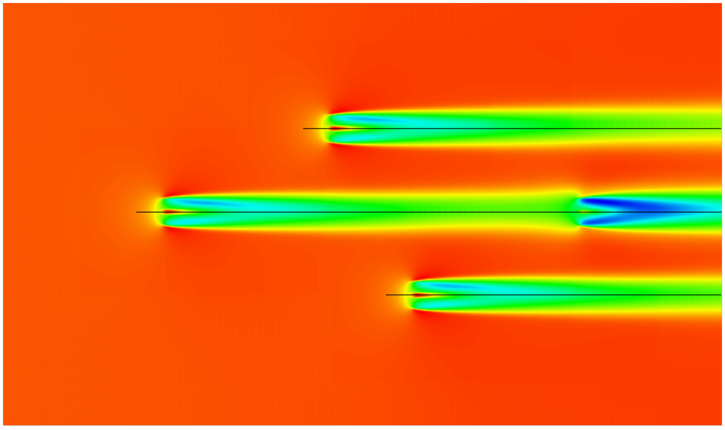

(c) $WD = +8.834°$

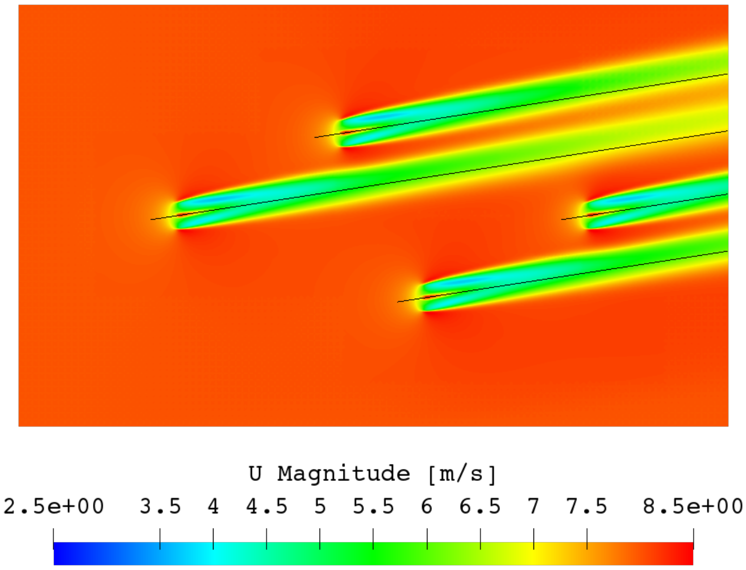

Figure 6.14: Contour plots of velocity magnitude $|\vec{U}|$ at hub height $z = 90$ m. Wind direction value of 8.834° correspond to the maximum quadrature point with order $p = 11$. Inflow wind speed is set to $U_0 = 8$ m/s. Black lines showing inflow WD were added passing through the turbine axes.

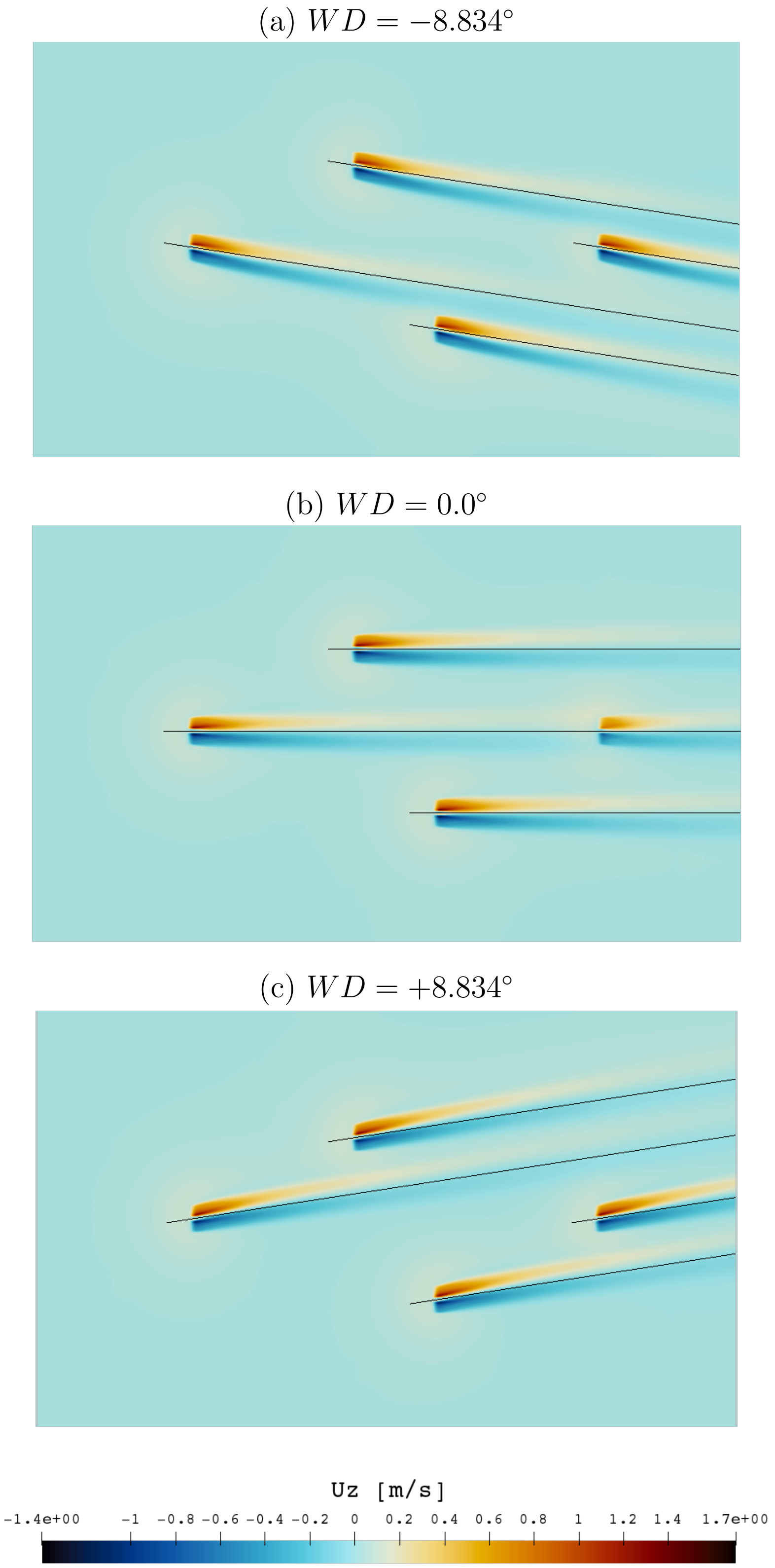

Figure 6.15: Contour plots of vertical velocity component U_z at hub height $z = 90$ m. Wind direction value of 8.834° correspond to the maximum quadrature point with order $p = 11$. Inflow wind speed is set to $U_0 = 8$ m/s. Black lines showing inflow WD were added passing through the turbine axes.

6.4.3.2 Response Surfaces

The power response for the four turbines $T1$, $T2$, $T3$ and $T4$ is shown in Figure 6.16. Clearly, turbines $T1$, $T2$ and $T3$, which operate in free flow, have a very similar response to $T1$ in the previous cases with array $A1$ (See Figure 6.7). However, looking very closely it is noted that the response surfaces of $T2$ and $T3$ are not completely symmetric respect to the wind direction, as they may appear at first sight, due to the influence of $T1$'s wake.

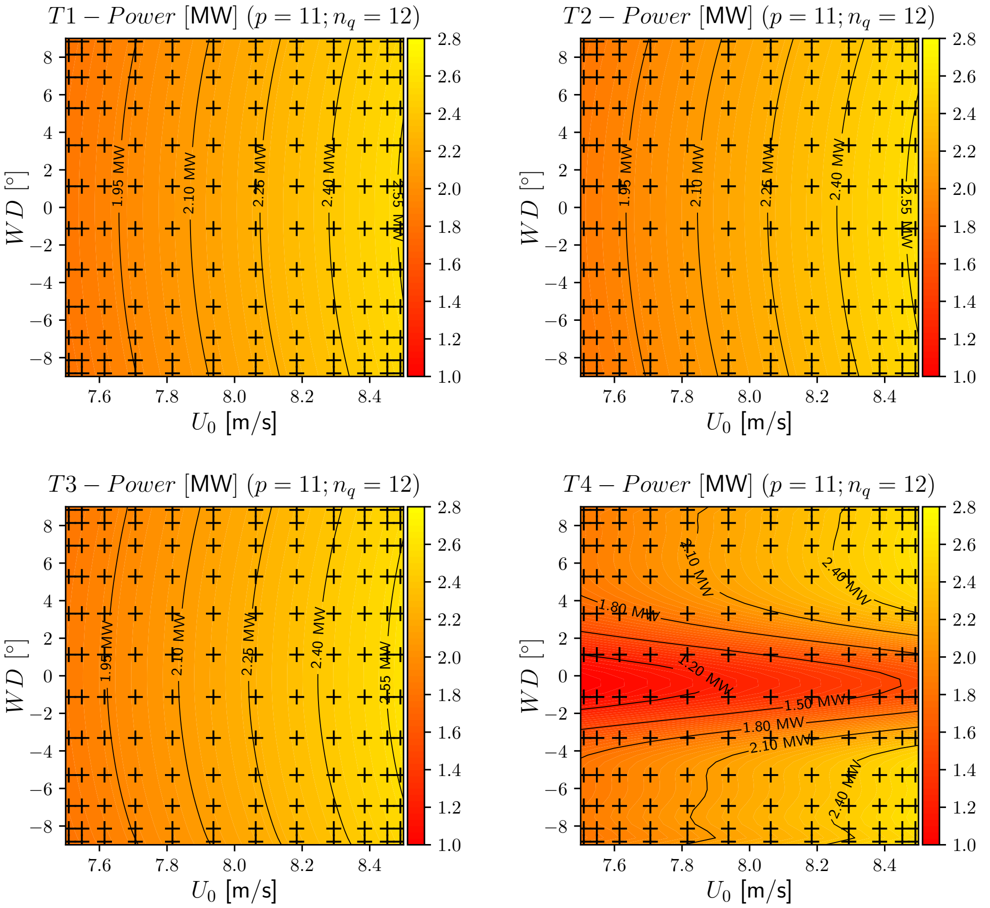

Figure 6.16: Response surface of **Power** at turbines $T1$, $T2$, $T3$ and $T4$ with the highest order $p = 11$. The black cross symbols (+) indicate deterministic evaluations.

On the other hand, the response of $T4$ is the most interesting one since it is operating behind being affected by the wake of the other three turbines. The response surface of $T4$ power is presented in Figure 6.17 for increasing values of p. It is observed that there are still some differences between $p = 9$ and $p = 11$ revealing that the polynomial expansion has not yet fully converged, even though the main features might be seen with $p = 7$. Note that, the power deficit zone in red is narrower compared to those observed the cases with array $A1$. Following the observations in contour plots made in the previous section, it is believed that the blockage of turbines $T2$ and $T3$ produce a contraction of $T1$'s wake. Note that $T4$ is located approximately $15.7D$ behind $T1$ and therefore the power deficit is smaller. This narrower zone contains relatively few quadrature points to be fully captured by the polynomial expansion. Furthermore, towards the end points of the WD interval, $T4$ is influenced by the wakes of $T2$ (Figure 6.14(a)) and $T3$ (Figure 6.14(c)) reducing the power output. As a result, the response surface is harder to approximate with a polynomial expansion and more quadrature points would be required.

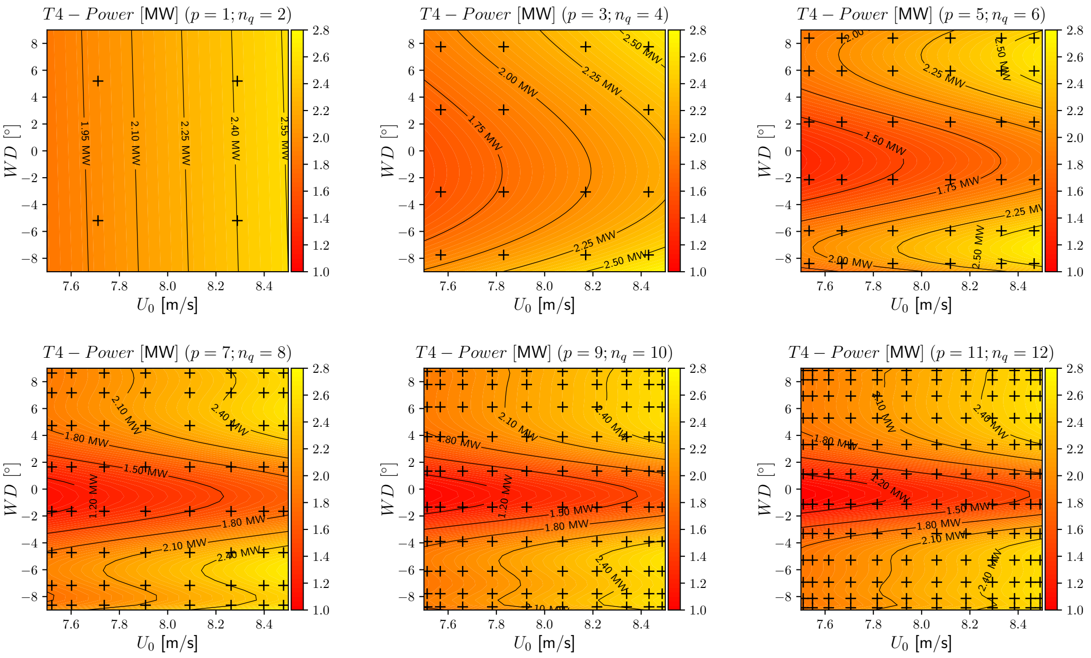

Figure 6.17: Response surface of **Power** at turbine $T4$ increasing order $p = 1, 3, 5, 7, 9, 11$. The black cross symbols (+) indicate deterministic evaluations.

Alternatively, one might be interested in the total power of the array instead of a single turbine. This was done in Figure 6.18 where the reponse surface of $Total$ power is shown for increasing order p. Clearly, adding up the outputs from all turbines results in a smoother surface compared to turbine $T4$ only, and so fewer simulations are needed to capture it accurately.

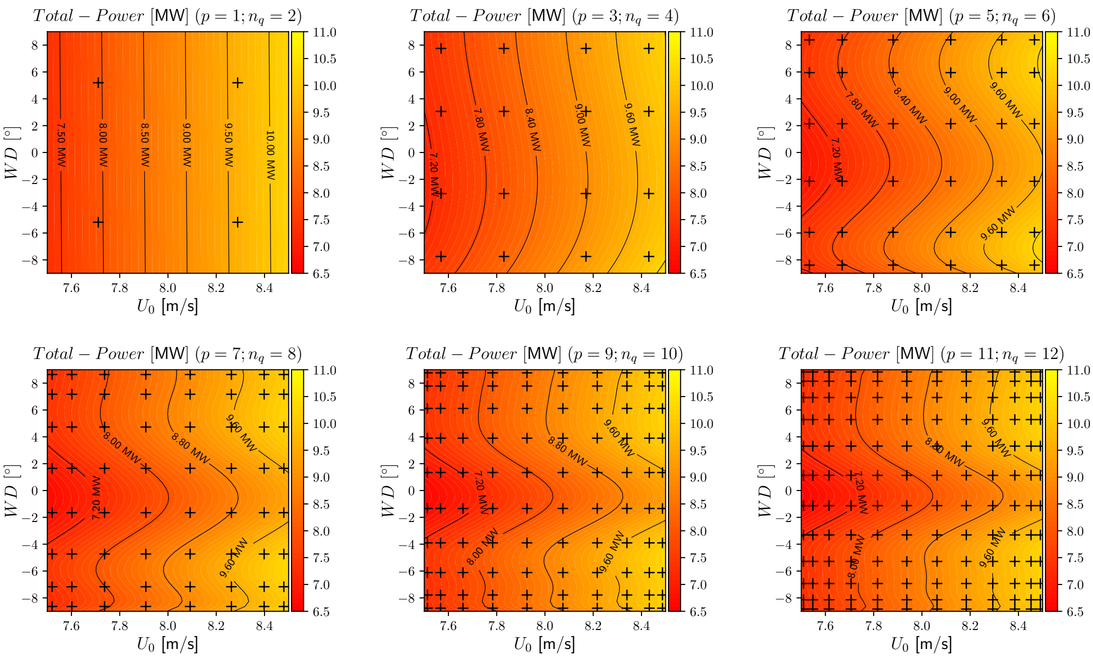

Figure 6.18: Response surface of the **Total Power** of the array increasing order $p = 1, 3, 5, 7, 9, 11$. The black cross symbols ($+$) indicate deterministic evaluations.

6.4.3.3 L^2 Norm error

Figure 6.19 shows the convergence of polynomial expansions for all turbines increasing the order p. These plots are consistent with previous observations. First of all, the smooth shape of the response of turbines $T1$, $T2$ and $T3$ is well captured with only 4 quadrature points. However, $T4$ and $Total$ have not fully converged with order $p = 9$.

6.4.3.4 Probability density functions

The same conclusions are obtained when looking at the probability density functions from random sampling in Figure 6.20. The PDFs of Power and Thrust for turbine $T4$ has not converged even with 12 quadrature points (144 simulations), which is a rather high number of simulations needed and probably shows one of the disadvantages of the generalized polynomial chaos method used here. Note however that the $Total$ Power and Thrust, 10 quadrature points ($p = 9$) does capture the probability density functions accurately.

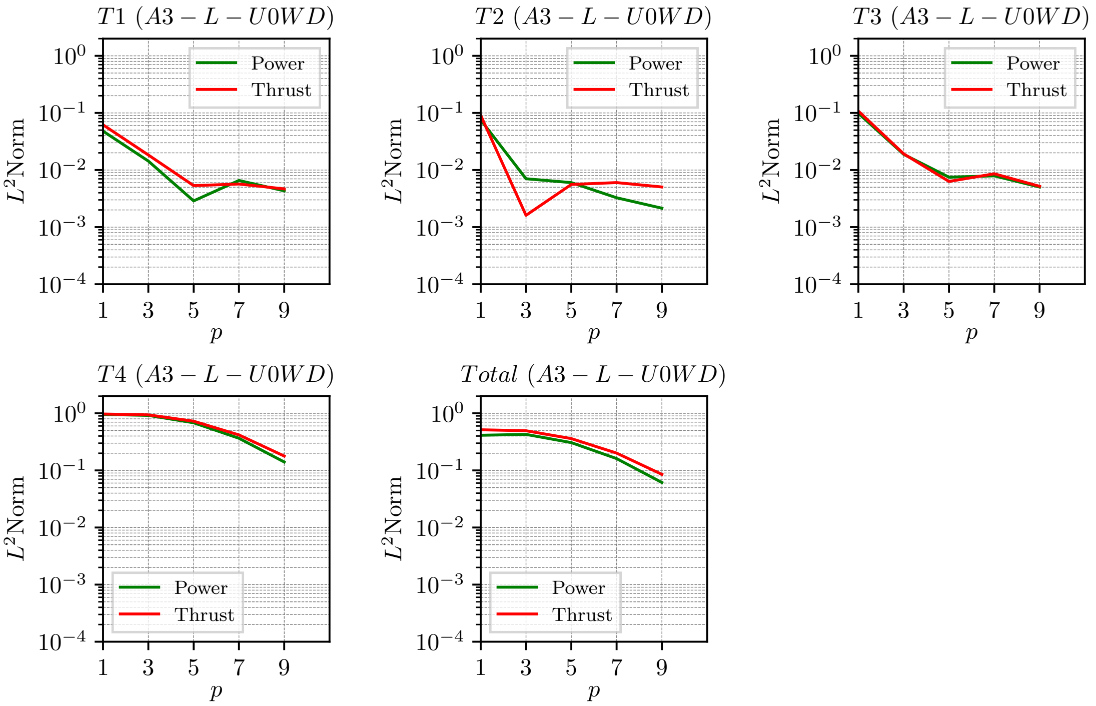

Figure 6.19: Convergence of L^2Norm for **Power** and **Thrust** at each turbine ($T1$,$T2$,$T3$ and $T4$), and the *Total* of the array, increasing polynomial order $p = 1, 3, 5, 7, 9$. Variance with $p = 11$ is used as reference.

6.4.3.5 Statistics summary

Finally, Table 6.5 shows the summary of statiscal parameters where it becomes clear that wind speed has a dominant impact in the responses in all turbines but $T4$, which operates downstream under the influence of the other three, and as such wind direction becomes dominant.

Table 6.5: Summary of statistical parameters for gpc case series gPC-A3-L-U0WD.

Turbine	[1]QOI	Mean $\bar{x}$	Variance σ^2	Std. dev. σ	S_{U_0}	S_{WD}	$S_{U_0,WD}$
$T1$	Power [MW]	2.184	$4.339e-2$	$2.083e-01$	$9.965e-01$	$3.494e-03$	$3.879e-05$
	Thrust [kN]	411.860	$3.393e+2$	$1.842e+01$	$9.953e-01$	$4.713e-03$	$1.898e-05$
$T2$	Power [MW]	2.197	$4.322e-2$	$2.079e-01$	$9.950e-01$	$4.926e-03$	$4.469e-05$
	Thrust [kN]	411.628	$3.344e+2$	$1.829e+01$	$9.934e-01$	$6.627e-03$	$2.101e-05$
$T3$	Power [MW]	2.203	$4.344e-2$	$2.084e-01$	$9.930e-01$	$6.980e-03$	$4.006e-05$
	Thrust [kN]	412.113	$3.350e+2$	$1.830e+01$	$9.923e-01$	$7.698e-03$	$1.736e-05$
$T4$	Power [MW]	1.956	$1.502e-1$	$3.875e-01$	$2.530e-01$	$7.443e-01$	$2.614e-03$
	Thrust [kN]	389.206	$1.450e+3$	$3.808e+01$	$2.285e-01$	$7.714e-01$	$1.332e-04$
Total	Power [MW]	8.540	$7.614e-1$	$8.726e-01$	$8.787e-01$	$1.209e-01$	$3.992e-04$
	Thrust [kN]	1.625	$6.267e-3$	$7.916e-02$	$8.512e-01$	$1.487e-01$	$3.502e-05$

[1] QOI = Quantity of interest (Power or Thrust).

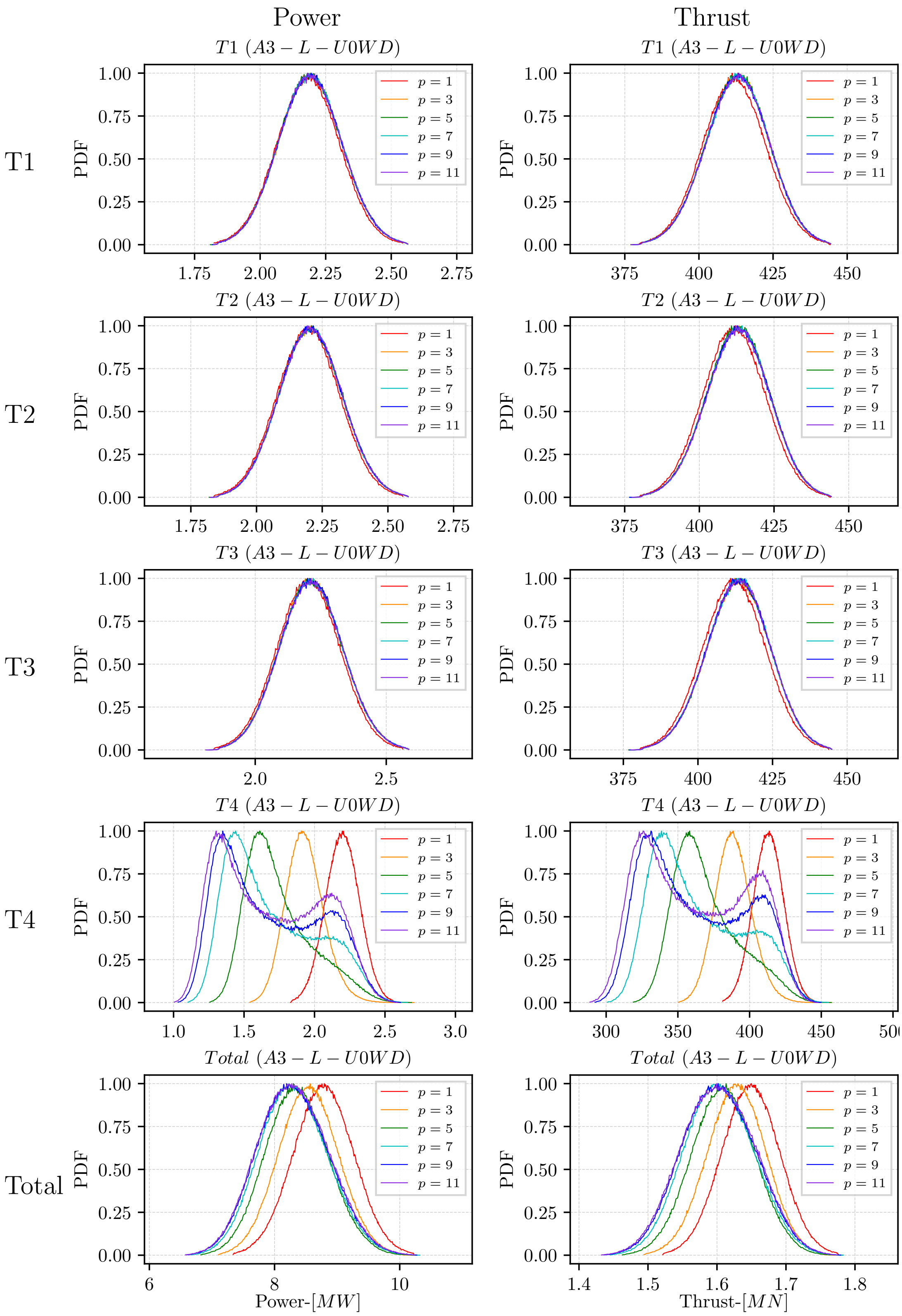

Figure 6.20: Probability density functions for **Power** (left) and **Thrust** (right) at each turbine ($T1$,$T2$,$T3$ and $T4$, and $Total$ of the array, from top to bottom) increasing order $p = 1, 3, 5, 7, 9, 11$.

6.4.4 Test 4: gPC-A3-L-z0WD

The last test case is performed with turbine array $A3$ as in the previous section, but using the aerodynamic roughness z_0 as a random parameter instead of wind speed U_0. This time however, only turbine $T4$ is briefly analysed.

6.4.4.1 Response Surfaces

The power response (shown in Figure 6.21) is dependent mainly on wind direction (as in Test 2, Section 6.4.2).

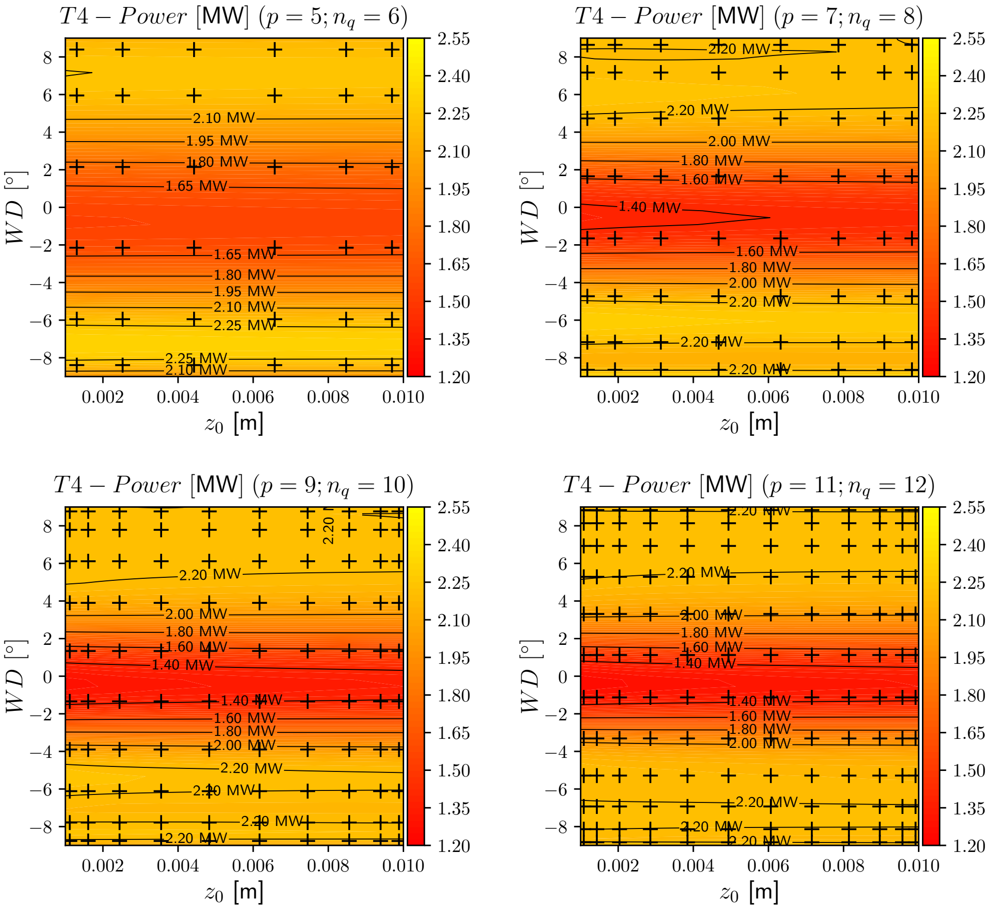

Figure 6.21: Response surface of **Power** at turbine $T4$ increasing order $p = 5, 7, 9, 11$. The black cross symbols (+) indicate deterministic evaluations. Response surfaces of power for turbines $T1$, $T2$ and $T3$ are not shown.

It is observed that 12 quadrature points is again not enough to capture the response of the system. The narrower power deficit region in red needs a higher resolution of quadrature points to be fully captured. Note how the quadrature points are closer together in the outer region of the random space, because Legendre polynomials have been used. These simulations do not bring much information about the response surface where is needed, showing again one of the disadvantages of this algorithm. Furture work might be needed to used sparse polynomial chaos to reduce even more the number of deterministic evaluations needed.

6.4.4.2 L^2 Norm error

Looking at the convergence of L^2Norm error in Figure 6.22, is noted that effectively more model evaluations are needed.

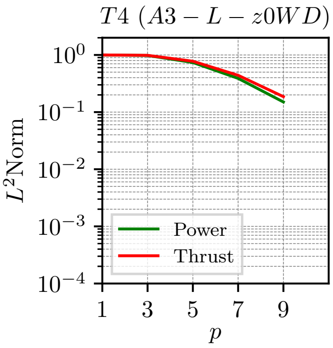

Figure 6.22: Convergence of L^2Norm for **Power** and **Thrust** at $T4$ increasing polynomial order $p = 1, 3, 5, 7, 9$. Variance with $p = 11$ is used as reference.

6.4.4.3 Probability density functions

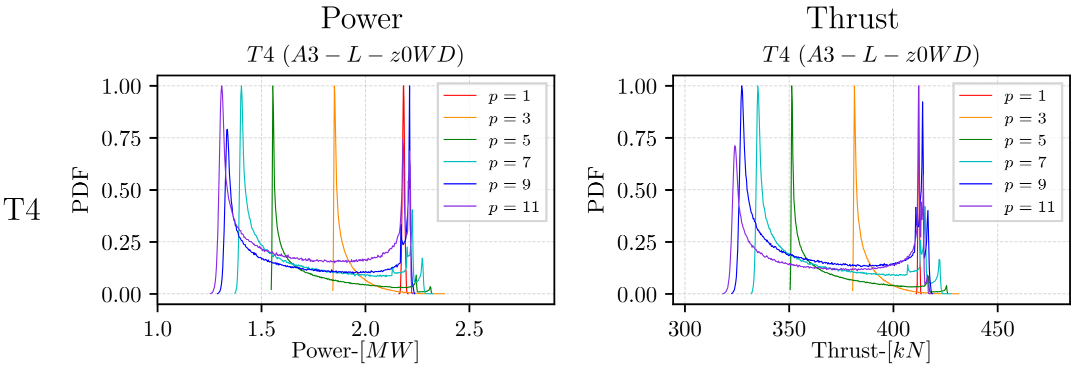

Figure 6.23: Probability density functions for **Power** (left) and **Thrust** (right) at each turbine ($T1$,$T2$,$T3$ and $T4$, and $Total$ of the array, from top to bottom) increasing order $p = 1, 3, 5, 7, 9, 11$.

Finally, the probability density functions are very distinctive showing spikes at the two extremes, operating directly in the wake (the red zone in the response surface) and in free wake (yellow zone). Even though the main characteristics of the PDFs are observed with 10 quadrature points ($p = 9$ and 100 simulations), changes are still considerably when moving to 12 quadrature points.

6.5 Summary and conclusions

A computational framework for uncertainty quantification in offshore wind farms was developed. This tool was used to propagate uncertainties with CFD models using polynomial chaos. The three main components, the `gpcPy`, the actuator disk model (ADM) and the atmospheric boundary layer model (ABL) were implemented and verified independently in the previous chapters. This chapter presented how these componentes are integrated and some cases were analysed, changing the turbine arrays, and testing three different parameters as random variables: the wind speed at hub height, the wind direction, and the aerodynamic roughness. Two quantities of interest have been used to determine the polynomial chaos expansions and determine their statistical parameters. This framework produces probability density functions for the outcomes instead of single value answer as it is typically done in CFD applications.

The number of deterministic evaluation is considerably less than other random sampling strategies, however, it has been shown that this highly depends on the shape of the response surface which is unkown a priori. Some parameters, here considered as random variables, will have a strong influence on the shape of the response surface. For instace, wind direction becomes the predominant parameters for power and thrust of a turbine operating in the wake of another turbine, but it not as important when the turbine is operating in free flow conditions. It is also crucial to consider the effect of the size of the random space, especially when the parameters shows a non-linear behaviour as the wind direction. Increasing the wind direction intervals (e.g. higher standard deviation) would bring additional wake interactions that will appear as more complex response surfaces. Also, in some cases it is observed that a great resolution of quadrature points (CFD model information) is used in zones of the random space where the response surface is smooth, whereas not as good resolution is used where high gradients are present. This is considered an important oppotunity for further improvement.

Unfortunately, due to the limitiations of the models used here, it was not possible to test more interesting situations, such as the effects of atmospheric stability, or some of the active wake control strategies mentioned in Chapter 2. Nonetheless, the framework is working, and it will be further improved in the future.

Chapter 7

Conclusions and future work

This thesis described the implementation of a computational framework for uncertainty quantification in offshore wind farms. All the chapters were intended to be self-contained, each one focused on a distinctive aspect of this work having their respective summaries and conclusions. This chapter intends to take a step back to look at these and other aspects from a broader perspective, highlighting the main conclusions and questions that remain open for future research.

Wind energy and climate change

Humanity is facing one of the biggest challenges in modern history, global warming and climate change. We need to put our efforts into limiting the increase in the averaged global temperature. Decarbonising the power generation sector should no longer be a political opinion but a shared goal. Current estimations indicate that wind energy will play an essential role in fighting climate change, and by 2050 it is expected to account for about one-quarter to one-third of the total power generation worldwide. However, one of its main disadvantages is its natural variability and low predictability, which makes difficult its integration into the grid. The physical system where wind energy is harvested is very complex and chaotic, involving a wide range of time and length scales. Nevertheless, the wind energy industry has managed to be commercially competitive, based on statistical methods for long term wind resource assessments and simplified engineering models that rely on fundamental physical principles.

A rapid evolving scenario

Over the last decade, the overall scenario has changed, turbines and wind farms are increasing in size, and some of the underlying assumptions in engineering models are no longer suitable. Fortunately, computers have also become increasingly powerful over the last decades, opening a great opportunity to build more advance computational models. Consequently, this has increased our understanding of wind turbine aerodynamics and wake interactions, leading to improved designs and better engineering models. In this regard, computational fluid dynamics (CFD) has become a powerful tool, offering a wide range of alternative methods to simulate engineering flows, varying in accuracy and computational costs (i.e. DNS, LES, RANS). However, CFD models have been mostly used to provide single value predictions based on fixed input parameters, without much consideration about the underlying uncertainties.

The contribution of this work

This work aims to fill the gap between CFD models and uncertainty quantification, which is usually overlooked, either because of the limited computational resources available or because of the lack of a detailed characterisation of the different sources of uncertainties. It is believed that uncertainty quantification will enhance our knowledge of such a complex physical system, which can potentially further reduce the costs of wind energy. As discussed in Chapter 3, uncertainty quantification can be thought of as a two-stage process starting with uncertainty characterisation and followed by uncertainty propagation. In this project, the scope was limited to the second stage building a computational framework for uncertainty propagation called `gpcADM`. One of the crucial aspects to consider is the cost of the propagation algorithms and computational models used. Currently, the chosen methods are primarily limited by the computational resources available.

Propagation algorithm: Polynomial Chaos

In this work, the generalised Polynomial Chaos (gPC) method was used as a regression algorithm to propagate uncertainties and determine the response surface of wind turbine arrays over the random space spanned by the random variables.

Polynomial chaos reduces significantly the number of model evaluations required compared to random sampling strategies such as Monte Carlo, which is straightforward and perfectly fine for simple models, but prohibitively expensive for CFD applications. Nevertheless, one of the main limitations of gPC is the curse of dimensionality, where the number of model evaluations increases exponentially with the number of random variables considered. It was shown that the number of simulations needed also depends on the shape of the response surface, which will determine the number of quadrature points required and which is usually unknown a priori. More importantly, it was noted that the distribution of quadrature points is not always efficient, having some time high resolution in zones with low gradients and low resolution in zones with high gradients. This offers a good opportunity to improve the performance of `gpcADM` by using sparse polynomial chaos or adaptive polynomial chaos. Besides, the shape of the response surface is dictated by the parameters that are used as random variables and therefore, experience can help to identify which ones show a linear behaviour reducing the number of quadrature points, and which ones are highly non-linear that need a higher resolution.

Computational models: ADM and ABL models

Furthermore, the CFD models implemented here are relatively inexpensive: a non-axisymmetric RANS-BEM actuator disk model to represent the wind turbines, and a simplified model for a neutral horizontally homogeneous boundary layer to represent the typical wind shear flow. Nonetheless, even though the models have been tested and validated individually, they have important limitations that must be considered.

The actuator disk model (`turbineDisk`) has a very low cost compared to actuator line models. Even though ADMs are not able to capture the flow features in the near wake region, other studies have shown that they are good enough to reproduce the behaviour in the far wake. However, `turbineDisk` has two important limitations as is currently implemented. The first one is the lack of a control system that adjusts the turbine operating conditions (e.g. pitch and rpm) based on the local inflow conditions. The second is that it was designed to work with structured uniform grids (at least in the rotor region) that have the cells aligned at the rotor plane. These limitations impede the study of active wake control strategies, which are currently an active area of research.

On the other hand, the atmospheric boundary layer model used here is only valid for neutral stratification and it assumes a constant shear and turbulence intensity across the entire domain, which is not actually what is observed in field measurements. Atmospheric stability conditions are crucial in the performance of wind farms, particularly at wind speeds between the cut-in and rated speeds. Nevertheless, the main limitations in modelling the atmospheric boundary layer come from turbulence modelling. Atmospheric flows are characterised by very high Reynolds numbers, and turbulence models are needed. Nevertheless, the linear eddy viscosity models used here are isotropic and their model coefficients have been tuned with standard flows that are not necessarily comparable with atmospheric flows. Thus, the intrinsic turbulence anisotropy of shear flows in the atmospheric boundary layer and wind turbine wakes is lost. As a result, the turbulence model itself represents a significant source of uncertainty and further research is needed to improve the modelling of atmospheric boundary layer flows, accounting not only for thermal stratification but also for other phenomena, such as wind veer. This of course needs to be complemented with the appropriate set of boundary conditions.

What is good about `gpcADM`

The framework for uncertainty quantification was successfully implemented. The library was made to be as general as possible so that any parameters could be considered as random variables for any wind turbine configuration (array). The framework has been designed to automatically construct all the OpenFOAM cases, generate the computational grids, run the simulations, and post-process the information, providing as output the complete system response and probability density functions for the quantities of interest. All this is done relatively fast because most of the processes were automated. For instance, when using the Computational Shared Facility (CSF3), with 4 cores in each simulation, using a computational mesh with about 3-4 million cells, about 100 simulations could be run within 12 hours. This of course depends on the availability of computational nodes, but it gives a rough idea of what is possible with the current CSF3 infrastructure. Besides, `gpcADM` can be used no only for uncertainty propagation, but also for sensitivity analysis or parametric studies. So, this computational tool opens an opportunity to perform a variety of studies but its limitations must be considered.

What are the limitations

The main limitations of `gpcADM` are essentially those imposed by their main components: the generalised polynomial chaos and the CFD models used.

From the polynomial chaos perspective, the number of random variables that can be analysed every time is currently limited to 2 or 3, but more than that will increase considerably the computational cost both in term of computing time and storage required. That is why finding more efficient ways to define the quadrature points can result in significant savings. Alternatively, storage can be reduced by reducing the amount of information written to files by OpenFOAM. Furthermore, more mesh sensitivity analyses could be carried out to determine if coarser grids can be used.

On the other hand, the studies that can be carried out are limited by the ability of the CFD models to capture the relevant physical phenomena. As mentioned above, currently `gpcADM` cannot be used to study active wake control strategies or test different atmospheric stability conditions.

Uncertainty charaterisation

As mentioned before, an important aspect of uncertainty quantification that was left outside of this work is uncertainty characterisation which aims to establish the state of knowledge of every source of uncertainty in the system. This is of course challenging and ambitious when dealing with wind power. We do not have currently the capacity to measure all the pertinent variables at all the time and length scales. Unquestionably, as research continues to make technological advances, progress will be made in measuring techniques (e.g. masts, LIDAR, satellite, drones, etc). Also, computational models also offer alternative ways to characterise uncertainties. For instance, re-analysis data sets from climate and weather prediction models can be used to characterise the long term variability of wind characteristics.

Future work

On the positive side, everything can be improved and `gpcADM` is not the exception. Some the task that can be done in future work are:

- To optimise the polynomial chaos library (`gpcPy`) to further reduce the number of simulations needed looking at sparse polynomial chaos expansions.
- To further improve the ADM by:
  - Adding individual turbine control algorithms to adjust operating conditions based on local inflow conditions.
  - Implementing an alternative method that work with unstructured grids that can be used for yawed and tilted rotors.
- To improve the modelling of the ABL by:
  - Implementing new models for the atmospheric boundary layer that better represents field measurements, under different stability conditions.
  - Improving turbulence modelling specifically designed for wind turbine wakes under different stability conditions.
- To characterise different sources of uncertainty, not only in inflow conditions, but also in model coefficients, and assess their impact.

Final remarks

As a final remark, I want to highlight the importance of collaboration and teamwork. Most of this work relies on the work of others, from countless lines of code written in different programming languages by people all over the world (e.g. OpenFOAM, Python) to comprehensive experimental work with international collaboration (e.g. MEXICO, NREL-Phase-VI). One of the biggest difficulties I faced during this project is not having access to measured data to validate the models implemented. I strongly believe if we want to face big challenges as climate change, we need to increase collaboration between researchers and institutions from the private and public sectors. Wind power is a beautifully challenging subject and it needs multidisciplinary teams to move forward.

Bibliography

S. A. Abdulqadir, H. Iacovides, and A. Nasser. The physical modelling and aerodynamics of turbulent flows around horizontal axis wind turbines. *Energy*, 119: 767–799, 2016. ISSN 03605442. doi: 10.1016/j.energy.2016.11.060.

I. Afgan, J. McNaughton, S. Rolfo, D. D. Apsley, T. Stallard, and P. Stansby. Turbulent flow and loading on a tidal stream turbine by LES and RANS. *International Journal of Heat and Fluid Flow*, 43:96–108, 2013. ISSN 0142727X. doi: 10.1016/j.ijheatfluidflow.2013.03.010.

J. Ainslie. Calculating the flowfield in the wake of wind turbines. *Journal of Wind Engineering and Industrial Aerodynamics*, 27:213–224, 1988. ISSN 01676105. doi: 10.1016/S0167-6105(13)00239-0.

J. Annoni, P. M. O. Gebraad, A. K. Scholbrock, P. A. Fleming, and J.-W. van Wingerden. Analysis of axial-induction-based wind plant control using an engineering and a high-order wind plant model. *Wind Energy*, 19(6):1135–1150, jun 2016. ISSN 10954244. doi: 10.1002/we.1891.

E. G. Antonini, D. A. Romero, and C. H. Amon. Improving CFD wind farm simulations incorporating wind direction uncertainty. *Renewable Energy*, 133:1011–1023, 2019. ISSN 18790682. doi: 10.1016/j.renene.2018.10.084.

D. D. Apsley and P. K. Stansby. Unsteady thrust on an oscillating wind turbine: Comparison of blade-element momentum theory with actuator-line CFD. *Journal of Fluids and Structures*, 98:103141, 2020. ISSN 10958622. doi: 10.1016/j.jfluidstructs.2020.103141.

D. D. Apsley, T. Stallard, and P. K. Stansby. Actuator-line CFD modelling of tidal-stream turbines in arrays. *Journal of Ocean Engineering and Marine Energy*, 2018. ISSN 2198-6444. doi: 10.1007/s40722-018-0120-3.

M. H. Baba-Ahmadi and P. Dong. Numerical simulations of wake characteristics of a horizontal axis tidal stream turbine using actuator line model. *Renewable Energy*, 113:669–678, dec 2017a. ISSN 09601481. doi: 10.1016/j.renene.2017.06.035.

M. H. Baba-Ahmadi and P. Dong. Validation of the actuator line method for simulating flow through a horizontal axis tidal stream turbine by comparison with measurements. *Renewable Energy*, 113:420–427, 2017b. ISSN 18790682. doi: 10.1016/j.renene.2017.05.060.

B. H. Bailey. *Wind resources for offshore wind farms: Characteristics and assessment*. Elsevier Ltd, 2016. ISBN 9780081007808. doi: 10.1016/B978-0-08-100779-2.00003-9.

G. E. Barter, A. Robertson, and W. Musial. A systems engineering vision for floating offshore wind cost optimization. *Renewable Energy Focus*, 34(September):1–16, 2020. ISSN 17550084. doi: 10.1016/j.ref.2020.03.002.

R. Barthelmie, O. F. Hansen, K. Enevoldsen, J. Højstrup, S. Frandsen, S. Pryor, S. Larsen, M. Motta, and P. Sanderhoff. Ten Years of Meteorological Measurements for Offshore Wind Farms. *Journal of Solar Energy Engineering*, 2005. ISSN 01996231. doi: 10.1115/1.1850489.

R. J. Barthelmie. The effects of atmospheric stability on coastal wind climates. *Meteorological Applications*, 6(1):39–47, 1999. ISSN 13504827. doi: 10.1017/s1350482799000961.

R. J. Barthelmie and L. E. Jensen. Evaluation of the wind farm efficiency and wind turbine wakes at the Nysted offshore wind farm. *Wind Energy*, 13(June 2010): 573–586, 2010. ISSN 1099-1824. doi: 10.1002/we.

R. J. Barthelmie, K. Hansen, S. T. Frandsen, O. Rathmann, J. G. Schepers, W. Schlez, J. Phillips, K. Rados, A. Zervos, E. S. Politis, and P. K. Chaviaropoulos. Modelling and measuring flow and wind turbine wakes in large wind farms offshore. *Wind Energy*, 12(5):431–444, 2009. ISSN 10954244. doi: 10.1002/we.348.

R. J. Barthelmie, S. T. Frandsen, O. Rathmann, K. Hansen, E. S. Politis, J. Prospathopoulos, J. G. Schepers, K. Rados, A. R. J. Barthelmie, and E. Politis. *Flow and wakes in large wind farms : Final report for UpWind WP8 Risø-R-Report*, volume 1765. 2011. ISBN 9788755038783.

A. C. M. Beljaars and A. A. M. Holtslag. A software library for the calculation of surface fluxes over land and sea. *Environmental Software*, 5(2):60–68, 1990. ISSN 02669838. doi: 10.1016/0266-9838(90)90002-N.

A. Betz. Das Maximum der theoretisch möglichen Ausnützung des Windes durch Windmotoren. *Zeitschrift für das gesamte Turbinenwesen*, 1920.

J. Bleeg, M. Purcell, R. Ruisi, and E. Traiger. Wind farm blockage and the consequences of neglecting its impact on energy production. *Energies*, 11(6), 2018. ISSN 19961073. doi: 10.3390/en11061609.

B. Blocken, T. Stathopoulos, and J. Carmeliet. CFD simulation of the atmospheric boundary layer: wall function problems. *Atmospheric Environment*, 41(2):238–252, jan 2007. ISSN 13522310. doi: 10.1016/j.atmosenv.2006.08.019.

B. J. E. Blocken and J. Carmeliet. Modelling atmospheric-boundary-layer flow with Fluent: curing the wall-function roughness incompatibility. In *Proceedings of the Fluent Benelux 2004 User Group Meeting*, 2004.

F. Blondel, G. Ferrer, M. Cathelain, and D. Teixeira. Improving a BEM Yaw Model Based on NewMexico Experimental Data and Vortex/CFD Simulations. *23ème Congrès Français de Mécanique*, (August), 2017.

S. Boersma, B. M. Doekemeijer, P. M. Gebraad, P. A. Fleming, J. Annoni, A. K. Scholbrock, J. A. Frederik, and J. W. Van Wingerden. A tutorial on control-oriented modeling and control of wind farms. *Proceedings of the American Control Conference*, (July 2018):1–18, 2017. ISSN 07431619. doi: 10.23919/ACC.2017.7962923.

K. Boorsma and J. G. Schepers. New MEXICO experiment: Preliminary overview with initial validation. (September), 2014.

K. Boorsma, F. Grasso, and J. Holierhoek. Enhanced approach for simulation of rotor aerodynamic loads. *Proceedings of the EWEA Offshore*, (FEBRUARY), 2011. doi: ECN-M--12-003.

K. Boorsma, M. Hartvelt, and L. M. Orsi. Application of the lifting line vortex wake method to dynamic load case simulations. *Journal of Physics: Conference Series*, 753(2), 2016. ISSN 17426596. doi: 10.1088/1742-6596/753/2/022030.

M. L. Buhl Jr. A New Empirical Relationship between Thrust Coefficient and Induction Factor for the Turbulent Windmill State. *Technical Report NREL/TP-500-36834*, (August), 2005.

J. A. Businger, J. C. Wyngaard, Y. Izumi, and E. F. Bradley. Flux-Profile Relationships in the Atmospheric Surface Layer. *Journal of the Atmospheric Sciences*, 28(2):181–189, 1971. ISSN 0022-4928. doi: 10.1175/1520-0469(1971)028⟨0181:FPRITA⟩2.0.CO;2.

D. Cabezon, E. Migoya, and A. Crespo. Comparison of turbulence models for the computational fluid dynamics simulation of wind turbine wakes in the atmospheric boundary layer. *Wind Energy*, 14(7):909–921, 2011. doi: 10.1002/we.516.

M. Calaf, C. Meneveau, and J. Meyers. Large eddy simulation study of fully developed wind-turbine array boundary layers. *Physics of Fluids*, 22(1):015110, jan 2010. ISSN 1070-6631. doi: 10.1063/1.3291077.

M. Calaf, M. B. Parlange, and C. Meneveau. Large eddy simulation study of scalar transport in fully developed wind-turbine array boundary layers. *Physics of Fluids*, 23(12), 2011. ISSN 10706631. doi: 10.1063/1.3663376.

L. P. Chamorro and F. Porté-Agel. Turbulent flow inside and above awind farm: A wind-tunnel study. *Energies*, 4(11):1916–1936, 2011. ISSN 19961073. doi: 10.3390/en4111916.

J. C. Chapman, I. Masters, M. Togneri, and J. A. Orme. The Buhl correction factor applied to high induction conditions for tidal stream turbines. *Renewable Energy*, 60:472–480, 2013. ISSN 09601481. doi: 10.1016/j.renene.2013.05.018. URL `http://dx.doi.org/10.1016/j.renene.2013.05.018`.

H. Charnock. Wind stress on a water surface. *Quart. J. Roy. Meteor. Soc.*, 81: 639–640, 1955. doi: 10.1029/2004jc002585.

Y. S. Chen and S. W. Kim. Computation of turbulent flows using an extended k-epsilon turbulence closure model. *NASA STI/Recon Technical Report N*, (NASA CR-179204):1–30, 1987.

M. B. Christiansen and C. B. Hasager. Wake studies around a large offshore wind farm using satellite and airborne SAR. pages 2–5, 2003.

M. Churchfield and S. Fleming, P Bulder, B White. Wind Turbine Wake-Redirection Control at the Fishermen's Atlantic City Windfarm. *Offshore Technology ...*, (May), 2015. ISSN 01603663. doi: 10.4043/25644-MS.

G. Corten, K. Lindenburg, and P. Schaak. Assembly of energy flow collectors, such as windpark, and method of operation, 2004.

G. G. Corten and P. Schaak. Heat and Flux - Increase of Wind Farm Production by Reduction of the Axial Induction. *European Wind Energy Conference*, page 6, 2003.

G. P. Corten. Heat Generation by a Wind Turbine Heat Generation by a Wind Turbine. *14th IEA Symposium on the Aerodynamics of wind turbines*, pages 1–8, 2000.

G. P. Corten and P. Schaak. Method and installation for extracting energy from a flowing fluid, 2004a.

G. P. Corten and P. Schaak. More power and less loads in wind farms: "heat and flux'. *Wind Energy*, (November):22–25, 2004b.

A. Crespo, T. Fraga, and J. Hernandez. Numerical simulation of wakes without recirculation in the earth's boundary layer. *ANAL.ING.MEC.*, 4(2 , Dec. 1986): 37–43, 1986.

L. Daróczy, G. Janiga, and D. Thévenin. Analysis of the performance of a H-Darrieus rotor under uncertainty using Polynomial Chaos Expansion. *Energy*, 113:399–412, 2016. ISSN 03605442. doi: 10.1016/j.energy.2016.07.001.

A. J. Dyer. A review of flux-profile relationships. *Boundary-Layer Meteorology*, 7 (3):363–372, 1974. ISSN 00068314. doi: 10.1007/BF00240838.

N. Earl, S. Dorling, R. Hewston, and R. Von Glasow. 2010-1980 Variability in U.K. surface wind climate. *Journal of Climate*, 26(4):1172–1191, 2013. ISSN 08948755. doi: 10.1175/JCLI-D-12-00026.1.

W. A. El-Askary, I. M. Sakr, A. M. AbdelSalam, and M. R. Abuhegazy. Modeling of wind turbine wakes under thermally-stratified atmospheric boundary layer. *Journal of Wind Engineering and Industrial Aerodynamics*, 160(November 2016): 1–15, 2017. ISSN 01676105. doi: 10.1016/j.jweia.2016.11.001.

A. El Kasmi and C. Masson. An extended k - epsilon model for turbulent flow through horizontal-axis wind turbines. *Journal of Wind Engineering and Industrial Aerodynamics*, 96(1):103–122, 2008. ISSN 01676105. doi: 10.1016/j.jweia.2007.03.007.

Y. El Khchine and M. Sriti. Tip Loss Factor Effects on Aerodynamic Performances of Horizontal Axis Wind Turbine. *Energy Procedia*, 118:136–140, 2017. ISSN 18766102. doi: 10.1016/j.egypro.2017.07.028.

S. Emeis. Current issues in wind energy meteorology, 2014. ISSN 14698080.

A. C. Fitch, J. B. Olson, J. K. Lundquist, J. Dudhia, A. K. Gupta, J. Michalakes, and I. Barstad. Local and Mesoscale Impacts of Wind Farms as Parameterized in a Mesoscale NWP Model. *Monthly Weather Review*, 140(9):3017–3038, 2012. ISSN 0027-0644. doi: 10.1175/MWR-D-11-00352.1.

P. A. Fleming, P. M. Gebraad, S. Lee, J. W. van Wingerden, K. Johnson, M. Churchfield, J. Michalakes, P. Spalart, and P. Moriarty. Evaluating techniques for redirecting turbine wakes using SOWFA. *Renewable Energy*, 70:211–218, 2014. ISSN 09601481. doi: 10.1016/j.renene.2014.02.015.

C. García-Sánchez, D. A. Philips, and C. Gorlé. Quantifying inflow uncertainties for CFD simulations of the flow in downtown Oklahoma City. *Building and Environment*, 78:118–129, 2014. ISSN 03601323. doi: 10.1016/j.buildenv.2014.04.013.

J. Garratt. Review: the atmospheric boundary layer. *Earth-Science Reviews*, 37 (12):89–134, 1994. ISSN 0012-8252. doi: 10.1016/0012-8252(94)90026-4.

M. Gaumond, P. Rethore, S. Ott, A. Peña, A. Bechmann, and K. Hansen. Evaluation of the wind direction uncertainty and its impact on wake modeling at the Horns Rev offshore wind farm. *Wind Energy*, 17(May 2013):1169–1178, 2014. ISSN 1099-1824. doi: 10.1002/we.

P. Gebraad, J. J. Thomas, A. Ning, P. Fleming, and K. Dykes. Maximization of the annual energy production of wind power plants by optimization of layout and yaw based wake control. *Wind Energy*, 20(1):97–107, jan 2017. ISSN 10954244. doi: 10.1002/we.1993.

General Electric. GE Renewable Energy launches the uprated Heliade-X 13 MW wind turbine for the UK's Dogger Bank Wind Farm. *Press Release. Retrieved from: https://www.ge.com/news/press-releases/ge-renewable-energy-launches-uprated-haliade-x-13-mw-wind-turbine-uk-dogger-bank*, 2020.

H. Glauert. Airplane Propellers. In *Aerodynamic Theory*, pages 169–360. Springer Berlin Heidelberg, Berlin, Heidelberg, 1935. doi: 10.1007/978-3-642-91487-4_3.

Global Wind Energy Council. Global Wind Report 2017 - Annual Market Update. Technical report, 2018.

S. Gómez-Iradi, R. Steijl, and G. N. Barakos. Development and validation of a cfd technique for the aerodynamic analysis of HAWT. *Journal of Solar Energy Engineering, Transactions of the ASME*, 131(3):0310091–03100913, 2009. ISSN 01996231. doi: 10.1115/1.3139144.

C. Gorlé, C. Garcia-Sanchez, and G. Iaccarino. Corrigendum to: "Quantifying inflow and RANS turbulence model form uncertainties for wind engineering flows" [J. Wind Eng. Ind. Aerodyn. 144 (2015) 202-212]. *Journal of Wind Engineering and Industrial Aerodynamics*, 152:59–60, 2016.

a. a. Grachev and C. W. Fairall. Dependence of the MoninObukhov Stability Parameter on the Bulk Richardson Number over the Ocean. *Journal of Applied Meteorology*, 36(4):406–414, 1997. ISSN 0894-8763. doi: 10.1175/1520-0450(1997)036⟨0406:DOTMOS⟩2.0.CO;2.

A. A. Grachev, E. L. Andreas, C. W. Fairall, P. S. Guest, and P. O. G. Persson. The Critical Richardson Number and Limits of Applicability of Local Similarity Theory in the Stable Boundary Layer. *Boundary-Layer Meteorology*, 147(1):51–82, 2013. ISSN 00068314. doi: 10.1007/s10546-012-9771-0.

S. E. Gryning, E. Batchvarova, B. Brümmer, H. Jørgensen, and S. Larsen. On the extension of the wind profile over homogeneous terrain beyond the surface boundary layer. *Boundary-Layer Meteorology*, 124(2):251–268, 2007. ISSN 00068314. doi: 10.1007/s10546-007-9166-9.

X. Han, P. Sagaut, D. Lucor, and I. Afgan. Stochastic response of the laminar flow past a flat plate under uncertain inflow conditions. *International Journal of Computational Fluid Dynamics*, 8562(February):37–41, 2012. ISSN 10618562. doi: 10.1080/10618562.2012.655687.

M. M. Hand, D. A. Simms, L. J. Fingersh, D. W. Jager, J. R. Cotrell, S. Schreck, and S. M. Larwood. Unsteady Aerodynamics Experiment Phase VI: Wind Tunnel Test Configurations and Available Data Campaigns. (January 2001), 2001. doi: 10.2172/15000240.

K. S. Hansen, R. J. Barthelmie, L. E. Jensen, and A. Sommer. The impact of turbulence intensity and atmospheric stability on power deficits due to wind turbine wakes at Horns Rev wind farm. *Wind Energy*, 2012. ISSN 10954244. doi: 10.1002/we.512.

M. O. L. Hansen. *Aerodynamics of Wind Turbines*, volume 7. 2008. ISBN 9788578110796. doi: 10.1017/CBO9781107415324.004.

D. M. Hargreaves and N. G. Wright. On the use of the k-epsilon model in commercial CFD software to model the neutral atmospheric boundary layer. *Journal of Wind Engineering and Industrial Aerodynamics*, 95(5):355–369, 2007. ISSN 01676105. doi: 10.1016/j.jweia.2006.08.002.

C. B. Hasager, P. Vincent, J. Badger, M. Badger, A. Di Bella, A. Peña, R. Husson, and P. J. Volker. Using satellite SAR to characterize the wind flow around offshore wind farms. *Energies*, 8(6):5413–5439, 2015. ISSN 19961073. doi: 10.3390/en8065413.

I. Herráez, B. Stoevesandt, and J. Peinke. Insight into rotational effects on a wind turbine blade using navier-stokes computations. *Energies*, 7(10):6798–6822, 2014. ISSN 19961073. doi: 10.3390/en7106798.

M. C. Holtslag, W. A. A. M. Bierbooms, and G. J. W. van Bussel. Extending the diabatic surface layer wind shear profile for offshore wind energy. *Renewable Energy*, 101:96–110, 2017. ISSN 18790682. doi: 10.1016/j.renene.2016.08.031.

B. Hrafnkelsson, G. Oddsson, and R. Unnthorsson. A Method for Estimating Annual Energy Production Using Monte Carlo Wind Speed Simulation. *Energies*, 9(4): 286, 2016. ISSN 1996-1073. doi: 10.3390/en9040286. URL `http://www.mdpi.com/1996-1073/9/4/286`.

IPCC. Summary for Policymakers. *In: Global warming of 1.5C. An IPCC Special Report on the impacts of global waming of 1.5C above pre-industrial levels and related global greenhouse emission pathways, in the context of strengthening the global response to the threat of climate change*, (Masson-Delmotte, V., P. Zhai, H.-O. Pörtner, D. Roberts, J. Skea, P.R. Shukla, A. Pirani, W. Moufouma-Okia, C. Péan, R. Pidcock, S. Connors, J.B.R. Matthews, Y. Chen, X. Zhou, M.I. Gomis, E. Lonnoy, T. Maycock, M. Tignor, and T. Waterfield (eds.)):In Press, 2018.

IRENA. *Future of Wind: Deployment, investment, technology, grid integration and socio-economic aspects*. 2019. ISBN 9789292601553.

N. O. Jensen. A note on wind generator interaction. *Risø-M-2411 Risø National Laboratory Roskilde*, pages 1–16, 1983. ISSN 01676105. doi: Riso-M-2411.

A. Jimenez, A. Crespo, E. Migoya, and J. Garcia. Advances in large-eddy simulation of a wind turbine wake. *Journal of Physics: Conference Series*, 75:012041, 2007. ISSN 1742-6596. doi: 10.1088/1742-6596/75/1/012041.

Á. Jiménez, A. Crespo, and E. Migoya. Application of a LES technique to characterize the wake deflection of a wind turbine in yaw. *Wind Energy*, 13(6):559–572, dec 2009. ISSN 10954244. doi: 10.1002/we.380.

W. P. Jones and B. E. Launder. The prediction of laminarization with a two-equation model of turbulence. *International Journal of Heat and Mass Transfer*, 15(2):301–314, 1972. ISSN 00179310. doi: 10.1016/0017-9310(72)90076-2.

J. Jonkman, S. Butterfield, W. Musial, and G. Scott. Definition of a 5-MW Reference Wind Turbine for Offshore System Development. (February), 2009. ISSN 01487299. doi: 10.2172/947422.

S. K. Kanev, F. J. Savenije, and W. P. Engels. Active wake control: An approach to optimize the lifetime operation of wind farms. *Wind Energy*, 21(7):488–501, 2018. ISSN 10991824. doi: 10.1002/we.2173.

M. S. Karimi, S. Salehi, M. Raisee, P. Hendrick, and A. Nourbakhsh. Probabilistic CFD computations of gas turbine vane under uncertain operational conditions. *Applied Thermal Engineering*, 148(October 2018):754–767, 2019. ISSN 13594311. doi: 10.1016/j.applthermaleng.2018.11.072. URL `https://doi.org/10.1016/j.applthermaleng.2018.11.072`.

I. Katic, J. Hojstrup, and N. O. Jensen. A simple model for cluster efficiency. *Ewea 1986*, (October):407–410, 1986.

T. Knudsen, T. Bak, and M. Svenstrup. Survey of wind farm control-power and fatigue optimization. *Wind Energy*, 18(8):1333–1351, aug 2015. ISSN 10954244. doi: 10.1002/we.1760.

M. A. Lackner, A. L. Rogers, and J. F. Manwell. Uncertainty analysis in wind resource assessment and wind energy production estimation. *Collection of Technical Papers - 45th AIAA Aerospace Sciences Meeting*, 21:14572–14587, 2007. doi: 10.2514/6.2007-1222.

L. Landberg. *Meteorology for Wind Energy - An Introduction.* DNV GL, Copenhagen, Denmark, 2016. ISBN 9781118913444.

G. C. Larsen. A simple stationary semi-analytical wake model. *Denmark. Forskningscenter Risoe. Risoe-R*, 1713(August):1–21, 2009.

J. W. Larsen, S. R. K. Nielsen, and S. Krenk. Dynamic stall model for wind turbine airfoils. *Journal of Fluids and Structures*, 23(7):959–982, 2007. ISSN 08899746. doi: 10.1016/j.jfluidstructs.2007.02.005.

B. E. Launder and B. I. Sharma. Application of the energy-dissipation model of turbulence to the calculation of flow near a spinning disc. *Letters in Heat and Mass Transfer*, 1(2):131–137, 1974. ISSN 00944548. doi: 10.1016/0094-4548(74)90150-7.

O. P. Le Maître and O. M. Knio. *Spectral Methods for Uncertainty Quantification.* 2010. ISBN 978-90-481-3519-6. doi: 10.1007/978-90-481-3520-2.

J. Lee and F. Zhao. GWEC Global Wind Report. *Contributing authors: Alastair Dutton, Ben Backwell, Ramon Fiestas, Liming Qiao, Naveen Balachandran, Shuxin Lim, Wanliang Liang, Emerson Clarke, Anjali Lathigaralead*, (March), 2020.

C. Lindenburg. PHATAS Release "NOV-2003" and "APR-2005" USER'S MANUAL. (May), 2005.

H. Lu and F. Porté-Agel. Large-eddy simulation of a very large wind farm in a stable atmospheric boundary layer. *Physics of Fluids*, 23(6), 2011. ISSN 10706631. doi: 10.1063/1.3589857.

H. Machielse. Controlling Wind , tunnel theorie . *ECN-E–11-065*, (November), 2011.

L. Machielse, S. Barth, E. Bot, H. Hendriks, and G. Schepers. Evaluation of Heat and Flux Farm Control. *Technical Report. Ecn-E-07-105, ECN*, 2007.

G. Marmidis, S. Lazarou, and E. Pyrgioti. Optimal placement of wind turbines in a wind park using Monte Carlo simulation. *Renewable Energy*, 33(7):1455–1460, 2008. ISSN 09601481. doi: 10.1016/j.renene.2007.09.004.

L. A. Martinez, C. Meneveau, and R. Stevens. Wind Farm Large-Eddy Simulations on Very Coarse Grid Resolutions using an Actuator Line Model. *34th Wind Energy Symposium*, (January):1–7, 2016. doi: 10.2514/6.2016-1261.

D. Medici. Experimental studies of wind turbine wakes: power optimisation and meandering; KTH Mechanics, Ph.D. thesis (KTH Mechanics, Royal Institute of Technology, Sweden. (December), 2005.

D. Mehta, A. H. van Zuijlen, B. Koren, J. G. Holierhoek, and H. Bijl. Large Eddy Simulation of wind farm aerodynamics: A review. *Journal of Wind Engineering and Industrial Aerodynamics*, 133:1–17, 2014. ISSN 01676105. doi: 10.1016/j.jweia.2014.07.002.

F. Menter. Improved two-equation k-omega turbulence models for aerodynamic flows. *NASA Technical Memorandum*, (103978):1 – 31, 1992.

F. Menter. Zonal Two Equation k-w Turbulence Models For Aerodynamic Flows. In *23rd Fluid Dynamics, Plasmadynamics, and Lasers Conference*, 1993. ISBN 103975. doi: 10.2514/6.1993-2906. URL `http://arc.aiaa.org/doi/10.2514/6.1993-2906`.

F. Menter and T. Esch. 16th Brazilian congress of mechanical engineering elements of industrial heat transfer predictions. 2001.

F. R. Menter. Two-equation eddy-viscosity turbulence models for engineering applications. *AIAA Journal*, 32(8):1598–1605, 1994. ISSN 0001-1452. doi: 10.2514/3.12149.

J. Michelsen. Basis3D-a Platform for Development of Multiblock PDE Solvers. 1992.

J. A. Michelsen. Block structured multigrid solution of 2D and 3D elliptic PDE's. *Lyngby: Dept. of Fluid Mechanics, Technical University of Denmark.*, 1994.

R. Mikkelsen. *Actuator Disc Methods Applied to Wind Turbines.* 2003. ISBN 8774752960.

S. MirHassani and A. Yarahmadi. Wind farm layout optimization under uncertainty. *Renewable Energy*, 107:288–297, 2017. ISSN 09601481. doi: 10.1016/j.renene.2017.01.063.

M. Motta, R. J. Barthelmie, and PVølund. The influence of non-logarithmic wind speed profiles on potential power output at danish offshore sites. *Wind Energy*, 8 (2):219–236, 2005. ISSN 10954244. doi: 10.1002/we.146.

J. P. Murcia, P. E. Réthoré, A. Natarajan, and J. D. Sørensen. How many model evaluations are required to predict the AEP of a wind power plant? *Journal of Physics: Conference Series*, 625:012030, 2015. ISSN 1742-6588. doi: 10.1088/1742-6596/625/1/012030.

J. Nikuradse. Stromungsgesetz in rauhren rohren, vDI Forschungshefte 361. (English translation: Laws of flow in rough pipes). Tech. Rep. NACA Technical Memorandum 1292. National Advisory Commission for Aeronautics, Washington, DC, USA (1950). Technical report, 1933.

S. E. Norris, P. J. Richards, and G. D. Mallinson. Improved finite volume discretisations of entropy generation and turbulence production. *Computers and Fluids*, 49(1):302–311, 2011. ISSN 00457930. doi: 10.1016/j.compfluid.2011.06.009.

A. Obukhov. Turbulence in an atmosphere with a non- uniform temperature. *Tr. Inst. Teor. Geofiz. Akad. Nauk. SSSR.*, (1):95–115, 1946.

Ørsted. Hornsea Project One & Two Offshore Wind Farms. *Community Newsletter*, (March), 2018.

Ørsted. Ørsted presents update on its long-term financial targets. *Retrieved from: https://orsted.com/en/company-announcement-list/2019/10/1937002*, 2019.

J. P. O'Sullivan, R. A. Archer, and R. G. J. Flay. Consistent boundary conditions for flows within the atmospheric boundary layer. *Journal of Wind Engineering and Industrial Aerodynamics*, 99(1):65–77, 2011. ISSN 01676105. doi: 10.1016/j.jweia.2010.10.009.

A. S. Padrón, A. P. J. Stanley, J. J. Thomas, J. J. Alonso, and A. Ning. Polynomial chaos for the computation of annual energy production in wind farm layout optimization. *Journal of Physics: Conference Series*, 753(April 2013):032021, 2016. ISSN 1742-6588. doi: 10.1088/1742-6596/753/3/032021.

P. Parking, R. Holm, and D. Medici. The application of PIV to the wake of a wind turbine in yaw. In *Particle Image Velocimetry; Gottingen; 17 September 2001 through 19 September 2001. DLR Mitteilung*, pages pp.155–162, 2001.

B. Plaza, R. Bardera, and S. Visiedo. Comparison of BEM and CFD results for MEXICO rotor aerodynamics. *Journal of Wind Engineering and Industrial Aerodynamics*, 145:115–122, 2015. ISSN 01676105. doi: 10.1016/j.jweia.2015.05.005.

F. Porté-Agel, Y.-T. Wu, H. Lu, and R. J. Conzemius. Large-eddy simulation of atmospheric boundary layer flow through wind turbines and wind farms. *Journal of Wind Engineering and Industrial Aerodynamics*, 99(4):154–168, 2011. ISSN 01676105. doi: 10.1016/j.jweia.2011.01.011.

F. Porté-Agel, Y. T. Wu, and C. H. Chen. A numerical study of the effects of wind direction on turbine wakes and power losses in a largewind farm. *Energies*, 6(10): 5297–5313, 2013. ISSN 19961073. doi: 10.3390/en6105297.

F. Porté-Agel, H. Lu, and Y.-T. Wu. Interaction between Large Wind Farms and the Atmospheric Boundary Layer. *Procedia IUTAM*, 10(0):307–318, 2014. ISSN 22109838. doi: 10.1016/j.piutam.2014.01.026.

J. M. Prospathopoulos, E. S. Politis, and P. K. Chaviaropoulos. Modelling wind turbine wakes in complex terrain. *European Wind Energy Conference and Exhibition 2008*, 1(May 2014):382–398, 2008.

J. M. Prospathopoulos, E. S. Politis, K. G. Rados, and P. K. Chaviaropoulos. Evaluation of the effects of turbulence model enhancements on wind turbine wake predictions. *Wind Energy*, 14(2):285–300, mar 2011. ISSN 10954244. doi: 10.1002/we.419.

Python. Python, 2020. URL `https://www.python.org/`.

P. E. Réthoré. Wind Turbine Wake in Atmospheric Turbulence. *Aalborg: Department of Civil Engineering, Aalborg University. (DCE Thesis; No. 22).*, 2009.

P.-E. Réthoré, P. van der Laan, N. Troldborg, F. Zahle, and N. N. Sørensen. Verification and validation of an actuator disc model. *Wind Energy*, 17(6):919–937, jun 2014. ISSN 10954244. doi: 10.1002/we.1607.

P. Richards and R. Hoxey. Appropriate boundary conditions for computational wind engineering models using the k-epsilon turbulence model. *Journal of Wind Engineering and Industrial Aerodynamics*, 46-47:145–153, 1993. ISSN 01676105. doi: 10.1016/0167-6105(93)90124-7.

P. J. Richards and S. E. Norris. Appropriate boundary conditions for computational wind engineering models revisited. *Journal of Wind Engineering and Industrial Aerodynamics*, 99(4):257–266, 2011. ISSN 01676105. doi: 10.1016/j.jweia.2010.12.008.

H. Ritchie and M. Roser. Emissions by sector. *Published online at OurWorldInData.org. Retrieved from: 'https://ourworldindata.org/global-rise-of-education'*, 2020.

C. J. Roy and W. L. Oberkampf. A comprehensive framework for verification, validation, and uncertainty quantification in scientific computing. *Computer Methods in Applied Mechanics and Engineering*, 200(25-28):2131–2144, 2011. ISSN 00457825. doi: 10.1016/j.cma.2011.03.016.

B. Sanderse, S. P. van der Pijl, and B. Koren. Review of computational fluid dynamics for windturbine wake aerodynamics. *Wind Energy*, 14(February 2011): 799–819, 2011. ISSN 1099-1824. doi: 10.1002/we.

S. Sarmast, W. Z. Shen, W. J. Zhu, R. F. Mikkelsen, S. P. Breton, and S. Ivanell. Validation of the actuator line and disc techniques using the New Mexico measurements. *Journal of Physics: Conference Series*, 753(3), 2016. ISSN 17426596. doi: 10.1088/1742-6596/753/3/032026.

J. Schepers. Analysis of 4.5 years EWTW wake measurements. *Technical Report. Ecn-E-09-057, ECN*, 2007.

J. G. Schepers. *Engineering models in wind energy aerodynamics.* Number november. 2012. ISBN 9789461915078.

J. G. Schepers and H. Snel. Model Experiments in Controlled Conditions - Final Report. *ECN Report: ECN-E-07-042*, page 54, 2007. doi: ECN-E-07-042.

J. G. Schepers, K. Boorsma, A. Bon, C. Kim, and T. Cho. Results from Mexnext :. (March):14–17, 2011.

J. G. Schepers, K. Boorsma, T. Cho, S. Gomez-Iradi, P. Schaffarczyk, A. Jeromin, W. Z. Shen, T. Lutz, K. Meister, B. Stoevesandt, S. Schreck, D. Micallef, R. Pereira, T. Sant, H. A. Madsen, and N. Sorensen. Final report of IEA Task 29 , Mexnext (Phase 1): Analysis of Mexico wind tunnel measurements. (ECN-E12-004), 2012.

J. G. Schepers, K. Boorsma, P. Schaffarczyk, H. A. Madsen, N. N. Sørensen, W. Z. Shen, T. Lutz, C. Schulz, I. Herráez, and S. Schreck. Final report of IEA Wind Task 29 : Mexnext (Phase 2). (December), 2014.

J. G. Schepers, K. Boorsma, S. Gomez-Iradi, P. Schaffarczyk, H. A. Madsen, N. N. Sørensen, W. Z. Shen, T. Lutz, C. Schulz, I. Herraez, and S. Schreck. Final report of IEA Wind Task 29, Mexnext (Phase 3). *Researchgate.Net*, (January), 2018.

S. Schreck. December 2008 IEA Wind Annex XX HAWT Aerodynamics and Models Final Report. (December):91, 2008.

S. Schreck and M. Robinson. Rotational augmentation of horizontal axis wind turbine blade aerodynamic response. *Wind Energy*, 5(2-3):133–150, 2002. ISSN 1095-4244. doi: 10.1002/we.68.

W. Z. Shen, R. Mikkelsen, J. N. Sørensen, and C. Bak. Tip loss corrections for wind turbine computations. *Wind Energy*, 8(4):457–475, 2005a. ISSN 10954244. doi: 10.1002/we.153.

W. Z. Shen, J. N. Sørensen, and R. Mikkelsen. Tip loss correction for actuator/Navier-Stokes computations. *Journal of Solar Energy Engineering, Transactions of the ASME*, 127(2):209–213, 2005b. ISSN 01996231. doi: 10.1115/1.1850488.

W. Z. Shen, W. J. Zhu, and J. N. Sørensen. Actuator line/Navier-Stokes computations for the MEXICO rotor: comparison with detailed measurements. *Wind Energy*, 15(5):811–825, jul 2012. ISSN 10954244. doi: 10.1002/we.510.

M. Shives and C. Crawford. Adapted two-equation turbulence closures for actuator disk RANS simulations of wind & tidal turbine wakes. *Renewable Energy*, 92: 273–292, 2016. ISSN 18790682. doi: 10.1016/j.renene.2016.02.026.

Siemens Gamesa Renewable Energy. SG 14-222 DD: The winds of change have never been stronger. *Retrieved from: https://www.siemensgamesa.com/en-int/products-and-services/offshore/wind-turbine-sg-14-222-dd*, 2020.

D. a. Simms, M. M. Hand, L. J. Fingersh, and D. W. Jager. Unsteady aerodynamics experiment phases II-IV test configurations and available data campaigns. *National Renewable Energy Laboratory, NREL/TP-500-25950, Golden, CO*, (July), 1999.

H. Snel, R. Houwink, and W. J. Piers. Sectional Prediction of 3D Effects for Separated Flow on Rotating Blades, 1993.

J. N. Sørensen and W. Z. Shen. Numerical Modeling of Wind Turbine Wakes. *Journal of Fluids Engineering*, 124(2):393, 2002. ISSN 00982202. doi: 10.1115/1.1471361.

J. N. Sørensen, W. Z. Shen, and X. Munduate. Analysis of wake states by a fullfield actuator disc model. *Wind Energy*, 1(2):73–88, 1998. ISSN 10954244. doi: 10.1002/(sici)1099-1824(199812)1:2⟨73::aid-we12⟩3.0.co;2-l.

J. N. Sørensen, R. F. Mikkelsen, S. Dan, S. Ivanell, S. Sarmast, and S. J. Andersen. Simulation of wind turbine wakes using the actuator line technique. *Philosophical transactions. Series A, Mathematical, physical, and engineering sciences*, (373), 2015. doi: http://dx.doi.org/10.1098/rsta.2014.0071.

N. N. Sørensen. *General purpose flow solver applied to flow over hills.* PhD thesis, Technical University of Denmark, 1995.

N. N. Sørensen, F. Zahle, K. Boorsma, and G. Schepers. CFD computations of the second round of MEXICO rotor measurements. *Journal of Physics: Conference Series*, 753:022054, sep 2016. ISSN 1742-6588. doi: 10.1088/1742-6596/753/2/022054.

R. J. Stevens and C. Meneveau. *Flow Structure and Turbulence in Wind Farms*, volume 49. 2016. ISBN 0108160602. doi: 10.1146/annurev-fluid-010816-060206.

R. J. Stevens, L. A. Martínez-Tossas, and C. Meneveau. Comparison of wind farm large eddy simulations using actuator disk and actuator line models with wind tunnel experiments. *Renewable Energy*, 116:470–478, 2017. ISSN 09601481. doi: 10.1016/j.renene.2017.08.072.

The OpenFOAM Foundation. OpenFOAM, 2020. URL `openfoam.org`.

L. A. M. Tossas and S. Leonardi. Wind Turbine Modeling for Computational Fluid Dynamics. Technical Report December 2012, 2013.

I. Troen and E. Lundtang Petersen. *European wind atlas.* 1989. ISBN 8755014828. doi: 10.1016/0014-2999(86)90768-5.

N. Troldborg, J. Sørensen, and R. Mikkelsen. *Actuator Line Modeling of Wind Turbine Wakes.* PhD thesis, Technical University of Denmark, 2009.

N. Troldborg, G. C. Larsen, H. A. Madsen, K. S. Hansen, J. N. Sørensen, and R. Mikkelsen. Numerical simulations of wake interaction between two wind turbines at various inflow conditions. *Wind Energy*, 14(7):859–876, oct 2011. ISSN 10954244. doi: 10.1002/we.433.

N. Troldborg, F. Zahle, P.-E. Réthoré, and N. N. Sørensen. Comparison of wind turbine wake properties in non-sheared inflow predicted by different computational fluid dynamics rotor models, 2015. ISSN 1099-1824.

M. Türk and S. Emeis. The dependence of offshore turbulence intensity on wind speed. *Journal of Wind Engineering and Industrial Aerodynamics*, 98(8-9):466–471, 2010. ISSN 01676105. doi: 10.1016/j.jweia.2010.02.005.

UK Government. UK becomes first major economy to pass net zero emissions law. *Retrieved from: https://www.gov.uk/government/news/uk-becomes-first-major-economy-to-pass-net-zero-emissions-law*, (June), 2019.

UK Government. New plans to make UK world leader in green energy. *Retrieved from: https://www.gov.uk/government/news/new-plans-to-make-uk-world-leader-in-green-energy*, (October), 2020.

United Nations. United Nations Treaty Collection, Chapter XXVII, Environment, 7.d Paris Agreement. *Retrieved from: https://treaties.un.org*, 2015.

United Nations Environment Programme. *Emissions Gap Report 2020.* 2020.

L. van den Bos and B. Sanderse. Uncertainty quantification for wind energy applications. *Scientific Comupting SC-1701*, (August), 2017.

D. van der Hoek, S. Kanev, J. Allin, D. Bieniek, and N. Mittelmeier. Effects of axial induction control on wind farm energy production - A field test. *Renewable Energy*, 140:994–1003, 2019. ISSN 18790682. doi: 10.1016/j.renene.2019.03.117.

M. P. van der Laan, N. N. Sørensen, P.-E. Réthoré, M. C. Kelly, and J. Mann. *Efficient Turbulence Modeling for CFD Wake Simulations.* PhD thesis, DTU Wind Energy. (DTU Wind Energy PhD; N0. 0047 (EN))., 2014.

M. P. van der Laan, N. N. Sørensen, P.-E. Réthoré, J. Mann, M. C. Kelly, and N. Troldborg. The k-e-fp model applied to double wind turbine wakes using different actuator disk force methods. *Wind Energy*, 18:2223–2240, 2015a. ISSN 1099-1824. doi: 10.1002/we.

M. P. van der Laan, N. N. Sørensen, P. E. Réthoré, J. Mann, M. C. Kelly, N. Troldborg, K. S. Hansen, and J. P. Murcia Leon. The k-e-fp model applied to wind farms. *Wind Energy*, 18(12):2065–2084, 2015b. ISSN 1099-1824. doi: 10.1002/we.

M. P. van der Laan, N. N. Sørensen, P.-E. Réthoré, J. Mann, M. C. Kelly, N. Troldborg, J. G. Schepers, and E. Machefaux. An improved k-e model applied to a wind turbine wake in atmospheric turbulence. *Wind Energy*, 18(April 2014):889–907, 2015c. ISSN 1099-1824. doi: 10.1002/we.

M. T. van Dijk, J.-W. van Wingerden, T. Ashuri, Y. Li, and M. A. Rotea. Yaw-Misalignment and its Impact on Wind Turbine Loads and Wind Farm Power Output. *Journal of Physics: Conference Series*, 753:062013, 2016. ISSN 1742-6588. doi: 10.1088/1742-6596/753/6/062013.

A. Van Garrel. Development of a Wind Turbine Aerodynamics Simulation Module. *ECN Wind Energy*, (August):106, 2003.

G. A. M. van Kuik, J. Peinke, R. Nijssen, D. Lekou, J. Mann, J. N. Sørensen, C. Ferreira, J. W. van Wingerden, D. Schlipf, P. Gebraad, H. Polinder, A. Abrahamsen, G. J. W. van Bussel, J. D. Sørensen, P. Tavner, C. L. Bottasso, M. Muskulus, D. Matha, H. J. Lindeboom, S. Degraer, O. Kramer, S. Lehnhoff, M. Sonnenschein, P. E. Sørensen, R. W. Künneke, P. E. Morthorst, and K. Skytte. Long-term research challenges in wind energy a research agenda by the European Academy of Wind Energy. *Wind Energy Science*, 1(1):1–39, 2016. ISSN 2366-7451. doi: 10.5194/wes-1-1-2016.

A. Vasel-Be-Hagh and C. L. Archer. Wind farms with counter-rotating wind turbines. *Sustainable Energy Technologies and Assessments*, 2016. ISSN 22131388. doi: 10.1016/j.seta.2016.10.004. URL `http://dx.doi.org/10.1016/j.seta.2016.10.004`.

P. Veers, K. Dykes, E. Lantz, S. Barth, C. L. Bottasso, O. Carlson, A. Clifton, J. Green, P. Green, H. Holttinen, D. Laird, V. Lehtomäki, J. K. Lundquist, J. Manwell, M. Marquis, C. Meneveau, P. Moriarty, X. Munduate, M. Muskulus, J. Naughton, L. Pao, J. Paquette, J. Peinke, A. Robertson, J. S. Rodrigo,

A. M. Sempreviva, J. C. Smith, A. Tuohy, and R. Wiser. Grand challenges in the science of wind energy. *Science*, 366(6464), 2019. ISSN 10959203. doi: 10.1126/science.aau2027.

J. W. Wagenaar and J. G. Schepers. Leaflet : Controlling Wind in ECN ' s Scaled Wind Farm. (April):1–2, 2012.

S. Wahono. Development of Virtual Blade Model for Modelling Helicopter Rotor Downwash in OpenFOAM. *Australian Government - Department of Defence - Aerospace Division - Defence Science and Technology Organisation.*, (DSTO-TR-2931), 2013.

D. C. Wilcox. Reassessment of the scale-determining equation for advanced turbulence models. *AIAA Journal*, 26(11):1299–1310, nov 1988. ISSN 0001-1452. doi: 10.2514/3.10041.

A. Wimshurst. Tip Flow Corrections for Horizontal Axis Wind and Tidal Turbine Rotors. 2018.

A. Wimshurst and R. H. Willden. Analysis of a tip correction factor for horizontal axis turbines. *Wind Energy*, 20(9):1515–1528, 2017. ISSN 10991824. doi: 10.1002/we.2106.

Wind Europe. The European offshore wind industry - Key trends and statistics 2016. *Key trends and statistics 2016*, (January):33, 2017.

Wind Europe. Wind in power 2017 - Annual combined onshore and offshore wind energy statistics. 2018.

Wind Europe. Wind energy in Europe in 2019. *Trends and statistics*, (Published in February 2020), 2020.

Y. T. Wu and F. Porté-Agel. Large-Eddy Simulation of Wind-Turbine Wakes: Evaluation of Turbine Parametrisations. *Boundary-Layer Meteorology*, 138(3): 345–366, 2011. ISSN 00068314. doi: 10.1007/s10546-010-9569-x.

Y. T. Wu and F. Porté-Agel. Simulation of Turbulent Flow Inside and Above Wind Farms: Model Validation and Layout Effects. *Boundary-Layer Meteorology*, 146 (2):181–205, 2013. ISSN 00068314. doi: 10.1007/s10546-012-9757-y.

Y. T. Wu and F. Porté-Agel. Modeling turbine wakes and power losses within a wind farm using LES: An application to the Horns Rev offshore wind farm. *Renewable Energy*, 75:945–955, 2015. ISSN 18790682. doi: 10.1016/j.renene.2014.06.019.

D. Xiu. *Numerical Methods for Stochastic Computations.* 2010. ISBN 9780691142128.

Y. Yang, M. Gu, S. Chen, and X. Jin. New inflow boundary conditions for modelling the neutral equilibrium atmospheric boundary layer in computational wind engineering. *Journal of Wind Engineering and Industrial Aerodynamics*, 97(2): 88–95, 2009. ISSN 01676105. doi: 10.1016/j.jweia.2008.12.001.

BLANK PAGE

Appendix A

Orthogonal Polynomials

A.1 Orthogonal Polynomials

In this work family of orthogonal polynomials are used to construct polynomial chaos expansions. Considering a set of polynomials $\{\psi_n(\xi)\}_{n=1}^{\infty}$ of order n, they are orthogonal if the inner product $\langle \psi_p, \psi_q \rangle$ vanishes anytime that $p \neq q$. The inner product is defined as:

$$\langle \psi_p, \psi_q \rangle = \int \psi_p(\xi) \psi_q(\xi) w(\xi) d\xi \tag{A.1}$$

where $w(\xi)$ is a positive weight function. Depending on the weight function, different orthogonal families of polynomials can be obtained. Two of such families are Legendre and Hermite polynomials described briefly in the next sections. These constitute the building blocks for the polynomial chaos expansions used in this work.

A.2 Legendre Polynomials

The Legendre polynomials are an orthogonal basis with respect to the weight function $w(\xi) = 1/2$ for $\xi \in [-1, 1]$. These polynomials satisfy the recurrence relation:

$$Le_{n+1}(\xi) = \frac{2n+1}{n+1}\xi\, Le_n(\xi) - \frac{n}{n+1}Le_{n-1}(\xi) \tag{A.2}$$

The first six Legendre polynomials are shown in Figure A.1 (See Eqs A.3 - A.8).

$$Le_0(\xi) = 1 \tag{A.3}$$
$$Le_1(\xi) = \xi \tag{A.4}$$
$$Le_2(\xi) = \frac{1}{2}\left(3\,\xi^2 - 1\right) \tag{A.5}$$
$$Le_3(\xi) = \frac{1}{2}\left(5\,\xi^3 - 3\,\xi\right) \tag{A.6}$$
$$Le_4(\xi) = \frac{1}{8}\left(35\,\xi^4 - 30\,\xi^2 + 3\right) \tag{A.7}$$
$$Le_5(\xi) = \frac{1}{8}\left(63\,\xi^5 - 70\,\xi^3 + 15\,\xi\right) \tag{A.8}$$

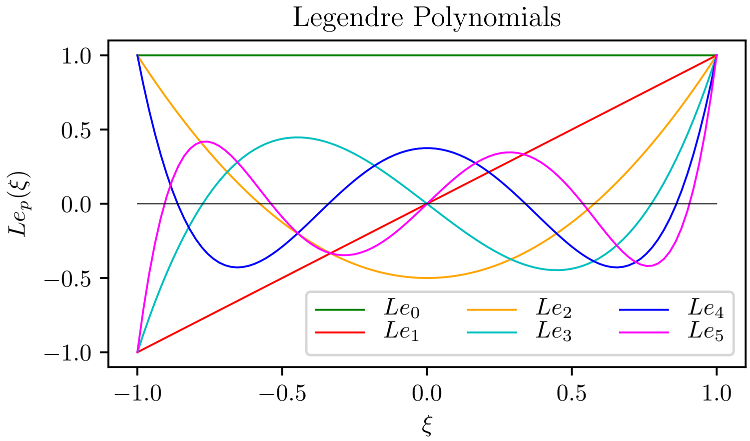

Figure A.1: The first six Legendre polynomials up to order $p = 5$.

A.3 Hermite Polynomials

Two definitions of Hermite polynomials exist depending on the weight function used in the inner product. Here the weight function is defined by Eq.A.9 for $\xi \in (-\infty, \infty)$. These polynomials satisfy the recurrence relation given in Eq.A.10. The first six Hermite polynomials are shown in Figure A.2 (See Eqs A.11 - A.16).

$$w(\xi) = \frac{1}{\sqrt{2\pi}} \exp\left(-\frac{\xi^2}{2}\right) \tag{A.9}$$

$$He_{n+1}(\xi) = \xi\, He_n(\xi) - n\, He_{n-1}(\xi) \tag{A.10}$$

$$He_0(\xi) = 1 \tag{A.11}$$

$$He_1(\xi) = \xi \tag{A.12}$$

$$He_2(\xi) = \xi^2 - 1 \tag{A.13}$$

$$He_3(\xi) = \xi^3 - 3\,\xi \tag{A.14}$$

$$He_4(\xi) = \xi^4 - 6\,\xi^2 + 3 \tag{A.15}$$

$$He_5(\xi) = \xi^5 - 10\,\xi^3 + 15\,\xi \tag{A.16}$$

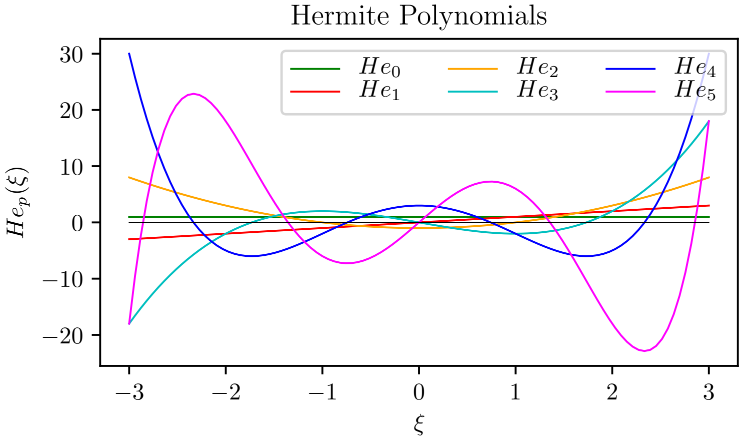

Figure A.2: The first six Hermite polynomials up to order $p = 5$.

BLANK PAGE

Appendix B

Experimental test cases

This appendix contains some complementary details about the experimental test cases used for validation of the ADM, including blade geometries and 2D airfoil data.

B.1 NREL UAE Phase VI (NREL-VI)

Blade geometry

The NREL UAE Phase VI turbine blade geometry is shown in Table B.1 (values taken from Hand et al. (2001)). Note that in the `turbineDisk` library, the transition zone between $r = 0.883$ m and $r = 1.257$ m are not included. The values are directly interpolated between CYL and S809 sections.

Airfoil data

The corresponding S809 airfoil lift (C_l) and drag (C_d) coefficients used for validation of the ADM in Chatper 4 are shown in Table B.2 and Table B.3 respectively. The coefficients are tabulated as a function of AOA and Re_c. These values were taken from Hand et al. (2001), however, they have been interpolated to the listed angles of attacks (i.e. integer values) so they were consistent at different Re_c.

Table B.1: NREL UAE Phase VI blade geometry.

Airfoil	Radius r [m]	r/R [%]	[1]Twist angle β [°]	Chord length c [m]
CYL	0.5080	10.1	0.0000	0.218
CYL	0.6600	13.1	0.0000	0.218
CYL	0.8830	17.6	0.0000	0.183
[2]TRANSITION	1.0080	20.0	8.5146	0.349
[2]TRANSITION	1.0670	21.2	11.7146	0.441
[2]TRANSITION	1.1330	22.5	15.2146	0.544
S809	1.2570	25.0	21.8546	0.737
S809	1.3430	26.7	19.8886	0.728
S809	1.5100	30.0	16.1066	0.711
S809	1.6480	32.8	13.7236	0.697
S809	1.9520	38.8	9.7936	0.660
S809	2.2570	44.9	7.1226	0.636
S809	2.3430	46.6	6.5296	0.627
S809	2.5620	50.9	5.2396	0.605
S809	2.8670	57.0	3.8976	0.574
S809	3.1720	63.1	2.9646	0.543
S809	3.1850	63.3	2.9296	0.542
S809	3.4760	69.1	2.3086	0.512
S809	3.7810	75.2	1.7996	0.482
S809	4.0230	80.0	1.4336	0.457
S809	4.0860	81.2	1.3396	0.451
S809	4.3910	87.3	0.8946	0.420
S809	4.6960	93.4	0.4626	0.389
S809	4.7800	95.0	0.3456	0.381
S809	5.0000	99.4	0.0396	0.358
[3]S809	5.0290	100.0	0.0000	0.355

[1] The twist angle are listed such that is zero at the tip. Note that Hand et al. (2001) used the 75% span as the reference zero twist angle.

[2] According to Hand et al. (2001), there is a transition zone between $r = 0.8830$ m (cylindrical section) and $r = 1.257$ m (S809 airfoil). However, the transition sections are not included when using the `turbineDisk` library. Instead, the library interpolates linearly between these two surrounding values.

[3] The blade geometry reported in Hand et al. (2001) does not include data at $r = 5.029$ m, but it does includes values for $r > 5.029$ m (The radius can be increased by changing the tip piece). So the values of shown for $r = 5.029$ m, were interpolated between the values given at $r = 5.0$ m and $r = 5.305$ m.

B.2 MEXICO Experiments

Blade geometry

The blade geometry was digitised from Schepers and Snel (2007). Table B.4 shows the raw values obtained. However, three aerodynamic airfoil profiles are used along the blades. The airfoil DU91-W2-250 is used between 20% and 46% span, the

Table B.2: S809 lift coefficient C_l as function of AOA and Re_c. Values taken from Hand et al. (2001). Note that values were interpolated at integer values of AOA for consistency.

$Re_c =$	0.3×10^6	0.5×10^6	0.65×10^6	0.75×10^6	1.0×10^6	
[1]AOA [°]	[2]CSU	[2]CSU	[2]CSU	[3]OSU	[3]OSU	[4]DUT
0	0.1050	0.1731	0.1764	0.0382	0.0700	0.1402
1	0.2065	0.2796	0.2779	0.1684	0.1795	0.2557
2	0.3081	0.3848	0.3791	0.3000	0.2890	0.3722
3	0.4220	0.4839	0.4796	0.4143	0.4125	0.4888
4	0.5359	0.5820	0.5794	0.5286	0.5375	0.6053
5	0.6370	0.6735	0.6761	0.6471	0.6580	0.7210
6	0.7370	0.7608	0.7688	0.7662	0.7780	0.8331
7	0.8059	0.8133	0.8158	0.8363	0.8371	0.9021
8	0.8709	0.8628	0.8596	0.8942	0.8895	0.9444
9	0.8792	0.8861	0.8538	0.9129	0.9168	0.9686
10	0.8782	0.8689	0.8489	0.9271	0.9379	0.9562
11	0.8716	0.8704	0.8920	0.9227	0.9318	0.9480
12	0.8572	0.8940	0.8880	0.9463	0.9620	0.9935
13	0.8744	0.9372	0.9270	0.9827	0.9918	1.0257
14	0.8923	0.9290	0.9100	1.0060	1.0156	1.0495
15	0.8915	0.9084	0.9100	1.0173	1.0280	1.0604
16	0.7848	0.9120	0.9280	1.0060	1.0140	1.0472
17	0.6252	0.6550	0.6860	0.9475	0.9620	0.9847
18	0.5919	0.5880	0.6390	0.8590	0.9056	0.9440
19	0.5822	0.5870	0.5760	0.7150	0.8018	0.9306
20	0.5992	0.5970	0.5520	0.6640	0.6700	0.9240

[1] Values given in Hand et al. (2001) were interpolated at the listed angles of attack for consistency between different Re_c values.

[2] Values obtained at the Colorado State University (CSU) wind tunnel (Hand et al., 2001).

[3] Values obtained at Ohio State University (OSU) wind tunnel(Hand et al., 2001).

[4] Values obtained at the Delft University of Technology (DUT) Low Speed Laboratory low-turbulence wind tunnel(Hand et al., 2001).

airfoil RISO-A1-21 from 54% to 66% span, and the NACA-64-418 from 74% outwards (Schepers et al., 2012). Therefore, the raw values were linearly interpolated to include the airfoil sections and their transition zones (See Table B.5). The `turbineDisk` library will also interpolate linearly between the given data points, including the transition zones where lift and drag coefficients will be interpolated between values from the surrounding airfoils.

Table B.3: S809 drag coefficient C_d as function of AOA and Re_c. Values taken from Hand et al. (2001).

$Re_c =$	0.3×10^6	0.5×10^6	0.65×10^6	0.75×10^6	1.0×10^6	
[1]AOA [°]	[2]CSU [5]C_{dp}	[2]CSU [5]C_{dp}	[2]CSU [5]C_{dp}	[3]OSU [5]C_{dp}	[3]OSU [5]C_{dp}	[4]DUT [6]C_{dw}
0	0.0117	0.0042	0.0019	0.0028	0.0022	0.0094
1	0.0116	0.0052	0.0014	0.0042	0.0029	0.0096
2	0.0116	0.0062	0.0011	0.0056	0.0036	0.0099
3	0.0127	0.0071	0.0016	0.0061	0.0043	0.0100
4	0.0138	0.0081	0.0024	0.0066	0.0049	0.0100
5	0.0137	0.0086	0.0043	0.0075	0.0056	0.0097
6	0.0135	0.0094	0.0064	0.0083	0.0062	0.0095
7	0.0163	0.0134	0.0108	0.0103	0.0077	0.0121
8	0.0194	0.0177	0.0155	0.0125	0.0093	0.0161
9	0.0266	0.0246	0.0233	0.0190	0.0153	0.0231
10	0.0344	0.0354	0.0312	0.0260	0.0224	0.0349
11	0.0429	0.0398	0.0430	0.0295	0.0235	0.0652
12	0.0486	0.0480	0.0490	0.0361	0.0342	0.0656
13	0.0605	0.0622	0.0430	0.0484	0.0501	0.0688
14	0.0720	0.0740	0.0750	0.0620	0.0603	0.0800
15	0.0841	0.0824	0.0750	0.0741	0.0688	0.1023
16	0.1836	0.1060	0.1070	0.0875	0.0845	0.1349
17	0.2418	0.2710	0.2780	0.0984	0.1010	0.1762
18	0.2631	0.2650	0.2760	0.2175	0.1294	0.1853
19	0.2765	0.2810	0.2730	0.3058	0.3083	0.1853
20	0.2942	0.2990	0.2750	0.3182	0.3211	0.1853

[1] Values given in Hand et al. (2001) were interpolated at the listed angles of attack for consistency between different Re_c values.
[2] Values obtained at the Colorado State University (CSU) wind tunnel (Hand et al., 2001).
[3] Values obtained at Ohio State University (OSU) wind tunnel (Hand et al., 2001).
[4] Values obtained at the Delft University of Technology (DUT) Low Speed Laboratory low-turbulence wind tunnel(Hand et al., 2001).
[5] C_{dp} values correspond to pressure drag coefficients (Hand et al., 2001).
[6] C_{dw} values correspond to total drag coefficient from wake traverse measurements (Hand et al., 2001).

Airfoil data

The lift (C_l) and drag (C_d) coefficients for the airfoils DU91-W2-250 and RISO-A1-21 are given in Table B.6 and Table B.7 respectively. For the NACA-64-418 the values are given for two different surfaces clean and rough (tripping tape) in Table B.8 and Table B.9 respectively. The values are taken from Boorsma and Schepers (2014) for single Re_c number. The values were interpolated at integer values of AOA.

Table B.4: MEXICO rotor blade geometry. Raw values digitised from Schepers and Snel (2007).

Radius [m]	Twist angle β [°]	Chord length c [m]
0.4504	16.4025	0.2396
0.6766	12.0951	0.2082
0.9005	8.3296	0.1797
1.1266	6.1046	0.1597
1.3506	4.8209	0.1426
1.5767	3.7084	0.1312
1.8006	2.0253	0.1169
2.0267	1.5118	0.1026
2.2507	0.0000	0.0855

Table B.5: MEXICO rotor blade geometry. Values interpolated to match airfoils sections and corresponding transition zones. Note that a cylindrical section (CYL) is added at the root between the hub radius and the reported blade geometry.

Airfoil	Radius r [m]	r/R [%]	Twist angle β [°]	Chord length c [m]
HUB	0.0000	0	0.0000	0.1950
HUB	0.2100	9.3	0.0000	0.1950
CYL	0.2100	9.3	0.0000	0.0900
CYL	0.3375	15.0	0.0000	0.0900
DU91-W2-250	0.4500	20.0	16.4025	0.2396
DU91-W2-250	0.7425	33.0	10.9873	0.1998
DU91-W2-250	1.0350	46.0	7.0066	0.1678
RISO-A1-21	1.2150	54.0	5.5982	0.1530
RISO-A1-21	1.4850	66.0	4.1597	0.1358
NACA-64-418	1.6650	74.0	3.0450	0.1256
NACA-64-418	1.9575	87.0	1.6692	0.1071
NACA-64-418	2.2500	100.0	0.0000	0.0856

Table B.6: 2D Airfoil data for DU91-W2-250 airfoil. Values digitised from Boorsma and Schepers (2014) (2D rough $Re_c = 0.5 \times 10^6$).

AOA [°]	C_d [−]	C_l [−]	AOA [°]	C_d [−]	C_l [−]
−18	0.09326	−0.95015	1	0.01926	0.36892
−17	0.09468	−0.89011	2	0.01916	0.49123
−16	0.08748	−0.81694	3	0.01918	0.60784
−15	0.07976	−0.72568	4	0.01991	0.71130
−14	0.07303	−0.66456	5	0.02091	0.81039
−13	0.07097	−0.62869	6	0.02258	0.89928
−12	0.06827	−0.59385	7	0.02542	0.96879
−11	0.06343	−0.54726	8	0.03114	1.02056
−10	0.05669	−0.48400	9	0.03881	1.06373
−9	0.04973	−0.43794	10	0.04104	1.07553
−8	0.04048	−0.37968	11	0.05417	1.10764
−7	0.03563	−0.31322	12	0.06860	1.16225
−6	0.03024	−0.25320	13	0.07713	1.17742
−5	0.02597	−0.19528	14	0.08366	1.18990
−4	0.02350	−0.13590	15	0.09063	1.20080
−3	0.02096	−0.06409	16	0.10045	1.20111
−2	0.01808	0.02015	17	0.11388	1.19156
−1	0.01629	0.12042	18	0.13337	1.18176
0	0.01493	0.24805			

Table B.7: 2D Airfoil data for RISO-A1-21 airfoil. Values digitised from Boorsma and Schepers (2014) (2D rough $Re_c = 1.6 \times 10^6$).

AOA [°]	C_d [−]	C_l [−]	AOA [°]	C_d [−]	C_l [−]
−10	0.02971	−0.60052	3	0.01085	0.68918
−9	0.02654	−0.52519	4	0.01087	0.79780
−8	0.02337	−0.44985	5	0.01117	0.90496
−7	0.02020	−0.37451	6	0.01185	1.01711
−6	0.01703	−0.29918	7	0.01288	1.12740
−5	0.01446	−0.21177	8	0.01486	1.22332
−4	0.01332	−0.09206	9	0.01764	1.29822
−3	0.01205	0.02660	10	0.02504	1.33742
−2	0.01897	0.13637	11	0.05091	1.30850
−1	0.01233	0.24930	12	0.08841	1.23995
0	0.01006	0.35940	13	0.10953	1.17683
1	0.01006	0.46800	14	0.11674	1.11028
2	0.01032	0.57803	15	0.13071	1.09177

Table B.8: 2D Airfoil data for NACA-64-418 airfoil. Values digitised from Boorsma and Schepers (2014) (2D clean $Re_c = 0.7 \times 10^6$).

AOA [°]	C_d [−]	C_l [−]
−1	0.01019	0.04643
0	0.01019	0.16648
1	0.01013	0.28397
2	0.00990	0.39139
3	0.00960	0.49826
4	0.00901	0.60252
5	0.00864	0.70591
6	0.00923	0.80420
7	0.01114	0.89558
8	0.01861	0.95719
9	0.02637	1.01184
10	0.03526	1.02986
11	0.04510	1.04487
12	0.05875	1.04803
13	0.07262	1.05406
14	0.08738	1.07372

Table B.9: 2D Airfoil data for NACA-64-418 airfoil. Values digitised from Boorsma and Schepers (2014) (2D rough $Re_c = 0.7 \times 10^6$).

AOA [°]	C_d [−]	C_l [−]	AOA [°]	C_d [−]	C_l [−]
−15	0.07121	−0.80137	2	0.01378	0.46249
−14	0.05868	−0.79555	3	0.01416	0.57232
−13	0.04799	−0.78468	4	0.01493	0.67593
−12	0.03871	−0.76923	5	0.01535	0.77434
−11	0.02832	−0.74223	6	0.01651	0.86508
−10	0.02417	−0.70894	7	0.01837	0.95237
−9	0.02057	−0.65261	8	0.02077	1.02139
−8	0.01797	−0.58081	9	0.02530	1.06681
−7	0.01592	−0.49833	10	0.03076	1.10378
−6	0.01490	−0.40179	11	0.04094	1.14094
−5	0.01356	−0.29794	12	0.05213	1.15221
−4	0.01318	−0.18909	13	0.06457	1.16883
−3	0.01318	−0.08020	14	0.07583	1.18141
−2	0.01318	0.03243	15	0.08965	1.18517
−1	0.01318	0.14128	16	0.10545	1.18534
0	0.01318	0.25012	17	0.12003	1.18017
1	0.01338	0.35631	18	0.13474	1.16221

BLANK PAGE

Appendix C

Benchmark models

Computational models are a cost-effective way of improving wind turbine design. However, the models still need to be validated. Typically, experimental measurements are used to assess the accuracy of a model. In Appendix B, two well-known wind tunnel experiments for wind turbines are briefly described: The NREL Ames Phase VI, and the MEXICO experiment. These experiments were developed to enhance the understanding of wind turbine aerodynamics and provide detail measurements for model validation under a wide range of operating conditions. As a result, several codes have been tested and compared as part of the MexNext project (Schepers, 2012; Schepers et al., 2014, 2018). These codes use a wide variety of modelling techniques, from simple Blade Element Momentum (BEM) theory and 1D momentum theory to full rotor simulations. Therefore, these simulation results also offer a great source to benchmark the performance of the ADM implemented in `turbineDisk`. Thus, in the validation section in Chapter 4, some results from other codes were included for comparison. The codes included were selected trying to have the four main types of models (e.g. BEM, ADM, ALM, and Full Rotor Simulations) and are briefly described in this appendix.

Uppsala-AD

The Uppsala-AD simulation were carried out at Uppsala University (See Sarmast et al. (2016)) with an actuator disk model implemented in EllipSys3D, a Navier-Stokes solver developed by Michelsen (1992), Michelsen (1994) and Sørensen (1995) at the RISØ-DTU National Laboratory. The data points used were digitised from Sarmast et al. (2016). In this study, both, actuator disk (ADM) and actuator line (ALM) models were used with and without the nacelle and hub geometry. However, here only the ADM without the nacelle/hub is considered (Schepers et al. (2018) also includes the Uppsala-AD). No specific details on the ADM implemented in EllipSys3D are given by Sarmast et al. (2016), but a description can be found in Réthoré et al. (2014). Moreover, Troldborg et al. (2015) indicates that this ADM used local inflow conditions to compute the forcing terms for momentum equations, and thus it is can also work in non-axisymmetric flow conditions. The simulations are run using Large Eddy Simulation for the New-MEXICO experiment, with a grid containing around 11.8 million cells, with the smallest cell size being $D/80$. The 2D airfoil data employed were provided by Boorsma and Schepers (2014), and applied without 3D corrections but using a tip-loss correction. Overall, this model is to some extent similar to the one implemented in `turbineDisk` (described in Chapter 4), and therefore it is considered a very good benchmark model for comparison.

ECNAero-BEM

The benchmark simulations labelled as ECNAero-BEM were performed with the ECN Aero Module developed by Boorsma et al. (2011) and Boorsma et al. (2016). This software has BEM based on PATHAS (Lindenburg, 2005) and a lifting line free vortex formulation AWSM based on Van Garrel (2003), and according to what is stated in Schepers et al. (2018), it also includes the state of the are engineering extension developed over several years of research in wind turbine aerodynamics (Prandtl corrections, 3D effects corrections, dynamic stall models, yaw corrections, pitch action, rotational speed variation). Note, however, that the data points used in Chapter 4 correspond only to BEM and are labelled as ECNAero-BEM for both, the New-MEXICO, and the NREL-VI experiments. The values were digitised from plots in Schepers et al. (2018) and Schepers et al. (2014) respectively. The simulation used 20 blade elements for the New-MEXICO experiment, and it was not specified for the NREL experiment. 3D corrections were applied in both cases. More details can be found in the above-mentioned references.

DTU-BEM

The DTU-BEM benchmark simulation used in Chapter 4 was carried out at the Technical University of Denmark. The blades are divided into 15 elements and the Shen et al. (2005a) tip-loss correction model was applied directly to the loading coefficients C_n and C_t. No root correction was used. The axial and rotational inductions factors were calculated also using the tip-loss correction factor. The BEM code also has a dynamic stall model implemented. This Blade Element Momentum model is described in more details in Schepers et al. (2018). Note that this benchmark model is only used with the NREL-VI experiment.

DTU-HAWC2

The HAWC2 model was developed at the RISØ National Laboratory of Denmark (nowsadays DTU Wind Energy). The model couples a structural model with an aerodynamic model. The aerodynamic part is an axisymmetric actuator disc model based on BEM and 1D momentum theory. It includes corrections for infinite number of blades, tip-losses, and yaw modelling. More details are described in Schepers et al. (2014) and Schepers et al. (2018). The benchmark data used in Chapter 4 were digitised from plots in Schepers et al. (2018) for the New-MEXICO experiment, and in Schepers et al. (2014) for the NREL-VI experiment.

DTU-AL

The DTU-AL benchmark is an Actuator Line Model (ALM) implemented in EllipSys3D code, a Navier-Stokes solver developed by Michelsen (1992), Michelsen (1994) and Sørensen (1995) at the RISØ-DTU National Laboratory. The turbulence was modelled using Large Eddy Simulation (LES). The tower was not included in the simulations, while two different configurations were used to include or not the nacelle and hub (See also Sarmast et al. (2016)). The benchmark values were digitised from Schepers et al. (2018) for the New-MEXICO experiment, but it is not clear if these values correspond to the configuration with or without the nacelle.

DTU-EllipSys3D

The DTU-EllipSys3D benchmark corresponds to a full rotor simulation using the code EllipSys3D, a Navier-Stokes solver developed by Michelsen (1992), Michelsen (1994) and Sørensen (1995) at the RISØ-DTU National Laboratory. The simulations considered the full rotor geometry and the nacelle. The $k - \omega - SST$ eddy viscosity model is used (Menter, 1994) and the loads were calculated using pressure distributions at five spanwise locations, neglecting viscous forces. Other details can be found in Schepers et al. (2014) and Schepers et al. (2018). Benchmark data shown in Chapter 4 were digitised from Schepers et al. (2014) for the NREL-VI experiment, and Schepers et al. (2018) for the New-MEXICO experiment.

CENER-CFD

The CENER-CFD benchmark corresponds to a full rotor simulation performed in a CFD model developed in collaboration between The National Renewable Energy Centre of Spain (CENER) and The University of Liverpool. The code solves the compressible Unsteady Reynolds Averaged Navier Stokes (URANS) equations, and it is capable of accounting for blade motion and deformation. More details can be found in Gómez-Iradi et al. (2009) and Schepers et al. (2014). However, for the NREL-VI experiment, the simulation data shown in Chapter 4 (digitised from Schepers et al. (2018)) consider rigid blades and solves only one-third of the rotor, assuming axisymmetry with periodic boundary conditions. The turbulence was modelled with the $k - \omega - SST$ eddy viscosity model.

Appendix D

ADM Sensitivity to cell size and smearing parameter ϵ

D.1 Mesh Resolution Sensitivity

One of the advantages of low order models such as the ADM implemented in `turbineDisk` (see Chapter 4), is that much fewer cells are needed making them more suitable to model wind turbine arrays. Réthoré (2009) found that ten cells per rotor diameter give reasonable predictions when using an ADM implemented in EllipSys3D. Later, van der Laan et al. (2014) recommended using at least eight cells per rotor diameter when using the $k - \varepsilon - f_P$ turbulence model they developed. However, when looking carefully at the plots they provided, even though eight cells allow to obtain good approximations while significantly reducing the computational cost, it is still possible to see differences in wake traverses even with 32 cells per rotor diameter. In this section, a mesh sensitivity is carried out to determine what is the most appropriate grid resolution for this work.

Six mesh resolutions are compared with 10, 20, 30, 40, 50 and 60 cells per rotor diameter. The structured mesh has a uniform cell size across the rotor and near wake regions. The smearing parameter ϵ is set to $0.1D$ following the sensitivity analysis in Section D.2. Note that ϵ is given relative to the turbine diameter D, and therefore, it is independent of the mesh resolution. The Shen et al. (2005a) tip correction factor is used with default coefficients $c_1 = 0.125$ and $c_2 = 21$. The New-MEXICO experiment is used since flow field measurements are also provided. The case analysed is MEX2 from Table 4.3 with $TSR = 6.65$ at 425.1 rpm and a pitch angle of $-2.3°$.

Blade loadings

Figure D.1 shows the loadings predicted using the six grid resolutions. The results are practically the same when using 20 or more cells per rotor diameter. However, using 10 cells per rotor diameter is not enough, which results in one hand in lower loadings, but an increased axial induction. This observation may sound counter-intuitive since lower loading should result in lower induction. Nevertheless, as discussed in Section D.2, $\epsilon = 0.1D$ (or $1\Delta x$ when using ten cells per rotor diameter) is too small and leads to unphysical behaviour.

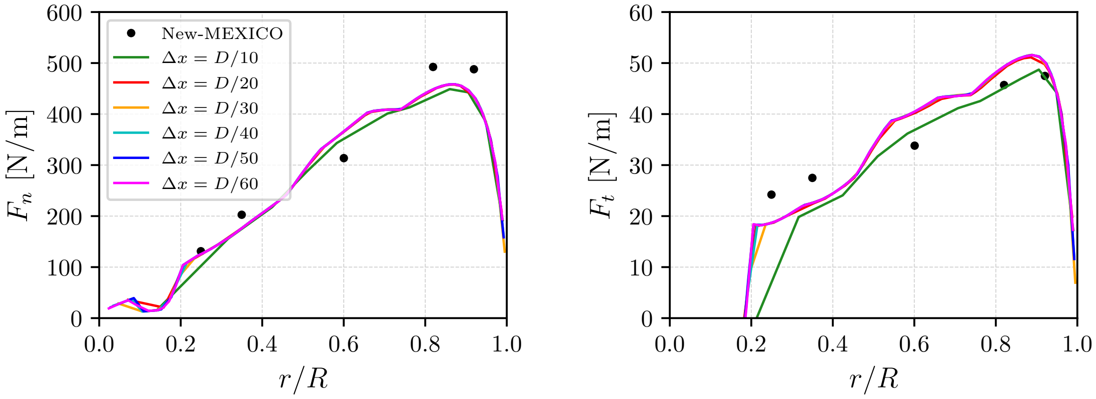

Figure D.1: Loadings along the blades of New-MEXICO experiment varying the grid resolution (i.e. cell size Δx). Experimental values digitised from Schepers et al. (2018).

Axial traverses

In Figure D.2, axial traverses of the three velocity components are shown. Note that the axial traverse is at a radius $r = 1.5$ m going from $x = -1D$ to $x = 1.5D$. Besides, the experimental values were measured at a specific azimuthal position and therefore are not directly comparable with ADM predictions that would represent azimuthal averages. Nevertheless, the comparison helps to assess how the ADM behaves. The axial and tangential velocity components U_x and U_t drop slightly more across the rotor with higher mesh resolution but changes become negligible when using 30 or more cells per rotor diameter. On the other hand, the radial velocity component is practically the same in all cases, except when using 10 cells across the rotor. These observations suggest that using 20 or more cells per rotor diameter is reasonable.

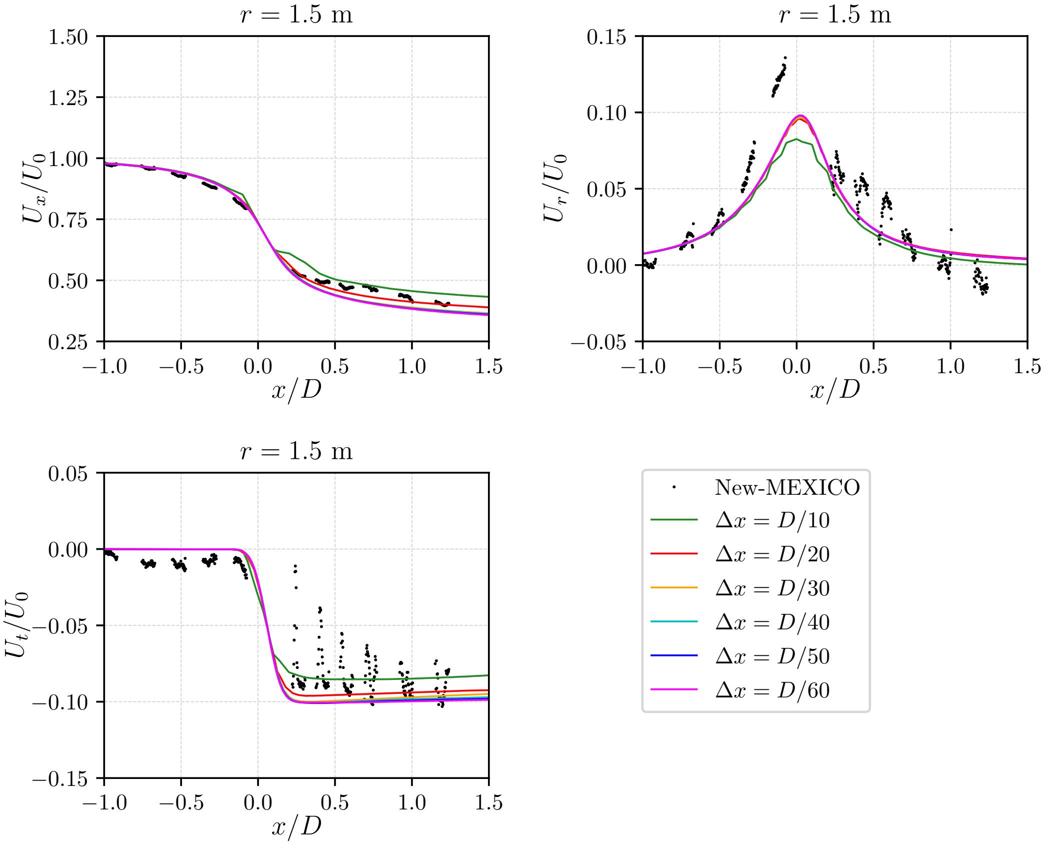

Figure D.2: Axial traverses for axial (U_x), radial (U_r) and tangential (U_t) velocity components. The traverse line is located at a radius $r = 1.5$ m and goes from $1D$ upstream to $1.5D$ downstream. The values are normalised with free flow velocity U_0. Experimental values were digitised from Schepers et al. (2018), and are measured at specific azimuthal position (0° azimuth.

Radial traverses

Radial traverses of velocity components are shown in Figure D.3. The traverses are located at $x = -0.3$ m upstream and $x = 0.3$ m downstream, and the experimental values are azimuthal averages. These plots show clearly that the ADM produces reasonable results when using at least 20 cells per rotor diameter. Using fewer cells does capture the main flow features, but accuracy is significantly affected, particularly in the outer region, which contributes the most to integral quantities.

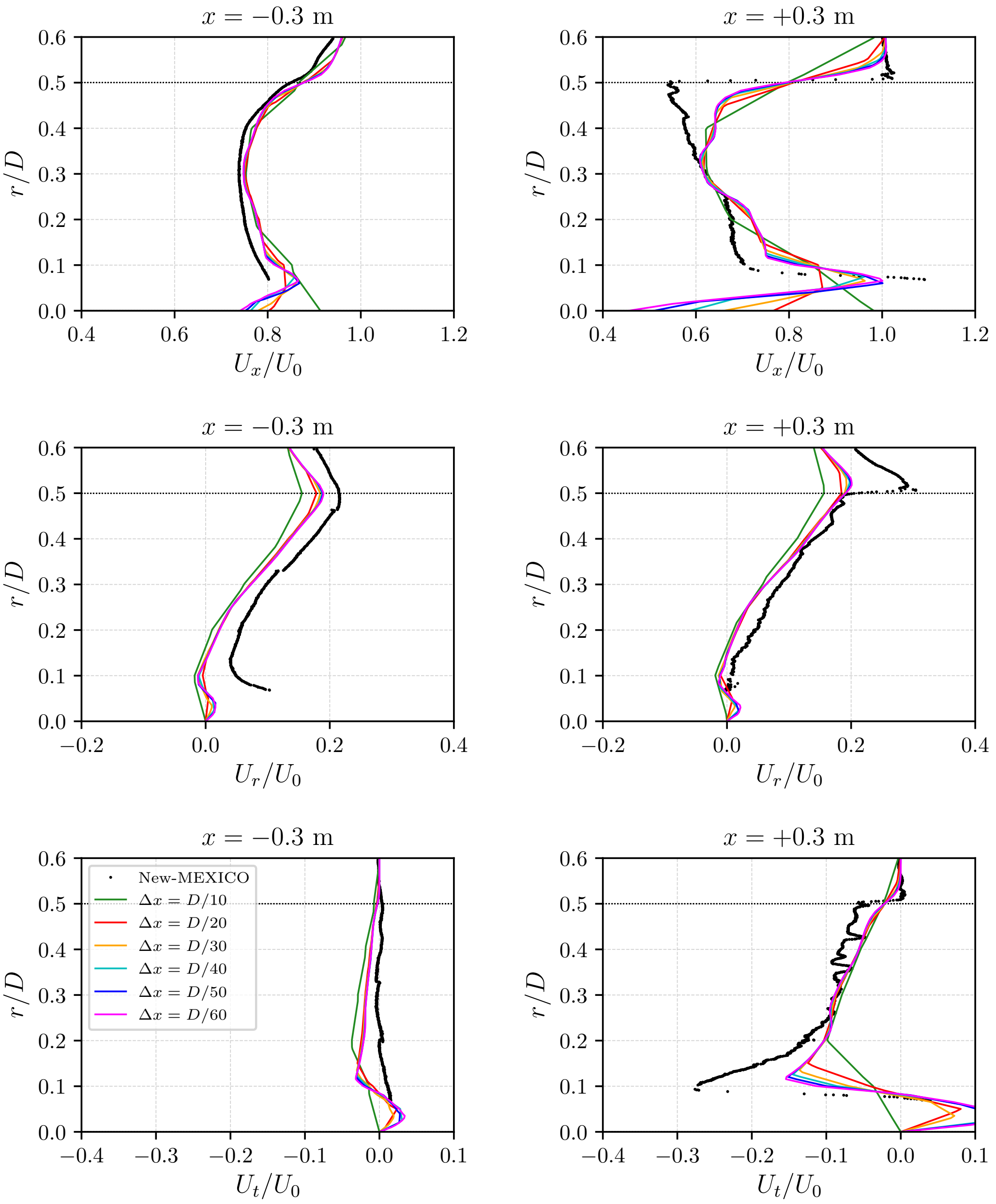

Figure D.3: Radial traverses for axial (U_x), radial (U_r) and tangential (U_t) velocity components (from top to bottom respectively) at two locations $x = -0.3$ m (upstream, to the left) and $x = 0.3$ m (downstream, to the right). The grid resolution is varied from $\Delta x = D/10$ to $\Delta x = D/60$. The values are normalised with free flow velocity U_0. Experimental values are azimuthal averages and were digitised from Schepers et al. (2018).

Increasing the mesh resolution results in two main effects: better prediction of the steep gradients of the axial velocity component U_x at the tip, and changes in velocities at the root and hub regions. This last observation reflects the fact that having a uniform mesh across the rotor results in a coarse mesh resolution in the inner region, that is not enough to capture the rather complex flow features. Therefore, predictions in this zone are indeed very sensitive to the mesh resolution. However, the differences do become smaller when changing between 50 and 60 cells per rotor diameter which suggest a grid independent result. Similar observations are made when looking at the near wake traverses of axial velocity U_x and turbulence intensity TI (not shown here).

Power and Thrust coefficients (C_P, C_T)

The impact of the mesh resolution on the power and thrust coefficients is shown in Figure D.4. The ADM predictions are very similar when using 20 or more cells per rotor diameter. The error, relative to the finest grid ($\Delta x = D/60$ marked with $*$), is less than 1% and 0.15% for C_P and C_T respectively. Furthermore, these integral quantities are practically the same when using 30 or 50 cells across the rotor, which indicates that using 30 cells is more cost-effective.

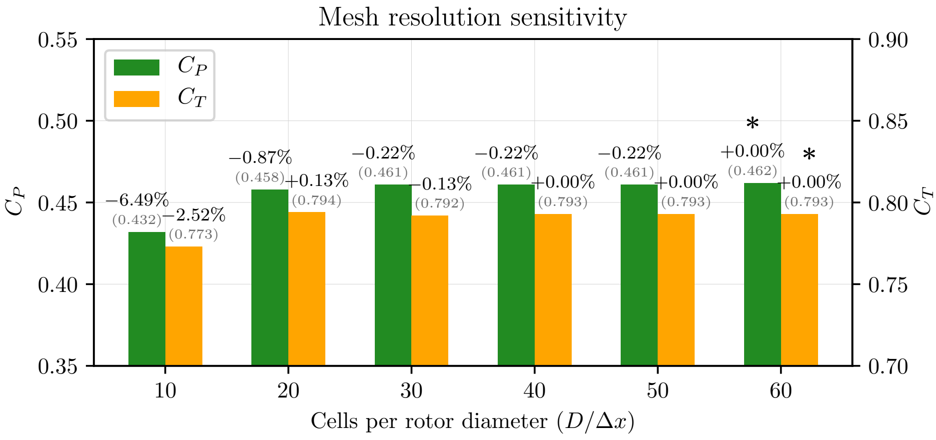

Figure D.4: Sensitivity of power and thrust coefficients (C_P, C_T) to the grid resolution (shown in the $x-$axis as cells per rotor diameter). The exact values are shown in brackets. Also, the error relative to the reference value X_{ref} (indicated with a $*$ symbol) is shown above the bars, which is calculated as $100(X - X_{ref})/X_{ref}$.

Mesh sensitivity conclusions

The effect of mesh resolution has been assessed. It was shown that using 10 cells per rotor diameter results in unphysical behaviour in the current setup since the smearing parameter ϵ is too small for such a coarse mesh. However, using 20 or more cells per rotor diameter results in reasonable predictions of the main flow features. As expected, grid refinement improves the results where high gradients occur, which is particularly important in the outer region, contributing the most to integral quantities. Nevertheless, power and thrust coefficients are practically the same when using 30 or more cells, and therefore it has been established that using 30 cells per rotor diameter is the most cost-effective alternative. Finally, it has been noticed one drawback of using a uniform grid across the rotor, the rather low resolution in the inner region, which is certainly not enough to capture the complex flow features. Nevertheless, this is expected for such a low-order model, and in general, the results are satisfactory.

D.2 Smearing parameter ϵ

Different values for ϵ have been used in the literature. Sørensen et al. (1998) analysed the influence of ϵ using values based on the mesh cell size (i.e. $\epsilon = 1\Delta x$, $\epsilon = 2\Delta x$ and $\epsilon = 1\Delta x$) with an actuator disk model reporting smooth variations of the velocity at the tip as ϵ is increased, but finally choosing $\epsilon = 1\Delta x$. Mikkelsen (2003) also reported that the values should be $1\Delta x < \epsilon < 4\Delta x$. Wu and Porté-Agel (2011), following Mikkelsen (2003), used $\epsilon = 1\Delta x$. Sarmast et al. (2016) used $\epsilon = 2.5\Delta x$ with the finest cells size of about $\Delta x \sim D/80$. In this section, the sensitivity of the ADM to the value of ϵ is assessed.

For this analysis, five different values of ϵ are used: $\epsilon = 0.025D = 0.75\Delta x$, $\epsilon = 0.05D = 1.5\Delta x$, $\epsilon = 0.10D = 3.0\Delta x$, $\epsilon = 0.15D = 4.5\Delta x$, and $\epsilon = 0.20D = 6.0\Delta x$. Here Δx corresponds to the cell size, which is kept uniform in all directions, and equal to $\Delta x = D/30$ (30 cells per rotor diameter). This grid resolution was choosen based on the mesh sensitivity analysis in Section D.1. The same case of the New-

MEXICO experiment is used.

Blade loadings

Figure D.5 shows the normal and tangential forces along the blades with different values of ϵ. The smearing parameter has very little effect on the loading that is slightly more noticeable for the tangential force F_t, increases slightly with higher values of ϵ. This is in agreement with Troldborg et al. (2015) who said that loads predicted by AD models are independent of smearing parameters. However, a small ϵ value results in an over-prediction of the axial induction leading to reduced loads along the blades.

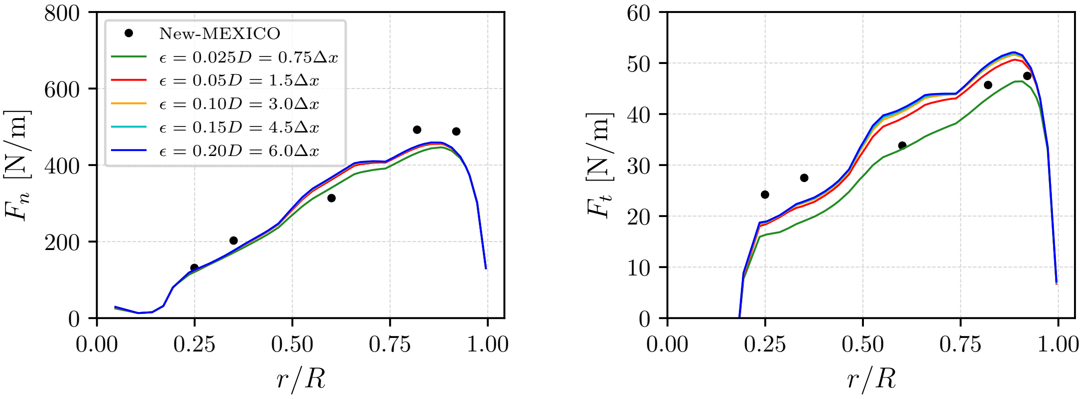

Figure D.5: Loadings along the blades of New-MEXICO experiment varying the smearing parameter ϵ. Experimental values digitised from Schepers et al. (2018).

Axial traverses

Figure D.6 shows axial traverses of velocity components. As expected, larger values of ϵ smooth out the velocity changes, which is more noticeable when looking at the radial and tangential velocity components. The smallest $\epsilon = 0.025D = 0.75\Delta x$ value is too small for the grid resolution resulting in unphysical behaviour. Increasing the mesh resolution does allow to use smaller values of ϵ, but even with 50 cells per rotor diameter, $\epsilon = 0.025D = 1.25\Delta x$ is too small. On the other hand, the rather large $\epsilon = 0.20D = 6.0\Delta x$ fails to capture the spike in radial velocity component U_r and predicts smoother velocity changes. Therefore, ϵ values between $0.05D = 1.5\Delta x$

and $0.15D = 4.5\Delta x$ result in a better balance between radial and tangential velocity predictions.

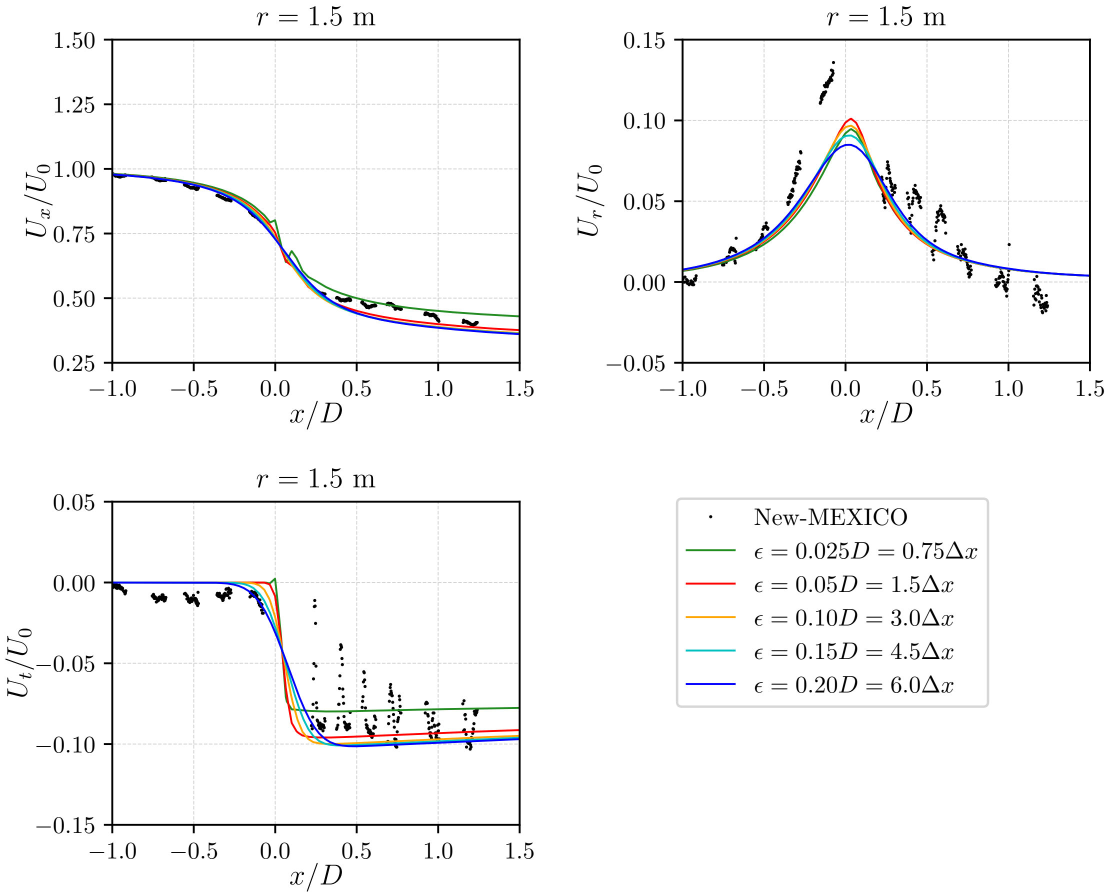

Figure D.6: Axial traverses for axial (U_x), radial (U_r) and tangential (U_t) velocity components. The traverse line is located at a radius $r = 1.5$ m and goes from $1D$ upstream to $1.5D$ downstream. The values are normalised with free flow velocity U_0. Experimental values were digitised from Schepers et al. (2018), and are measured at specific azimuthal position (0° azimuth.

Radial traverses

Figure D.7 shows the effect of the smearing parameter ϵ in the velocity components along radial traverses located at $x = -0.3$ m upstream and $x = 0.3$ m downstream. The AMD captures the main flow features but fails to reproduce the steep gradients of axial velocity U_x in the inner and outer regions. Some of the reason were discussed in Section D.1. In addition, large values of ϵ result in smoother changes of velocities at the tip, because the flow *feels* the presence of the turbine sooner, having more time to spread in all directions (diffusive effect). Thus, from these observations, a smaller value of ϵ should be preferred. The ϵ parameter has a negligible effect in the near wake traverse profiles (not shown here).

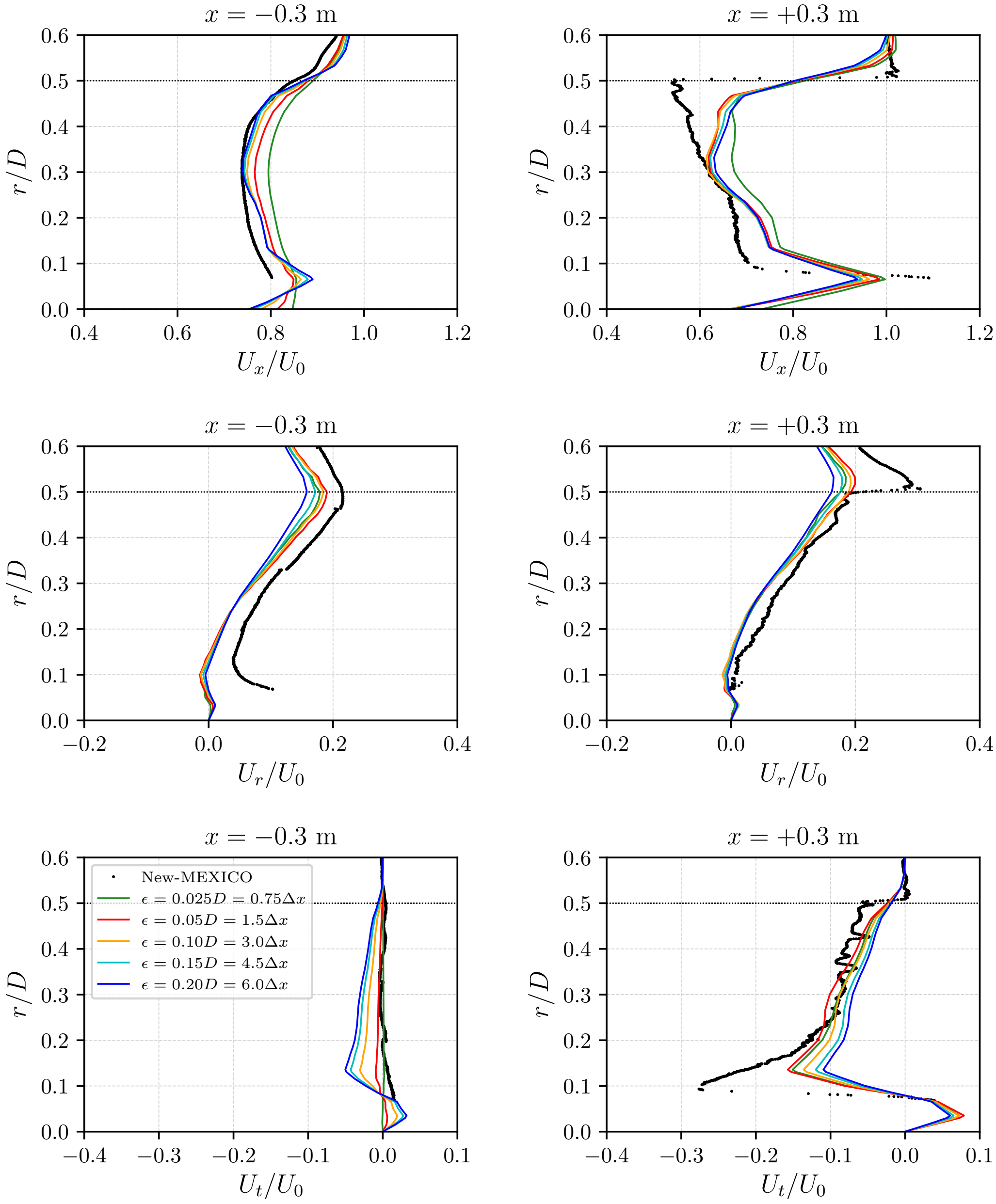

Figure D.7: Radial traverses for axial (U_x), radial (U_r) and tangential (U_t) velocity components (from top to bottom respectively) at two locations $x = -0.3$ m (upstream, to the left) and $x = 0.3$ m (downstream, to the right). The grid resolution is $\Delta x = D/30$. The values are normalised with free flow velocity U_0. Experimental values are azimuthal averages and were digitised from Schepers et al. (2018).

Power and Thrust coefficients (C_P, C_T)

Figure D.8 shows the effects of ϵ on the power and thrust coefficients. The power increases with ϵ as a result of the increased loadings. Note that the unphysical behaviour when using $\epsilon = 0.025D$ has a significant impact on the predicted power with an error of -11.93% compared to the case with $\epsilon = 0.1D$. For $\epsilon > 0.01D$ the relative error is within 1% for C_P and less than 0.4% for C_T.

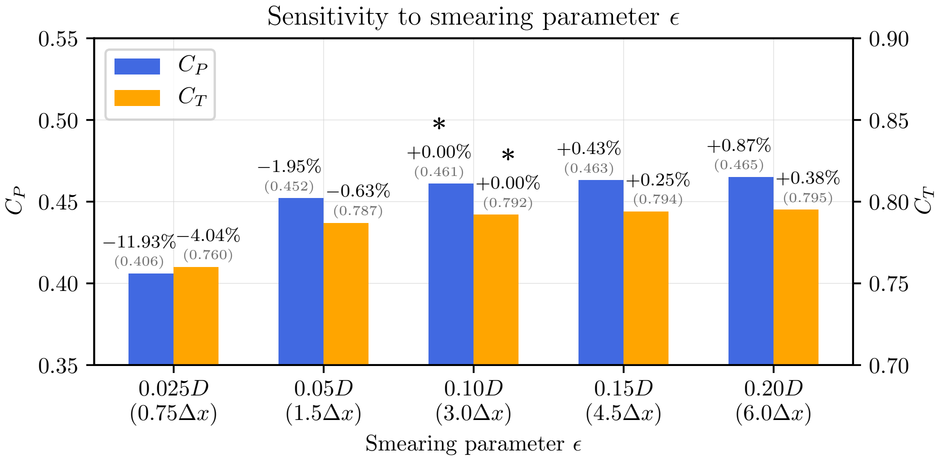

Figure D.8: Sensitivity of power and thrust coefficients (C_P, C_T) to the smearing parameter ϵ. The exact values are shown in brackets. Also, the error relative to the reference value X_{ref} (indicated with a $*$ symbol) is shown above the bars, which is calculated as $100(X - X_{ref})/X_{ref}$.

Conclusions on sensitivity to smearing parameter ϵ

The influence of the smearing parameter ϵ was assessed. Values of ϵ lower than $1.5\Delta x$ result in non-physical behaviour (with 30 cells per rotor diameter) and inaccurate predictions. When ϵ is large ($\epsilon > 0.1D$) the flow experiences the momentum source terms further upstream, having more time to spread smoothing out the velocity changes at the rotor, particularly in zones with high shear. This situation is especially significant near the tip, where velocity changes contribute the most to power and thrust. Following this analysis, it is concluded that $\epsilon = 0.1D$ is the most appropriate.